Phenothiazine based Polymers for Energy and Data Storage Application

Dissertation

zur Erlangung des Grades
"Doktor der Naturwissenschaften"
im Promotionsfach Chemie

am Fachbereich Chemie, Pharmazie und Geowissenschaften
der Johannes Gutenberg-Universität Mainz

Seyed Ahmad Ali Golriz
geboren in Teheran/Iran
Mainz, März 2013

Contents

Zusammenfassung

Die vorliegende Arbeit befasst sich mit der Synthese und Charakterisierung von Polymeren mit redox-funktionalen Phenothiazin-Seitenketten. Phenothiazin und seine Derivate sind kleine Redoxeinheiten, deren reversibles Redoxverhalten mit electrochromen Eigenschaften verbunden ist. Das besondere an Phenothiazine ist die Bildung von stabilen Radikalkationen im oxidierten Zustand. Daher können Phenothiazine als bistabile Moleküle agieren und zwischen zwei stabilen Redoxzuständen wechseln. Dieser Schaltprozess geht gleichzeitig mit einer Farbveränderung an her.

Im Rahmen dieser Arbeit wird die Synthese neuartiger Phenothiazin-Polymere mittels radikalischer Polymerisation beschrieben. Phenothiazin-Derivate wurden kovalent an aliphatischen und aromatischen Polymerketten gebunden. Dies erfolgte über zwei unterschiedlichen synthetischen Routen. Die erste Route beinhaltet den Einsatz von Vinyl-Monomeren mit Phenothiazin Funktionalität zur direkten Polymerisation. Die zweite Route verwendet Amin modifizierte Phenothiazin-Derivate zur Funktionalisierung von Polymeren mit Aktivester-Seitenketten in einer polymeranalogen Reaktion.

Polymere mit redox-funktionalen Phenothiazin-Seitenketten sind aufgrund ihrer Elektron-Donor-Eigenschaften geeignete Kandidaten für die Verwendung als Kathodenmaterialien. Zur Überprüfung ihrer Eignung wurden Phenothiazin-Polymere als Elektrodenmaterialien in Lithium-Batteriezellen eingesetzt. Die verwendeten Polymere wiesen gute Kapazitätswerte von circa 50-90 Ah/kg sowie schnelle Aufladezeiten in der Batteriezelle auf. Besonders die Aufladezeiten sind 5-10 mal höher als konventionelle Lithium-Batterien. Im Hinblick auf Anzahl der Lade- und Entladezyklen, erzielten die Polymere gute Werte in den Langzeit-Stabilitätstests. Insgesamt überstehen die Polymere 500 Ladezyklen mit geringen Veränderungen der Anfangswerte bezüglich Ladezeiten und -kapazitäten. Die Langzeit-Stabilität hängt unmittelbar mit der Radikalstabilität zusammen. Eine Stabilisierung der Radikalkationen gelang durch die Verlängerung der Seitenkette am Stickstoffatom des Phenothiazins und der Polymerhauptkette. Eine derartige Alkyl-Substitution erhöht die Radikalstabilität durch verstärkte Wechselwirkung mit dem aromatischen Ring und verbessert somit die Batterieleistung hinsichtlich der Stabilität gegenüber Lade- und Entladezyklen.

Des Weiteren wurde die praktische Anwendung von bistabilen Phenothiazin-Polymeren als Speichermedium für hohe Datendichten untersucht. Dazu wurden dünne Filme des Polymers auf leitfähigen Substraten elektrochemisch oxidiert. Die elektrochemische Oxidation erfolgte mittels Rasterkraftmikroskopie in Kombination mit leitfähigen Mikroskopspitzen. Mittels dieser Technik gelang es, die Oberfläche des Polymers im nanoskaligen Bereich zu oxidieren und somit die lokale Leitfähigkeit zu verändern. Damit konnten unterschiedlich große Muster lithographisch beschrieben und aufgrund der Veränderung ihrer Leitfähigkeit detektiert werden. Der Schreibprozess führte nur zu einer Veränderung der lokalen Leitfähigkeit ohne die

topographische Beschaffenheit des Polymerfilms zu beeinflussen. Außerdem erwiesen sich die Muster als besonders stabil sowohl mechanisch als auch über die Zeit.

Zum Schluss wurden neue Synthesestrategien entwickelt um mechanisch stabile als auch redox-funktionale Oberflächen zu produzieren. Mit Hilfe der oberflächen-initiierten Atomtransfer-Radikalpolymerisation wurden gepfropfte Polymerbürsten mit redox-funktionalen Phenothiazin-Seitenketten hergestellt und mittels Röntgenmethoden und Rasterkraftmikroskopie analysiert. Eine der Synthesestrategien geht von gepfropften Aktivesterbürsten aus, die anschließend in einem nachfolgenden Schritt mit redox-funktionalen Gruppen modifiziert werden können. Diese Vorgehensweise ist besonders vielversprechend und erlaubt es unterschiedliche funktionelle Gruppen an den Aktivesterbürsten zu verankern. Damit können durch Verwendung von vernetzenden Gruppen neben den Redoxeigenschaften, die mechanische Stabilität solcher Polymerfilme optimiert werden.

Abstract

My work described in the current thesis is focused on the synthesis and characterization of polymers with phenothiazine pendant moieties. Phenothiazine and its derivatives are small redox units with reversible redox and optical properties. The crucial aspect about phenothiazine is the formation of stable radical cation in the oxidized state. Therefore, phenothiazine derivatives are useful as bistable molecules which can be switched between two stable redox states which in addition are accompanied by a change in color.

Within the scope of this thesis, the synthetic approach to a new type of phenothiazine polymers by radical polymerization is described. In this context, phenothiazine derivatives were attached to aliphatic and aromatic backbones. Two synthetic routes were studied; one starting from a double bond monomer and the other from an amine containing monomer for post-functionalization with activated ester polymers. Both synthetic routes offer simple and effective approaches to obtain polymers with redox functionality.

Polymers with phenothiazine redox functionality are promising candidates as cathode active materials due to their electron donating properties. In order to prove their applicability and examine their performance, phenothiazine polymers were implemented as electrode material in battery cells. The phenothiazine polymers possess decent charging capacities between 50 and 90 Ah/kg at charging rates 5 to 10 times faster than conventional lithium batteries. With respect to long-term charging and discharging, phenothiazine baring polymers are very robust for over more than 500 charge-discharge cycles. It appeared that the stability depends strongly on the formation and the stabilization of the radical cation which is formed by reversible oxidation of the phenothiazine moieties. Long alkyl spacers between the backbone and the phenothiazine moiety help to stabilize the radical cation species and increase the life time of the battery regarding the number of charge and discharge cycles.

In addition to applications in batteries the bistability of phenothiazine polymers for high density data storage purposes was studied. Using the conductive mode of scanning force microscopy (SFM), nano-scaled patterning of spin-coated polymer films induced by electrochemical oxidation was successfully demonstrated. The scanning probe experiments revealed differences in the conductive states of written patterns before and after oxidation with no significant change in topography. Remarkably, the patterns were stable with respect to the storage time as well as mechanical wear.

Finally, new synthetic approaches towards mechanically nanowear stable and redox active surfaces were established. Via grafting from methods based on Atom Transfer Radical Polymerization (ATRP), redox active polymer brushes with phenothiazine moieties were prepared and characterized by SFM and X-ray techniques. In particular, a synthetic route based on polymer brush structures with activated ester functionality appeared as a very promising and versatile fabrication method. The activated ester brushes were used for

attachment of phenothiazine moieties in a successive step. By using crosslinkable diamine moieties, polymer brushes with redox functionalities and with increased surface wear resistance were successfully synthesized.

In summary, this work offers deep insights into the electronic properties of polymers with phenothiazine redox active moieties. Furthermore, the applicability of phenothiazine polymers for electronic devices was explored and improved from synthetic polymer chemistry point of view.

I. Introduction

1. General introduction

Conjugated polymers with alternating single and double bonds have gained rising interest in the field of electronics since the discovery of the conducting polymer polyacetylene by MacDiarmid and Heeger in the late 70's.[1] The discovery proved that polymers, so far known as isolating materials, are conductive[2,3] covering the range between semi-conductor and metallic conductors. Polymers as light weight functional materials are nowadays one of the most common components used for electronic device fabrication. A revolutionary trend in the electronic sector during the last ten years was set by printable electronics (PE).[4] Functional polymers are processed in solution with techniques like roll to roll process[5] or spin, dip and spray coating[6]. They allow the production of cheap and flexible integrated circuits (IC) that can be used e.g. for disposable electronics[7- 12] and packaging[13]. As an example, ultra thin layered and flexible batteries[14,15] were fabricated recently by printing techniques. This type of battery can find application in identification cards such as Radio Frequency Identification (RFID) card or IC card embedded in the electric circuit. The market for flexible, cheap and disposable devices is constantly growing in the present due to our consumer friendly world. It is estimated that the demand for PE will reach $ 21.6 billion by the year 2015.[16]

One of the biggest challenges for the PE is the aspect of processing.[17] Due to their inflexible molecular design, conjugated polymers have limited solubility and are therefore not often appropriate materials for device fabrication. The limited solubility leads also to phase separation. As a consequence, the polymer is detached from the surface by dewetting[18] or delamination[19]. Another big challenge is related to the low chemical stability of the conjugated polymers.[20] Oxidation process and depolymerization depending on the doping state are well established degradation mechanisms.[21,22] To improve the solution processability and chemical stability of the π-conjugated polymers, the only approach so far is the functionalization of the polymer with solubilizing substituents[23] or by integrating electron deficient groups[24] into the polymer backbone. The synthetic approach for modification of conjugated polymers is however a quite elaborate process.

As an alternative concept to conjugated polymers, my focus was placed on the synthesis of new polymers with isolating aliphatic or aromatic backbones having pendant redox functionalities (Scheme 1, b). Polymers with pendant redox functionalities are interesting because of their electronic properties. Redox moieties can be attached to a variety of polymer backbones and immobilized in close vicinity to each other by covalent bonds. The neighboring groups interact with each other enabling fast electron exchange (Scheme 1b). By electrochemical oxidation, the doping level of these polymers is increased. The increase of the doped sites supports the electron exchange which leads to a decrease of the electrical resistance and to an increase of conductivity. In contrast to conjugated polymers, the electronic functionality of

polymers with pendant redox moieties is localized on the polymer side chains instead of the main chain (Scheme 1, a).

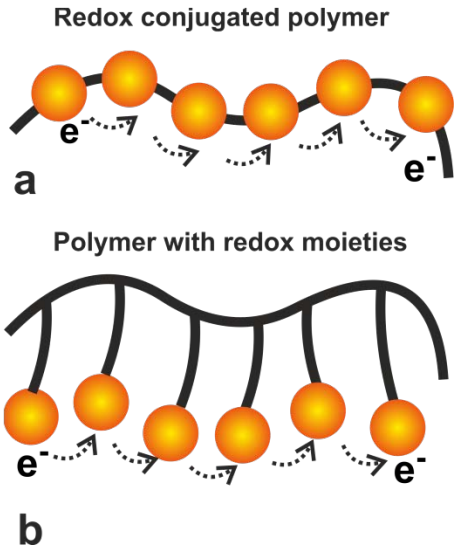

Scheme 1. Difference between a) conjugated polymer with functional redox units incorporated in the main polymer chain, b) polymer with redox moieties attached to the polymer backbone. Electrons are transferred by exchange between the moieties

The big advantage is that the polymer main chain can be selected individually to obtain good solubility in a desired solvent. In many cases these polymers can be dissolved in common organic solvents.[111] Thus, the redox functionality is concealed and combined for example with physical properties of a standard thermoplastic. This property is important for good material processing in manufacturing processes. The flexibility of the synthesis allows precise and easy control over the physical properties such as viscosity, elastic modulus and glass transition temperature. The right choice of the polymer backbone as well as the redox moiety results in functional polymers with high material performance for electronic devices. Despite all the advantages of polymers with redox moieties, only few works were dedicated so far to this type of polymers.[25,197]

Polymers with large metal organic moieties were reported as redox active materials.[26,27] However, smaller redox moieties are more advantageous. They generally have fast redox chemistry and higher charge storage capacity due to their low molecular weight. As immobilized moieties in a redox active polymer, they can easily get into the proper junction position by rotational freedom. In this context, polymers with N-carbazole moieties were proposed as good p-donating materials with high charge carrier mobility.[28] In 2009, Oyaizu and Nishide introduced the concept of non-conjugated polymers with stable radical redox moieties for battery devices.[29] Using small nitroxide moieties, a new type of fast ultra fast charging organic batteries were accessible.[112] This battery type can be fully charged within less than a minute.[113] The greatest advantage of this type of battery is the possibility of using printing technique to obtain flexible ultra thin layered batteries for supplying small electronic devices like active RFID cards.[30,31]

In 1985, Morishima et al. discovered that polymers with phenothiazine redox moieties can electrochemically be switched from isolating state to semi-conducting state with five orders of magnitude increase in conductivity.[85] The switching results from the orientation of the side chains in an adequate juxtaposition via π-π stacking which enables electron exchange between the moieties. Phenothiazines[32] are small heterocyclic molecules with well studied reversible redox properties. By oxidation, phenothiazine molecules can reversibly form stable radical cations which change the conformation of the molecules from bent to planar. The presence of the nitrogen and sulfur atom in phenothiazine enables the synthetic approach to a variety of polymers with redox properties.

In the current work, various new polymers with phenothiazine pendant moieties were synthesized for application in the field of energy and data storage media. The novelty of the work is the development of simple and effective synthetic strategies to these polymers as well as their application in the mentioned fields. Monomers bearing phenothiazine moieties were synthesized to obtain polymers with redox functional properties. In this context, the usefulness of activated ester polymers for attachment of phenothiazine moieties via polymer analogous reaction was approved. In a unique approach, grafted activated ester brushes were functionalized with phenothiazine moieties. Grafted polymers brushes have an increased surface energy and cannot dewet or delaminate. The activated ester approach is a new versatile synthetic method to obtain redox active polymer surfaces. This method could for example be applied on electrode surfaces to prevent phase separation of organic materials and to improve surface wear resistance. With electrochemical measurement methods, the redox activity of some synthesized phenothiazine polymers was investigated. Due to the reversible formation of the stable radical species by oxidation, phenothiazine based polymers are interesting as storage medium. They could serve as p-type cathode material in battery cells to store energy in the stabilized charged state. Phenothiazine polymers have so far not been used as energy storage materials. The stability of the radical cation could help to improve polymer self discharge phenomena due to decomposition of the charged species. The stability of the radical cation is also useful to store information. Bistable switching by oxidation should lead to changes in conductivity in the polymer film. Particularly, switching of the polymer film on the nanoscale was induced locally by scanning force microscopy (SFM). The use of the SFM technique in combination with the phenothiazine polymer is a new promising approach to high density data storage application.

2. Objectives and motivation

In chapter II, different synthetic options are presented for synthesis of redox active polymers with phenothiazine moieties. The aim of this chapter is to evaluate and compare different strategies for the synthesis of polymers with phenothiazine moieties regarding to their molecular design and their yield of the reaction. Monomers containing vinyl groups are synthesized for polymerization via standard radical approach. Alternative routes are presented

which start from activated ester polymers by means of post-functionalization. Phenothiazine derivatives with amine substitution were synthesized and converted with the activated ester polymers to result in polymers with pendant phenothiazine moieties. The molecular design has influence on the processing of the polymers as well as on their physical and electrochemical properties. The flexibility of the side chains for example affects the glass transition temperature and the thermal stability of the polymers. For the post-functionalization approach, a quantitative conversion of the activated ester moieties to phenothiazine moieties is desirable. The quantitative conversion guarantees that redox moieties are attached to the polymer backbone in close vicinity to each other. The high density of the redox moieties should improve electron self exchange rate and increase the charging capacity of the polymer. Also for grafting of redox active phenothiazine polymers presented in chapter V, knowledge of monomer reactivity and steric aspects are crucial issues.

In chapter III, a selection of phenothiazine bearing polymers is characterized with respect to their electrochemical redox behavior. The goal is to find adequate polymers which can find application as a cathode material in lithium battery devices. I performed the experiments to this part of the thesis in Japan investigating my synthesized phenothiazine polymers as a collaboration with the group of Prof. Hiroyuki Nishide from the Waseda University in Tokyo. The performance of the polymers as cathode active materials depends on the radical stability as well as the electrochemical properties. Thus, in this section, the effect of molecular design on the electrochemical properties and radical stability is studied. The overall apparent charge diffusion and the electron exchange rate of the polymer electrode material are determined by electrochemical methods cyclic voltammetry and chrono amperometry. The stability of the redox state especially for the formation of the radical cation is important with respect to storage of charges. To answer the question how molecular design affects the radical stability, decay process of the oxidized state is investigated by means of UV/Vis spectroscopy as well as electron spin resonance technique. The radical stability is an important property regarding the long-term cycle stability and the self discharge of batteries. For the battery performance, charge and discharge speed, charge capacity as well as the cell potential are parameters which depend on the electrochemical properties of the electrode material. In chrono potentiometry experiments, these parameters are investigated. The charge and discharge performance is examined by integration of the polymers as cathode active materials in lithium coin cell batteries. Finally, the performance of the polymers is compared and related to the effect of the molecular design.

Chapter IV deals with patterning of a polymer film with phenothiazine moieties. The goal of this project is not only to use the redox active polymers to store charges but also electrical information on the nanometer scale. Thus, redox active polymers with phenothiazine moieties are investigated as possible media for data storage application. For investigating the data storage process on the nanoscale level, spin coated films of a polymer with phenothiazine moieties were oxidized electrochemically by using a conductive SFM tip. This project was done

in a collaboration with Dr. Tassilo Kaule from Prof. Hans-Jürgen Butt's group at the Max Planck Institute for Polymer Research in Mainz. My part was the preparation of the samples and the evaluation of the SFM data. With the electrical mode of SFM, a bias potential is applied to an electrically conducting tip while scanning the surface of the polymer film. The bias potential induces oxidation which in turn leads to changes in local conductivity in the polymer film. The local change in conductivity can be then detected with the same tip. Writing, reading and erasing electrochemically induced patterns are studied with SFM. In addition, the ability of the polymer films to store and retain data as electrochemically induced patterns was studied in long-term SFM experiments. At the end of the chapter IV, the mechanical nanowear stability of the polymer film is examined with SFM. The effect of the applied force on mechanical stability is discussed with respect to possible application of a phenothiazine polymer as data storage medium. The results of this chapter were the motivation for development of new polymer architectures with increased mechanical stability. Therefore, synthetic techniques such as grafting and crosslinking of polymers were considered as alternative strategies.

Finally, grafting techniques are applied to attach redox polymers as tethered chain to conductive surfaces in chapter V. Polymer chains with phenothiazine moieties are immobilized on the substrate by surface initiated atomic transfer radical polymerization (SI-ATRP). The objective of this chapter is to evaluate a synthetic route to obtain redox active polymer surfaces with homogeneous morphology and with increased nanowear stability. Grafted structures help to increase mechanical nanowear stability and reduce surface detachment. Two different synthetic routes are chosen to design the grafted polymer brush films. In the first route, monomers with phenothiazine moieties were directly polymerized from the surface in a grafting from approach. In the second route, activated ester monomers were polymerized in a grafting from approach. Then, subsequently the grafted polymers were post-functionalized with phenothiazine moieties. The direct polymerization is a simple approach allowing the attachment of the redox polymers as grafted brushes in a one step process. The post-functionalization route involves the attachment of the redox moieties to the polymer brush as moieties in a subsequent reaction. This approach is more complicated but at the same time more versatile for different redox moieties. The difference between the synthetic routes is reflected by the surface morphology. Surface morphology with low nanoscale roughness is preferred for patterning of the redox polymer films via SFM. The polymer brush films are examined with regard to their redox behavior, their surface morphology and their chemical composition with the help of SFM and X-ray techniques. Furthermore, the surface nanowear stability of the grafted brushes is investigated and compared for both synthetic routes. Especially, for the post-functionalization route, the effect of crosslinkable redox moieties on the surface nanowear is examined. Thus, the two synthetic routes offer alternatives to redox active polymer surfaces for individual applications.

II. Synthesis of phenothiazine based monomers and polymers

1. Introduction

Stability of the redox state is an important issue for obtaining bistable materials. Phenothiazine and its derivatives can form so called "persistent radicals" in the oxidized state. The redox chemistry and the reactivity of phenothiazines are important for synthesizing phenothiazine based polymers. Many groups have focused on synthesizing conjugated polymers using phenothiazine as a p-donating group. However, phenothiazine based polymers with pendant moieties attached to an isolating polymer backbone have hardly been investigated. The redox properties of phenothiazine based polymers have been widely used in electronic application such as organic light emitting diodes (OLED).

In this chapter, the synthetic approach to different monomers and polymers with phenothiazine redox moieties is described. The aim is to evaluate easily accessible and versatile synthetic approaches to polymers which allow the tuning of the physical properties such as solubility and redox behavior. For the synthetic approach two different routes can be used. The first route involves the direct attachment of the phenothiazine redox moieties to a polymerizable monomer unit with a double bond. A series of phenothiazine based monomers with vinyl backbone were synthesized for radical polymerization. Position of the polymerizable group and bulkiness of the monomers has an influence on their reactivity. Monomers with vinyl groups at different position and spacer length have been chosen as target molecules. The aim is to obtain monomers which can easily be polymerized via radical polymerization especially under controlled conditions. This way homogeneous polymer film can be synthesized e.g. by surface initiated polymerization technique. Attachment of the phenothiazine redox moiety to the polymerizable unit has the advantage that all the moieties in the polymer bear a redox moiety, thus increasing the density of functional units. For the second route, a functional polymer was used to attach the redox moieties to the polymer backbone via a polymer analogous reaction. Here, I examined activated ester polymers, which were functionalized with amine substituted phenothiazine redox moieties. This approach might be interesting, if the polymerization of the phenothiazine monomers fails due to steric reasons or lack of reactivity of the monomers. The variation of spacer length between the phenothiazine moiety and the polymer backbone was achieved by taking advantage of diamines protected on one side. Commercially available diamines with varying spacer length were attached to phenothiazine after protection and could react further with the activated ester polymers after subsequent deprotection. However, this approach can only be useful, when the substitution of the redox moieties proceeds quantitatively. This means, ideally all moieties must be functionalized to obtain a high density of redox functional groups. Nevertheless, the polymer analogous reaction reveals certain advantages due to its chemical versatility and flexibility. Different backbone and side chain architecture can be incorporated inside the polymer chains which influence the redox behavior

and the redox stability of the polymers. Longer spacer length stabilizes the oxidized radical species and also facilitates the orientation of the redox moieties.

In the following section the concept of stable and persistent radicals is presented with focus on phenothiazine and its derivatives. Furthermore, an overview of phenothiazine based polymers is given. Finally, the synthetic approach is further elucidated and the results are presented and discussed.

2. Theoretical background

2.1. Stable radicals

Radicals are molecules or atoms consisting of typically one unpaired electron. The unpaired electron in the singly occupied molecular orbital (SOMO) is under normal circumstances quite reactive. Radicals can react with oxygen, dimerize, disproportionate or abstract hydrogen in solution.[33] The unstable or "transient" radicals undergo bi- or monomolecular decay reactions at the limit of diffusion controlled kinetics.[34] In some cases however the radical can be stabilized and possesses an elongated life time, thus enabling its spectroscopic characterization. This means that the bimolecular self reaction is slow and the unimolecular decay reaction like the β-elimination is extremely slow or does not take place. In this case, the radical species is called "persistent" radical. In some cases, the radical can even be isolated and stored under ambient conditions, where it is then defined as "stable" radical. Inorganic stable radicals are for example dioxygen (O_2) or nitric oxide (NO). The first persistent organic radical was discovered by Gomberg in 1900[35] where he describes (Scheme 2) the formation of substituted triphenylmethyl radical (Scheme 2, b) from triphenylmethylchloride (Scheme 2, a). Gomberg stated that the radical reacts with oxygen forming a peroxide species (Scheme 2, c). In other works, Gomberg and Wieland showed the formation of the triphenylmethyl and phenyl (Scheme 2, e) radical from phenylazotriphenylmethane (Scheme 2, d) by heating. [36,37]

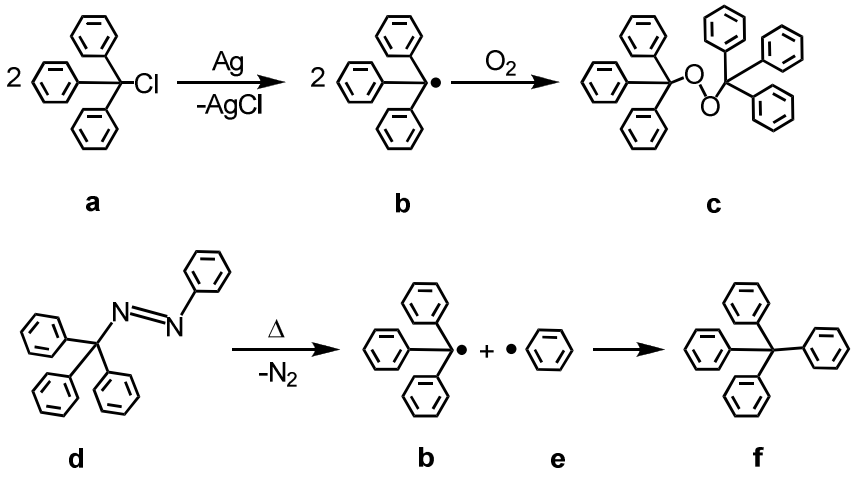

Scheme 2. Formation and subsequent reaction of triphenyl radicals: a) triphenylmethylchloride, b) triphenylmethyl radical, c) bis(triphenyl) peroxide, d) phenylazotriphenylmethane, e) phenyl radical and f) tetraphenylmethane.

There are several reasons for stability of radicals. In case of triphenylaryl radicals, Mosberg already recognized the steric effect of the substituents on the central C-atom. The more substituents are attached to the phenyl rings and the more sterically hindered they are, the more stable are the radicals. Some substitutes lead to formation of twisted geometry[38] (Scheme 3, a, b and c), which prevents the spin delocalization of the singly occupied p-orbital of the sp^2 hybridized C-atom (Scheme 3, c).[39] Also bulky and purely aliphatic groups without β-hydrogens like *tert*-butyl groups can help to stabilize the carbon radical and prevent dimerization like in the case of tri-*tert*-butylmethyl radical (Scheme 3, d).

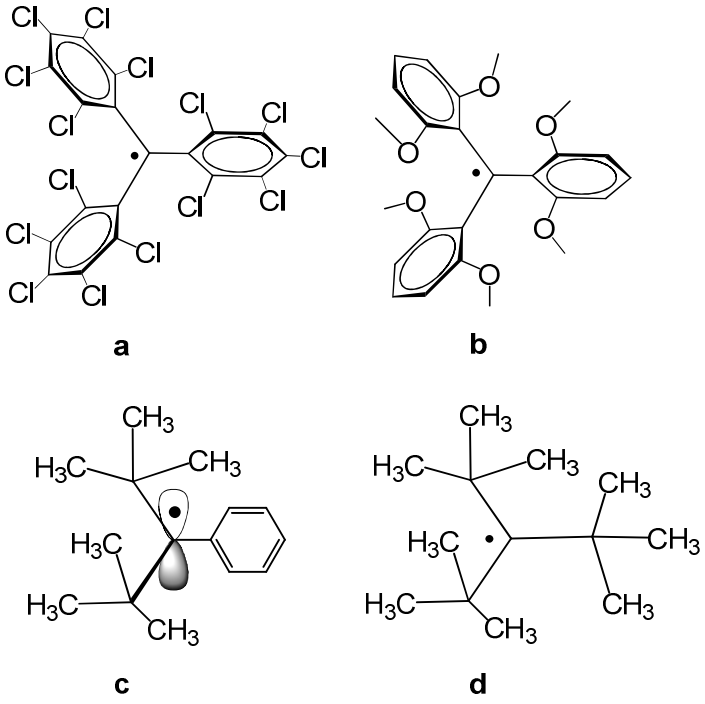

Scheme 3. Stable radicals stabilized by twisted geometry and steric hindrance: a) tris(perchlorophenyl) radical, b) tris(2,6-dimethoxyphenyl)methyl radical, c) di-*tert*-butylphenylmethyl radical and d) tri-*tert*-butylmethyl radical.

Except for the steric shielding, which is responsible for kinetic stability of radicals, resonance effects of delocalized electron can lead to thermodynamic stability. Koelsch and coworkers synthesized in 1931 a delocalized carbon based radical (Scheme 4, a) that was confirmed and identified later in 1957.[40] Subsequently, other types of Koelsch radicals like Nitrogen analogues and diradicals have been reported.[41] The more delocalized resonance states can be formed, the more stabilized the radical can be. Among the stable radicals, nitrogen based radicals like nitroxide reveal the highest stability due to the delocalization of the unpaired electron between nitrogen and oxygen atom (Scheme 4, b).

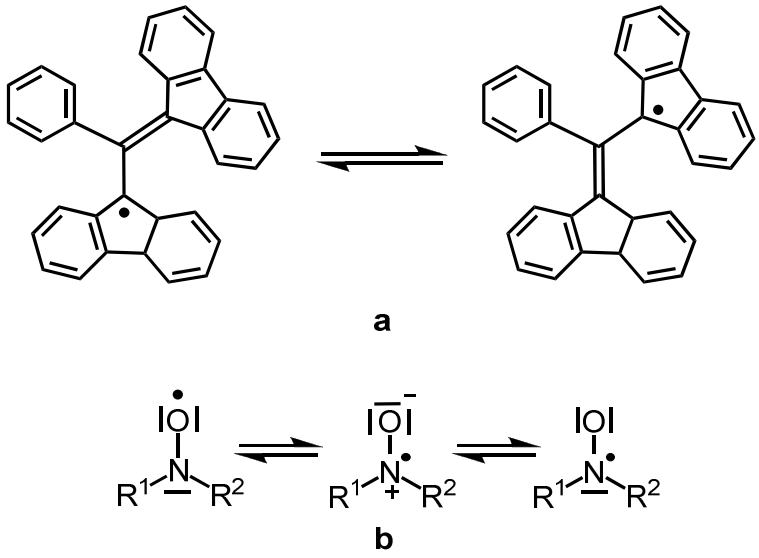

Scheme 4. Stable radicals stabilized by delocalization: a) Koelsch radical and b) nitroxide radical.

In addition, using bulky substituents without hydrogen atoms in α-position and conjugated aromatic groups, radicals with high stability in solid as well as in solution can be obtained. A series of nitroxide[42-45], nitronyl nitroxide[46-48] and hydrazyls[49-51] have been synthesized and characterized by several groups (Scheme 5). One of the most prominent candidates are 2,2,6,6-tetramethylpiperidine-1-oxyl (TEMPO; Scheme 5, a), N,N di-*tert*-butyl nitroxide (DBN; Scheme 5, b), 4,4,5,5-tetramethyl-2-(4-nitrophenyl)-4,5-dihydro-1H-imidazole-3-oxide-1-oxyl (TNPIO; Scheme 5, c) and 1,3-nitroxide N,N -diphenyl-N-picrylhydrazyl (DPPH; Scheme 5, d).

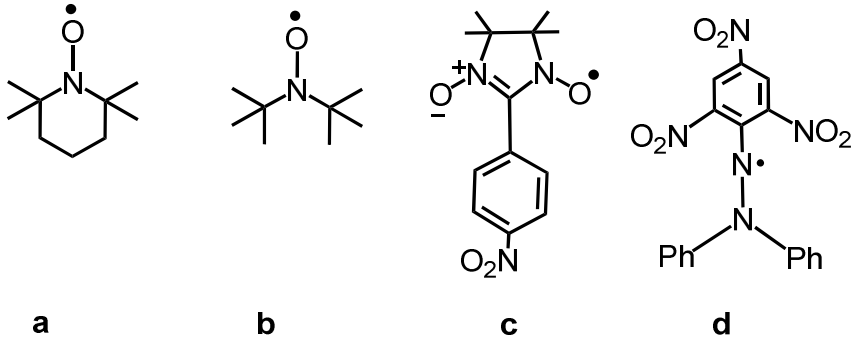

Scheme 5. Stable radicals based on nitoxide (a, b), nitronyl nitroxide (c) and hydrazyl (d) groups: a) 2,2,6,6-tetramethylpiperidine-1-oxyl (TEMPO), b) N,N di-*tert*-butyl nitroxide (DBN), c) 4,4,5,5-tetramethyl-2-(4-nitrophenyl)-4,5-dihydro-1H-imidazole-3-oxide-1-oxyl (TNPIO) and d) 1,3-nitroxide N,N -diphenyl-N-picrylhydrazyl (DPPH).

Among persistent radicals, charged radical like cations or anions are quite common. These types of radicals are mainly stabilized by resonance effects. Ring annealed aromatic and hetero aromatic groups (Scheme 6) like phenoxazine (Scheme 6, a)[52], phenoxathiine (Scheme 6, b), thianthrene (Scheme 6, c)[53] and phenothiazine (Scheme 6, d)[32] form persistent radical cations. This class of molecules and specially their radical cation species are quite well known to interact with living organisms in pharmacological and biological processes. Especially phenothiazine and its derivatives are well studied in the literature.[54-56]

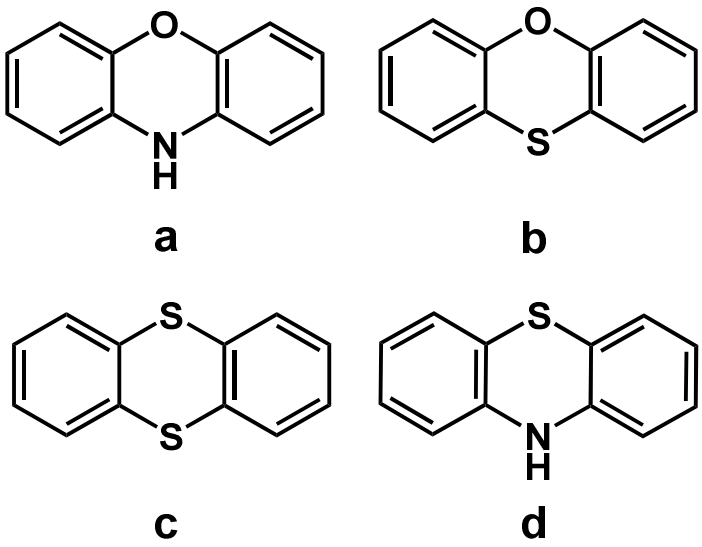

Scheme 6. Ring annealed molecules forming persistent radicals: a) phenoxazine, b) phenoxathiine, c) thianthrene and d) phenothiazine.

2.2. Phenothiazine and its derivatives

10H- phenothiazine (phenothiazine) is an electron rich heterocyclic molecule with interesting physical and chemical properties (Scheme 7). Phenothiazine and its derivatives are sensitive to light and oxygen and can mainly be dissolved in organic solvents.

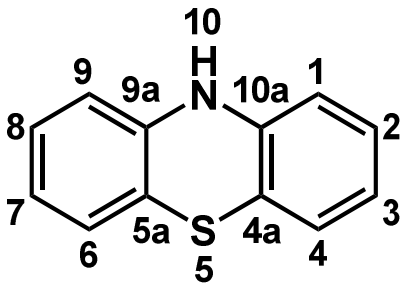

Scheme 7. Phenothiazine molecules with the substitution nomenclature.

One of the first derivatives of phenothiazine called “methylene blue” (MB) was synthesized by Caro at BASF in 1876 (Scheme 8, a). The first synthetic approach to phenothiazine succeeded by Bernthsen in 1883.[57] Bernthsen characterized the quinoide structure of MB and another dye called “Lauth’s violet” (Scheme 8, b). In the same year, Paul Ehrlich reported the bactericide properties of MB. In the field of molecular biology, MB is further used as a staining agent and dye for DNA and RNA as well as specific tissue types.[58] Since then, many other types of dyes and derivatives like new methylene blue (NMB; Scheme 8, c) were synthesized based on phenothiazine. One of the most frequent applications for phenothiazine derivatives is in the field of pharmacy. Promethazine (ATOSIL®; Scheme 8, d) and chlorpromazine (MEGAPHEN®; Scheme 8, e) as well as trifluorpromazine (PSYQUIL®; Scheme 8, f) are used as antihistaminic and psychotropic agents, respectively.[32]

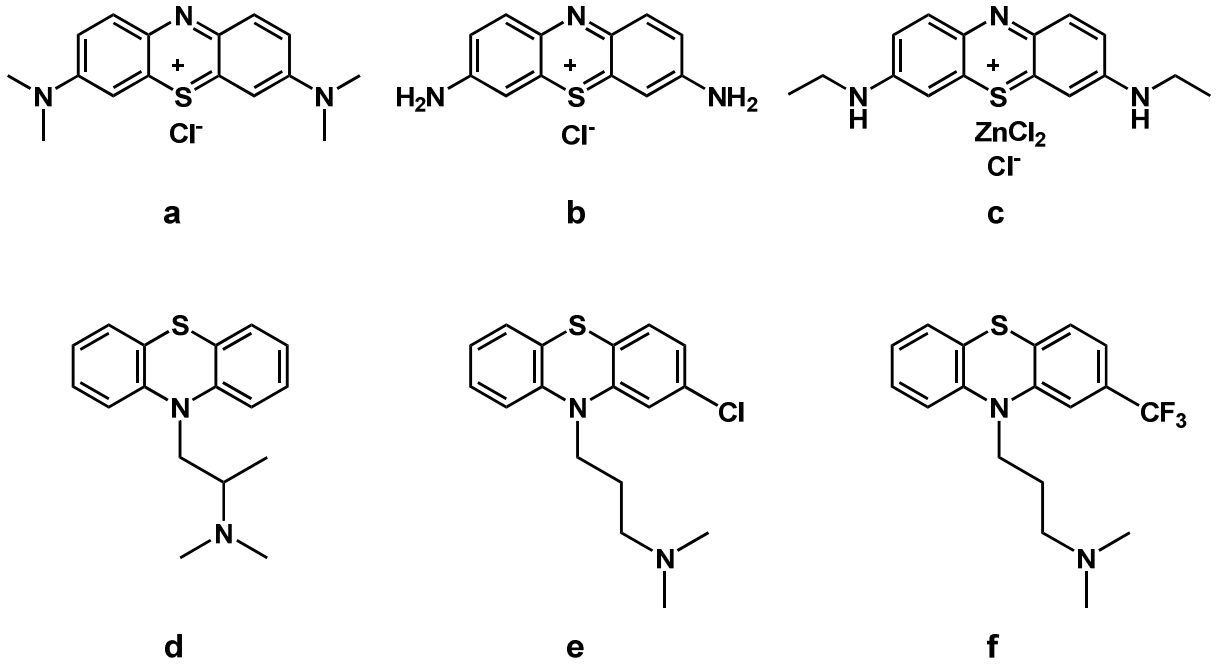

Scheme 8. Phenothiazine derivatives in the literature: a) methylene blue (MB)[57], b) Lauth's violet[58], c) new methylene blue (NMB), d) promethazine (ATOSIL®), e) chlorpromazine (MEGAPHEN®) and f) trifluorpromazine (PSYQUIL®).[32]

The molecule phenothiazine has an angulated structure with respect to the N-S axis which is called "butterfly" structure (Scheme 9). This angulated structure allows the H-atom located at the N-position to take in the "H-intra" or "H-extra" conformation, with the H-atom being in the quasi equatorial or quasi axial position, respectively. Concerning their electrical properties, both conformations are not equivalent. The intra conformation is energetically preferred, because the free electron pair on N-atom can better overlap with the π-delocalized system of the annealed benzene rings. Therefore, unsubstituted phenothiazine derivatives prefer the intra conformation, whereas substituents on the N-position enforce the aromatic system to align in the extra conformation due to steric reasons. Thus, the oxidation potential of the N-substituted phenothiazines is increased due to the reduced contribution of the free electron pair of nitrogen inside the π-delocalized system. The oxidized state of phenothiazine leads to the formation of a radical cation species with an almost planar structure.[59] In this state, N- and S-atom can overlap with the π-orbital of the aromatic C-ring. According to the electron spin resonance (ESR) data, the nitrogen centre changes from pyramidal to a planar structure in the radical cation state where the free electron pair is mainly localized at the N-atom.[60] The oxidized radical cation can be further oxidized to the dication species with the oxidation taking place at the free electron pair of the S-atom.

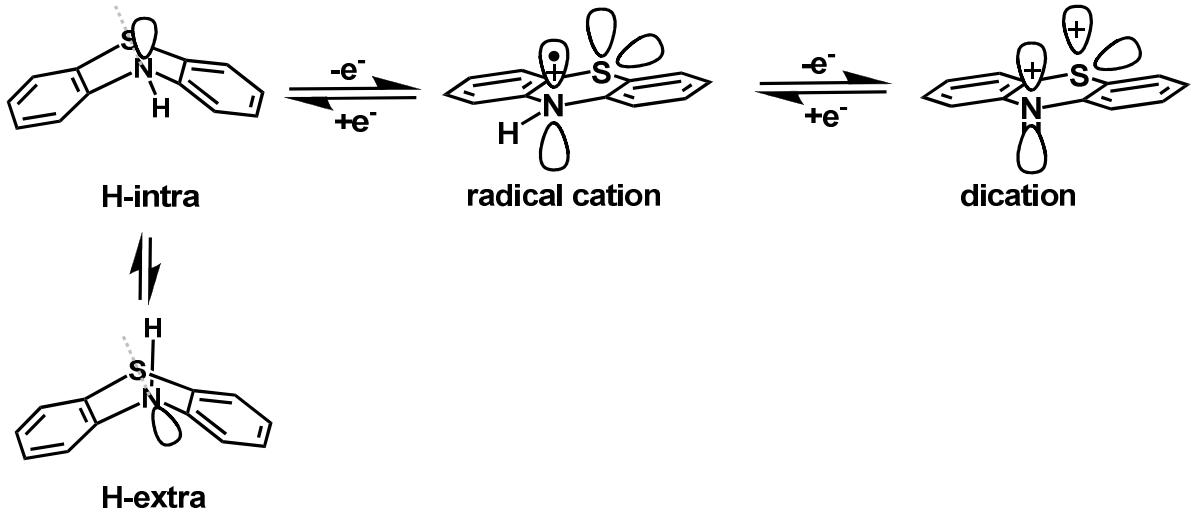

Scheme 9. Conformational geometry of phenothiazine depending on the oxidation state.

Recently, phenothiazines have been investigated because of their redox and electric properties. They possess low and reversible oxidation potential and can serve as electron donating molecules with semi conducting properties.[61] Billon and coworkers demonstrated two separate single electron oxidation processes for phenothiazine.[62] Besides, the radical cation species is a persistent molecule which does not undergo further successive reaction. Due to their electron donating properties, phenothiazine derivatives have been used to examine electron transfer processes. König et al. observed photo induced electron transfer in a phenothiazine riboflavin donor acceptor dyad complex resulting from large fluorescence deactivation.[63] Miles et al. examined multiple electron transfer from phenothiazine units coupled to gold nano particles via hexanthiole groups.[64] Due to their inter-molecular electron transfer ability, phenothiazines have also been used to build up molecular wires. In a study by Hunag[65] et al., stilbazol units tethered together as a molecular donor-acceptor unit to quarz substrate were reduced by electron transfer from phenothiazine. Alkynated and aryl bridged phenothiazine dyads and triads[66] were attached to gold substrates to form a monolayer of molecular wires with switchable conductivity.[67,68]

Phenothiazines have also been reported for application in analytical chemistry. Owing to the high stability (persistence) of the phenothiazine radical cation, the formation and interaction of the radical species with the metabolism is widely examined especially in the pharmaceutical sector.[69,70] Huiwang et al. reported the stabilization of N-substituted phenothiazine radical cation in β-cyclodextrin.[71] In other works phenothiazine, moieties have been covalently anchored in the mesoporous structure of silica. Hence, the orientation of the phenothiazine moieties was predefined and radical cations were formed after oxidation in the pore matrix. The generated radical cation species was proved by ESR and revealed very high stability for the period of several days.[72] Due to their conductive properties, many phenothiazine containing polymers have been reported in the literature as described in the upcoming section.

2.3. Phenothiazine based polymers in the literature

Due to the hole conductivity of the phenothiazine, and its ability to reversibly form a stable radical cation, oligomers and polymer molecules containing phenothiazine units are also of great interest for electronic application (Scheme 10). For poly-phenothiazines as homopolymers[73-75] (Scheme 10, a, b and c) conductivities in the range of 10^{-3} to 10^{-7} S/cm after doping with iodine or protons were reported. The hole conductivity of poly-phenothiazines mainly results from the formation of polarons in p-doped state. Especially for Polymer Light Emitting Diodes (PLED), polymers with conjugated phenothiazine moieties have proved to be appropriate. Copolymers containing thiophene (Scheme 10, d)[76] as well as phenothiazine and fluorene (Scheme 10, e)[77,78] were used as emitting layers in PLEDs. These polymers are not only good hole transporting materials but they also reveal an increase of the fluorescence compared to the homo polymers.[79] Polymers with pendant groups using phenothiazine moieties have been reported as hole transporting host polymers by Thesen and coworkers.[80] The polymers consist of triphenylamine backbone and reveal a luminous efficiency of around 30 cd/A and a brightness of approximately 6000 cd/m^2.

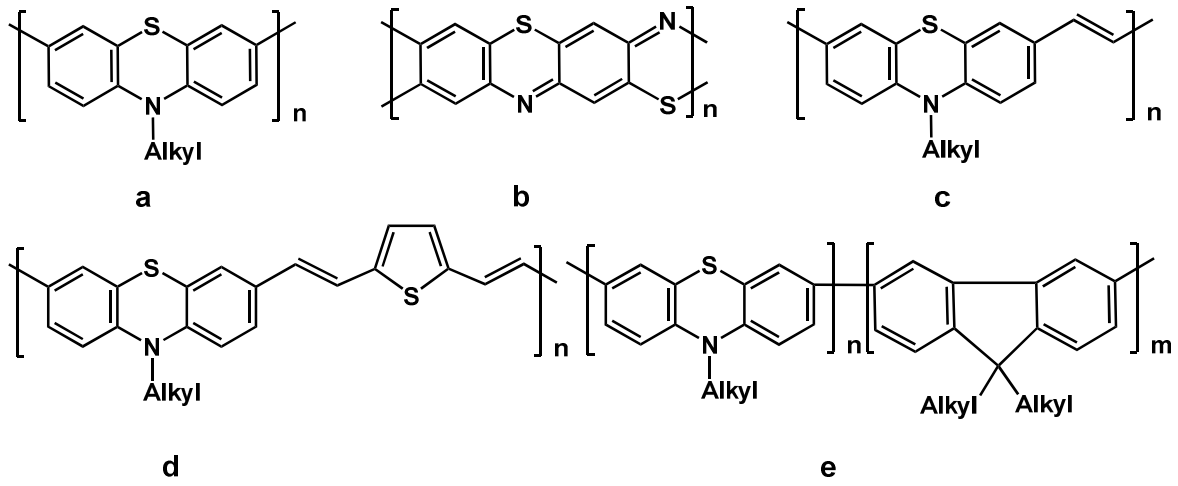

Scheme 10. Conjugated phenothiazine polymers reported in the literature: a), b) and c) are conjugated homopolymers[73-75] while d) and e) are copolymerized with thiohphene[76] and fluorene[77,78].

For electronic applications conjugated polymers are generally used. A few works have been done on polymers with non-conjugated backbones with phenothiazine moieties. Klöpffer and coworkers were the first group to synthesize polyacetal and polyvinyl compound with phenothiazine moieties as electron donating groups.[81] However, the obtained vinyl polymer was rather a byproduct of a spontaneous side reaction. The latter polymer called "poly-3-vinyl-N-methylphenothiazine" (PVMPT; Scheme 11, a), was later synthesized by Gipstein and coworkers using free radical polymerization.[82] Other polymers with phenothiazine pendant groups based on silane (Scheme 11, b)[83] and epoxide (Scheme 11, c)[84]backbones were synthesized as new photosensitizers.

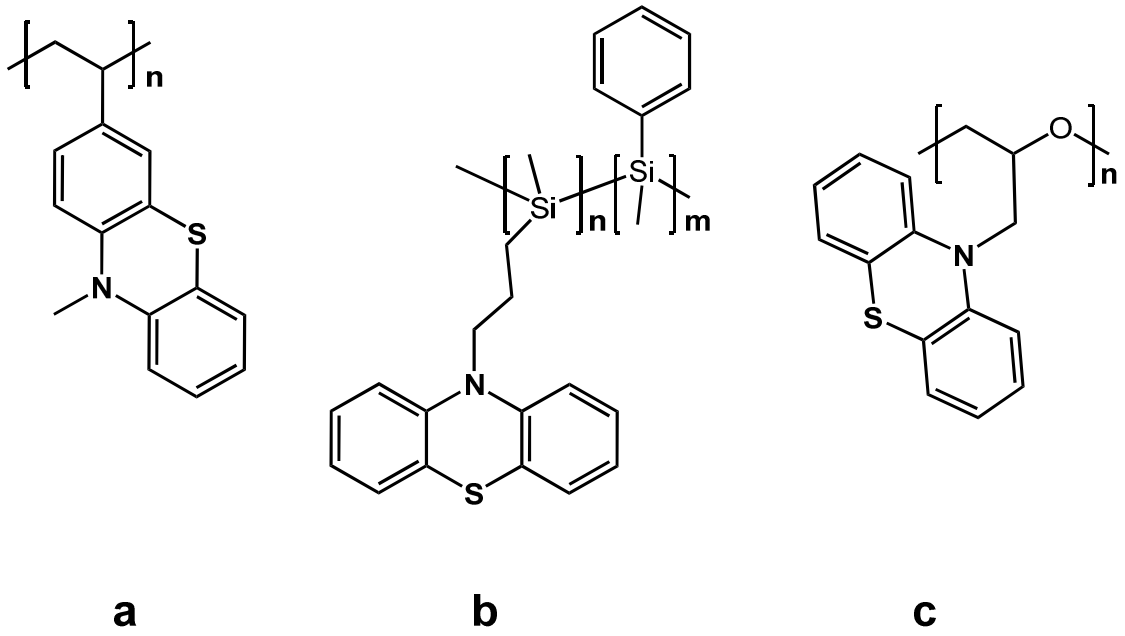

Scheme 11. Polymers with phenothiazine pending moieties: a) poly-3-vinyl-N-methylphenothiazine (PVMPT)[82], b) silane based[83] and c) epoxide based[84] phenothiazine polymer.

Morishima and coworkers studied conductive properties of PVMPT and other copolymers containing methylmethacrylate as monomer. They observed that the intrinsically insulating PVMPT illustrates an abrupt increase of the conductivity upon partial electrochemical oxidation.[85] Upon oxidation of 3-4 mol% of the phenothiazine moieties, the conductivity increased from 10^{-10} S/cm to the semiconducting level at 10^{-5} S/cm. The abrupt increase of five orders in magnitude was ascribed to self exchange electron transfer between neighboring oxidized and reduced groups. Proofs for interaction of phenothiazine moieties in PVMPT were presented in other studies.[86] Herein, Morishima et al. stated that homopolymers of PVMPT can be electrochemically oxidized up to 90%, whereas copolymers always remained unoxidized to a certain extent.[85] This behavior can mainly be explained by the proximity of phenothiazine moieties in the homopolymer which facilitates the interaction in the spherical polymer coil. Unlike homopolymers, the copolymer methyl methacrylate (MMA) increases the spacing distance between the electroactive centers. The increased spacing prevents site-to-site interaction like π-π-stacking which then reduces the oxidation probability. In order to interact with each other, oxidized and reduced moieties have to move into the right position for effective electron transfer. This process requires a loss of entropy due to polymer chain deformation which has to be compensated by exothermic electronic interaction of the redox sites.[87] For electron self exchange, the rate constant (k_{ex}) for PVMPT has been determined between 10^5 and 10^6 $M^{-1}s^{-1}$.[87] In comparison to free phenothiazine moieties in solution, the value is 3 orders in magnitude lower.[88] The lower value for k_{ex} can be explained by the additional restriction due to the segmental motion of the moieties to a proper exchange position. However for PVMPT, k_{ex} is still in the same order of magnitude as for self exchange between iron Fe^{+II}/Fe^{+III} complex in solutions.[89,90] Thus, the switching between the oxidized and reduced state must be a fast process.

Except for the large increase of conductivity by partial oxidation, PVMPT exhibits a reversible electrochemical oxidation accompanied by a significant color change from colorless to reddish purple. The oxidation results in the N-methylphenothiazine radical cation which was reported to be a persistent radical species.[91] Under ambient open circuit conditions, oxidized PVMPT retains its color and thus its oxidation state for several months. Morishima et al. stated that PVMPT displays a "memory effect" related to the oxidation state.[86] Due to the stability of the radical cation species and the mentioned memory effect, phenothiazine based polymers are appropriate candidates for long-term storage of charges. This ability can be used for storing information or energy in the charged state. In the following section, an overview of synthetic approaches to polymers with phenothiazine moieties is presented. Possible synthetic strategies to monomers with vinyl moieties for direct polymerization and amine moieties for post-functionalization are discussed and elucidated.

3. Synthetic approach

3.1. Monomers with phenothiazine moieties

There are several synthetic approaches to phenothiazine based monomers and their subsequent polymerization. For the synthesis of the monomer, phenothiazine molecule can be attached at the N-position or from a side position at the aromatic ring. Due to increased reactivity of the amine bond, it's more likely to use the N-position to attach vinyl containing groups by nucleophilic substitution reaction (Scheme 12). To enable the reaction, the phenothiazine has to be deprotonated at the N-position to serve as a nucleophilic agent. Halogenated vinyl substituents will then react with phenothiazine to give the desired monomer:

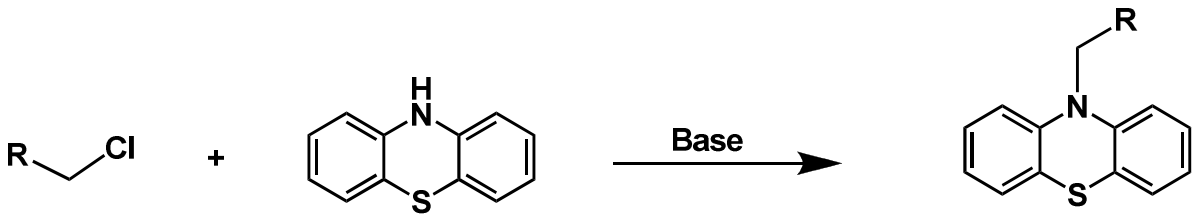

Scheme 12. Nucleophilic substitution of phenothiazine at N-position.

It is also possible to use coupling reactions to attach phenothiazine to a halogenated aromatic ring with an aldehyde group via copper as coupling agent in a classical Ullmann reaction (Scheme 13).[92] As aromatic aldehyde, 4-bromobenzaldehyde (BBA; Scheme 13, a) can be used which results in 4-(10H-phenothiazine-10-yl)benzaldehyde (PBA; Scheme 13, b) after the coupling. In a second step, the aldehyde reacts via a Wittig synthesis to form the desired double bond monomer 10-(4-vinylphenyl)-10H-phenothiazine (VPP; Scheme 13, c). This way, a phenothiazine monomer with extended π-conjugation along the aromatic backbone is obtained.

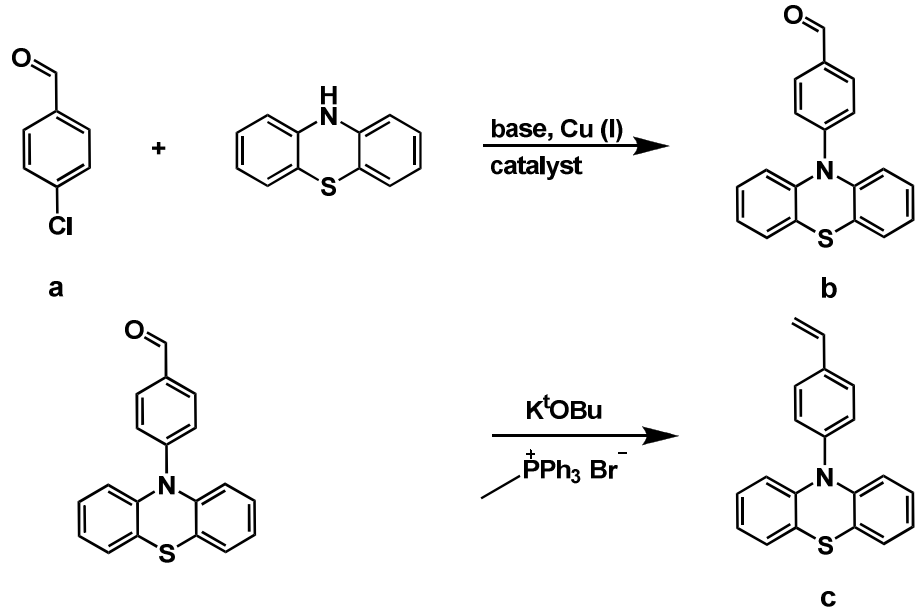

Scheme 13. Ullmann coupling reaction for N- substitution at phenothiazine: a) 4-bromobenzaldehyde(BBA), b)4-(10H-phenothiazine-10-yl)benzaldehyde (PBA) and c) 10-(4-vinylphenyl)-10H-phenothiazine (VPP).

As an alternative to N-substitution, a further approach could follow by substituting aromatic ring positions of phenothiazine (Scheme 14). Phenothiazine derivatives like N-methylphenothiazine (MP; Scheme 14, a) can be turned into the corresponding aldehyde 10-methyl-10H-phenothiazine-3-carbaldehyde (MPCA, Scheme 14, b) by the Vilsmeier-Haack reaction. In the following step, the aldehyde group is turned into a vinyl double bond via the Wittig reaction. The end product is 10-methyl-3-vinyl-10H-phenothiazine (MVPT; Scheme 14, c).

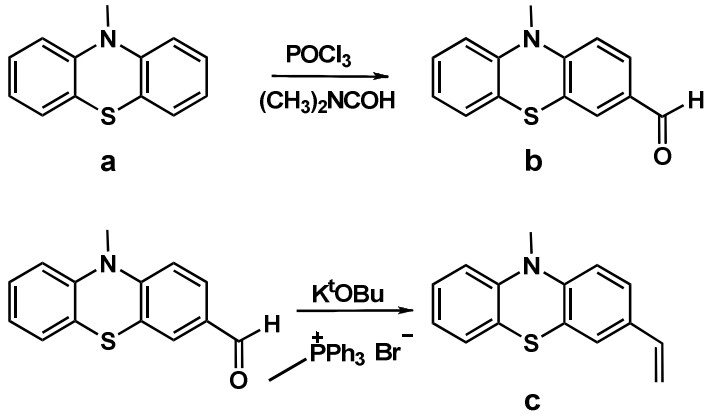

Scheme 14. Combination of Vilsmeier-Haack and Wittig reaction for synthesis of phenothiazine vinyl monomer at position 3 in the aromatic ring: a) N-methylphenothiazine (MP), b) 10-methyl-10H-phenothiazine-3-carbaldehyde (MPCA) and c) 10-methyl-3-vinyl-10H-phenothiazine (MVPT).

The aldehyde functionality is quite useful for other synthetic steps. For example, it can be used to attach a methyl methacrylate group in the substitution position 3, which serves as the polymerizable group (Scheme 15). Methacrylate monomers can be introduced by the reaction

with phenothiazines containing alcohol or amine moieties. It is also possible to deprotonate the amine group of phenothiazine itself using a strong base (as for the nucleophilic substitution) and attach the phenothiazide salt to (meth)acryloyl chloride. However, due to the steric reasons, it might be difficult to polymerize the monomer. Therefore, I decided to use the alcohol, since the carbaldehyde/aceto phenothiazine could easily be converted to alcohol by hydration (Scheme 15, a). The substituted group can then react with (meth)acryloyl chloride (Scheme 15, b) to result in the desired monomer (Scheme 15, c).

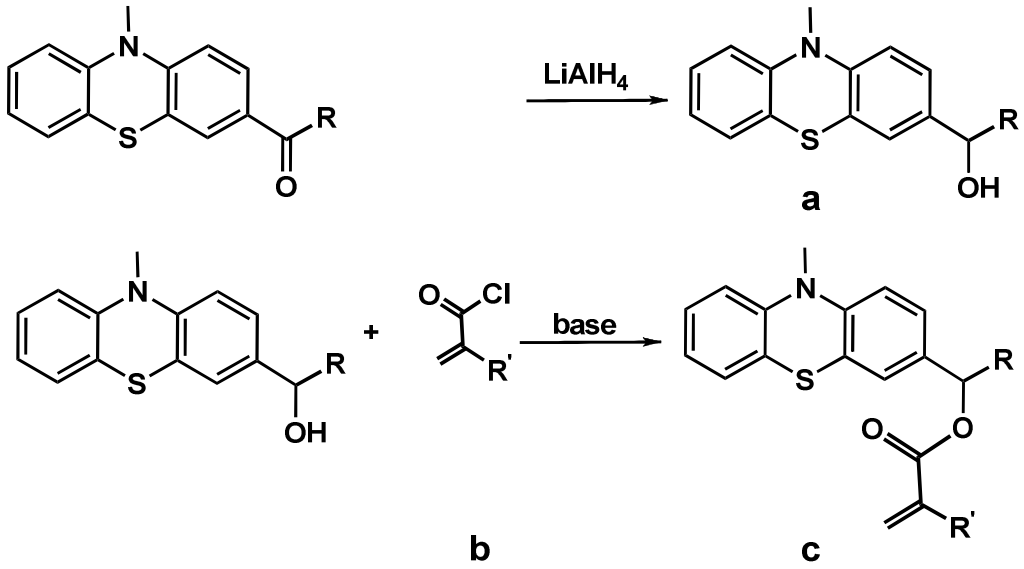

Scheme 15. Synthesis of (meth)acrylate based phenothiazine monomer: a) methylphenothaizine-alcohol, b) (meth)acryloyl chloride and c) phenothiazine (meth)acrylate. R,R′= H, alkyl.

After obtaining the monomers, polymer synthesis is performed first via standard radical polymerization to test the monomer reactivity and the processing of the resulting polymer. Proper candidates can then be examined for further synthetic approaches e.g. via controlled radical polymerization.

3.2. Monomers for attachment to activated esters

As an alternative method to double bond containing monomers, phenothiazine redox moieties are attached to polymers with activated ester groups. Activated ester groups can be easily replaced by amine containing moieties, whereas primary amines are more reactive then secondary amines. Phenothiazine has one secondary amine group in the aromatic ring. By activating this group, redox moieties can be directly attached to the backbone of the activated ester polymer. Activated ester polymers with succinimide (Scheme 16, a) and pentafluorphenol (Scheme 16, c) moieties are chosen to covalently attach phenothiazine moieties as described in the literature.[93] These polymers can substitute their moieties via a “click chemistry” like reaction to build a stable amide bond (Scheme 16, b and d).

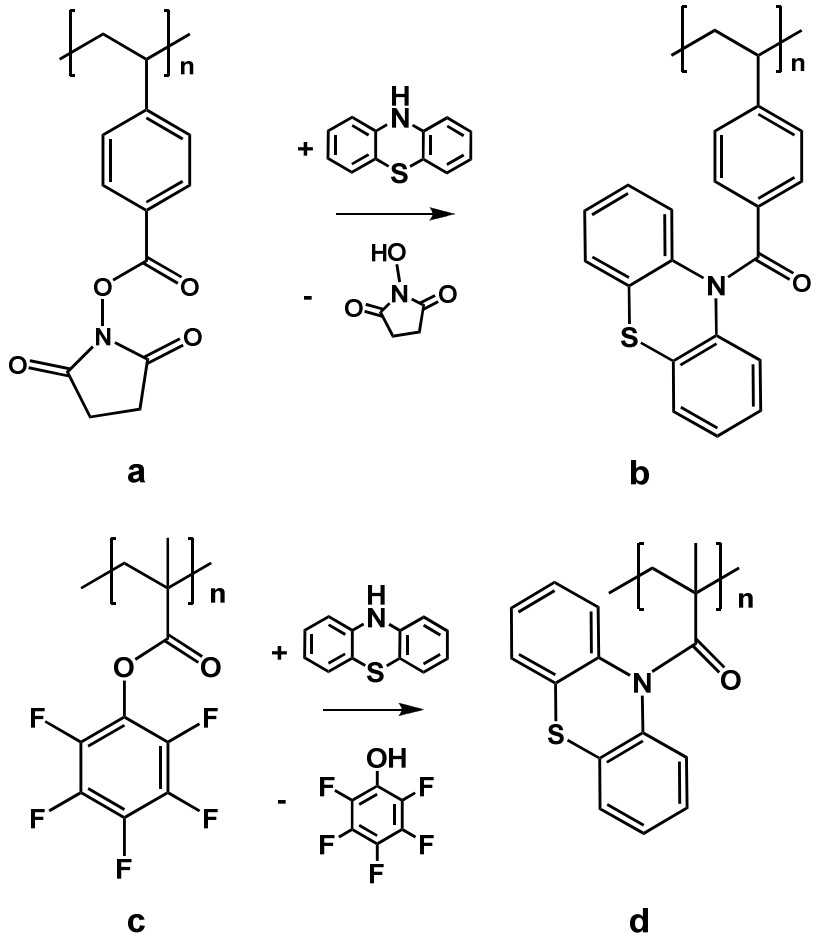

Scheme 16. Reaction of phenothiazine with activated esters based on succinimide and pentafluorphenol: a) aromatic polymer with succinimide moieties, b) formation of the amide bonds with phenothiazine, c) aliphatic polymer with pentafluorphenol moieties, d) formation of the amide bonds with phenothiazine.

If the reactivity of the amine group in phenothiazine doesn't allow the reaction with activated ester, additional amine groups can alternatively be introduced in the phenothiazine molecule. Therefore, the activated ester approach opens up many synthetic possibilities to obtain redox active polymers with phenothiazine moieties. A series of phenothiazines is synthesized using mono-protected primary amines. Commercially available diamines can be used to modify the spacer length between the polymer backbone and the phenothiazine redox moieties. As a protecting group, a N-*tert*-butoxycarbonyl (BOC) group is inserted on one side of a diamine as described by Pittelkow (Scheme 17).[94] Two different diamines with different spacer length are chosen as a reactive amine (Scheme 17, a). By protection of the diamines with *tert*-butyl phenyl carbonate (BPC; Scheme 17, b), a mono-BOC (mBOC) protected diamine is obtained (Scheme 17, c).

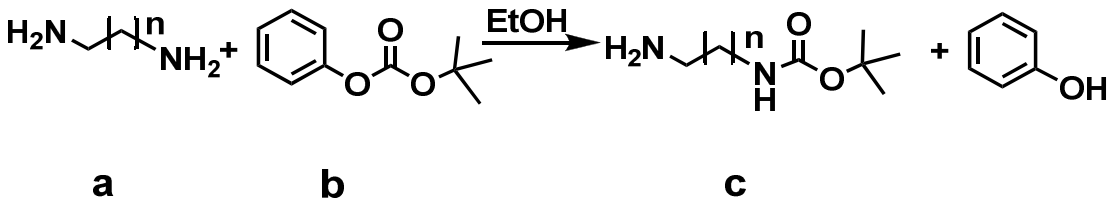

Scheme 17. BOC protection of diamines according to Pittelkow and coworkers[94]: a) alkyl diamine, b) *tert*-butyl phenyl carbonate (BPC) and c) mono-BOC (mBOC) protected diamine. n: alkyl chain length

These mBOC modified primary amines can then be attached to phenothiazine derivatives containing reactive groups such as aldehydes. The primary amines react with phenothiazine aldehydes via a reductive amination. At first an imine intermediate is formed (Scheme 18, a). which is reduced to amine (Scheme 18, b). The deprotection of the BOC group follows in the next step releasing the desired amine (Scheme 18, c).

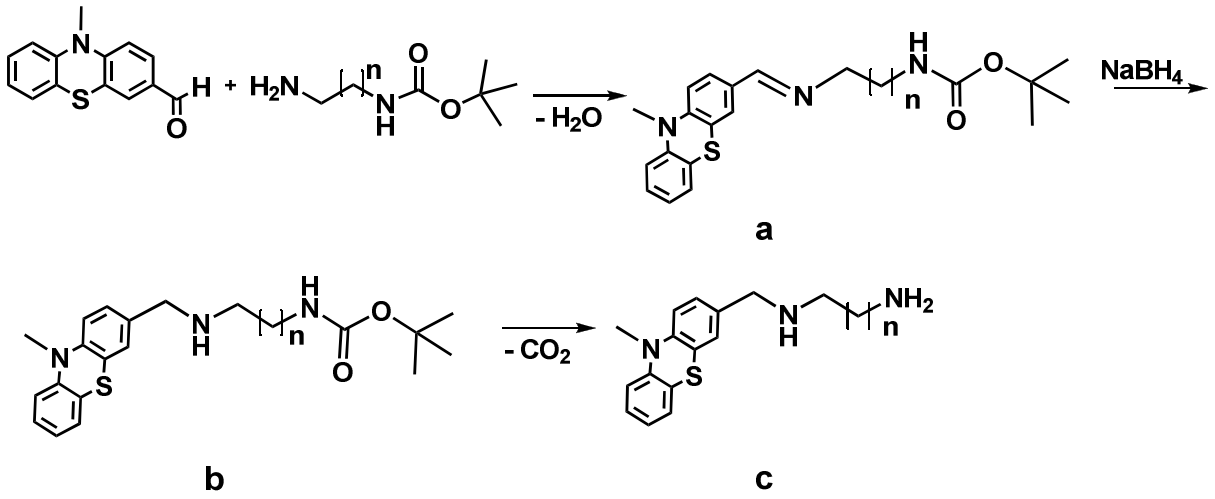

Scheme 18. Reaction of mBOC functionalized amine with phenothiazine carbaldehyde and successive deprotection to primary amine: a) phenothiazine imine intermediate is reduced to b) amine, c) deprotection of BOC group forms the desired primary amine.

Apparently, there are one primary and one secondary group in the target molecule (Scheme 18, c). The secondary amine group could also react with the activated ester moieties. The presence of two amine moieties leads to formation of crosslinked polymers.[93] The crosslinked polymer is mechanically more stable compared to non-crosslinked polymer but cannot be processed by dissolution. To prevent crosslinking, the second amine group can be blocked for example by methylation. Alternatively, another synthetic route based on the reaction of amine could solve the problem. Amide groups are usually stable and do not react further with amines. Crosslinking could be prevented when chemically stable functional groups like amides are present in the molecule. Therefore, mBOC functionalized diamines are converted to amides reacting with an acyl halide group like phenothiazine-10-carbonyl chloride (PCC; Scheme 19, a).

The reaction forms an amide species which is stable against deprotection (Scheme 19, b). After deprotection of the BOC functional group, the primary amine is obtained (Scheme 19, c).

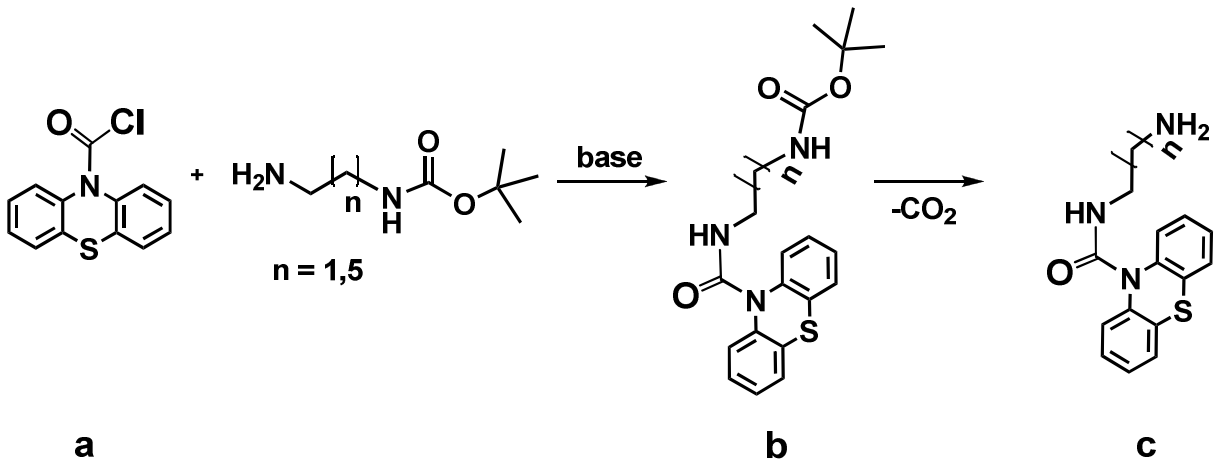

Scheme 19. Reaction of acyl halide phenothiazine with BOC functionalized diamine and successive deprotection: a) phenothiazine-10-carbonyl chloride (PCC), b) mBOC functionalized phenothiazine amide and c) deprotection to primary amine.

As a final alternative, a small phenothiazine moiety with an amine group is synthesized using the aldehyde phenothiazine. For this purpose, the phenothiazine aldehyde is converted to the oxime 10-methyl-10H-phenothiazine-3-carbaldehyde oxime (MPCO; Scheme 20, a). The oxime is converted to 10-methyl-10H-phenothiazine-3-carbonitrile (MPCN; Scheme 20, b) with a nitrile functional group by water removal. In the final step the nitrile is converted to the desired amine (10-methyl-10H-phenothiazin-3-yl)methanamine (MPMA; Scheme 20, c) by reduction. The small moiety should reveal the highest reactivity due to the low steric hindrance and due to the presence of an aliphatic primary amine group.

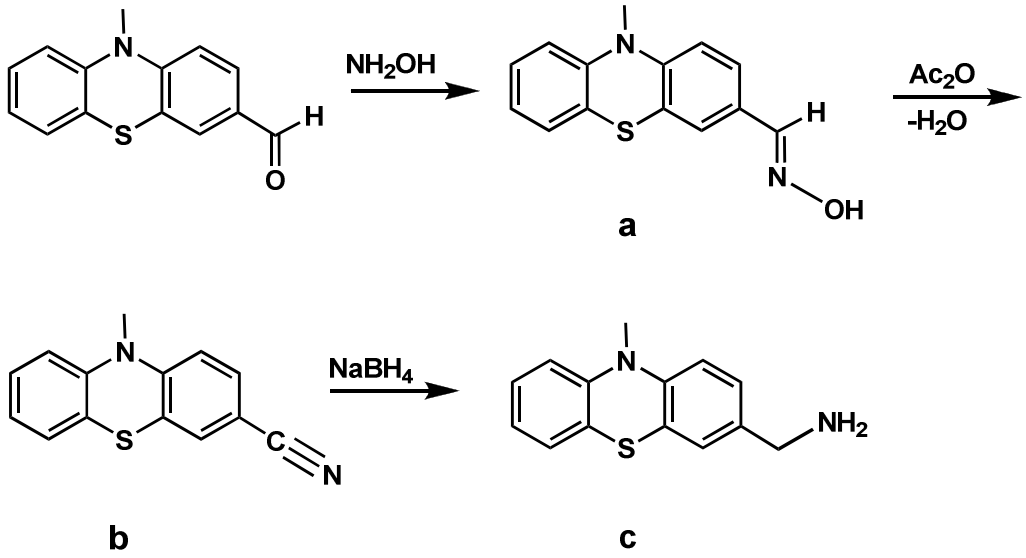

Scheme 20 Synthesis of phenothiazine with one primary amine functionality: a) 10-methyl-10H-phenothiazine-3-carbaldehyde oxime (MPCO), b) 10-methyl-10H-phenothiazine-3-carbonitrile (MPCN) and c) (10-methyl-10H-phenothiazin-3-yl)methanamine (MPMA).

Thus, many synthetic approaches to redox active polymers with phenothiazine moieties are theoretically possible because of the versatile chemistry of phenothiazine. In the experimental part these approaches were investigated with respect to their practical implementation.

4. Experimental part

4.1. Materials

10H-phenothiazine (phenothiazine; Acros, 99%), potassium *tert*-butoxide (PTBO; Sigma Aldrich, 95%), 1-(chloromethyl)-4-vinylbenzene (CVB; Sigma Aldrich, 95%), allyl bromide (Merck, for synthesis), 1-bromo-3-chloropropane (BCP; Acros, 98%), 4-vinylbenzoic acid (VBA; Sigma Aldrich, 97%), dilithium tetrachlorocuprate (Li_2CuCl_4; Sigma Aldrich, 0.1 M in THF), 4-bromobenzaldehyde (BBA; Sigma Aldrich, 99%), 4-(dimethylamino)-pyridine (DMAP; Sigma Aldrich, 99%), hydroxylamine hydrochloride (Sigma Aldrich, 99.0%), lithium aluminum hydride (LAH; Alfa Aesar, 97%), Sodium boron hydride ($NaBH_4$; Sigma Aldrich, 99%), 2-acetylphenothiazine (ACP; Sigma Aldrich, 95%), phenothiazine-10-carbonyl chloride (PCC; Sigma Aldrich), N-hydroxysuccinimide (NHS; Sigma Aldrich, 98%), methyltriphenyl-phosphonium bromide (MTPPB; Sigma Aldrich, 98%), N,N'-Dicyclohexylcarbodiimide (DCC; Acros, 99%) were used without further purification. Anisole (Aldrich, 99%) was used after deaerating by bubbling argon for 1.5 h. Dry tetrahydrofuran (THF; Acros, 99.8%), dry toluene (Acros, 99.8%) and acetone (Sigma Aldrich, 99.5%) were filtered through aluminium oxide to remove the stabilizer. Ethylenediamine (EDA; Acros, 99% extra pure), 4-bromostyrene (PBS; Sigma Aldrich, 97%) and methacryloyl chloride (MAC; Sigma Aldrich, 97%) were distilled prior to use. Triethylamine (TEA; Sigma Aldrich, ≥99.5%) was distilled prior to use and kept under dried argon atmosphere. Azobisisobutyronitrile (AIBN; Sigma Aldrich, 98%) was crystallized from ethanol and dried under vacuum prior to use and kept under argon atmosphere in the refrigerator. *Tert*-butyl phenyl carbonate (BPC; Sigma Aldrich, 97%), N-methylphenothiazine (MP; Alfa Aesar, 98%), N-methylfomanilid (NMF; Sigma Aldrich, 99%), phosphorus oxychloride (POC; Acros,99%), pentafluorphenol (PFF; Sigma Aldrich, ≥99%), pyridine (Merck, dried), acetic anhydride (Sigma Aldrich, ≥99%), 1,6-hexanediamine (HDA; Sigma Aldrich,99%), hexane (Fisher Scientific, 95%), p-toluenesulfonic acid monohydrate (Acros, 98%), trifluoroacetic acid (TFA; Acros, 99%), ethyl acetate (Sigma Aldrich, ≥99%), dichloromethane (DCM; Acros, 98%), dry acetonitrile (ACN; Sigma Aldrich, 99.8%), sodium bisulfite (Fisher Scientific, ACS reagent), methanol (Fisher Scientific, HPLC grade) , aluminum oxide (Fluka, for chromatography) were used as received.

4.2. Methods

Thermogravimetry analysis (TGA) was performed in nitrogen atmosphere (30 mL min^{-1}) at a heating rate of 10 °C min^{-1} from 40 °C to 800 °C with a Mettler Toledo TGA/SDTA851e. For the Differential Scanning Calorimetry (DSC), a Mettler Toledo DSC/823e was used in nitrogen atmosphere (30 mL min min^{-1}) at a heating rate of 10 °C min^{-1} from 40 °C to 220 °C.

4.3. Monomer synthesis

4.3.1. Synthesis of 10-allyl-10H-phenothiazine (APT)

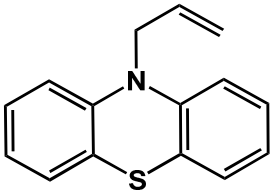

13.2 g of phenothiazine (0.067 mol) were dissolved in 166 ml THF. To the yellow colored solution 7.85 g PTBO (0.07 mol) was added. The resulting yellow dark colored dispersion was stirred at room temperature for 1 hour. 10.5 ml allyl bromide (0.12 mol) were added slowly over one hour to the dispersion using a drop funnel. Afterwards, the green yellow dispersion was heated to reflux over night under argon atmosphere. After cooling, the reaction mixture was extracted three times with DCM and the organic phase was extracted twice with saturated sodium bisulfite. The organic phase was dried over $MgSO_4$, and the red orange colored solution was removed under vacuum. The residue was purified over column chromatography using a mixture of 15 : 1 hexane/acetone to result in light yellow colored oil. (11.2 g, 70%). ^{1}H-NMR (250 MHz, $CDCl_3$): δ 7.03 (t, 4H), 6. 80 (m, 4H), 5.93 (m, 1H), 5.23 (t, 2H), 4.40 (p, 2H).

4.3.2. Synthesis of 10-(4-vinylbenzyl)-10H-phenothiazine (VBPT)

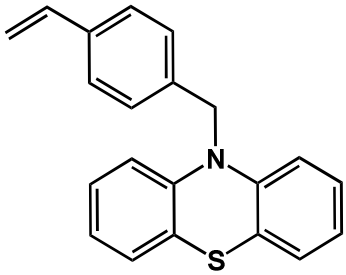

13.2 g phenothiazine (0.067 mol) were dissolved in 200 ml dry THF and 7.85 g PTBO (0.07 mmol) were added to the solution and stirred for 3 hours at room temperature under argon. Then, 17.5 ml CVB (0.12 mmol) were added to the dispersion using a dropping funnel and the mixture was refluxed over night. 100 ml distilled water were added and the organic phase was extracted twice with Na_2SO_4 solution. Subsequently, the water phase was extracted three times with DCM. Finally the organic phases were washed twice with distilled water, dried over $MgSO_4$, and the solvent was removed under vacuum. The residue was crystallized three times from ethanol to obtain 15.36 g (74%) of light yellow crystals as the product. M.p. 121-124 °C. ^{1}H-NMR (250 MHz, $CDCl_3$): δ 7.29 (d, 2H), 7.18 (d, 2H), 7.01 (d, 2H), 6.87 (t, 2H), 6.77 (t, 2H), 6.59 (dd, 1H), 6.52 (d, 2H), 5.67 (d, 1H), 5.16 (d, 1H), 4.97 (s, 2H).^{13}C-NMR (300 MHz, $CDCl_3$): δ 144.1 (C-N), 136.1 (C_{quart}), 126.9 (CH_{aromat}), 126.5 (CH_{aromat}), 126.3 (CH_{aromat}), 122.9 (C-S), 122.2 (CH_{aromat}), 115.1 (CH_{aromat}), 113.5 (C=C), 52.2 (CH_2).

4.3.3. Synthesis of 1-(3-bromopropyl)-4-vinylbenzene (BPVT)

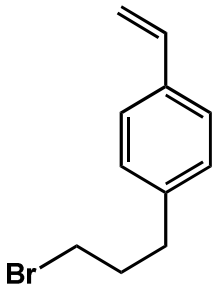

A Grignard mixture of 1.34 g magnesium and 10 g (0.055 mol) PBS was made in 50 ml THF. In another beaker, a mixture of 17.2 g BCP (0.11mol) and 7.6 ml 0.1M Li_2CuCl_4 in 50 ml THF was prepared and cooled to 0 °C. The Grignard was slowly dropped to the latter mixture and the reaction continued at room temperature over night. Finally, 100 ml 2n HCl solution was added to the reaction. The water phase was separated and washed twice with ether. The organic phases were then unified, washed three times with water, dried over $MgSO_4$, and the solvent was removed under vacuum. The resulting oil was purified by distillation to result in a colorless oil. (5.88 g, 60%, b.p.: 70-75 °C). ^{1}H-NMR (250 MHz, $CDCl_3$): δ 7.37 (d, 2H), 7. 16 (d, 2H), 6.72 (m, 1H), 5.71 (d, 1H), 5.22 (d, 1H), 3.56 (t, 2H), 2.81 (t, 2H), 2.11 (p, 2H).

4.3.4. Synthesis of 10-(3-(4-vinylphenyl)propyl)-10H-phenothiazine (VPPP)

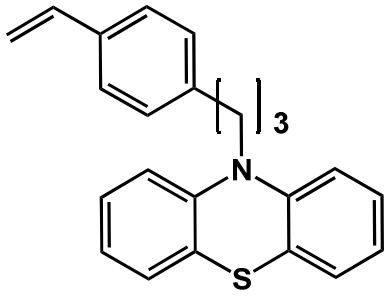

4.3 g phenothiazine (0.022 mol) was dissolved in 50 ml THF. 2.6 g PTBO (0.023 mol) were added to the solution and the reaction stirred for 3h at room temperature. 3.9 g BVPT (0,022 mol) were added to the reaction which was then refluxed for 48 hours. After adding 100 ml water to the reaction, the water phase was separated and washed three times with DCM. The organic phase was washed once with sodium bisulfate solution and twice with water, dried over $MgSO_4$, and the solvent was removed under vacuum. The crude product was purified twice over column chromatography using a mixture of 9 : 1 petroleum ether/DCM and 10:1 hexane/ethyl acetate, respectively. A light yellow colored powder was obtained as the product. (5.23 g, 71%). ^{1}H-NMR (250 MHz, $CDCl_3$): δ 7.31 (d, 2H), 7. 18 (m, 6H), 6.96 (t, 2H), 6.86 (d, 2H), 6.66 (dd, 1H), 5.70 (d, 1H), 5.20 (d, 1H), 3.89 (t, 2H), 2.77 (t, 2H), 2.13 (t, 2H).

4.3.5. Synthesis of 4-(10H-phenothiazine-10-yl)benzaldehyde (PBA)

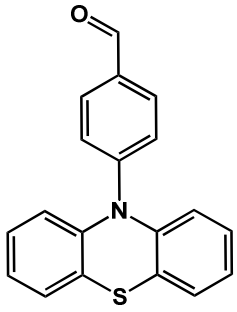

Two different synthetic routes were tried out:

Route a): [92]

4.64 g 4-bromobenzaldahyde (0.025 mol), 5 g phenothiazine (0.025 mol), 7.46 g potassium carbonate (0.054 mol) and 3.2 g freshly activated copper bronze (0.05 mol) with 0.66 g 18-crown-6 (0.002 mol) in 15 ml 1,2-dichlorbenzene were mixed together and refluxed for 48 h. TLC plate shows that no product has been formed.

Route b): [95]

5 g 4-bromobenzaldahyde (0.027 mol), 5.38 g phenothiazine (0.027 mol), 7.46 g potassium carbonate (0.054 mol) and 3.43 g freshly activated copper bronze (0.054 mol) were mixed together and heated up to 210 °C for 48 h. TLC plate shows, that no product has been formed.

4.3.6. Synthesis of 10-methyl-10H-phenothiazine-3-carbaldehyde (MPCA)

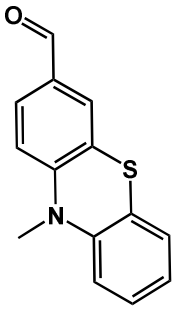

15 g MP (70.3 mmol), 10 g NMF (74.0 mmol) and 11.4 g POC (74.4 mmol) were added to 15 ml 1,2-dichlorobenzene and heated at 95 °C under argon for 17 hours under vigorous stirring. After cooling, 30 g of sodium acetate solution in 100 ml distilled water were added to the reaction. The mixture was distilled at 130°C/10 mbar to remove N-methylaniline. The residue was taken up and washed several times with THF. The organic phase was dried over $MgSO_4$, and the solvent was removed under vacuum. The crude product was purified using the column chromatography with DCM. Finally the crude oil was recrystallized from methanol to obtain yellow colored crystals. (12.1 g, 71%, m.p.: 87-90 °C.). ^{1}H-NMR (250 MHz, $CDCl_3$): δ 9.72 (s, 1H), 7.56 (d, 1H), 7.51 (s, 1H), 7.06 (m, 2H), 6.90 (d, 1H), 6.75 (d, 2H), 3.34 (s, 3H). ^{13}C-NMR (300

MHz, CDCl3): δ 190.10 (C_{Ald}), 151.09 (C-N_{aromat}), 144.19 (C-N_{aromat}), 131.19 (C_{quart}), 130.47 (CH_{aromat}), 127.96 (CH_{aromat}), 127.78 (CH_{aromat}), 127.31 (CH_{aromat}), 124.00 (CH_{aromat}), 123.64 (C-S), 122.55 (C-S), 114.78 (CH_{aromat}), 113.72 (CH_{aromat}), 35.84 ($CH_{aliphat}$).

4.3.7. Synthesis of 10-methyl-3-vinyl-10H-phenothiazine (MVPT)

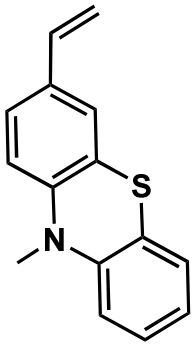

5 g PTBO (0.031 mol) were suspended in THF and 11.1 g MTPPB (0.031 mol) were added to the suspension. After 15 minutes, a solution of 5 g MPCA (0.021 mol) in 30 ml THF was added to the reaction and stirred for 3 hours at room temperature. Then, 100 ml water wer added and the water phase washed three times with ethyl acetate. After washing the organic phase three times with water, the unified organic phase was dried over $MgSO_4$, and the solvent removed in vacuum. The crude product was purified via column chromatography with DCM to obtain a yellow colored powder. (4.15 g, 84%, m.p.: 91-94 °C). ^{1}H-NMR (250 MHz, $CDCl_3$): δ 7.20 (m, 4H), 6.96 (t, 1H), 6.80 (dd, 2H), 6.62 (dd, 1H), 5.61 (d, 1H), 5.15 (d, 1H), 3. 40 (s, 3H).

4.3.8. Synthesis of 1-(10-methyl-10H-phenothiazin-3-yl)ethanone (MPE)

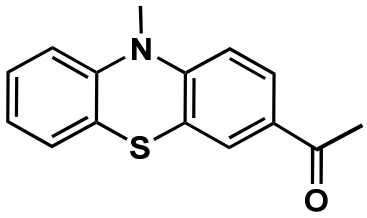

16.2 g ACP (0.067 mol) were dissolved in 166 ml THF. To the yellow orange colored solution, 7.85 g (0.07 mol) PTBO were added and the dispersion stirred at room temperature for 1 hour. Subsequently, 7.5 ml methyl iodide (0.12 mol) was dropped slowly (30 minutes) to the mixture. Next, the reaction was refluxed under argon over night and the mixture was extracted three times with sodium bisulfate solution (150 ml each time). The water phase was then washed four times with DCM (100 ml each time). The organic phases were unified, dried over $MgSO_4$ and aluminum oxide and the solvent was evaporated in vacuum. The crude product was purified using the column chromatography with chloroform/acetone 20:1. Finally, the resulting oil was crystallized from hexane to give light yellow crystals. (11.35 g, 66%, m.p.: 98-101°C). ^{1}H-NMR

(250 MHz, $CDCl_3$): δ 7.38 (d, 1H), 7.28 (s, 1H), 7.05 (m, 3H), 6.86 (t, 1H), 6.73 (d, 1H), 3.33 (s, 3H), 2. 49 (s, 3H).

4.3.9. Synthesis of 1-(10-methyl-10H-phenothiazin-3-yl)ethanol (MPET)

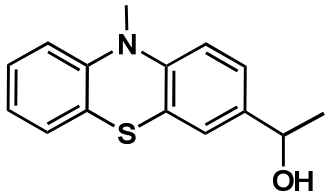

594 mg LAH (0.016 mol) were suspended in 30 ml dry ether. 2 g MPE (0.008 mol) in 12 ml dry THF were slowly added to the suspension under argon and the mixture was refluxed for 5 hour. Then, the mixture was stirred under argon over night at room temperature. 20 ml water were added to the reaction while cooling with ice followed by 30 ml diluted HCl solution. The water phase was extracted three times with ether and the organic phase washed three times with water. The unified organic phases were dried over $MgSO_4$, and the solvent removed under vacuum. The product was obtained as slight yellow colored oil. (1.82 g, 90%). ^{1}H-NMR (250 MHz, $CDCl_3$): δ 7.05 (m, 3H), 6.77 (m, 4H), 4.70 (q, 1H), 3.26 (s, 3H), 1.35 (d, 3H).

4.3.10. Synthesis of 1-(10-methyl-10H-phenothiazin-3-yl)ethyl methacrylate (MPEMA)

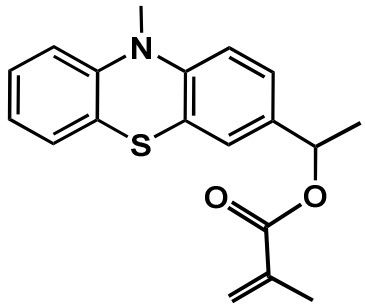

1.82 g MPET (0.007 mol) were dissolved in 10 ml DCM followed by 1.14 ml TEA (0.008 mol). Subsequently, 0.85 g MAC (0.008 mol) were added to the solution under argon using an ice bath. The mixture was left to react under argon over night at room temperature while stirring. After adding water to the reaction, the water phase was extracted twice with DCM and the organic phase washed three times with water. Finally the organic phase was dried over $MgSO_4$, and the solvent was removed in vacuum to obtain yellow colored oil as the product. (1.92 g, 84%). ^{1}H-NMR (250 MHz, $CDCl_3$): δ 7.04 (m, 3H), 6.81 (m, 4H), 6.07 (s, 1H) 5. 50 (s, 1H), 5.74(q, 1H), 3.31(s, 3H), 1.87(s, 3H), 1.47(d, 3H).

4.3.11. Synthesis of tert-butyl 2-aminoethylcarbamate (TBAEC)

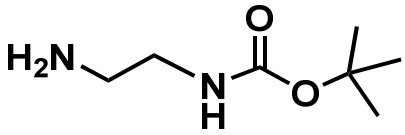

2.01 g EDA (0.03 mol) were dissolved in 20 ml ethanol abs. and 6.45 g (0.03 mol) BPC were added to the solution. The reaction mixture was stirred under reflux for 18 hours. After removing the solvent in vacuum, the yellow colored residue was adjusted to pH 3 using 30 ml distilled water and 2M HCl solution. Subsequently, the water phase was extracted three times with 40 ml DCM and adjusted to pH 12 using a 2M NaOH solution. After further extraction with 50 ml DCM (three times), the organic phase was dried over Na_2SO_4 and the solvents were removed under vacuum to obtain slightly yellow colored oil as the product. (2.56 g, 53%). ^{1}H-NMR (250 MHz, $CDCl_3$): δ 5.24 (br s, 1H), 3.10 (q, 2H), 2.72 (t, 2H), 1.59 (s, 2H), 1.37 (s, 9H).

The same procedure was used to obtain *tert*-butyl 2-aminohexylcarbamate (TBAHC): 9.60 g HDA (0.08 mol), 16.16 g BPC (0.08 mol), 50 ml ethanol abs. were used for the reaction. The neutralization was performed with 75 ml distilled water and the extraction with three times 100 ml and three times 125 ml DCM. The colorless product was obtained after removing the solvents. (12.72 g, 36%).^{1}H-NMR (250 MHz, $CDCl_3$): δ 4.69 (br s, 1H), 3.03 (q, 2H), 2.61 (t, 2H), 1.66 (s, 2H), 1.24-1.43 (m, 17H).

4.3.12. Synthesis of tert-butyl 2-((10-methyl-10H-phenothiazin-3-yl)methylamino) ethylcarbamate(TBPEC)

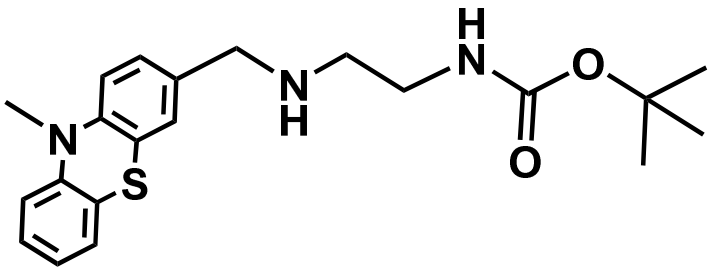

1.71 g MPCA (7 mmol), 1.36 g TBAEC (9 mmol) and 1.4 mg p-toluenesulfonic acid (8 µmol) were dissolved in 1.5 ml toluene and refluxed over night to remove the water. After removal of toluene, the residue was dissolved in 15 ml methanol and 0.67 g $NaBH_4$ (18 mmol) were added to the reaction. The reaction was continued for 48 hours at room temperature. Then, the solvent was removed under vacuum and the residue dissolved in ether. The organic phase was washed three times with sodium chloride solution, dried over Na_2SO_4 and the solvents were removed under vacuum. The remaining yellow brown colored oil was crystallized from a 1:1 mixture of ether/petroleum ether. The crude product was purified via column chromatography using DCM: ethyl acetate 5:1 to result in 0.24 g (9%) of yellow oil as the product with remaining impurities. ^{1}H-NMR (250 MHz, $CDCl_3$): 7.07-7.18 (m, 7H,) δ 4.96 (br s, 1H), 3.59 (s, 2H), 3.35 (q, 2H t, 2H), 3.07 (s, 3H), 1.36 (s, 9H).

The same procedure was used for the synthesis of *tert*-butyl 2-((10-methyl-10H-phenothiazin-3-yl)methylamino)hexylcarbamate (TBPHC). 2.60 g TBAHC (10 mmol), 1.92 g MPCA (7 mmol) and 1.6 mg p-toluenesulfonic acid (9 µmol) were dissolved in 1.6 ml toluene. 0.76 g $NaBH_4$ (20 mmol) were added in 30 ml methanol. The remaining yellow brown colored oil was crystallized from a 1:1 mixture of ether/petroleum ether to result in 0.98 g (25%) of yellow crystals as the product. ^{1}H-NMR (250 MHz, $CDCl_3$): δ 7.05-7.09 (m, 4H), 6.86 (t, 2H), 6.71 (t, 1H), 4.45 (br s, 1H), 3.63 (s, 2H), 3.41 (q, 2H), 3.28 (t, 2H), 2.5 (t, 2H) 1.43-1.46 (m, 1H), 1.37 (s, 9H), 1.11-1.17 (m, 8H).

4.3.13. Synthesis of N-((10-methyl-10H-phenothiazin-3-yl)methyl)hexane-1,2-diamine (MPHDA)

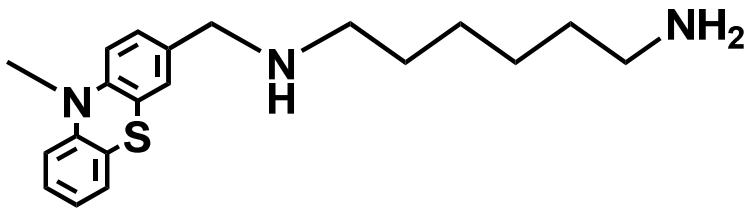

0.23 g TBPHC (0.52 mmol) were dissolved in 25 ml DCM and 15 ml TFA (0.19 mol) were added to the solution. The slightly red colored solution was left to stir at room temperature for 4 hours and the solvent was removed under vacuum. The red colored residue was dissolved in 10 ml DCM and 0.05 g TEA (0.52 mmol). The organic phase was washed three times with water and the solvent was removed under vacuum. 0.12 g (81%) of a colorless oil was obtained as the product. ^{1}H-NMR (250 MHz, $CDCl_3$): δ 7.02-7.12 (m, 4H), 6.67-6.87 (m, 3H), 3.63 (s, 2H), 3.61 (s, 2H), 3.29 (s, 3H), 2.48-2.63 (m, 4H), 1.93 (s, 1H), 1.74 (s, 2H), 1.20-1.54 (m, 8H). ESI-Ms m/z (M+H): 341.80.

4.3.14. Synthesis of tert-butyl 2-(10H-phenothiazine-10-carboxamido)ethylcarbamate (TPCEC)

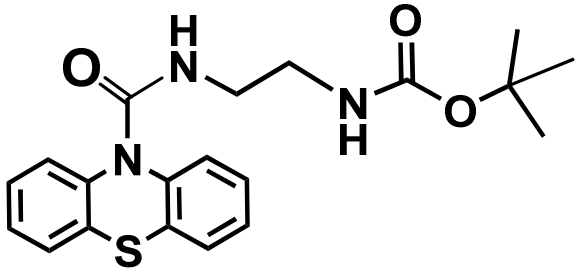

o.5 g TBAEC (3.1 mmol) in 1.5 ml dry THF and 0.95 g TEA (9.4 mmol) and the solution were kept stirring in an ice bath. 0.82 g PCC (3.1 mmol) were dissolved in 15 ml dry THF and the solution was added slowly under argon to the TBAEC solution. After adding the carbonyl chloride, the reaction was continued over night at room temperature. Distilled water was added to the mixture and the water phase was extracted three times with 60 ml DCM. The organic phase was dried over $MgSO_4$, and the solvent removed under vacuum. A white colored powder

was obtained as the product. (0.67 g, 56%). ^{1}H-NMR (250 MHz, THF-d_8): δ 7.51 (d, 2H), 7.00-7.25 (m, 6H), 6.10 (br s, 2H), 3.10 (m, 4H), 1.25 (s, 9H).

The same procedure was used for the synthesis of *tert*-butyl 2-(10H-phenothiazine-10-carboxamido)hexylcarbamate (TPCHC): 1.0 g TBAEC (4.6 mmol), 1.4 g TEA (13.8 mmol) and 1.2 g PCC (4.6 mmol) in 20 ml THF were used. For the extraction three times 100 ml DCM were used. The product was obtained as a light yellow powder. (1.24 g, 61%). ^{1}H-NMR (250 MHz, $CDCl_3$): δ 7.5 (d, 2H), 7. 12 - 7.26 (m, 4H), 7.00 (t, 2H), 5.75 - 5.90 (m, 2H), 3.07 (q, 2H), 2.80 (q, 2H), 1.19 - 1.48 (m, 17H).

4.3.15. Synthesis of N-(2-aminoethyl)-10H-phenothiazine-10-carboxamide (AEPCA)

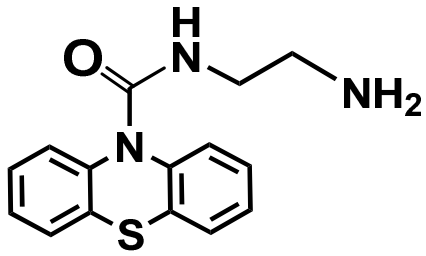

0.5 g TPCEC (1.3 mmol) were dissolved in 35 ml DCM and 37 ml TFA (0.48 mol) were added to the solution. The red colored solutions were stirred at room temperature for 4 hours and the solvent was removed under vacuum. The residue was dissolved in 70 ml DCM and 0.13 g TEA (1.3 mmol) were added to the solution to set the pH value to alkaline. Finally, the organic phase was washed three times with water, dried over $MgSO_4$ and the solvent removed under vacuum. A colorless oil is obtained as the desired product. (0.32 g, 85%). ^{1}H-NMR (250 MHz, $CDCl_3$): δ 7.12 - 7.76 (m, 8H), 6.55 (t, 2H), 3.5 (q, 2H), 3.12 (t, 2H). ESI-MS m/z (M+H): 285.10.

The same procedure was used for the synthesis of N-(6-aminohexyl)-10H-phenothiazine-10-carboxamide (AHPCA): 0.5 g TPCHC (1.1 mmol), 32 ml TFA (0.41 mol) and 0.11 g TEA (1.1 mmol) were used and the residue was dissolved in 100 ml DCM. 0.34 g (91%) of the product were obtained. ^{1}H-NMR (250 MHz, $CDCl_3$): δ 7.24-7.51 (m, 8H), 5.87 (s, 2H), 4.94 (t, 1H), 3.2 (q, 2H), 1.09-1.44 (m, 10H). ESI-MS m/z (M+H): 341.1.

4.3.16. Synthesis of 10-methyl-10H-phenothiazine-3-carbaldehyde oxime (MPCO)

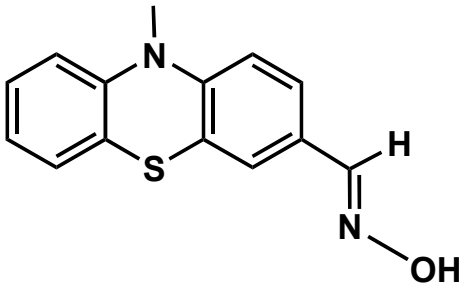

The synthesis was done according to the following procedure:[96] 2 g MPCA (8.3 mmol) and 2 g hydroxylamine hydrochloride (28.8 mmol) were heated to 60°C in 10 ml pyridine for 45 minutes. Distilled water (50 ml) was added and the mixture extracted three times with DCM.

The organic phase was dried over $MgSO_4$, and the solvent was removed under vacuum. The residue was crystallized twice from ethanol to obtain 1.6 g (75%) of yellow colored crystals. M.p.: 159-162 °C. . ^{1}H-NMR (250 MHz, $CDCl_3$): δ 7.95 (s, 1H), 7.37 (d, 1H), 7.29 (m, 1H), 7.07 (m, 3 H), 6.73 (t, 2H), 3.38 (s, 3H). ^{13}C-NMR (300 MHz, $CDCl_3$): δ 149.41 ($C_{aldoxime}$), 147.24 ($C\text{-}N_{aromat}$), 145.03 ($C\text{-}N_{aromat}$), 127.59 (C_{quart}), 127.22 (CH_{aromat}), 126.74 (CH_{aromat}), 126.34 (CH_{aromat}), 125.24 (CH_{aromat}), 123.99 (CH_{aromat}), 122.89 (C-S), 122.81 (C-S), 114.29 (CH_{aromat}), 113.96 (CH_{aromat}), 35.47 ($CH_{aliphat}$).

4.3.17. Synthesis of 10-methyl-10H-phenothiazine-3-carbonitrile (MPCN)

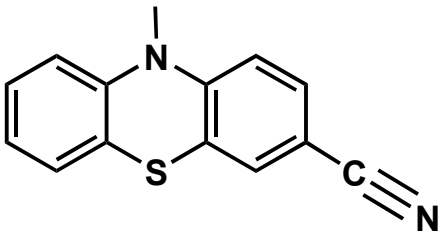

A mixture of 1.6 g of MPCO (6.2 mmol) and 9.4 ml acetic anhydride was heated for 3 hours at 190 °C. The mixture was added to 75 ml ice water and the organic phase was extracted three times with DCM. The organic phase was washed with charcoal and dried over $MgSO_4$. The solvent was removed under vacuum and the remaining yellowish oil was crystallized twice from ethanol to yield 1.24 g (84%) of yellow colored crystals. M.p.: 120-123 °C. ^{1}H-NMR (250 MHz, THF-D_8): δ 7.35 (d, 1H), 7.25 (s, 1H), 7.10 (m, 2H), 6.92 (t, 1H), 6.73 (dd, 2H), 3.32 (s, 3H). ^{13}C-NMR (300 MHz, $CDCl_3$): δ 149.64 ($C\text{-}N_{aromat}$), 144.17 ($C\text{-}N_{aromat}$), 131.95 (CH_{aromat}), 130.02 (CH_{aromat}), 127.96 (CH_{aromat}), 127.35 (CH_{aromat}), 124.60 (C-S), 123.73 (CH_{aromat}), 122.09 (C-S), 118.82 (C≡N), 114.78 (CH_{aromat}), 113.93 (CH_{aromat}), 105.35 (C_{quart}), 35.61 ($CH_{aliphat}$).

4.3.18. Synthesis of (10-methyl-10H-phenothiazin-3-yl)methanamine (MPMA)

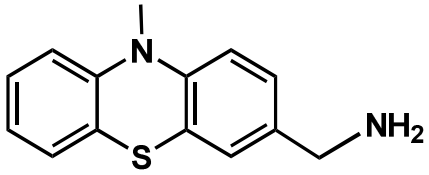

To 0.75 g of MPCN (3.1 mmol) in 15 ml THF, 1.18 g LAH (31.1 mmol) were added under argon atmosphere. The reaction was continued for 4 hours at room temperature. The reaction mixture was carefully neutralized using a saturated Na_2SO_4 solution. The precipitated $Al(OH)_3$ was removed by filtration and the filtrate washed with copious amount of DCM. Finally, the water phase was washed four times with DCM, the organic fractions dried over $MgSO_4$, and the solvent was removed under vacuum. The residue was crystallized from ethanol to obtain 0.51 g (68%) of the product as yellow colored crystals. M.p.: 114-117 °C. ^{1}H-NMR (250 MHz, DCM-D2): δ 7.05 (m, 4H), 6.85 (d, 1H), 6.71 (t, 2H), 3.69 (s, 2H), 3.29 (s, 3H), 1.70 (b s, 2H). ^{13}C-NMR (300 MHz, THF-D_8): δ 146.07 ($C\text{-}N_{aromat}$), 144.21 ($C\text{-}N_{aromat}$), 138.73 (C_{quart}), 127.03 (CH_{aromat}), 126.55 (CH_{aromat}), 125.77 (CH_{aromat}), 125.43 (CH_{aromat}), 123.40 (C-S), 123.10 (C-S), 121.79 (CH_{aromat}), 113.74 (CH_{aromat}), 113.59 (CH_{aromat}), 45.43(CH_2), 34.49 ($CH_{aliphat}$).

4.3.19. Synthesis of 2,5-di oxopyrrolidin- 1-yl 4-vinylbenzoate (DPVB)

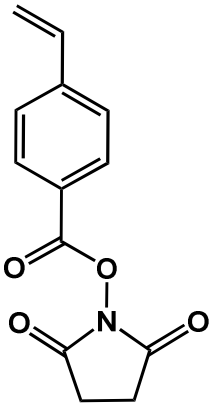

5 g of VBA (33.8 mmol) and 5.8 g of NHS (50.6 mmol) were dissolved in 130 ml ethyl acetate. Subsequently, 10.44 g of DCC (50.6 mmol) and 220 mg of DMAP (1.7 mmol) were added to the solution and stirred at room temperature for 48 hours. The precipitate was filtered off and the organic solution was washed twice with saturated $NaHCO_3$ solution and three times with water. The solution was dried over $MgSO_4$, and the solvent was removed under vacuum. The residue was dissolved in 50 ml DCM and crystallized by adding 150 ml ether. The crystals were washed three times to obtain 5.9 g (71%) of the white crystalline product. M.p.: 137-140 °C. ^{1}H-NMR (250 MHz, $CDCl_3$): δ 8.13 (d, 2H), 7.53 (d, 2H), 6.78 (dd, 1H), 5.91 (d, 1H), 5.47 (d, 1H), 2.93 (s, 4H). ^{13}C-NMR (300 MHz, $CDCl_3$): δ 169.33 ($C{=}O_{succinimid}$, 2C), 161.65 (C=O), 143.92 (C_{quart}), 135.65 ($CH_{C=C}$), 130.93 (CH_{aromat}, 2C), 126.52 ($C_{Haromat}$, 2C), 124.02 (C_{quart}), 117.90 ($CH_{2C=C}$), 25.69 (CH_3). ESI-MS m/z (M+H): 245.07.

4.3.20. Synthesis of perflourphenyl methacrylate (PFMA)

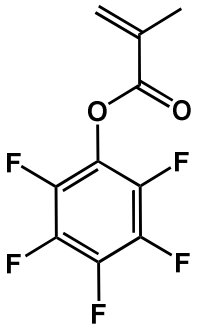

4 g of PFF (22 mmol) were dissolved in a mixture of 12 ml pyridine and 24 ml ether under argon. Using ice bath cooling, 2.27 g of MAC (22 mmol) were slowly added to the solution and stirred over night at room temperature. The mixture was poured on ice and 12.5 ml of concentrated hydrochloric acid were slowly added. The water phase was extracted three times with ether and the organic phase was washed four times with water. The organic phase was dried over $MgSO_4$ and the solvent was removed under vacuum. The remaining oil was distilled at 50°C and a pressure of 0.2 mbar to obtain 17.8 g (80%) of colorless oil as the product. n_D^{25}: 1.4389. ^{1}H-NMR (250 MHz, $CDCl_3$): δ 6.38 (s, 1H), 5.84 (s, 1H), 2.01 (s, 3H). ^{19}F-NMR (500 MHz, $CDCl_3$): δ -161.81 (dd, 2F), -156.55 (t, 1F), -153.36 (d, 2F).

4.4. Polymer synthesis

4.4.1. Vinyl monomer polymerization

The synthesis was carried out using 1 g of the monomer dissolved in 4 ml of the solvents. With the adequate amount of the initiator AIBN, molecular weights M_n of 10000 and 25000 g/mol were achieved according to Table 1. Solvents were degassed with argon prior to use. All reaction mixtures were pretreated with 3 freeze-thaw cycles in order to degas the monomer solution. The reaction was performed over night at 60°C to check the conversion degree and molecular weight. To purify the polymer, the reaction solution was precipitated twice from methanol (except from poly-DPVB which was precipitated from THF) and dried at 60°C under vacuum Then ^{1}H-NMR studies were performed for the resulting polymer (Table 1).

Table 1. List of the phenothiazine monomers, their reaction solvent and the resulting ^{1}H-NMR spectra of their polymers with M_n = 25000 g/mol.

Monomer	Solvent	NMR for M_n = 25000 g/mol
APT	THF	No polymer
		-
VBPT	anisole	^{1}H-NMR (250 MHz, $CDCl_3$): δ 6.88 (br, 4H), 6.55 (br, 4H),6.35
		(br, 2H), 6.17 (br, 2H), 4,69 (br, 2H),1.77 (br, 1H),1,18 (br, 2H)
VPPP	THF	^{1}H-NMR (250 MHz, $CDCl_3$): δ 7.07 (br, 4H), 6.62 (br, 4H), 6.25
		(br, 4H), 2.47 (br, 2H), 1.90 (br, 4H), 7.07 (br, 4H), 1.17 (br,3H)
MVPT	THF	^{1}H-NMR (250 MHz, THF-D_8): δ 6.91 (br, 2H), 6.65 (br, 2H),
		6.40 (br, 3H), 3.02 (br, 3H), 1.78 (br, 1H), 1.35 (br, 2H)
MPEMA	anisole	No polymer
		-
DPVB	DMF	^{1}H-NMR (250 MHz, DMSO-D_6): δ 7.85 (br, 2H), 6.87 (br, 2H),
		2.86 (br, 4H), 1.77 (br, 3H)
PFMA	anisole	^{1}H-NMR (250 MHz, $CDCl_3$): δ 2.41 (br, 2H), 1.37 (br, 3H)
		^{19}F-NMR (500 MHz, $CDCl_3$): δ -161.51 (br, 2F), -156.59 (br, 1F),
		-153.23 (br, 2F)

4.4.2. Attachment of phenothiazine to poly-PFMA (PPFMA)

158 mg phenothiazine (0.79 mmol) were dissolved in 2 ml dry THF. 200 mg poly-PFMA (0.79 mmol referred to monomer units) with a molecular weight of 23800 g/mol PDI of 2.21 and 122 µL (0.87 mmol) TEA were dissolved in 3 ml dry THF and the solution added to the phenothiazine solution. The reaction was stirred at 60 °C under argon over night. Finally the polymer was precipitated twice from 50 ml hexane. After drying at 60 °C over night, 160 mg of polymer were obtained. GPC (M_n = 24000 g/mol, PDI = 2.22). ^{1}H-NMR (250 MHz, $CDCl_3$): δ 2.34

(br, 2H), 1.36 (br, 3H). The resulting polymer was examined with Fourier Transformed Infrared spectroscopy (FTIR) using Attenuated Total Reflection (ATR).

4.4.3. Attachment of phenothiazine to poly-DPVB (PDPVB)

The reaction was performed according to II.4.4.2: 163 mg phenothiazine (0.82 mmol), 200 mg PDPVB (0.82 mmol referred to monomer units) with a molecular weight of 28900 g/mol and PDI of 2.77), 125 µL TEA (0.90 mmol) and 2 ml DMF were used, respectively. The polymer was precipitated from 50 ml ethyl acetate. 143 mg of polymer were obtained after drying. GPC (M_n = 29200 g/mol, PDI = 2.76). ^{1}H-NMR (250 MHz, DMSO-d_6): δ 7.86 (br, 2H), 6.88 (br, 2H), 2.89 (br, 4H), 1.76 (br, 3H). The resulting polymer was examined with FTIR as described in II.4.4.2.

4.4.4. Attachment of MPHDA to PPFMA

269 mg MPHDA (0.79 mmol) were dissolved in 3 ml dry THF and 125 µL TEA (0.88 mmol) were added to the solution. 200 mg PPFMA (0.79 mmol referred to monomer units) with a molecular weight of 23800 g/mol and PDI of 2.21 were dissolved in 2 ml dry THF. The solution was added to the MPHDA solution and the reaction was stirred at 60 °C under argon over night. On the next day, white colored agglomerates precipitated. The white precipitate could not be dissolved in any solvent.

4.4.5. Attachment of AEPCA to PPFMA

125 mg of AEPCA (0.44 mmol) were dissolved in 1 ml dry THF and 44 mg TEA (0.44 mmol) were added to the solution. 111 mg PPFMA (0.44 mmol referred to monomer units) with a molecular weight of 23800 g/mol and PDI of 2.21 were dissolved in 2 ml dry THF. The solution was added to the AEPCA solution which turns the solution into slightly turbid. The reaction was stirred at 40 °C under argon over night. The polymer was precipitated twice from methanol and dried in vacuum at 60°C. 157 mg of polymer were obtained. GPC (M_n = 26800 g/mol, PDI = 2.18). ^{1}H-NMR (250 MHz, $CDCl_3$): δ 5.63 (br, 1H), 3.31 (br, 2H), 1.94 (br, 2H), 1.18 (br, 3H). The resulting polymer was examined with FTIR as described in II.4.4.2.

4.4.6. Attachment of AHPCA to PPFMA

The reaction was performed according to II.4.4.5: 185 mg AHPCA (0.54 mmol), 55 mg TEA (0.54 mmol) and 131 mg PPFMA (0.54 mmol referred to monomer units) were used. After drying 206 mg of polymer were obtained. GPC (M_n = 26800 g/mol, PDI = 2.15). ^{1}H-NMR (250 MHz, $CDCl_3$): δ 7.0 - 7.51 (br, 8H), 5.03 (br, 1H), 3.62 - 3.8 (m, 12H), 2.36 (br, 2H), 1.25 (br, 3H). The resulting polymer was examined with FTIR as described in II.4.4.2.

4.4.7. Attachment of MPMA to PDPVB

150 mg poly-DPVB (0.61 mmol referred to monomer units) a molecular weight of 28900 g/mol and PDI of 2.77 was dissolved in 3 ml dry DMF. 104 µL TEA (0.74 mmol) was added to the solution. Finally, 150 mg MPMA (0.62 mmol) was dissolved in 2 ml dry DMF and added to the

polymer solution and stirred at 60 °C under argon for 24 h. The polymer was precipitated twice from isopropanol to yield 220 mg of the polymer after drying at 60 °C in vacuum. GPC (M_n = 31100 g/mol, PDI = 2.71). ^{1}H-NMR (250 MHz, $CDCl_3$): δ 8.88 (br, 2H), 7.66 (br, 2H), 7.14 (br, 3H), 6.78 (br, 6H), 4.47 (br, 2H), 3.21 (br, 3H), 1.45 (br, 3H). The resulting polymer was examined with FTIR as described in II.4.4.2.

5. Results and discussion

5.1. Phenothiazine baring monomers and polymers

From the synthetic aspect, the nucleophilic substitution at the N-position of the phenothiazine was a quite promising approach. By activation of the secondary amine group using strong base like PTBO, it was possible to attach phenothiazine successfully to a series of halogenated aliphatic and aromatic vinyl compounds. This synthetic approach was done in a single step reaction, resulting in high yields above 70%. Using the reactivity of the phenothiazine aromatic carbons, carbonyl groups were introduced in C-3 ring position. The carbonyl group was then further changed to a vinyl group via a wittig reaction. In addition, carbonyl group could successfully be converted to alcohol in order to be attached to methacrolyl chloride. Thus, phenothiazine monomers with aliphatic and aromatic vinyl groups as well as methacrylate group could be obtained for radical polymerization. However, the Ulmann coupling of phenothiazine to obtain π-conjugated PBA could not be performed. Both methods from McKeown[92] and Li[95] using a ligand containing and ligand free version were investigated. The coupling reactions were used to attach aromatic phenyl rings to phenothiazine. However, it seems that the reactivity of 4-bromobenzaldehyde is substantially low due to the -M effect of the aldehyde group. Other coupling reactions like Buchwald-Hartwig based on palladium catalysts offer an alternative to obtain PBA.[97-99]

After obtaining the vinyl containing phenothiazine monomers, polymerization followed in the second step as shown in Table 1. Interestingly, phenothiazine itself serves as an inhibitor for radical polymerization reactions. As a consequence the polymerization reaction can only take place because the polymerization step is faster than the inhibition reaction. In the case of VBPT, VPPP and MVPT, the polymerization was successful. According to the GPC results in Table 2, for both molecular weights M_n of 10000 and 25000 g/mol polymers could be obtained with high yield ranging between 77% and 85% at desired molecular weight. The polydispersity is within the expected range for uncontrolled radical polymerization. For APT as well as for MPEMA, no polymer was formed after the reaction. After the reaction, the solution turned red colored and no change in viscosity was observed. For MPEMA, an oligomer like product was obtained as low viscosity oil. One reason for the lack of reactivity for APT is related to the isolated position of allyl group. Allyl groups are generally less reactive than vinyl groups which on their turn are less

Table 2. Experimental and theoretical molecular weight, polydispersity and yield of phenothiazine based polymers.

Monomer	Structure	Theoretical M_n	Experimental M_n	Polydispersity	Yield
APT	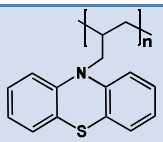	10000	No polymer	-	-
		25000	No polymer	-	-
VBPT	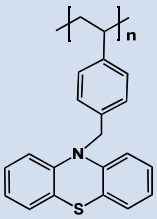	10000	8200	1.23	85%
		25000	27300	2.32	81%
VPPP	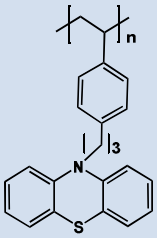	10000	5300	1.28	77%
		25000	25800	1.96	84%
MVPT	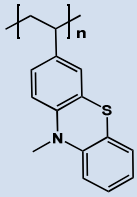				
		25000	26300	2.53	85%
MPEMA	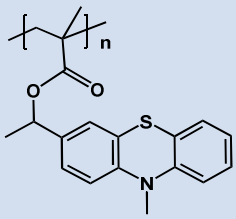	10000	800	1.12	3%
		25000	No polymer	-	-
DPVB	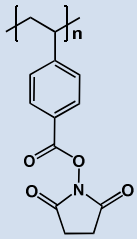	-	-	-	-
		25000	28900	2.77	91%
PFMA	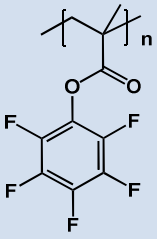	-	-	-	-
		25000	23800	2.21	76%

reactive than acrylates. Besides, a substitution at the N-position making the monomer sterically more hindered is probably the reason why APT cannot polymerize. Acrylates and methacrylates

are typically highly reactive monomers. Therefore, it seems not to be plausible why MPEMA having a methacrylate group cannot be polymerized. Phenothiazine, however, is also used as a stabilizer for acrylate monomers like acrylic acid as shown by Becker and coworkers.[100] The typical red color change after the polymerization for MPEMA and also for APT indicates that a stable phenothiazine radical must have formed. As a consequence, the polymerization must be then inhibited or stopped at low conversion degree like in the case of MPEMA. Nevertheless, it is possible to obtain polymers with molecular weights M_n at around 25000 g/mol, using styrene based phenothiazine monomers.

One important aspect for processing polymers except for the molecular weight is their thermal stability. According to the thermogravimetry experiments, the onset decomposition temperature of the polymers PVBPT, PVPPP and PVMPT were 283, 330 and 385 °C (appendix Figure A 1, Figure A 2 and Figure A 3). Thus, the polymers reveal remarkably high thermal stability and could find application in thermally sensitive storage devices. Another major issue for processing is the solubility of the polymer to make homogeneous polymer films for conductive SFM experiments. Homogenous films are necessary for recording data points on the nanometer scale. Small inhomogeneities would lead to increased writing and reading errors. On the other hand solubility is an important aspect for radical battery application. The redox polymer must be immobilized on the electrode and not dissolved during the electrochemical processes. Especially, they should show insolubility in organic carbonates (propylene carbonate (PC), ethylene carbonate (EC), diethylene carbonate (DEC)) and dimethoxyethane (DME) which are often used as an electrolyte for battery cells. Table 3 shows a list of solubility for the polymers poly-VBPT (PVBPT), poly-VPPP (PVPPP) and poly-VMPT (PVMPT) with a molecular weight around 25000 g/mol in different solvents.

Table 3. Solubility table for the polymers PVBPT, PVPPP and PVMPT.

Polymers	anisole	ACN	DMF	THF	Solubility in toluene	DCM	PC/EC/ DEC	DME
PVBPT	+	-	0	+	-	+	-	-
PVPPP	+	-	0	+	+	+	-	-
PVMPT	-	-	0	0	-	-	-	-

The degree of solubility is shown with +, 0 and – being well soluble, less soluble (under heating) and non-soluble, respectively. PVBPT and PVPPP showed good solubility for the standard organic solvents like THF and DCM and anisole. PVPPP can additionally be well dissolved in toluene which is a good solvent for spin-coating process. PVPPP exhibited a better solubility compared to PVBPT due to the free motion of the moiety and the backbone resulting from the

spacer. PVMPT revealed modest solubility only under heating. The determination of the glass transition temperature T_g confirmed the results of the solubility experiments with respect to molecular polymer design. The T_g was determined to 84, 153 and 183 °C for PVPPP, PVBPT and PVMPT, respectively for a molecular weight around 25000 g/mol (appendix, Figure A 4, Figure A 5 and Figure A 6). The value reflects the degree of rotational freedom of the redox moieties which decreases in the latter order. PVPPP has the highest rotational freedom and the long spacer length thus decreases the T_g resulting in a softer polymer morphology. Thus, PVPPP as well as PVBPT should result in more homogeneous films and more useful for processing, e.g. by spin-coating. Nevertheless, it should be mentioned that the T_g is higher than room temperature for all three polymers. Polymer with T_g at or below room temperature would be too soft for patterning experiment with SFM. In addition, it should be stated that all polymers show any solubility either in PC, EC, DEC or in DME. These polymers could be used in organic lithium batteries as immobilized cathode material. However, the use of vinyl containing monomers is limited to their bulkiness. Phenothiazine monomers with high steric properties are difficult to polymerize. Therefore, other more versatile synthetic approaches could help to access a wide variety of redox active polymers with phenothiazine moieties. One of the synthetic approaches examined in the following section is based on activated ester polymers.

5.2. Phenothiazine baring polymers using activated esters

For the synthesis of phenothiazine baring polymers, activated ester polymers were used as an alternative. Both activated ester monomers PFMA and DPVB were obtained easily in a single step reaction. Both the pentafluoro and the succcinimide active ester leaving groups are often used in the literature for the preparation of hydrogels[101], multifunctional acrylamides[102] and chromatography support.[103] The above mentioned monomers were easily polymerized with high yields up to 91% at molecular weights M_n above 25000 g/mol (Table 2) and showed high chemical stability. From the IR data of poly-PFMA (PPFMA) and poly-DPVB (PDPVB) (Figure 1), the ester bond was clearly identified to be at the region between 1730 and 1800 cm^{-1}. The C-F bond for PPFMA is visible in the range of 1090-992 cm^{-1} together with the C-O-C symmetrical vibration. PDPVB reveals additional peaks at around 1600 cm^{-1} and 1200 cm^{-1} which are related to the p-substitution stretching and C-N stretching, respectively. Additionally, the C-O-C symmetrical stretching and C-H deformation vibration are visible for PDPVB at 1064 and between 994 and 640 cm^{-1}, respectively.

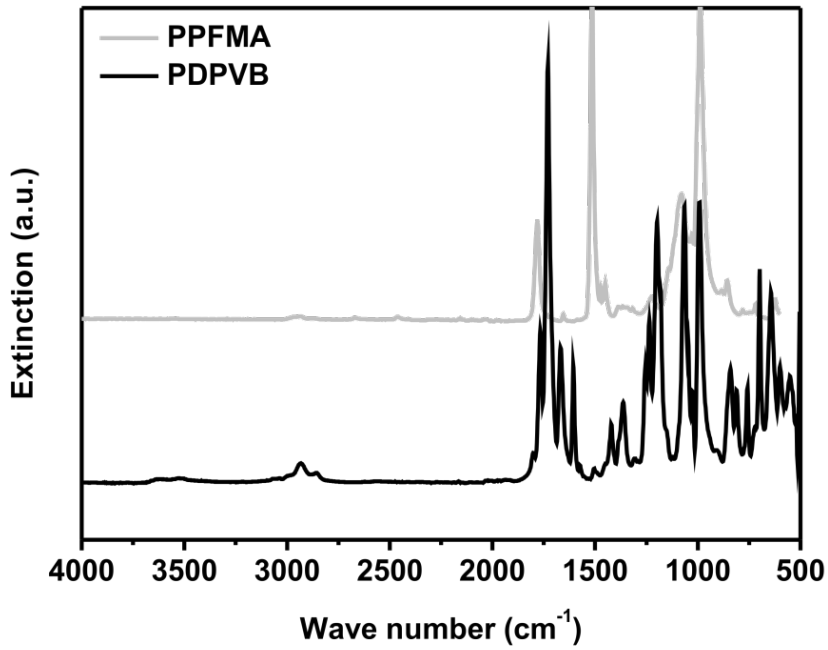

Figure 1. FTIR spectra of the activated ester polymers PPFMA and PDPVB.

No signs for the formation of carboxyl group or amide group (O-H or N-H valence bonds between 2500 and 3300 cm^{-1} are missing) could be observed after the polymerization. Thus, both polymers must still retain their activated ester groups.

To follow the reaction of phenothiazine molecules with activated ester polymers, NMR studies were performed before and after the reaction. According to the ^{19}F-NMR results, the perfluorinated group exhibited almost the same chemical shift as the monomer, thus it must be attached to the methacrylate backbone (Table 1). The ^{1}H-NMR showed no additional carboxyl or amide peak which is another proof for the stability of the PPFMA (Figure 2). The two peaks at 2.41 and 1.37 ppm correspond to the protons from the polymer backbone (Figure 2, black spectrum). The integrals of 3.00 to 1.93 correspond to the number of protons for the methyl (Figure 2, position number 1) and methylene (Figure 2, position number 2) group. The position and the intensity of the signals remained almost constant after the reaction with phenothiazine. For the attachment with phenothiazine, peaks in the aromatic region above 6 ppm were expected. However, only some impurities were visible at around 3 ppm, which could be related to the TEA used for the reaction. After the reaction with phenothiazine, no significant changes were observed (Figure 2, red spectrum). Thus, it was concluded that no reaction has taken place between phenothiazine and the activated ester PPFMA. TEA could not activate the secondary amine group of phenothiazine by deprotonation and resulted in PPFMA as the product.

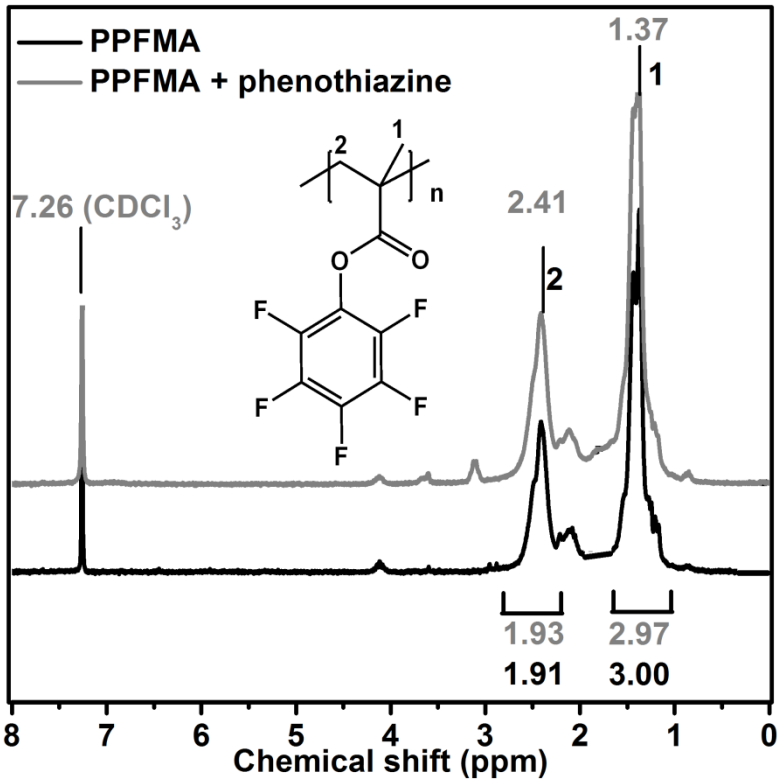

Figure 2. ^{1}H-NMR spectra of PPFMA before and after reaction with phenothiazine.

The reaction of the activated ester polymer PDPVB with phenothiazine was also followed by NMR. For PDPVB, the ^{1}H-NMR spectrum indicated that the activated ester group is attached to the polymer backbone bone, as expected (Figure 3, black spectrum). The position of the aromatic peaks was determined at 7.90 and 6.87 ppm (Figure 3, position 4 and 3). Furthermore, from the integral of the broad peaks, the right ratio between the four aromatic and four aliphatic protons of the succinimide unit at 2.89 ppm (Figure 3, position 2) was deduced. For the aliphatic backbone protons, a broad peak with the intensity of 3 protons was observed at 1.72 ppm (position 1). Additionally, the DMSO-D_6 showed two strong peaks which were related to the non-deuterated DMSO and the water absorbed in the solvent. However, after the reaction with phenothiazine, almost no change in the NMR spectrum was detected (Figure 3, red spectrum). The peak positions almost remained unchanged at the same shift. Furthermore, the ratio between the peaks almost did not show any difference. Thus, in conclusion the PDPVB did not react with phenothiazine. One possible explanation is the low acidity of the phenothiazine.

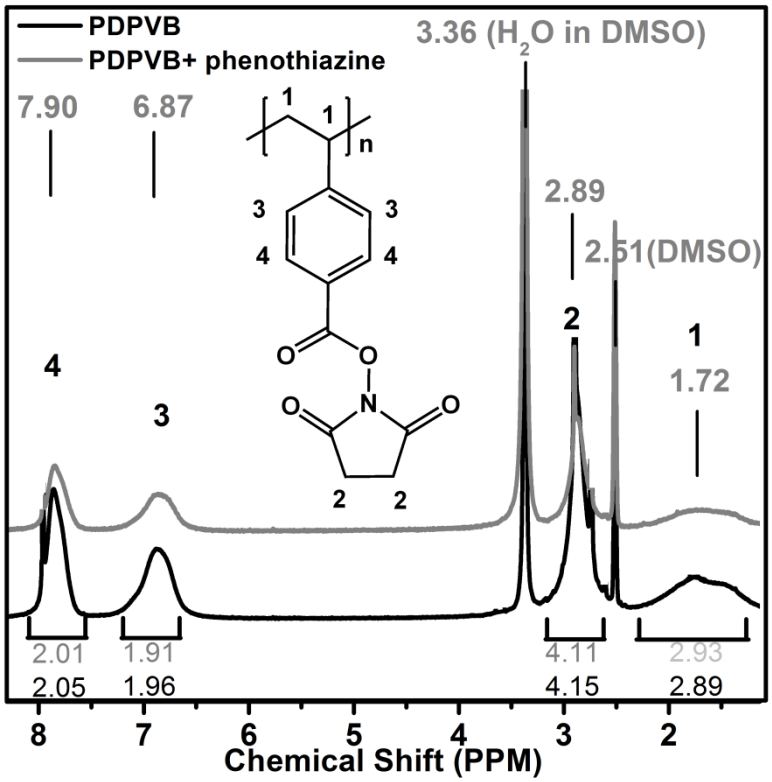

Figure 3. ^{1}H-NMR spectra of PDPVB before and after reaction with phenothiazine.

The pk_a values of phenothiazine and similar structure like carbazole[104] are around 20-25. Besides, the pk_a value increases, the more bulky substituents are attached to the amine. Thus, phenothiazine is a very weak acid and the N-position can only be activated by using strong bases like PTBO. However, the reaction would not be named activated ester conversion since the amine molecules typically react readily with the activated ester without or with small activation barrier. For the use of activated esters, phenothiazine moieties with higher reactivity are necessary.

To increase the reactivity of phenothiazine moieties towards activated esters, a new type of phenothiazine substituents with amine moieties were synthesized. Since diamines are commercially available monomers for the synthesis of polyamides[105] in the industry, my aim was to find an easy synthetic approach to polymers with different spacer length between the backbone and the redox group. From the synthetic point of view, it was quite easy to protect the diamines from one side using a BOC protecting group to obtain mBOC protected diamine. The only crucial issue for the selective protection of the diamine is a good control of the pH-value. In the first step, the desired mBOC protected diamine was obtained by adjusting the pH value to acidic pH to remove the non-functionalized diamine. In a second step, the pH value was set to basic to remove bi-functionalized diamine. The mBOC protected diamine was then successfully used for further reaction with phenothiazines containing aldehyde or carbonyl chloride functional groups. Both approaches were successful and the subsequent deprotection of the BOC group led to formation of phenothiazine moieties namely MPHDA, AEPCA and AHPCA (Scheme

21, a, b and c). Furthermore, the small moiety MPMA was synthesized using the phenothiazine aldehyde MPCA (Scheme 21, d).

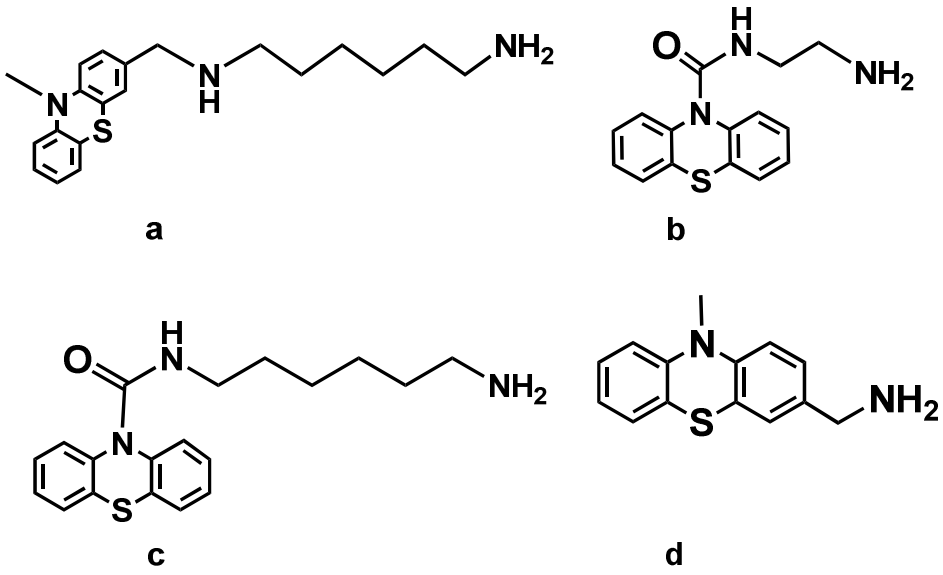

Scheme 21. Structure of the amine functionalized phenothiazines: a) MPHDA, b) AEPCA, c) AHPCA and d) MPMA.

The three moieties were left to react with the active ester polymer PPFMA. After the reaction of MPHDA with the activated ester, a white insoluble precipitate was formed. After drying the precipitate and redissolving it in DCM, a white gel like polymer was formed. Obviously, both amine groups reacted with activated ester moieties, which formed a crosslinked polymer network. This crosslinked network could not be dissolved and behaved like a gel by swelling after adding the solvent DCM. The secondary amine group, although being sterically hindered by the long hexyl spacer, obviously could still react with the activated ester moieties. One possibility to prevent the crosslinking reaction is to block the secondary amine group, e.g. by methylation (Scheme 22, a). This way, the secondary amine group cannot further react with the activated ester. After the cleavage of the BOC group (Scheme 22, b), there will still be a secondary amine group, which will then react with the activated ester.

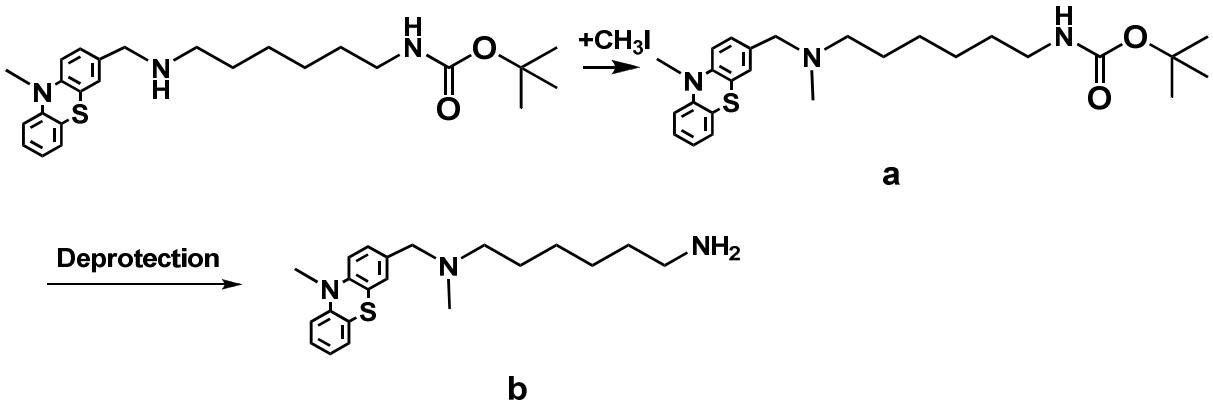

Scheme 22. Protection of secondary amine group with methyl iodide and successive deprotection: a) methylated MPHDA and b) methylated MPHDA after deprotection of the BOC group.

The moieties AEPCA and AHPCA could be obtained after selective cleavage of the BOC group. Due to the low reactivity of the amide groups, it is assumed that no crosslinking takes place and only the primary amine group is available for the reaction with PPFMA. The reaction of AEPCA and AHPCA was followed by ^{1}H-NMR (Figure 4).

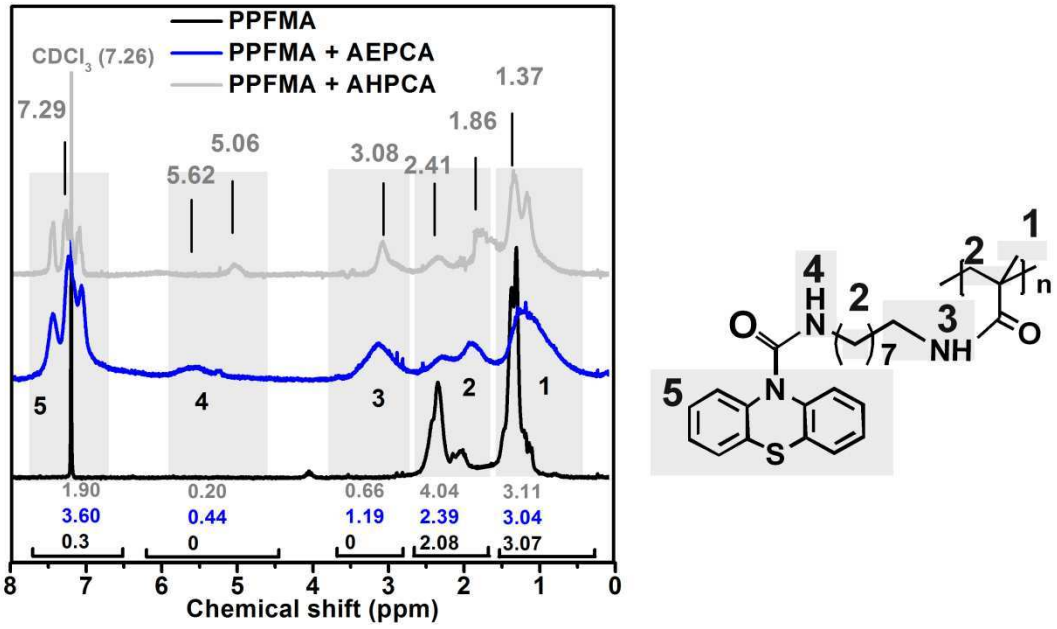

Figure 4. ^{1}H-NMR spectra of PPFMA before and after reaction with AEPCA and AHCPA.

In the NMR spectra, the aromatic peak of the attached phenothiazine for AEPCA as well as for AHPCA was clearly identified in the area between 6.5 and 7.5 ppm (Figure 4, position 5). The broad peak splits into three peaks from left to right which is related to the aromatic protons of phenothiazine in vicinity of nitrogen and sulfur as well as meta and para position with respect to nitrogen, respectively. The amide bond of the AEPCA and AHPCA was detected at 5.62 and 5.06 ppm, respectively (Figure 4, position 4). Furthermore, an additional broad peak was observed at 3.08 ppm for which had a broad distribution of 0.7 ppm and 0.5 ppm in the case of AEPCA and AHPCA (Figure 4, position 3). In addition, the backbone signal of the PPFMA was broadened and new signals were observed (Figure 4, position 2 and 1). From the signal evolution in the aromatic region, it was concluded, that both AEPCA and AHPCA reacted with PPFMA. From the integrals below the peaks, the conversion degree of the PPFMA with both amines AEPCA and AHPCA was estimated. For PPFMA converted with AEPCA, the assumption was made that all the peaks related to this moiety must appear above 2 ppm according to the NMR results. Thus, the backbone signal only contains the protons of the methyl group of the backbone (Figure 4, position 1). The integral ratio between the aromatic peaks at position 5 and the methyl peak at position 1 must be 3.0:8.0. In the case of AEPCA, the ratio is 3.60:3.04. Therefore, the conversion reaction did not proceed quantitatively. From the latter ratio, a conversion degree of 45 ± 19% was calculated as a rough estimation for the reaction of AEPCA and PPFMA. Calculating the conversion degree of AHPCA with PPFMA from the NMR data is even more difficult, since the hexyl spacer of AHPCA has a signal around 1.2 ppm to 1.6 ppm. However, from the low intensity

new signals were observed (Figure 4, position 2 and 1). From the signal evolution in the aromatic region, it was concluded, that both AEPCA and AHPCA reacted with PPFMA. From the integrals below the peaks, the conversion degree of the PPFMA with both amines AEPCA and AHPCA was estimated. For PPFMA converted with AEPCA, the assumption was made that all the peaks related to this moiety must appear above 2 ppm according to the NMR results. Thus, the backbone signal only contains the protons of the methyl group of the backbone (Figure 4, position 1). The integral ratio between the aromatic peaks at position 5 and the methyl peak at position 1 must be 3.0:8.0. In the case of AEPCA, the ratio is 3.60:3.04. Therefore, the conversion reaction did not proceed quantitatively. From the latter ratio, a conversion degree of 45 ± 19% was calculated as a rough estimation for the reaction of AEPCA and PPFMA. Calculating the conversion degree of AHPCA with PPFMA from the NMR data is even more difficult, since the hexyl spacer of AHPCA has a signal around 1.2 ppm to 1.6 ppm. However, from the low intensity of the aromatic signal, it was estimated that the more bulky AHPCA has a lower conversion degree compared to AEPCA. From the integrals at position 5 and 1 in Figure 4, a conversion degree of 23 ± 18% was determined as a rough estimation.

FTIR was applied as an alternative technique to observe the conversion of PPFMA with the amines AEPCA and AHPCA. Therefore FTIR spectra of the PPFMA before and after the reaction with AEPCA and AHPCA were recorded (Figure 5 and appendix, Table T 1).

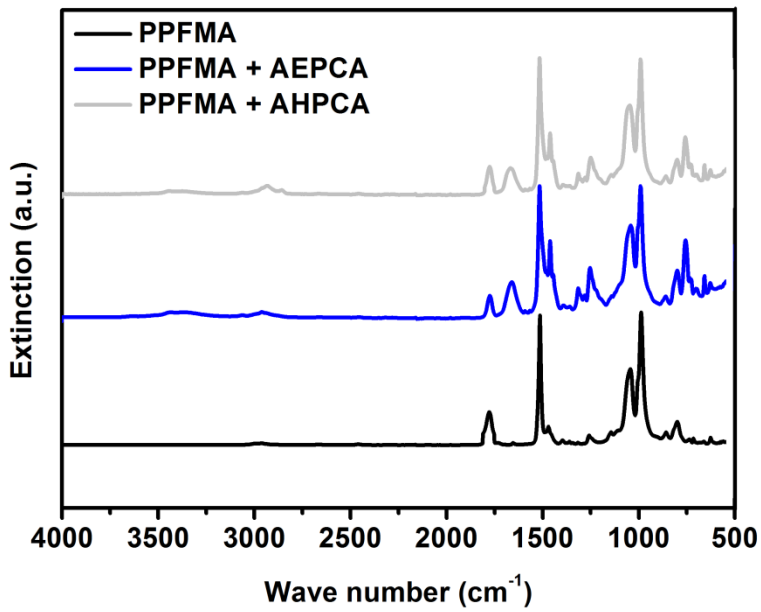

Figure 5. FTIR spectra of PPFMA before and after reaction with AEPCA and AHPCA.

The typical peak of the aromatic phenol esters was visible at around 1777 cm^{-1}, which is in good accordance with the literature.[106] After the reaction, a peak appeared at 1674 cm^{-1}, which was related to the amide bond. The ester peak at 1777 cm^{-1} was still visible, pointing out that the reaction did not proceed quantitatively. However, since AEPCA and AHPCA both contain amide groups, it is difficult to find out if the new peak comes from the already existing amide bond or

from a newly formed one. To calculate the conversion degree of the amines with PPFMA, all the spectra were normalized to the peak at 994 cm^{-1}, which corresponds to the C-F stretching vibration bond. The intensity of the ester peak at 1777 cm^{-1} was then compared to this peak. From the intensity ratio, a conversion degree of 33 ± 5% and 17 ± 7% was determined for AEPCA and AHPCA, respectively. This value is in good agreement with NMR conversion results. The AEPCA showed a two times higher conversion degree with PPFMA then AHPCA. In addition, the intensity of the amide peak at 1674 cm^{-1} is 1.3 higher for AEPCA then for AHPCA. Thus large moieties such as AECPA and AHPCA can be attached to activated ester polymers via the polymer analogous reaction. However, the reaction performed at room temperature is slowed down and leads to non-quantitative conversion.

To further increase the conversion degree of the phenothiazine moieties with activated esters, AEPCA was attached to PDPVB at elevated temperatures. From the IR data, the conversion reaction was examined (Figure 6 and appendix Table T 2). After the reaction, the ester peak at around 1773 cm^{-1} disappeared almost completely. A new amide peak was formed at 1649 cm^{-1}. From the comparison between the ester peak of both curves before and after the reaction, a conversion degree of 87 ± 15% was calculated. The conversion degree implies that the reaction is almost quantitative. Thus, AEPCA can be attached to activated ester groups at elevated temperatures with higher conversion degrees. Thus for the reaction, not only the catalyst TEA is necessary but also temperature activation is important.

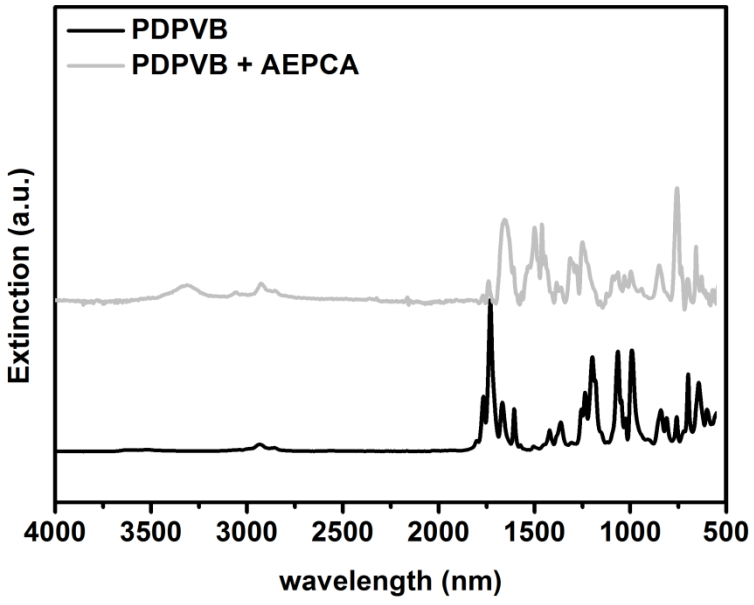

Figure 6. FTIR spectra of PDPVB before and after reaction with AEPCA at increased temperatures.

Typically, activated esters react with primary amines without any further activation at room temperature regardless of the activated ester reactivity.[93,107] The decreased reactivity can only be explained by the steric hindrance of the amine moieties due to its bulkiness. Thus, small amine moieties could improve the conversion and enable quantitative reaction. Therefore, in the

final step, MPMA as the smallest phenothiazine moiety was converted with PDPVB. From the ^{1}H-NMR data, the reaction progress was examined (Figure 7). The peak at 8.88 ppm was related to the new amide bond formed between the styrene backbone of PDPVB and MPMA (Figure 7, position 6). At 4.47 ppm, the methylene group of MPMA was observed (Figure 7, position 3). In addition, the peak at 3.21 ppm resulted from the methyl group of MPMA (Figure 7, position2). The peak at 3.21 ppm from PDPVB disappeared after the conversion with MPMA. From the ratio of the peak integrals between the amide peak (Figure 7, position 6), the methylene peak (Figure 7, position 3) and the aliphatic backbone of the styrene at 1.75 ppm (Figure 7, position 1), a proton ratio of 1.02 : 2.31 : 3.05 was calculated. This ratio corresponds to the ratio of 1 : 2 : 3 of the related protons. Thus, it was concluded, that reaction proceeded quantitatively. Further proof for the quantitative reaction of MPMA with PDPVB was obtained from the FTIR experiments (Figure 8 and appendix Table T 3).

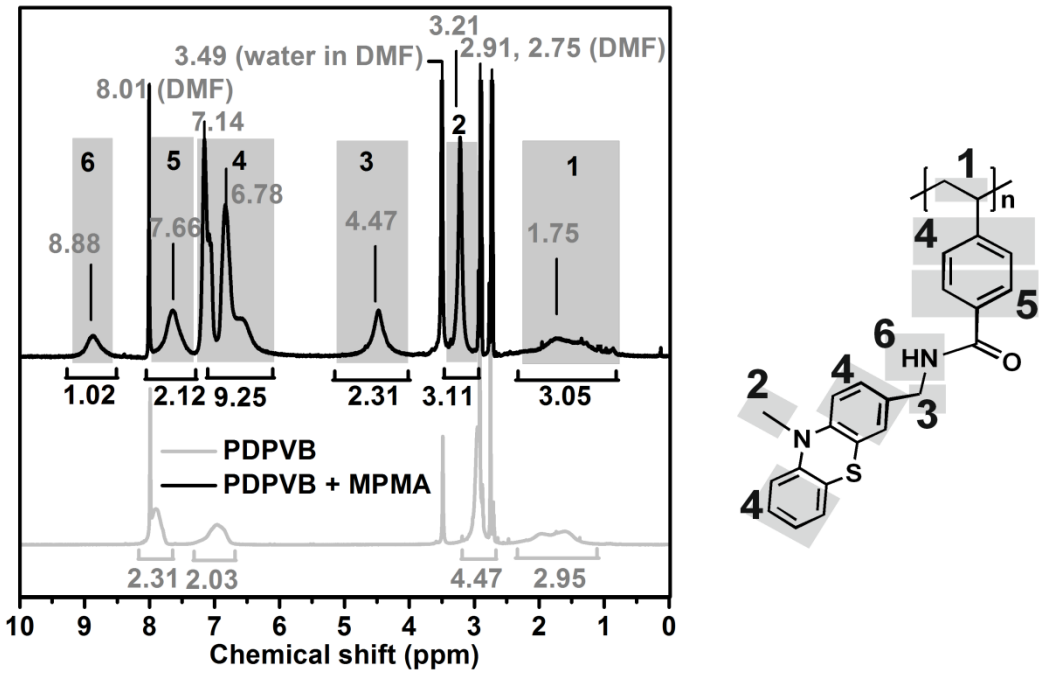

Figure 7. ^{1}H-NMR spectra of PDPVB before and after reaction with MPMA.

The ester peak at 1767 and 1729 cm^{-1} completely disappeared and a new broad peak was formed at 1641 cm^{-1} related to the amide bond. In addition, the ester peaks at 1234 and 1067 cm^{-1} corresponding to the C-O symmetrical stretching vibration disappeared. The strong peak at 1462 cm^{-1} was formed corresponding to the N-methyl group of MPMA and the peaks at 1337, 1253, 1205 and 1138 cm^{-1} resulted from the C-N stretching of the amide group.

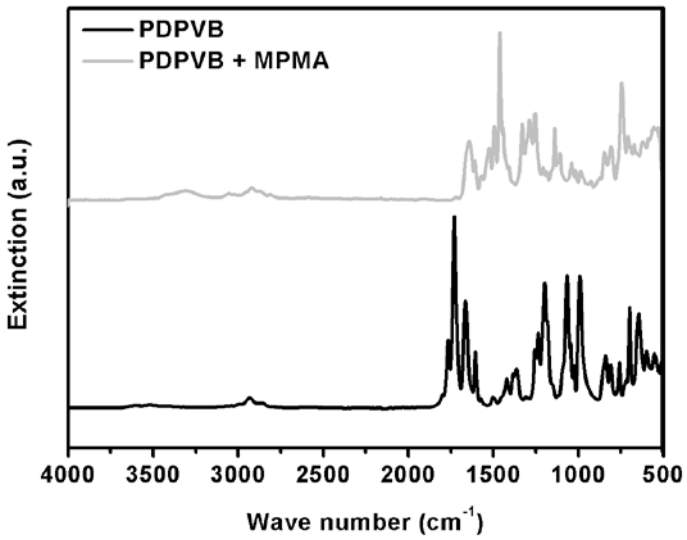

Figure 8. FTIR spectra of PDPVB before and after reaction with MPMA.

In conclusion, MPMA could react with PDPVB quantitatively. Obviously, the reaction between the activated ester polymers and phenothiazine containing amine moieties is limited by the size of the reactive amine. Small moieties have to be used if quantitative conversion is desired. For any other cases, primary amine groups are necessary for successful attachment of phenothiazine to activated ester polymers.

6. Summary and Conclusion

Phenothiazine was easily attached to styrene, vinyl and methacrylate which served as a polymerizable group. Among the synthetic routes, nucleophilic substitution of halogenated styrene proved to be a very effective and simple technique. The resulting monomers revealed a high thermal stability which is also related to the fact that the monomers were obtained as pure crystalline solids. In addition, carbaldehyde of phenothiazine offered an easy synthetic route to the vinyl monomer using the Wittig reaction. Methacrylate groups were introduced successfully by converting aceto phenothiazine into the corresponding alcohol. However, the coupling reaction between benzaldehyde and phenothiazine did not result in the desired π-conjugated monomer. The synthesis of the polymers based polymers was quite successful. Styrene based monomers like VBPT, VPPP and VMPT could be polymerized with the desired molecular weight via standard radical polymerization. Despite the inhibiting effect of phenothiazine, polymers with phenothiazine moieties were obtained with high yields. Due to steric effects and lack of reactivity, methacryl and vinyl based phenothiazine monomers MPEMA and APT could not be polymerized. Nevertheless, the obtained polymers PVBPT, and PVPPP revealed easy processing and could be dissolved in many organic solvents. However, they were not soluble in polar solvents such as ethylene and propylene carbonates used in the battery industry. Thus, the three polymers are attractive candidates for further application as electrode materials in the battery cell. Furthermore, the solubility affects the processing and film preparation for data storage application. Smooth and homogenous films are desirable for the latter application. Any

irregularities in the polymer film could have a negative effect on the reading and writing process. Thus, in conclusion styrene based phenothiazine monomers offer a simple synthetic approach for obtaining functional polymers with good chemical processability. Sterically less hindered conformation and high double bond reactivity are necessary for successful polymerization. Isolated vinyl groups and bulky methacrylates are therefore not proper candidates for polymerization.

Activated esters were used to attach phenothiazine to a methacrylate or styrene backbone. The amine group in phenothiazine was activated with a standard base TEA to further react with both activated ester polymers PPFMA and PDPVB. However, in neither case phenothiazine could be attached to the polymer backbone. The secondary amine group is not sufficiently reactive and probably too bulky for attachment to the activated ester moieties. Alternatively, polymers with methacryloyl chloride moieties should be used and phenothiazine should be activated with a stronger base. To attach phenothiazine moieties to activated ester polymers, primary amine groups were successfully integrated in phenothiazine using diamines and phenothiazine carbaldehydes as well as carbonyl chlorides. The amine containing moieties MPHDA, AEPCA and AHPCA could successfully react with the activated ester polymer PPFMA. For MPHDA, a crosslinked polymer was obtained due to the presence of two amine groups. To prevent the crosslinking, the additional amine group can be blocked by methylation prior to deprotection. The reaction of AEPCA and AHPCA with PPFMA took place partially leading to non-quantitative conversion. To improve the conversion degree, the reaction was performed at higher reaction temperature of 60 °C. In this case, the conversion degree was improved for the reaction of the AEPCA and the activated ester PDPVB. The conversion in the latter case was almost quantitative as seen from the IR spectra. Finally, the reaction of the moiety MPMA with PDPVB resulted in quantitative conversion according to the NMR and IR data. Thus, for obtaining functional polymers with phenothiazine redox moieties via activated esters, small molecules with reactive primary amine groups are adequate candidates. Furthermore, the control of the reaction conditions such as the temperature is a critical issue. The synthetic approach to phenothiazine based polymers using activated esters might be an interesting alternative when the polymerization of the phenothiazine monomers faces a problem. This might be the case, when other polymerization techniques fail or lead to undesired side reactions. In this case, activated ester polymers can be used, since their synthetic approach is well described in the literature.[93,102,106,107]

III.Phenothiazine based polymers for battery applications

Parts of the chapter are being prepared for publication in:

A. A. Golriz, T. Suga, R. Berger, H. Nishide, J.S. Gutmann, *J. Power Sources*, **2013**, in preparation.

1. Introduction and motivation

Polymers with redox active moieties have a high density of functional units per volume. The moieties cannot diffuse freely, since they are attached to the polymer backbone. Thus, if each moiety is accessible, the polymer can store many charge carriers which can be reversibly withdrawn from the moieties. Organic redox moieties immobilized by a polymer backbone offer therefore a source for storing charges by oxidation and reduction. By stabilizing the charged and discharged state, the polymer can be utilized as a reversible energy storage media. In a battery device polymers with redox moieties can serve as electron donating p-type cathode or electron accepting n-type anode. The low molecular weight and easy mechanical processing as well as flexibility are great advantages of polymers as electrode active material. Furthermore, due to the reduction of heavy metal content used in lithium batteries such as cobalt and vanadium, the polymers are interesting from the environmental aspect. The reversible and fast redox chemistry of phenothiazine[143] offers polymers with phenothiazine moieties a possible field of application as rechargeable electrode active cathode material.

In the following chapter, a selection of phenothiazine based polymers, namely PVBPT, PVPPP and PVMPT were tested with respect to their applicability as cathode active material in radical batteries. In particular, the effect of the molecular design on the redox properties was investigated. In this context, the effect of the propylene spacer in PVPPP on the redox properties was examined under consideration of the physical properties and compared with PVPBT and PVMPT.

In the first part, the phenothiazine polymers were characterized regarding their redox behavior. Therefore, cyclic voltammetry (CV) measurements were utilized to get information about the redox potential. The redox position defines the overall battery voltage. With increasing redox potential, the overall potential of the battery cell increases which is useful for high voltage applications. From chrono amperometry (CA) data, information about the diffusion process inside the polymer film was obtained. Additionally, CA data was used to calculate the heterogeneous electron transfer k^0 rate and homogeneous electron self exchange rate k_{ex} from the diffusion constants. With the help of k^0, it is possible to estimate whether the redox process is reversible or irreversible. A high k_{ex} indicates a fast electron transfer step between the redox moieties which is desirable for fast charging of the battery.

In the second part, the stability of the charged oxidized state of the phenothiazine polymers was examined with a combination of CV and UV/Vis spectroscopy as well as electron spin

resonance (ESR). The long-term stability is an important aspect regarding the life time of the battery.

In the third part, the polymers were used for the assembly of coin cell lithium batteries. These battery cells were finally examined via chrono potentiometry (CP) methods to find out the charging/discharging performance of the phenothiazine based polymers as cathode active material versus a lithium anode. In the following section, the principle of rechargeable batteries and polymer radical batteries are explained. Furthermore, the theoretical background of polymer conduction and electrochemical characterization is elucidated.

2. Theoretical Background

2.1. Batteries and performance

From electrochemical point of view, batteries consist of a series of galvanic cells. Within the cell, stored chemical energy is converted to electrical energy. A galvanic full cell consists of a positive and negative half cell with corresponding electrodes and electrolyte. The half cells are spatially isolated from each other by an ion permeable barrier. When the electrodes are connected by a cable, a discharging process occurs, leading to current flow. The electrode with the lower redox potential is referred to as the negative and the electrode with the higher redox potential as the positive electrode, respectively. During the discharging step, the negative electrode releases electron by oxidation whereas the positive electrode receives the corresponding electrons and is reduced. The electrons migrate via the external cable and the ions diffuse through the permeable barrier to compensate the adequate charges. Generally, there are two types of batteries, namely primary and secondary batteries. Primary batteries can only be discharged once whereas secondary batteries, also called “accumulators”, are rechargeable. For rechargeable batteries there are some important characteristic parameters concerning their performance:

- The open circuit potential or the so called “plateau voltage” is the potential difference between the negative and positive electrode, when no current is flowing. High potential difference is desirable for operating electronic devices.
- Storage capacity (Ah/kg) or power density (kW/kg) is related to the mass or volume of the electrode active material. It reveals the amount of charges stored in the battery. Low molar mass leads to high specific storage capacity which is a desirable factor.
- Energy density (Wh/kg) is related to the mass or volume of the electrode active material. This value reveals how much power can be taken from the battery within a period of time. Smaller battery size increases the power density.
- Self discharge rate or coulomb efficiency is a critical characteristic parameter. It correlates the amount of charges stored and withdrawn from the battery. The self

discharge rate is determined from the ratio of the charging and discharging capacity and should be equal to unity in an ideal case.

- The C-rate and E-rate indicate how fast a rechargeable battery can be charged or discharged. For example to charge a battery with 2000 mAh capacity at a C-rate = 1 means that it takes one hour to charge the battery completely at the current of 2 A. Consequently, at a C-rate =10, the same battery can be charged within 1/10 of an hour at 20 A.
- Overall life time of the batteries involves the charge and discharge cycles with respect to loss of the original capacity. This parameter also includes the memory effect existing in metal hydride and other transition metal based systems.

To reduce the mass of batteries and increase their power density, solid state light weight electrolytes can be used instead of conventional liquid electrolytes. In lithium-ion batteries, polymers have mainly been used as polyelectrolyte. The polymers are integrated as a solid state entangled polymer matrix, as a semi crystalline hybrid (gel) polymer network with crystalline and amorphous regions or as a poly olefin membrane with defined percolation pathways.[108] In addition to their low mass, polymers also offer flexible mechanical properties, which allow the fabrication of very thin and flexible battery devices.[112] Polymers with pendant redox moieties can incorporate many redox groups per repetition unit. Chemically stable moieties with fast and reversible redox chemistry have been immobilized on polymer backbones.[31,111] The synthesized polymers were utilized as electrode active mass in lithium batteries, showing high power density and high C-rates. The integration of stable radical moieties such as nitroxide groups as redox functional unit opened up a new field of investigations related to as radical batteries[111,112], which will be discussed in the next section.

2.2. Principle of radical batteries

The application of polymers as redox active material for rechargeable batteries was first introduced by MacInnes et al. using doped poly(acetylene).[109] Other redox active conducting polymers like poly(aniline)e have also been reported as positive electrode active material in zinc rechargeable batteries.[110] However, the latter concepts suffer from the chemical instability of the oxidized species. Especially under working conditions in the battery cell (electrolyte solution and high pH-value) conducting polymers tend to degrade.

In 2004 Nishide et al. introduced the concept of radical batteries.[111] They described the usage of polymers with pendant moieties based on stable redox active radicals. Among the stable radicals, nitroxide based moieties such as TEMPO (Scheme 5, a). The polymers are categorized into two groups as p- and n-type polymers. P-type polymers consist of an electron donating group (e.g. TEMPO) like in case of poly(2,2,6,6-tetramethylpiperidinyloxyl-4-yl methacrylate)[31] (PTMA; Scheme 23, a) and n-type polymers possess an electron accepting group (e.g. N-*tert*-butyl nitroxylamine) like in case of poly(N-*tert*-butyl-N-nitroxymethacrylamide) (PNMA; Scheme 23, b).

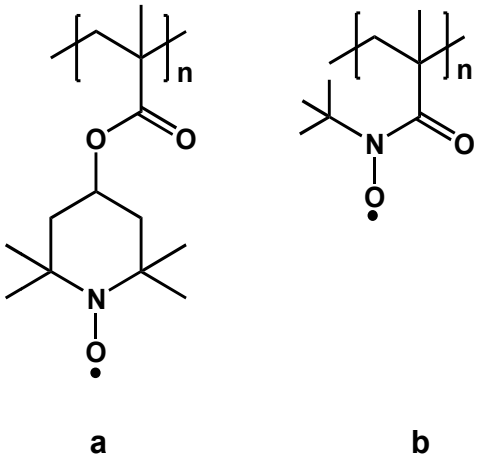

Scheme 23. Radical polymers based on nitroxide moieties: a) poly(2,2,6,6-tetramethyl-piperidinyloxyl-4-yl methacrylate) (PTMA) and b) poly(N-*tert*-butyl-N-nitroxymethacrylamide) (PNMA).

The concept of radical batteries has gained more importance in the last few years. Combination of p- and n-type polymers as positive and negative electrode respectively allows the production of fully organic flexible batteries.[112] The working principle of the radical battery is quite similar to the conventional rechargeable batteries (Scheme 24). During the charging step, the p-type cathode material is oxidized and releases its electrons. The electrons can then migrate to the negative electrode across a cable connection. PTMA has a low intrinsic conductivity which is why conducting carbon composite has to be added to the redox active mass to increase the current flow. The positive charge is compensated by the migration of counter ions in the electrolyte. For the discharging process, electrons migrate from the negative electrode, reducing the oxoammonium species back to the nitroxide.

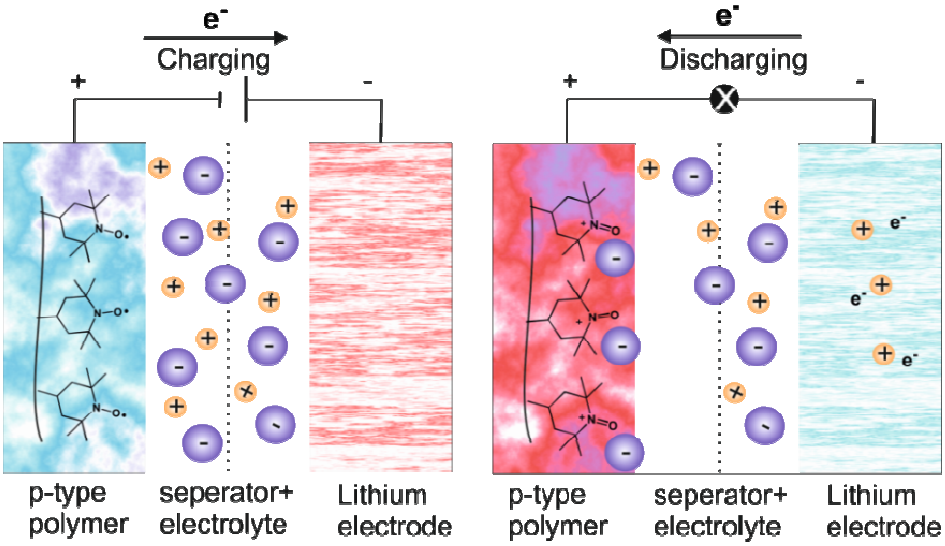

Scheme 24. Schematic view of a radical polymer battery design with p-type cathode material and lithium anode during charging and discharging operation.[31]

For PTMA as p-type electrode active material in the battery cell, Nishide et al. reported outstanding performance. PTMA showed a charge-discharge capacity of around 110 Ah/kg at a

cell potential of 3.5 V. Even at higher C-rates up to 10 or 50 C, 95% of the theoretical capacity could be achieved.[111] The fast redox chemistry of radical containing polymers allow a very fast charging rate up to 300 C.[113] This C-rate is far above the value for conventional lithium ion batteries. In addition, the low molecular weight and the high density of the moieties enables to further increase the storage and power density (Figure 9).

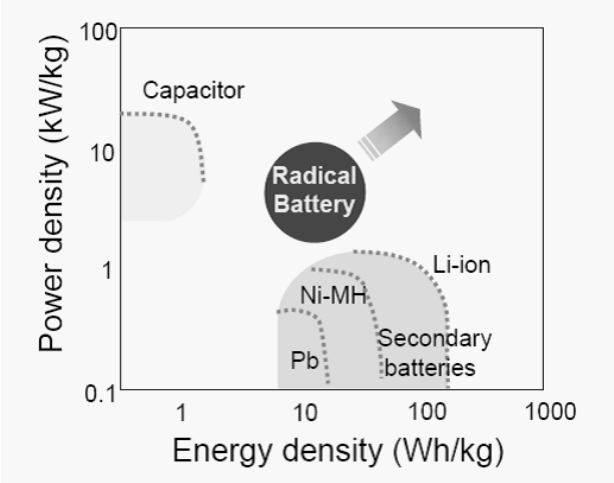

Figure 9. Performance of radical batteries with respect to power and energy density.[31]

Radical batteries have theoretical storage capacities up to 200 Ah/kg (energy density up to 50 Wh/kg) which is slightly lower than lithium ion batteries. At the same time, the power density of radical batteries is around 10 kW/kg which is comparable to the power density of capacitors. Moreover, radical batteries expose a low self discharging. The high life time allows the charge/discharge procedure to be repeated for over 1000 cycles without significant change of the capacity.[111] Another important advantage of radical batteries is the environmental factor. Polymer based radical batteries can easily be recycled compared to metal containing batteries. Based on their good performance, a series of nitroxide based polymers have been synthesized as electrode materials for radical batteries.[31]

Polymer with phenothiazine redox moieties have not been used so far as p-type electrode active materials. The low molecular weight and the fast and reversible redox chemistry of phenothiazine could be of potential application for radical batteries.[143] Another advantage of phenothiazine redox moiety is the easy synthesis of the polymer. Monomers containing radical moieties like nitroxide radicals can be polymerized either via anionic polymerization or by standard radical polymerization using a precursor. The precursor is oxidized to the nitroxide species in subsequent step.[111] However, phenothiazine containing monomers can as well be accessed directly by standard radical polymerization. Polymers with high density of phenothiazine moieties per each repetition unit like PVBPT, PVPPP and PVMPT can be obtained this way. A basic understanding of the conduction mechanisms in the polymers with redox moieties is necessary for investigating their electrochemical properties. In the following section, an overview of redox polymers and their conduction mechanism is presented. In particular, the focus is set on polymers with redox moieties.

2.3. Conduction mechanisms in redox polymers

A characteristic feature of redox polymers is the presence of electrostatically and spatially isolated electro active redox groups.[114] In contrast to conjugated polymers, the electrochemical process in redox polymers is localized to the redox sites and does not induce the reorganization of the double bond structure in the backbone. Redox polymers can be categorized into two major groups. The redox site can either be covalently bound as a unit built into the backbone of the polymer (Scheme 25, a) or as pendant side group (Scheme 25, b). Alternatively, the moieties can as well be attached via electrostatic binding like in polyelectrolytes (Scheme 25, c). The major field of application for redox polymers is electro catalysis[115] and fuel cells[213], where electrochemical reactions selectively control charge transfer rates between electrode and substrate.[114] A great advantage of redox polymers is their narrow potential peak.[111] The redox process takes place in a defined potential range allowing exact tuning of electron transfer and the doping level. The conductivity maximum occurs when the redox sites are oxidized at a doping level of 50%. At this point, the electron exchange between two neighboring moieties leads to an optimal charge carrier density which increases the conductivity.

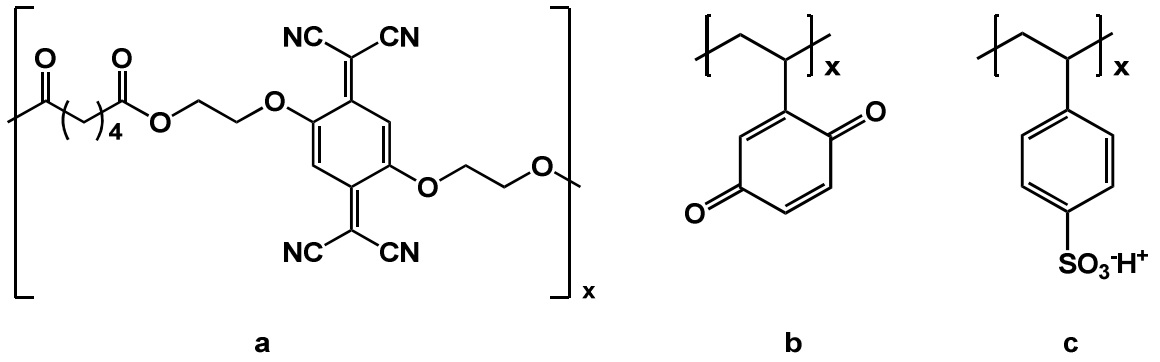

Scheme 25. Polymers with isolated redox moieties integrated in the chain and as pendant group: a) poly(tetracyanoquinodimethane), b) poly(vinyl-p-benzoquinone) and c) poly(styrene sulfonate).[114]

The conduction mechanism inside the redox polymer film is based on sequential self exchange (electron hopping) between neighboring redox groups (Scheme 26).[116] In the first step, the electron is transferred to a close by redox site at the polymer electrode interface. The mechanism of electron transfer between electrode and polymer is based on tunneling over short distances of tenth of a nanometer.[117] This process is driven by the electrical potential gradient according to Butler-Vollmer diffusion kinetics.[142] In a second step the adjacent reduced group serves as electron donor and the oxidized group as electron acceptor, respectively. Thus, the electron hops from the position A (Scheme 26, blue circle) to position B (Scheme 26, red circle) and can move towards the solution or back to the electrode.

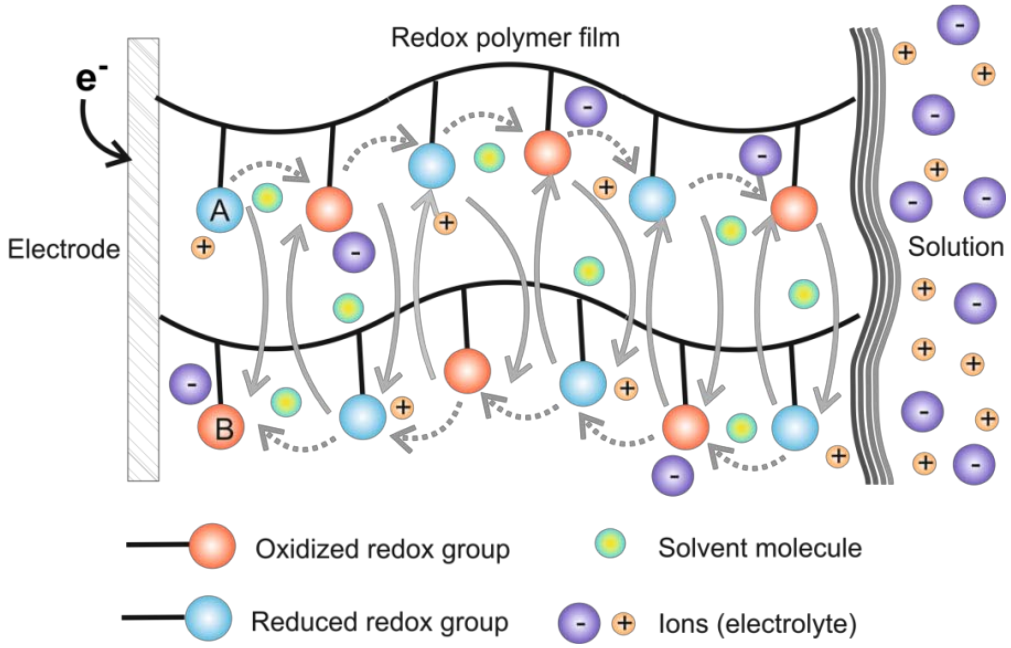

Scheme 26. Electron transfer through polymer film by hopping mechanism.

The hopping can either take place along a single polymer chain or between two adjacent polymer chains. Percolation of charges along the polymer film is mainly driven by the concentration gradient of the redox sites which is independent of the electrical potential gradient. The self exchange rate depends on the concentration of the oxidized and reduced groups. But to understand the diffusion process through the redox polymer coated electrodes, other aspects like polymer dynamics and ion mobility in the polymer film must be taken into account. The charge transfer at the electrode polymer interface is generally accompanied by transfer of the counterions to preserve electroneutrality. This means that for redox polymers ionic and electron conductivity are both important and the overall apparent diffusion rate constant D_{app} includes the electron as well as the ionic mobility in the polymer film. The solvent molecules influence the diffusion process by incorporation inside the polymer film, which leads to swelling of the polymer film and changes the film thickness. Furthermore, side reactions can take place because of presence of ions and solvents in the polymer film. The side reactions can include formation of ion pairs, cross-linking and dimerization as well as dissolution of the polymer. [118,197]

As mentioned before, D_{app} contains the diffusion rate of the ions and the electron in the polymer film. Immobilized moieties on a polymer film have a negligible ion diffusion rate compared to their electron diffusion.[126] To quantify the diffusion process in the polymer film, the rate of heterogeneous and homogeneous electron transfer has to be determined. Heterogeneous electron transfer describes the electron transfer (ET) process between the polymer film and the electrode surface.

A kinetic approach for describing heterogeneous ET processes for redox polymers at the electrode interface is given by the Butler-Volmer equation (1)[142]:

$$j = F \cdot k^0 \cdot \left\{ C_{Ox}(0,t) \cdot \exp\left[-\frac{\alpha_{ET} \cdot n_e \cdot (E - E_0)}{RT} \right] - C_{Red}(0,t) \cdot \exp\left[\frac{(1-\alpha_{ET}) \cdot n_e \cdot (E - E_0)}{RT} \right] \right\} \quad (1)$$

In this equation, the relationship between the current density j is described in dependence of the potential difference between the electrode E and the standard potential E_0. C(0,t) is the concentration of the redox species at the electrode interface (distance from the electrode x=0) at time t, k^0 is the standard heterogeneous rate constant of the electrode in equilibrium, F is the Faraday constant, R the universal gas constant, T the temperature and n_e the number of electrons. For the ET process, the difference between E and E_0 is mainly the driving force and α_{ET}, the so called "charge transfer coefficient" describes the symmetry of the ET according to the Marcus theory.[119] In equilibrium the driving force is described as the difference between E and E_{eq} which is the equilibrium potential:

$$\eta = E - E_{eq} \quad (2)$$

This difference is known as the overpotential η. With the help of the Butler-Volmer equation, k_0 can be calculated. This value is useful for estimation of the redox reaction regarding its reversibility. However, determining k_0 is complicated since many parameters are necessary. Besides, η is often influenced by diffusional or polarization effects.[142] In many cases, simplified model systems are used to fit the experimental data. For polymers with redox active moieties the homogenous electron self exchange between the moieties must be considered in addition to the heterogeneous electron transfer. The corresponding rate constant of the electron self exchange k_{ex} is useful to estimate the response time of the redox polymer. The response time is related to the C-rate and therefore is important information.[120] Thus, k_0 and k_{ex} have to be calculated to get a better understanding of ET processes in the polymer film and to estimate the performance of the polymer in the battery cell. Electrochemical measurement methods like CV and CA are appropriate methods and can help to obtain the desired rate constants.

2.4. Electrochemical characterization

2.4.1. Cyclic voltammetry

Cyclic voltammetry (CV) [121,122] is a method for acquiring qualitative and quantitative data of ongoing electrochemical processes. The setup consists of three electrodes. At the working electrode (WE), the so called "triangular potential" is applied versus time. That means the potential E at the WE is ramped up to a certain value and then ramped down to a desired end potential (Scheme 27). The scan rate or scan speed *v* is measured in mV/s. The potential is always applied between the WE and the so called "reference electrode" (RE). With the latter electrode RE, the nominal value of the potential can be defined precisely. Mainly, RE is a non-

polarizable electrode with a stable and constant potential value such as saturated calomel (SCE) or saturated Ag/AgCl. As soon as an electrochemical process takes place, the potential between the WE and RE is changed. To compensate the potential to the nominal value, a current flows from a third electrode, namely counter electrode (CE), to the WE. This current is registered and plotted against the ramping time. In order to obtain the CV-diagram, the ramped potential is plotted against the current. From the CV-diagram, individual current peaks can be derived, which are related to individual processes such as oxidation or reduction.

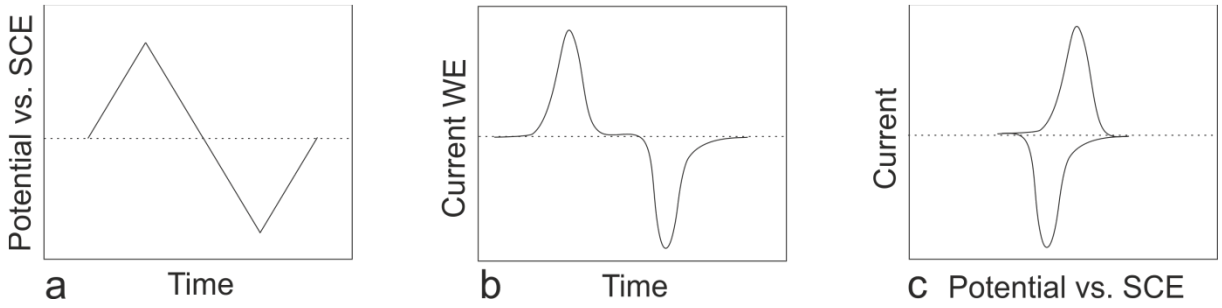

Scheme 27. Principle of cyclic voltammetry: a) triangular potential vs. time and b) current flow at the WE vs. time. c) This current flow is plotted against the driving potential in the resulting CV-diagram.

A typical CV-diagram is shown in Scheme 28. The scan starts at point *a* up to the turning point *e*. By increasing the potential, the current starts to increase at position *b*. Further increase of the potential leads to successive oxidation of the analyte until the maximum at point *c* is reached. The resulting current peak at this point is called "anodic peak current" (i_{pa}) and the resulting potential "anodic peak potential" (E_{pa}). At point *d*, all the analyte at the surface of the WE is oxidized and at turning point *e* the potential is reversed. When the potential is ramped in the negative direction, the current starts to decrease at point *f*. The reversed process takes place leading to the reduction of the analyte until at point *g* the minimum is reached. This peak position corresponds to the cathodic peak current (i_{pc}) and cathodic peak potential (E_{pc}). At point *h*, the analyte at the surface of the WE is reduced completely and the cycle can start from the beginning in point *a*. The point, at which the half current value of the corresponding oxidation or reduction peak with respect to the baseline is achieved (here for E_{pa}) is the so called "half-wave potential" ($E_{pa/2}$) and the corresponding current half-wave current ($i_{pa/2}$). The broadening of the peak at $E_{pa/2}$ is named $\Delta E_{pa,1/2}$ and is a characteristic parameter for determination of reversible processes. The peak separation between E_{pc} and E_{pa} is described as ΔE_p which also contains information about the reversibility of the redox reaction. $E_{1/2}$ is the average between the anodic and cathodic peak potential and can be used instead of E_{pa} or E_{pc} to identify the peak position without considering the peak separation.

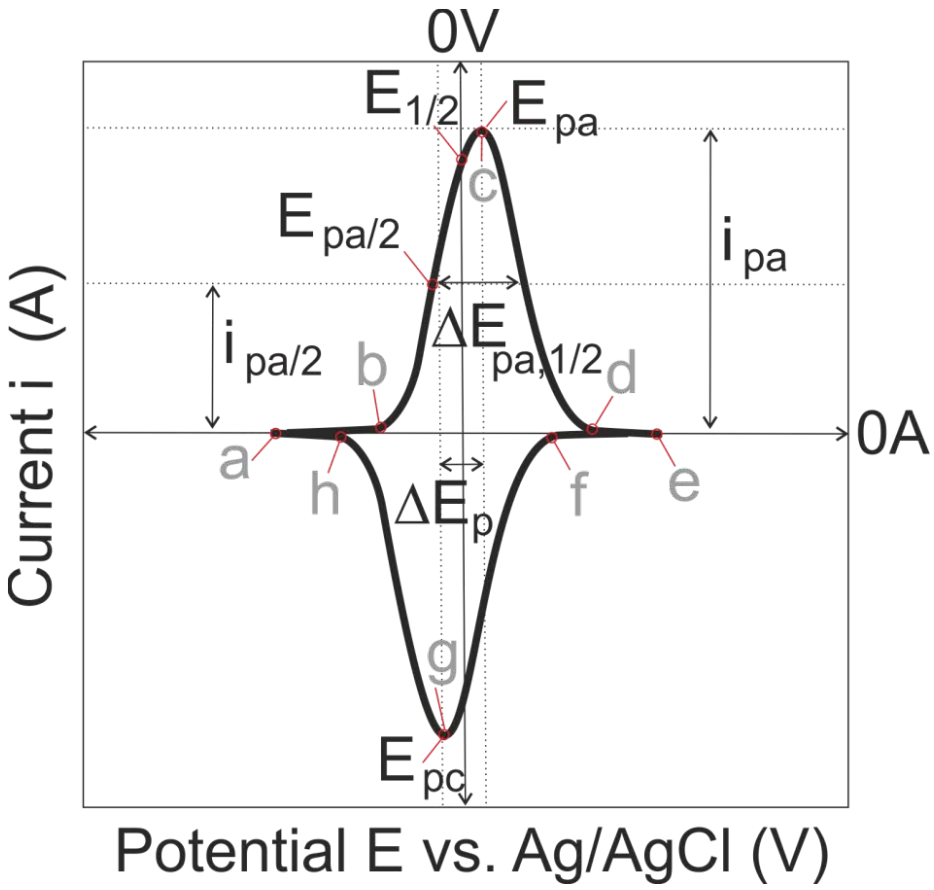

Scheme 28. Schematic CV diagram of a spin-coated polymer film.

Redox active substances can be examined with CV measurements. These substances can rather have a reversible, a quasi reversible or an irreversible electrochemical behavior. The thermodynamic description of reversible electrochemical processes in solution is given by the Nernst equation (3):

$$E = E_0 + \frac{RT}{n_e \cdot F} \cdot \ln\left(\frac{C_{Ox}}{C_{Red}}\right) \qquad (3)$$

According to the Nernst equation, the concentration of the oxidized and reduced species C_{Ox} and C_{Red} in the solution determine the potential of the electrochemical cell. From the experimental point of view, an indication for reversible redox chemistry is given by the standard heterogeneous rate constant for electron transfer k^0. For values of k^0 larger than 10^{-2} cm/s (smaller than 10^{-5} cm/s), the reaction is classified as reversible (irreversible). Values between 10^{-2} and 10^{-5} cm/s are classified as quasi reversible reactions.[121] However, k^0 is experimentally difficult to obtain and is usually indirectly accessible by theoretical assumption as mentioned before.[123-125] The reversibility of the electrochemical reaction can also be determined by simple criteria obtained from CV diagram especially with respect to the position and intensity of the oxidation and reduction peak. Especially the peak distance between E_{pc} and E_{pa} is important. This distance can easily vary due to overpotential polarizing effects at the electrode interfaces. The theoretical background of the overpotential η was previously in the context of the Butler-Volmer equation (1).

In the case of rapid and reversible redox couples in solutions (Nernst condition)[121], the distance between E_{pc} and E_{pa} can be described with:

$$\left|\Delta E_p\right| = \frac{0.0565}{n_e}(V) \tag{4}$$

ΔE_p for polymer films is equal to zero in the ideal case, since the diffusion process of the moieties does not lead to overpotential formation.[126] Under experimental conditions, peak separations around 20 mV for single electron transfer in confined surfaces can be found.[126] In the case of polymer films, a symmetrical peak distribution is expected. The peak width $\Delta E_{pa,1/2}$ in the ideal case has the following value for reversible reactions according to Langmuir adsorption isotherms[127]:

$$\left|\Delta E_{pa,1/2}\right| = \frac{0.0906}{n_e}(V) \tag{5}$$

Any deviation from ideal behavior results from the following facts: a) oxidized and reduced sites don't show equivalent adsorption ability. b) Interactions between the adsorbed redox sites influence the redox behavior. Furthermore, the ratio between i_{pa} and i_{pc} equals unity for an ideal reversible redox process and $E_{1/2}$ equals E_{pa} or E_{pc} since ΔE_p = 0. For surface confined redox polymers, the physical diffusion of the redox sites is neglected and the peak current i_p reveals a linear dependency on the scan speed ν:

$$i_p = \frac{A \cdot \Gamma \cdot (n_e \cdot F)^2}{4R \cdot T} \cdot \nu \tag{6}$$

By knowledge of the number of transferred electrons and the electrode surface area A, the surface coverage of the redox sites Γ can be estimated from the linear slope according to equation (6). For polymer films on an electrode, charge diffusion through the polymer film is crucial. Swelling of the polymer and the ability to rotate in the proper juxtaposition for electron exchange plays an important role. To examine these phenomena, more precise determination methods of the diffusion coefficients are necessary. One of these methods is the chrono amperometry

2.4.2. Chrono amperometry

In chrono amperometry (CA)[128] measurements the potential at the WE is instantaneously increased or decreased. The applied potential step function switches from a starting potential E_S up to a final potential E_E starting at the time t=0. The current response is recorded as a function of time (Scheme 29). Usually, E_S is set to a value where no electrochemical process can take place and E_E has a value where electrochemistry takes place easily.

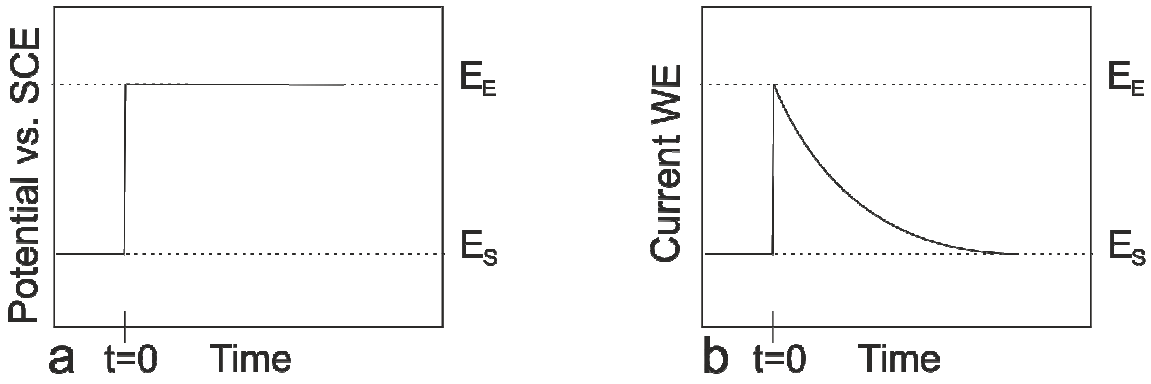

Scheme 29. Principle of CA: a) step potential and b) resulting current decay with time at the WE.

By instantaneously changing the potential, the concentration of the electrochemically oxidized or reduced species at the electrode surface decreases suddenly towards zero. From this point, the current starts to decrease and the remaining current originates from the analytes diffusing to the electrode surface. The redox process in the case of redox bearing polymers on a confined surface is dominated by the lack of the physical diffusion D_{phys} of the redox moieties due to their immobilization. Thus, the apparent diffusion D_{app} step can be derived by Dahms-Ruff equation[139] as follows:

$$D_{app} = D_{phys} + D_{ex} \approx D_{ex} \quad (7)$$

Since D_{phys} does not play a role for surface immobilized redox units, D_{app} is simplified to the contribution of the electron self exchange diffusion D_{ex} between the neighboring sites (homogeneous electron transfer). From CA experiments the information about D_{app} can be obtained. A relationship between the time decay t_d of the so called "faradaic current density" j_{Far} is described by the Cottrell equation:

$$j_{Far} = \frac{n_e \cdot F \cdot C_{Ox}^{*} \cdot \sqrt{D_{app}}}{\sqrt{\pi \cdot t_d}} \quad (8)$$

By plotting $t^{-1/2}$ against J_{Far}, the diffusion constant D_{app} can be determined from the slope. In equation (8), C_{Ox}^{*} is the concentration of the oxidized species at the electrode interface (C_{Red}^{*} for the reduced species). It is important not to influence the diffusion by convection through stirring the solution and also to do the measurement over a long time interval to receive reliable results. The polymer film should be insoluble in the electrolyte solvent to prevent physical diffusion. At short time intervals, capacitive currents are formed due to charging of double layers. The capacitive current depends on the uncompensated resistance (the resistance between the WE and the entire equipotential surface that traverses the tip of the RE)[129] and the capacitance of the double layer which decays exponentially with the time. Capacitive currents decay more rapidly than faradaic currents. At short time scales, the diffusion coefficient can be determined by the faradaic current density decay according to equation (8). Simultaneously, additional effects such as convection might have an effect on the concentration gradient at longer time scales. Thus, for

scales. Thus, for obtaining reliable results, the measuring time should be at least $t \geq 3\ R_U\ C_D$ and can vary between 0.001 and 10 s.

2.4.3. Chrono potentiometry

Chrono potentiometry (CP)[130] is an electro analytical method which measures potential changes at a constant current density. At the time t = 0 no oxidized species are available at the working electrode and small amounts of oxidized species are formed slowly due to the oxidation process (Scheme 30). The formation of the oxidized species suddenly changes the potential E from zero to an equilibrated value according to the Nernst equation (3). During the measurement process the concentration of the oxidized species increases continuously while the concentration of the reduced species decreases. The concentration of the reduced species at the electrode surface decays to zero at the time $t = \tau$. Consequently, the electrode potential increases rapidly to sustain the constant current density. The potential curve shape depends on the diffusion coefficient at the electrode surface and on the concentration of the analytes.

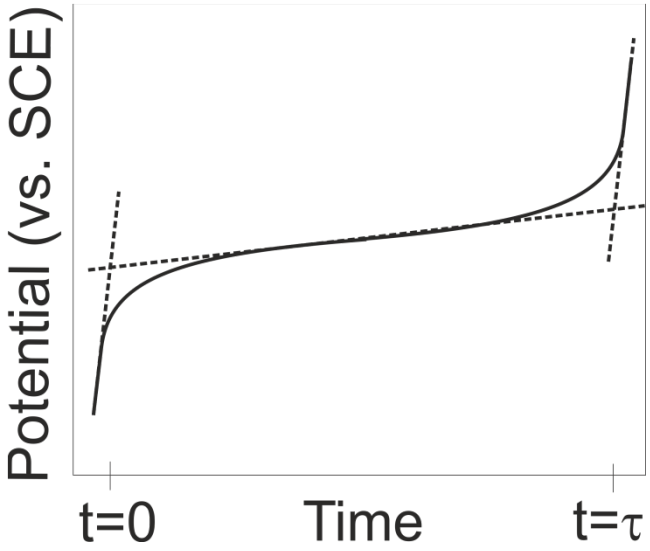

Scheme 30. Principle of CP: measurement of the charge potential over the time t at constant current density.

The transition time τ is the time gap between the potential jumps. At this point no oxidized species are available and the reduced species are consumed completely. The relationship between the transition time τ and the concentration of the oxidized species, the current density and the diffusion constant is given by the Sand[131] equation:

$$\tau = \left(\frac{n_e \cdot F \cdot C_{Ox}^{*} \cdot \sqrt{\pi \cdot D_{Ox}}}{2 \cdot j_{Far}} \right)^2 \qquad (9)$$

With the help of electrochemical measurement methods, information about redox activity and charge diffusion inside the polymer films is obtained. In the case of radical containing polymers, methods like UV-Vis spectroscopy and ESR can help to quantify the amount of radicals and observe the decay process. UV-Vis spectroscopy is useful when the radical species is a chromophore absorbing at ultraviolet or visible range.

2.4.4. UV-Vis spectroscopy

UV-Vis spectroscopy can be combined with CV to observe the absorbance of redox species like in the case of the chromophore phenothiazine.[69,150] In this technique, wavelengths in ultra-violet and visible light regions are used to excite valence electrons from the highest occupied molecular orbital (HOMO) to lowest unoccupied molecular orbitals (LUMO). To excite electrons from valence orbitals such as p- and d- orbitals, the wavelength λ (or the frequency f) must match the energy difference between the LUMO and HOMO according to the following equation:

$$\Delta E_{LUMO-HOMO} = h \cdot f = \frac{h \cdot c}{\lambda} \tag{10}$$

Here, h is the planck constant and c the speed of light. The transition of the valence electrons results in specific absorbance bands in the UV-Vis spectrum. The absorbance intensity A_i depends on the concentration c, the path length l and the molar extinction coefficient ε of the absorbing species described with the Lambert-Beer equation:

$$A_i = \varepsilon \cdot c \cdot l \tag{11}$$

Generally, in the UV-Vis spectrum, transition states from π -> π^* and n -> π^* can be observed between λ = 200 nm and 1100 nm. Other transitions such as n -> σ^* and σ -> σ^* require higher excitation frequency below λ = 200 nm and are therefore not observable with this technique. As an additional technique to UV-Vis, ESR was used to support the results. ESR is an appropriate method for selective determination of radical species.

2.4.5. Electron spin resonance

Electron spin resonance (ESR)[132] is a technique to quantify paramagnetic materials with unpaired electrons. Unpaired electrons are present in transition state metals, crystal lattice deficiencies and in radicals. Due to their angular momentum, also called ”spin”, unpaired electrons possess a magnetic moment. By applying an outer magnetic field, the spins are separated in two energy states. Spins with parallel orientation to the magnetic field are attracted and have less energy. Spins with anti-parallel orientation to the magnetic field experience a repulsive force with higher energy. Thus, the degenerate state is split into the parallel ground state and the anti-parallel excited state according to the Zeeman-effect (Scheme 31).

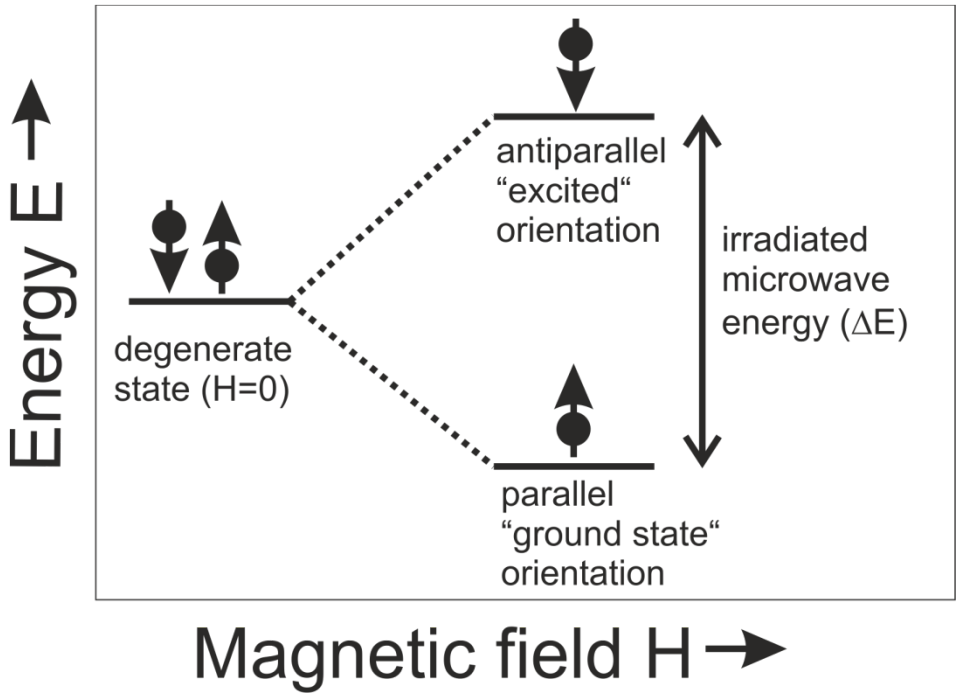

Scheme 31. Splitting of the degenerate state of the electron spin in the magnetic field of ESR.

To excite the spin from the ground state to the excited state microwave irradiation is used. The energy difference ΔE depends linearly on the magnetic field H and is described as follows:

$$\Delta E = h \cdot f = g \cdot \mu_B \cdot H \qquad (12)$$

Thereby, μ_B is the Bohr magneton and g the Landé factor, which describes the interaction of the spins with the magnetic field. Typically, the excitation frequency of the electron spin in ESR is in the range of 1 to 95 GHz. For the standard ESR measurement however, the excitation frequency is chosen between 9 and 10 GHz (also called “X-band ESR”) using a Gunn diode oscillator as irradiation source. The frequency determines the penetration depth of the microwave through the material which varies between several micrometers and a few centimeters. During the measurement, the frequency is kept constant, while the magnetic field amplitude is modulated. When the magnetic field matches the resonance condition according to equation (12), the microwave irradiation is absorbed. The modulation of the absorbance intensity with the magnetic field dI/dH (i.e. the first derivative) is then plotted against the magnetic field to obtain the ESR spectrum. The spectrum illustrates the interaction of the unpaired electron with its neighboring nuclei and with the magnetic field. For a free electron, the g-value is determined as 2.0023. However, when the electron is perturbed by neighboring interactions, the value can vary within $1*10^{-4}$ to $1*10^{-3}$. Splitting of the ESR signal can occur as well resulting from the coupling of the electron with the nucleus (hyperfine interaction) or with the magnetic field (electron Zeeman Term). ESR is a powerful technique to follow the kinetics of stable and persistent radicals and their interaction with their environment. Additionally this technique can be combined with CV to detect persistent radicals such as phenothiazine radical cations.

3. Experimental

3.1. Materials

Nitrosyl-tetraflouroborate ($NOBF_4$; Sigma Aldrich, 95%), tetrabutylammonium tetrafluoroborate (Sigma Aldrich, 99%), dry tetrahydrofuran (THF; Acros, 99.8%), hexane (Fisher Scientific, 95%), dichloromethane (DCM; TCI Japan, 99.5%), acetonitrile (ACN; TCI Japan, 99.5%) vapour grown carbon fiber (VGCF; Show Denko Japan), tetrabutylammonium perchlorate (TBAPC; TCI Japan, 98%), polyvinyldiflouridine (PVDF; Sigma Aldrich, average Mw ≈ 530000 g/mol) and 1-methyl-2-pyrrolidone (NMP; TCI Japan, 99%) were used as received.

3.2. Synthesis

The polymers were synthesized according to the method presented in II.4.4.1. For the experiments, following polymers were used: PVBPT (M_n =273000 g/mol, PDI = 2.32), PVPPP (M_n = 25800 g/mol, PDI = 1.96) and PVMPT (M_n = 26300 g/mol, PDI = 2.53). For the ESR experiments in solid state, PVBPT was synthesized via ATRP as described in V.3.3.1.

3.2.1. Synthesis of the radical cation polymer PVBPT$^{\bullet+}$ BF_4^-

To a solution of 50 mg PVBPT M_W = 13400 g/mol (M_w/M_n = 1.43) in 10 ml dry THF a molar equivalent of $NOBF_4$ (19 mg = 0.16 mmol, referred to the phenothiazine units) was added. The dark red precipitated polymer was then filtered off and washed several times with hexane. The resulting polymer was left to dry at room temperature over night. (61.5 mg, 96% yield)

3.3. Methods

The CV and CA experiments were performed on a BAS/100 W potentiostat system with indium tin oxide (ITO), Ag/AgCl and Pt-wire as WE, RE and CE, respectively. The polymer films were spin-coated on ITO at 1000 rpm/s for 30 s using a 10 and 20 g/L solution of the polymer. For PVBPT and PVPPP, DCM was used as solvent, whereas for PVMPT, THF under heating resulted in the desired solution. 0.1 M and 1 M TBAPC in ACN served as electrolyte. Glassy carbon (GC) and ITO platelets (2.5 cm x 2.5 cm) were cleaned with DCM and n-propanole prior to use.

The UV/Vis measurements were performed on a Jasco V-660. For electrochemical measurements, a standard potentiogalvanostat (Nikko Keisoku DPGS-1) was used. Pt-wire attached to the polymer film spin-coated on ITO served as WE. As RE and CE, Ag/AgCl and Pt-wire were used.

Electron spin resonance (ESR) spectra were obtained with a JEOL JES-TE200 ESR spectrometer at 100 kHz field modulation. A Pt-wire electrode covered with the polymer was placed in the ESR tube as WE. An isolated Pt-wire and a further isolated Pt-wire coated with silver were placed in the ESR tube as CE and RE, respectively. The potential was applied using a potentiogalvanostat (Nikko Keisoku DPGS-1). The ESR data for the dried PVBPT$^{\bullet+}BF_4^-$ was

obtained with a MiniScope MS 200 from Magnettech. The measurements were done in quartz capillary tubes sealed with Critoseal® at 80 °C under ambient atmosphere. Following parameters were chosen: frequency 9.4 GHz, centre field 3345.28 G, sweep 199.38 G, sweep time 60 s, step resolution 4096, number of scan 5, modulation amplitude 200 mG, micro wave attenuation 10 dB, gain 5. To calculate the g-value, manganese isotope with spin quantum number S = 5/2 and g-value of 2.0024 ± 0.003 from Magnettech was taken as a standard. For the spin density measurements, galvinoxyl free radical was used as a reference.

The polymer composite was prepared as follows: 50 mg PVDF were dissolved in 450 mg NMP after ultra sonification. 80 mg VGCF were mixed with 10 mg of the polymer (PVPPP or PVMPT) and 100 mg of the PVDF solution. After adding a few drops of NMP, the composite was well mixed in a mortar. The obtained paste was spread out over a GC-plate or aluminum foil. The weight of the GC-plate was determined beforehand. The prepared paste was left to dry over night under vacuum at 60 °C. For the CP measurements on GC, the weight was measured after drying to determine the polymer amount. For battery preparation, the dried paste on aluminum foil was punched out as circles with the same size and the pieces were weighed before use. The weight of aluminum foil without composite was determined from punched circles of the same size.

The battery assembly was performed in a glovebox using the aluminum pieces with the dried polymer composite paste. The aluminum piece was laid on the steel bottom part of the coin cell covered with the electrolyte solution (1 M $LiPF_6$ in 50/50 v%/v% EC/DEC) and a fitting ring. Then, the cathode was separated with a thin teflon membrane cut off in a circular shape. A piece of lithium metal was put on the teflon membrane and covered with a steel platelet and a feather. Finally, the coin cell was closed with the upper part and sealed under pressure. The battery coin cell was tested with respect to short circuits, showing an open circuit potential of over 2.8 V.

4. Results and Discussion

4.1. Cyclic voltammetry

To get an insight in the redox chemistry of phenothiazine baring polymers, CV measurements were performed for the three polymers PVBPT, PVPPP and PMPT. Phenothiazine was measured as reference (Figure 10a) to compare the difference between free and immobilized moiety. Phenothiazine itself, revealed two oxidation peaks at $E^{0/+1}$ = 0.64 V and $E^{+1/+2}$ = 1.25 V and two reduction peaks at $E^{+1/0}$ = 0.32 V and $E^{+2/+1}$= 0.90 V at ν = 100 mV/s in DCM as a solvent. The two oxidation peaks were related to the radical cation and dication species.[133] The value of the first oxidation peak was found to be in good agreement with the literature.[134] The chemical shift and the peak separation resulted from using a non-polar aprotic solvent. The stabilization of the charged radical cation and dication species is less pronounced in non-polar solvents then in polar solvents. Therefore, higher oxidation potentials are needed due

to lack of salvation shell.[134] Once oxidized, the phenothiazine planarized rings will form π-π-associates, which on the other hand are so stable that higher reduction potentials are necessary. For PVBPT in solution, two oxidation steps were observed at $E^{0/+1}$ = 0.66 V and $E^{+1/+2}$ = 0.92 V (Figure 10b). In addition, one reduction peak was observed at $E^{+1/0}$ = 0.59 V as well as a reduction peak with a shoulder at $E^{+2/+1}$= 0.80 V. The two oxidations peaks corresponded to the radical cation and dication of the pendant phenothiazine moieties. The peak separation between the anodic oxidation and cathodic reduction for the first oxidation step was around ΔE_p = 70 mV, which is slightly higher than theoretical calculations for a reversible redox behavior (equation(4)). The anodic and cathodic peak currents had the same absolute value. These characteristic features of the voltammograms indicate a reversible one electron process for the first oxidation step.[86] However, the second oxidation step in PVBPT was in contrast to phenothiazine not reversible. The peak current values and shape of the anodic oxidation and the cathodic reduction peak demonstrated no symmetric behavior. The peak shoulder for the second reduction peak at around E= 0.75 V in the reduction wave indicated that some side reactions take place. Side reactions occur due to the short life time of phenothiazine diactions. In the presence of remaining neutral phenothiazine moieties, dications can react to form the radical cation by synproportionation.[135] Generally, the second electron transfer step in phenothiazine is kinetically unstable and appears in some aprotic solvents without the reduction peak.[134]

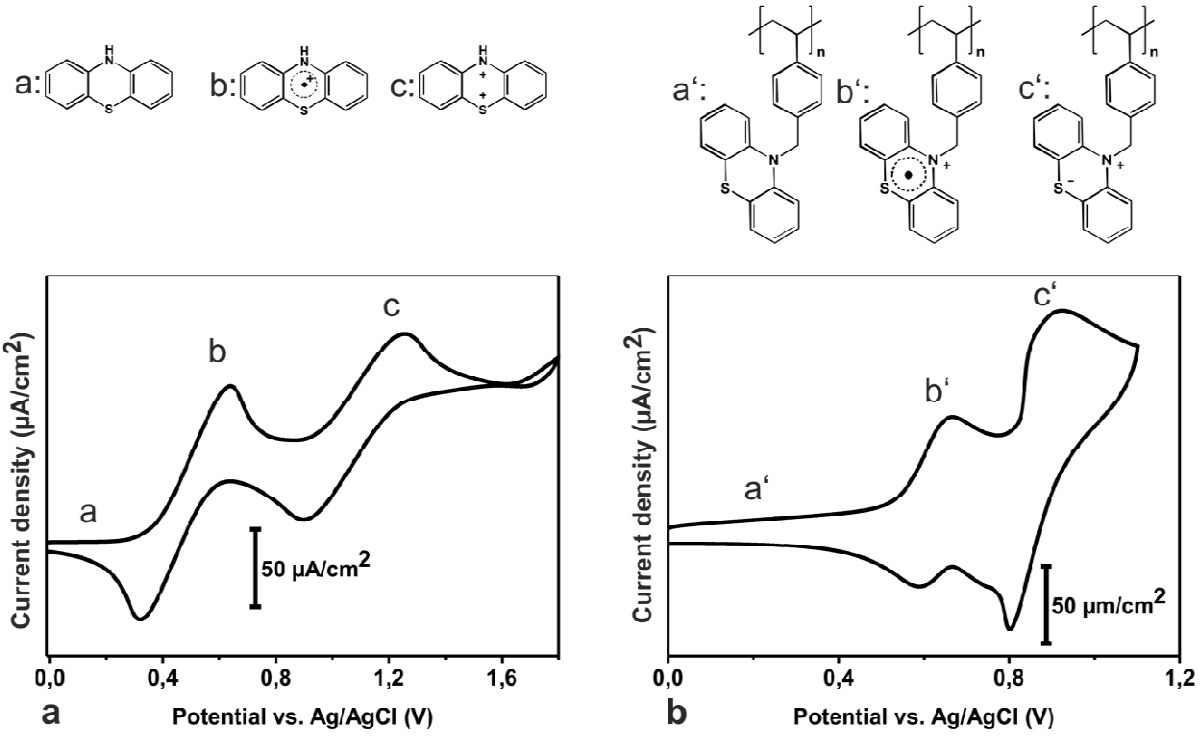

Figure 10. a) CV of 1mM phenothiazine in DCM with 0.1 M TBAPC, b) CV of 1mM PVBPT in DCM with 0.1 M TBAPC using GC, Ag/AgCl and Pt-wire as WE, RE and CE, respectively.

For more precise CV results, the formation of the radical cation species was examined on spin-coated films. The spin-coating process revealed different processability of the polymers. PVMPT films on ITO resulted in less homogeneous films compared to PVBPT and PVPPP. The

inhomogeneities are due the lack of solubility of PVMPT in organic solvents as shown in chapter II (Table 3). Since the polymer backbone is rigid (which is in accordance with the high T_g), PVMPT can only be dissolved in polar solvents such as DMF, THF and DMSO under heating. CV measurements were performed at scan speed varying from 1 to 50 mV/s for the first oxidation step as shown below for PVBPT (Figure 11).

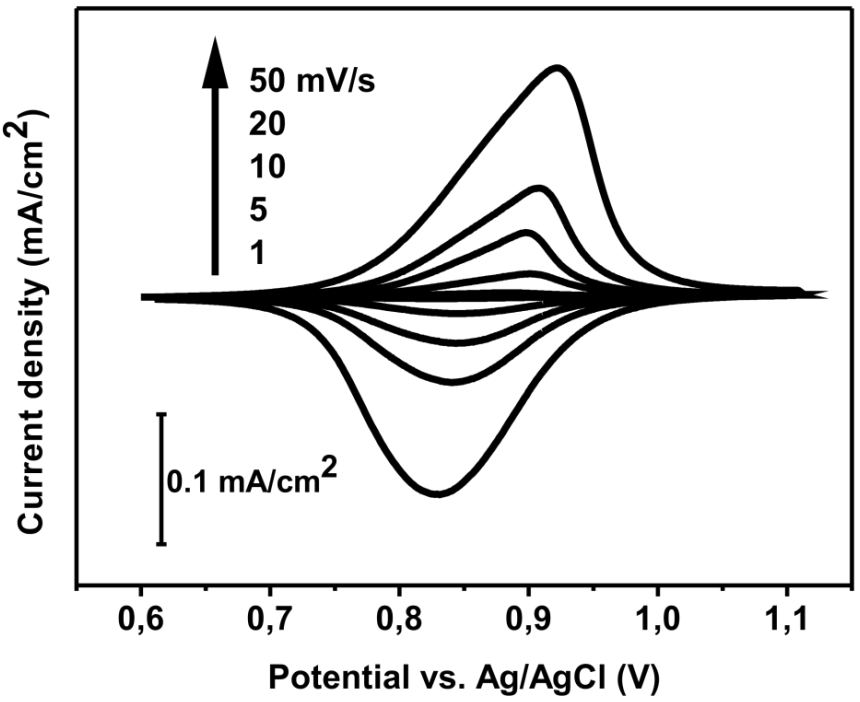

Figure 11. CV of PVBPT in ACN with 0.1 M TBAPC on ITO using Ag/AgCl and Pt-wire as RE and CE in 0.1 M TBAPC/ACN.

The half wave potential was situated at $E_{1/2}$= 0.87 V for the first oxidation step. The oxidation and reduction peak appeared at $E^{0/+1}$ = 0.89 V and $E^{+1/0}$ = 0.84 V and at $E^{0/+1}$ = 0.92 V and $E^{+1/0}$ = 0.82 V at ν = 1 mV/s and 50 mV/s. Thus, the peak separation increased from ΔE_p = 50 mV to 96 mV. The width of the redox waves at the half wave potentials for ν = 1 mV/s were $\Delta E_{pa,1/2}$ = 101 mV and $\Delta E_{pc,1/2}$ = 110 mV. Generally, for thin films slow scan speeds below 20 mV/s give more reliable data because the redox system has enough time to respond to the applied potential.[139] If the redox chemistry is fast, ΔE_p should remain unchanged at increasing scan speed. The value for ΔE_p indicates that the first redox step for PVBPT is a reversible process according to equation (4). For thin films ΔE_p is generally around 20 mV[126]. At increased scan speeds, a delayed electron transfer process in the polymer film leads to larger ΔE_p values. This delay is ascribed to diffusion limitation for charge compensation which in turn implies an overpotential. Thus, at increasing scan speed, the redox process turns from a reversible into a quasi-reversible reaction. Values of $\Delta E_{pa,1/2}$ and $\Delta E_{pc,1/2}$ also confirm that the redox reaction derives from ideal behavior according to equation (5) and is probably in the quasi-reversible regime.

CV experiments were also performed on PVPPP and PVMPT spin-coated films (appendix, Figure A 7a and Figure A 8a). Both polymers revealed a single oxidation wave with apparently reversible behavior according to CV results. The corresponding potential values of the three polymers were compared with each other (Table 4).

Table 4. Characteristic potentials determined from the CV experiments for PVBPT, PVPPP and PVMPT at ν = 1 mV/s. The values inside the parentheses were obtained at ν = 50 mV/s.

Polymer	$E^{0/+1}$ (V)	$E^{+1/0}$ (V)	$E_{1/2}$ (V)	ΔE_p (mV)	$\Delta E_{pa,1/2}$ (mV)	$\Delta E_{pc,1/2}$ (mV)
PVBPT	0.89 (0.92)	0.84 (0.82)	0.87 (0.87)	50 (96)	101 (119)	110 (127)
PVPPP	0.86 (0.90)	0.81 (0.79)	0.84 (0.85)	42 (109)	96 (140)	98 (127)
PVMPT	0.78 (0.80)	0.72 (0.70)	0.75 (0.75)	55 (100)	100(112)	101 (126)

For PVPPP and PVMPT the redox potential $E_{1/2}$ was shifted to lower values compared with PVBPT. At ν = 1mV/s the decrease in $E_{1/2}$ of 120 mV for PVMPT compared to PVBPT was attributed to the position of the substituents. Substitution at the N-position lowers the HOMO energy level of the phenothiazine because the interaction of the free electron pair with the aromatic ring is hindered.[136] The bulkier the substituent the more, the latter interaction is hindered. Therefore PVBPT and PVPPP with their large substituents at the N-position have higher oxidation potentials compared to methyl substituted PVMPT. The propylene spacer between the backbone and the phenothiazine in PVPPP is responsible for the slight shift in $E_{1/2}$ of 30 mV compared to PVBPT. The spacer increases the distance between the backbone and the moiety enabling interaction between the free electron pair and the aromatic ring. For battery application, high redox potentials like in the case of PVBPT and PVPPP are preferred. The high redox potential can increase the overall cell potential which is useful for electronic application as mentioned before. In comparison to PVBPT, ΔE_p of PVPPP is 8 mV lower and ΔE_p of PVMPT is 5 mV higher at ν = 1 mV/s. This value is below the 57 mV for a one electron process calculated from equation (4). With increasing scan speed, ΔE_p almost doubles. This observation implies a quasi-reversible redox chemistry also for PVPPP and PVMPT. The low peak separation in PVPPP and PVBPT is an evidence for the higher electron transfer rates. High electron transfer rate supports fast charge/discharge processes of the electrode active material and is therefore highly desirable.

Further information about the redox properties of the polymers was obtained from the shape of their CV curves. For all three polymers, slight asymmetry in the redox wave was observed. Especially for PVPPP, the oxidation and reduction waves showed asymmetric geometry (appendix, Figure A 7a). From the broadened and asymmetric shape of the CV curves on the anodic oxidation pathway compared to the cathodic reduction, it was concluded that oxidation and reduction have different mechanisms. Oxidized and reduced PVPPP species have different adsorption and desorption coefficients for the counterions and are not equivalent. Also some side reactions can take place during the oxidation step. The asymmetry and the width of

the redox waves at the half wave potentials confirmed the idea that the redox process differs from the ideal Nernstian reaction. From all three polymers, PVPPP with $\Delta E_{pa,1/2}$= 96 mV was closest to $\Delta E_{pa,1/2}$= 90.6 mV as ideal value according to equation (5). The explanation for this behavior is that the longer spacer length leads to separation of the redox moieties and less interaction between them. Interactions between the redox sites lead to deviations from ideal behavior and to broadening of the potential waves.[126] Due to the visible shoulder at ν = 50 mV/s, $\Delta E_{pa,1/2}$ increased to 140 mV and far above the ideal value.

From the CV curves, the surface coverage Γ of the redox species in the polymer film was estimated using equation (6). Γ correlates with the thickness of the polymer film assuming constant density and quantitative oxidation of the phenothiazine groups in the polymer film. Knowing the film thickness, the concentration of the redox active species C_{0x}^* can be calculated. C_{0x}^* is a necessary parameter to calculate D_{app} by equation (8). To determine Γ, the peak currents obtained from the CV curves were plotted against the scan speed. The plot resulted in a linear dependence for PVBPT (Figure 12) as well as PVPPP and PVMPT (appendix Figure A 7b and Figure A 8b).

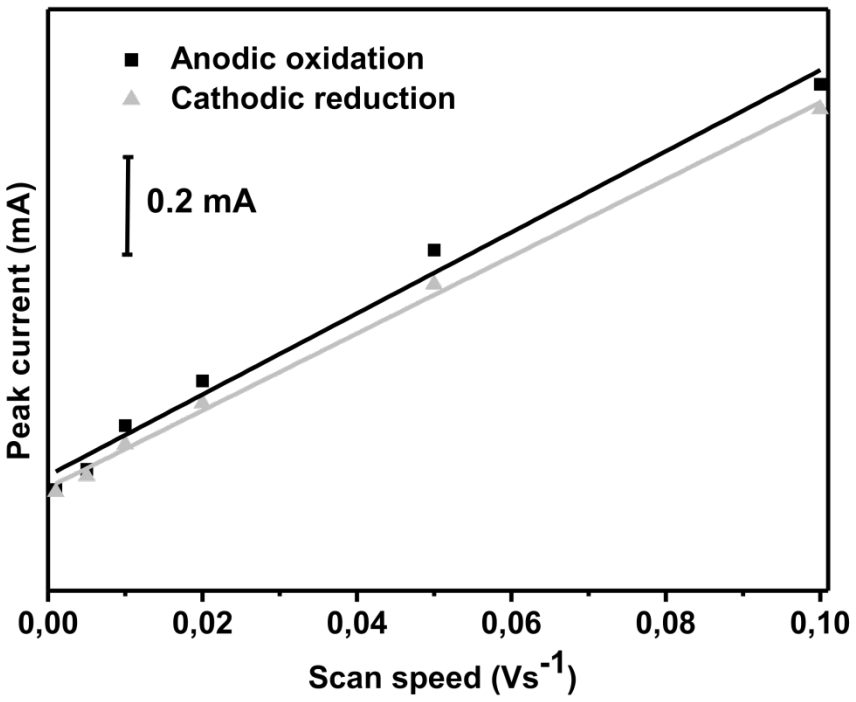

Figure 12. Plot of the peak current vs. scan speed for PVBPT.

For PVBPT, both linear fits for cathodic and anodic peaks showed similar slopes ($8.4*10^{-3}$ and $8.0*10^{-3}$ A*s/V) indicating that the ratio of the peak intensity was approximately unity (Figure 12 and appendix Table T 4). The slopes for PVPPP are also similar for cathodic and anodic step and almost two times smaller than for PVBPT (appendix, Figure A 7b and Table T 4). The small difference of the slopes from the cathodic and anodic steps (approximately

$5.0*10^{-4}$ A*s/V) implies that the oxidation and reduction steps have different mechanisms or some side reaction accompanies the redox process. For PVMPT, both linear fits for cathodic and anodic peaks are almost superimposed on each other with approximately $2.2*10^{-3}$ A*s/V (appendix, Table T 4). In the polymer series, the slope of the peak current versus scan speed increased in the order PVMPT, PVPPP and PVBPT. From the slopes, the surface coverage Γ was calculated according to equation (6) which increased in the same order from 0.9 to 1.5 and 3.38 nmol/cm^2 for the oxidized state (appendix, Table T 5). The latter order imposes the PVBPT film is the thickest among the polymer films assuming the same density and oxidation degree for all three polymers. The film thickness was determined as 51 ± 6 nm, 58 ± 9 and 61 ± 4 nm for the PVMPT, PVPPP and PVBPT film, respectively. By taking the film thickness into account, a concentration of 0.2, 0.3 and 0.7 mmol/cm^3 was calculated for C_{Ox}^* in the latter order. For PVMPT, a concentration of 4.2 mmol/cm^3 was reported for C_{Ox}^*.[87] For better comparison, Γ was calculated more precisely from chrono amperometry in the next section.

The oxidation process for all three polymer films was accompanied by an electrochromic effect. The formation of the oxidized radical cation species led to changes in color from colorless to dark red. This process was reversible and was followed optically as well as with UV/Vis spectroscopy for PVPPP spin-coated films on ITO (Figure 13). While the neutral polymer didn't reveal any absorption band in the visible region (Figure 13, transparent ITO film), the oxidized polymer exhibited two peaks at 517 and 859 nm (Figure 13, red colored ITO film). These values correspond to the absorption bands observed for the phenothiazine radical cation.[137,138] The first peak was attributed to the radical cation species while the second peak corresponds to the formation of a dimer with a face to face orientation of the radical cation species.[87] The red colored film was formed at an applied bias potential of +1.0 V and was switched back to the original colorless state at -1.0 V, as can be seen from the UV/Vis data.

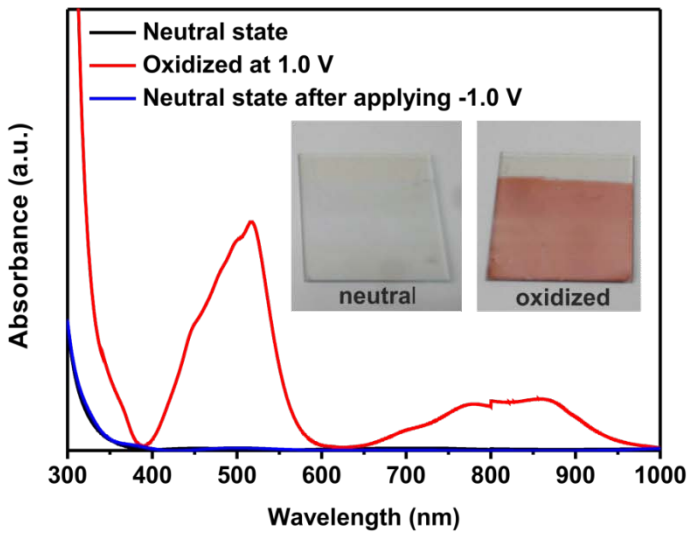

Figure 13. UV/Vis of PVPPP on ITO before and after oxidation and reversible reduction. Ag/AgCl and Pt-wire were used as RE and CE in 0.1 M TBAPC/ACN, respectively.

In conclusion the redox process is a quasi-reversible for the first oxidation step for all three polymers PVBPT, PVPPP and PVMPT with oxidation potentials ranging between $E_{1/2}$ = 0.75 and 0.87 V. PVBPT revealed the highest and PVMPT the lowest redox potential among the three polymers. Slight deviations from ideal Nernstian electrochemistry were observed in all three cases due to film inhomogeneities which lead to overpotential due to diffusion. From the CV experiments, a concentration of the redox active species C_{0x}^{*} < 1.0 mmol/cm^3 was calculated for all three polymers. PVBPT revealed the highest concentration with C_{0x}^{*} = 0.7 mmol/cm^3. The oxidation step was accompanied by a reversible color change between colorless and red for all three polymers proving strong electrochromic effect. For the precise calculation of C_{0x}^{*} and the diffusion coefficients, CA experiments were performed in the next stage.

4.2. Chrono amperometry

With the help of the CA, the surface coverage Γ of the polymer film was measured from the integral below the CA curves. This method allows more precise calculation by measuring the current decay over time resulting from the consumption of redox species. CA contains information about the electron diffusion for both anodic and cathodic step, as shown for PVBPT film on ITO (Figure 14). In the first 10 seconds, the polymer film was oxidized anodically leading to a decay of the current over time. Between 10 and 20 seconds, the cathodic reduction process took place leading to an increase of the current. Oxidation and reduction steps exhibit two different regimes indicated by different slopes in the CA curves. In regime 1, the current decays due to oxidation and consumption of the redox sites which is a time limited process. In the regime 2, the diffusion inside the polymer film takes place which is an infinite process.

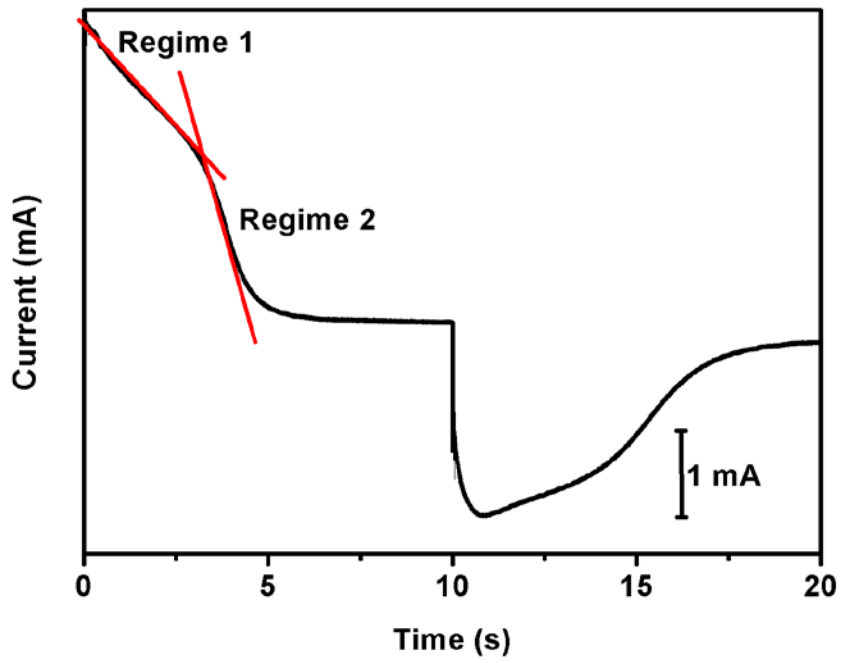

Figure 14. CA data of PVBPT film on ITO. Ag/AgCl and Pt-wire were used as RE and CE in 0.1 M TBAPC/ACN, respectively.

CA data was also recorded for PVPPP and PVMPT (appendix, Figure A 9 and Figure A 10). From the integration of the current decay over time, the number of redox sites is obtained as electric charge measured in coulomb. The number of the redox sites at the electrode interface n_{Ox}^* is directly accessible by dividing the integral (in coulomb) by F:

$$n_{Ox}^* = \frac{\text{integral}}{F} \tag{13}$$

After dividing n_{Ox}^* by the electrode surface area, Γ is obtained. C_{Ox}^* and C_{Red}^* were calculated dividing Γ by the thickness of the spin-coated polymer film. The calculation of the surface coverage Γ from n_{Ox}^* using equation (13) resulted in 2.2, 4.6 and 5.8 nmol/cm^2 for the oxidized species of PVPBT, PVMPT and PVPPP. The experimental results for Γ are in the same order of magnitude compared to the values calculated by CV. Γ calculated from CA is however more precise compared to results from CV. The integration range for CA data is well defined and contains fewer errors whereas the determination of the slope from CV is less precise. From the CA data, concentrations of 0.8, 0.6 and 0.6 mmol/cm3 were obtained for C_{Ox}^* for PVPBT, PVMPT and PVPPP. The values are in good accordance with the CV results (appendix, Table T 4 and Table T 5) but smaller compared to theoretical calculations for the concentration of the redox moieties on the electrode. In order to calculate a theoretical concentration of the redox moieties, a polymer density of 1.04 g/cm^3 (for polystyrene or PS) for the three polymers PVBPT, PVPPP and PVMPT was assumed. The density was divided by the molecular weight of the corresponding monomers to obtain concentrations of 3.3, 3.0 and 4.7 mmol/cm^3 for PVPBT, PVPPP and PVMPT. The variation of the experimental concentration C_{Ox}^* from the theory is due to errors in calculation of the film thickness or caused by non-quantitative oxidation of the redox moieties.

After determining C_{Ox}^*, D_{app} was calculated from equation (8). Therefore, the measured current was plotted against inverse square root of time $t^{-1/2}$. The obtained Cottrell plot was fitted linearly (intercept x=0, y=0) to obtain D_{app}. The cathodic step revealed a negative slope and the anodic slope a positive slope, respectively. For PVBPT the shape and the slope of the both anodic and cathodic step apparently revealed a symmetric behavior (Figure 15). Simultaneously, the slope decreased from 4.2 to 3.0 and 0.9 mA*s$^{1/2}$in the order of PVBPT, PVMPT and PVPPP (appendix, Figure A 9 and Figure A 10 and Table T 7).

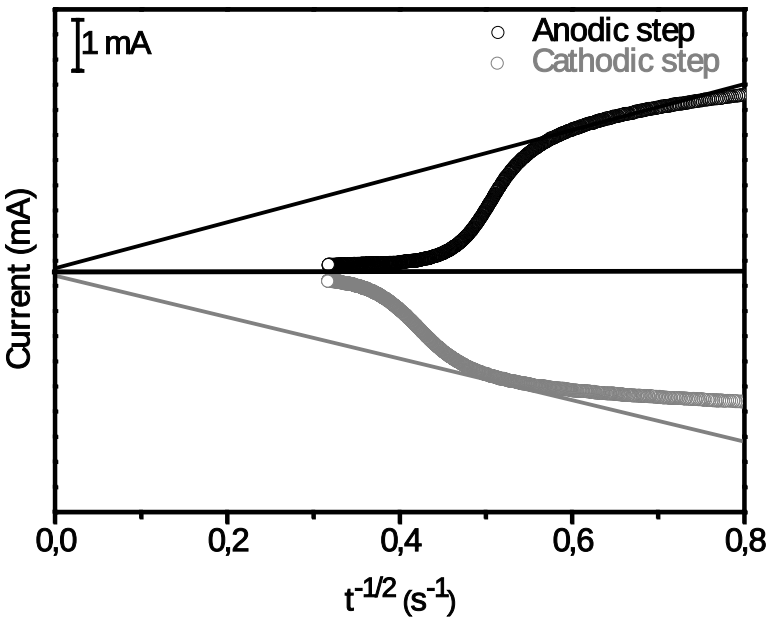

Figure 15. a) Chrono amperogram of PVBPT on ITO, b) Cottrell Plot of PVBPT. Ag/AgCl and Pt-wire were used as RE and CE in 0.1 M TBAPC/ACN, respectively.

In the chrono amperogramm and the corresponding Cottrell plot of PVPPP, different mechanisms were observed for the oxidation and reduction step (appendix, Figure A 9). The asymmetry in the CA data is in good accordance with the CV results for PVPPP. The interaction of the phenothiazine is different in the planaraized oxidation state compared to bent neutral state. Thus, the reorganization of the side chains in the oxidized and reduced step could lead to retardation of the electron transfer. The concentration values and the slopes from the CA experiments were inserted in equation (8) to calculate D_{app}. For PVBPT, D_{app} = 1.45*10^{-9} and 1.66*10^{-9} cm^2/s were found in the anodic and cathodic step (Table 5).

Table 5. Diffusion constants for PVBPT, PVMPT and PVPPP spin-coated films calculated from CA measurements.

Polymer	Diffusion constant D_{app} calculated from CA (10^{-9} cm^2/s)	
	Anodic step	Cathodic step
PVBPT	1.45 ± 0.29	1.66 ± 0.02
PVMPT	1.12 ± 0.07	0.64 ± 0.12
PVPPP	0.10 ± 0.20	0.03 ± 0.04

This value is in the same order of magnitude as for TEMPO based polymer PTMA with 10^{-8} cm^2/s.[139] PVPPP showed the lowest diffusion constant with D_{app} = 1.03*10^{-10} and 3.21*10^{-11} cm^2/s in the anodic and cathodic step. The longer spacer chain leads to separation of

the redox moieties which hinder the diffusion process. The low diffusion constant for PVPPP confirmed the observation from the CV data with respect to the interaction between the redox sites. The absence of interaction between the redox moieties was reflected in the width of the oxidation wave at $E_{pa/2}$. For PVMPT, diffusion constants for the electron exchange process of $1.6*10^{-9}$ and $2.6*10^{-9}$ cm^2/s for the cathodic and anodic step were reported by Morishima and coworkers measured by chrono coulometry.[87] From the CA measurements, diffusion constants of $1.1*10^{-9}$ and $0.6*10^{-9}$ cm^2/s were determined in good agreement with the literature for the anodic and cathodic step, respectively. Deviation from theory is related to the fact that polymers swell and deswell in the electrolyte solution. The polymer can swell during the measuring due to potential application which leads to an increase in the polymer film thickness. A resulting increase in volume reduces the concentration of the redox species, which in turn changes the diffusion process. Errors in determination of the slopes as well as the integral for the calculation of the concentration have to be taken into account as well. In addition, for the anodic step the diffusion constant is generally higher than for the cathodic step. Not all the oxidized moieties can be reduced back quantitatively and some self discharge process lead to loss of the oxidized state. From the ratio between the diffusion constants, the electron transfer efficiency was calculated. In the ideal case, the ratio of the diffusion constants for the forward and backward reaction should be equal unity. For PVBPT, PVMPT and PVPPP ratios of 1.14, 0.57 and 0.32 were calculated. This indicates that PVBPT has the best electron transfer efficiency compared to the other two polymers. In comparison to PVMPT and PVPPP, phenothiazine moieties in PVBPT are oxidized and reduced almost at the same speed. Oxidation and reduction steps are both equal which prevents electrons from being lost during the redox process. Having calculated D_{app}, the electron transfer rate can be accessed in the next step. The electron transfer rate gives details about the redox speed of the polymers. With the help of the following theoretical assumptions, the electron transfer k^0 and k_{ex} were measured from the CV and CA experimental results.

For the three polymers PVBPT, PVPPP and PVMPT, the heterogeneous electron transfer process constants k^0 were calculated first. This value gives information about the kinetics of the electrons transfer process and can be used to roughly determine the reversibility regime of the redox reaction. Values for the heterogeneous electron transfer k^0 can be determined using the diffusion constant obtained from the CA measurements and from the redox peaks characteristics obtained by CV measurements. A method described by Klinger and Kochi is based on the peak separation ΔE_p in the CV curve.[124] This method is derived from the Butler-Volmer equation (1) assuming a stationary redox process with clearly differentiable anodic and cathodic peaks according to the following equation:

$$k^0 = 2.18 \cdot \sqrt{\frac{\alpha_{ET} \cdot \nu \cdot n_e \cdot F \cdot D_{app}}{RT}} \cdot \exp\left(-\frac{{\alpha_{ET}}^2 \cdot n_e \cdot F \cdot \Delta E_p}{RT} \right) \qquad (14)$$

The charge transfer coefficient α_{ET} can be calculated from peak separation between the redox peak E_p and the half wave potential value of the corresponding peak which increases with the scan velocity. Generally, values for α_{ET} are in the order of 0.5 for reversible reactions.[140]

$$\alpha_{ET} = 1.857 \cdot \left[\frac{RT}{n_e \cdot F(E_p - E_{p/2})} \right] \quad (15)$$

Another approach for calculating k^0 was suggested by Gileadi and Eisner.[125] They proposed that for a heterogeneous electron transfer, the process will change from reversible to irreversible when the scan speed is increased. The authors suggest, that this change from reversible to irreversible occurs at a certain scan speed called "the critical scan speed" ν_c,.[141] To determine ν_c, the peak potentials are plotted against log (ν). The obtained plot is then extrapolated with two different slopes. From the intercept of the slopes, the value for ν_c can be calculated. For PVBPT, a value of 6.7 mV/s was calculated for the oxidation peaks (Figure 16). This means, that for PVBPT the redox system changes from a reversible into an irreversible process above the scanning velocity of approximately 7 mV/s. ν_c was determined from the oxidation as well as from the reduction peaks for PVBPT, PVPPP and PVMPT (appendix, Table T 8).

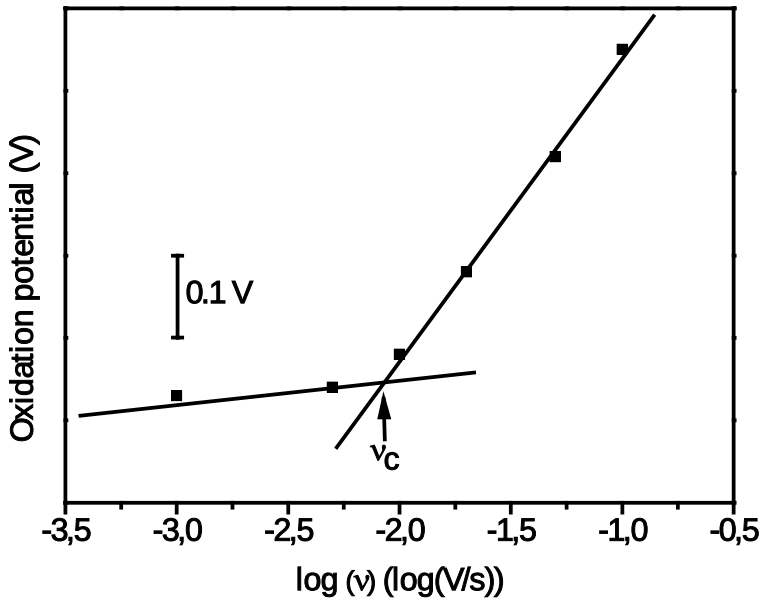

Figure 16. Calculating the critical scanning speed ν_c according to Gileadi and Eisner for PVBPT polymer film in the anodic step.

According to Gileadi and Eisner, the determined critical scanning speed is linearly dependent of k^0. Thus, k^0 can be calculated using the following equation:

$$k^0 = -0.48\alpha_{ET} + 0.52 + \log\sqrt{\frac{\alpha_{ET} \cdot \nu_c \cdot n \cdot F \cdot D_{app}}{2.303 \cdot R \cdot T}} \quad (16)$$

The heterogeneous electron transfer constant k^0 was calculated for the anodic and cathodic step by applying the methods according to Klinger and Kochi (equation (14) and (15)) as well as Gileadi and Eisner (equation (16)). For the calculation, the CV data from III.4.1 were analyzed to find the corresponding potential values. For the Klinger and Kochi method (equation (14) and (15)), E_{pa}, E_{pc}, $E_{pa/2}$ and $E_{pc/2}$ were determined from ν = 1 mV/s to ν = 50 mV/s at room temperature. For the Gileadi and Eisner method (equation (16)), ν_c was determined by plotting the potentials against log (ν) for both oxidation and reduction step (appendix, Table T 8). Furthermore, D_{app} value measured by CA (Table 5) were used for the calculation. The results for k^0 are presented in Table 6.

Table 6. Heterogeneous electron transfer constant according to Klinger and Kochi as well as Gileadi and Eisner for PVBPT, PVMPT and PVPPP films.

Polymer	k^0 according to Klinger and Kochi (10^{-5} cm/s)		k^0 according to Gileadi and Eisner (10^{-5} cm/s)	
	Anodic step	Cathodic step	Anodic step	Cathodic step
PVBPT	1.74 ± 1.07	1.42 ± 0.61	1.67 ± 0.07	1.70 ± 0.08
PVMPT	0.79 ± 0.67	0.29 ± 0.25	1.16 ± 0.34	1.21 ± 0.09
PVPPP	0.46 ± 0.38	0.14 ± 0.09	0.45 ± 0.16	0.35 ± 0.04

The values obtained for k^0 are in the order of 10^{-5} cm/s. This is the same order of magnitude as for the reduction of nitroso derivatives which depends on the type of working electrode.[142] Compared to free phenothiazine derivatives like the N-substituted promazine (2.6 *10^{-2} cm/s on GC), the electron transfer is 3 to 4 orders of magnitude smaller.[143] The large difference is related to the internal reorganization of the phenothiazine moieties. The phenothiazine redox moieties on the polymer side chains require segmental motion to get in a proper juxtaposition for electron transfer. Thus, the segmental motion is the rate determining step which is much slower than the electron transfer step. PVBPT showed the highest value for k^0 according to both methods. The average value was 1.70*10^{-5} and 1.56*10^{-5} cm/s for the anodic and the cathodic step. In comparison, PVPPP exhibited the lowest k^0 value with 0.46*10^{-5} and 0.14*10^{-5} cm/s. For k^0 the same tendency was observed as for the diffusion constant. The method used by Gileadi and Eisner is more sensitive to errors, since determining ν_c has to be done manually by fitting both slopes of the reversible and irreversible regime. By increasing the number of measurement points, the fitting becomes more precise. The method presented by Klinger and Kochi is more reliable taking more parameters of the CV data into account. Nevertheless, the heterogeneous electron transfer takes place in the quasi-reversible regime. This means, the redox process is fast enough to guarantee reversibility under slow scan speeds.

k^0 describes the heterogeneous electron transfer at the electrode polymer interface. To describe the electron exchange between the redox moieties k_{ex} is needed. The apparent diffusion D_{app} contains the overall electron transfer including the contribution of the electrode polymer

interface and the electron exchange process. Assuming the validity of Rahms-Duff equation for the spin-coated polymer films (equation (8)), the electron exchange coefficient k_{ex} can be determined by the following expression[144,145]:

$$k_{ex} = \frac{4D_{app}}{\pi \cdot \delta_c^{\,2} \cdot C_{ox}^{*}} \qquad (17)$$

The calculation includes the parameter δ_c as the center-to-centre distance between the redox moieties in the polymer chain. For simplicity, δ was set to 5 Å for all three polymers. From equation (17), electron self exchange coefficients k_{ex} were calculated for all three polymers. The fastest electron exchange was observed for PVBPT with $1.6*10^6$ and $2.0*10^6$ $M^{-1}s^{-1}$ in the anodic and cathodic step. Compared to PVMPT with $5.0*10^5$ and $2.0*10^5$ $M^{-1}s^{-1}$, the electron exchange rate is almost one order of magnitude larger. In the literature, k_{ex} of $4.0*10^5$ and $5.9\ 10^5$ $M^{-1}s^{-1}$ for the anodic and cathodic process of PVMPT was reported in good agreement.[87] The results of k_{ex} for PVBPT and PVMPT are in accordance with redox polymers based on PTMA reported by Nakahara[146] and Oyaizu.[147] Especially PVBPT revealed a remarkable performance with respect to the electron exchange ability. In comparison, PVPPP revealed the lowest electron exchange rate with $4.9\ *10^4$ and $1.5\ *10^4$ $M^{-1}s^{-1}$ for the anodic and cathodic step.

Table 7. Electron self exchange coefficients k_{ex} calculated by CA.

Polymer	k_{ex} calculated from CA (10^6 $M^{-1}s^{-1}$)	
	Anodic step	Cathodic step
PVBPT	1.67 ± 0,57	1.95 ± 0,05
PVMPT	0.58 ± 0.03	0.27 ± 0.01
PVPPP	0.05± 0.06	0.02 ± 0.01

The molecular geometry and position of the phenothiazine moieties has influence on the redox properties of the electron transfer. Substituting phenothiazine moiety at the N-position enables more rotational freedom for the aromatic rings to get in the proper juxtaposition for electron exchange. The rotation process involves additional activation which reduces the electron exchange rate. Compared to N-methylphenothiazine, the exchange rate k_{ex} of the covalently bound phenothiazine moieties is reduced by 3 to 5 orders of magnitude.[88]

Thus, k^0 was determined for PVBPT, PVPPP and PVMPT from the CA experimental results. Therefore, D_{app} was calculated using the integration and current decay of the CA curve. From the Cottrell plot D_{app} of approximately 10^{-9} cm^2/s was calculated for all three polymers. PVBPT revealed the highest value and PVPPP the lowest value for D_{app}. By using the models proposed by Klinger and Gileadi, k^0 was obtained from D_{app} and the CV results. The regime of the redox reaction was classified as quasi-reversible with $k^0 \approx 10^{-5}$ cm/s for all three polymers as also confirmed by the literature. Finally, using D_{app}, k_{ex} was determined with values ranging between

10^4 and 10^6 $M^{-1}s^{-1}$. PVBPT revealed the highest value for k_{ex} with an average of $1.8*10^6$ $M^{-1}s^{-1}$. PVPPP exhibited the lowest value for k_{ex} with an average of $3.2*10^4$ $M^{-1}s^{-1}$. The results imply that the longer spacer between the phenothiazine and the polymer backbone in PVPPP has a rather negative influence on the interaction between the moieties. As also observed by CV, in PVPPP the moieties are rather separated from each other and the electron transfer is impeded. Thus, increasing the spacer length is not favorable in terms of improving the redox speed by the increased motion of side chains. However, the propylene spacer could have influence on the stability of the radical cation state. The radical stability is important for maintaining the charge state in the battery cell. Therefore, the radical stability was examined with UV/Vis and ESR techniques in combination with CV.

4.3. Radical stability

The chemical stability of the oxidized state for the polymers PVBPT and PVPPP was studied by combining CV with UV/Vis and ESR. The chemical stability was measured in situ in the electrolyte solution with UV/Vis spectroscopy. Therefore, spin-coated films of PVBPT were prepared and oxidized at 1.2 V. Afterwards, the potential was turned off and the UV/Vis signal was recorded over time (Figure 17).

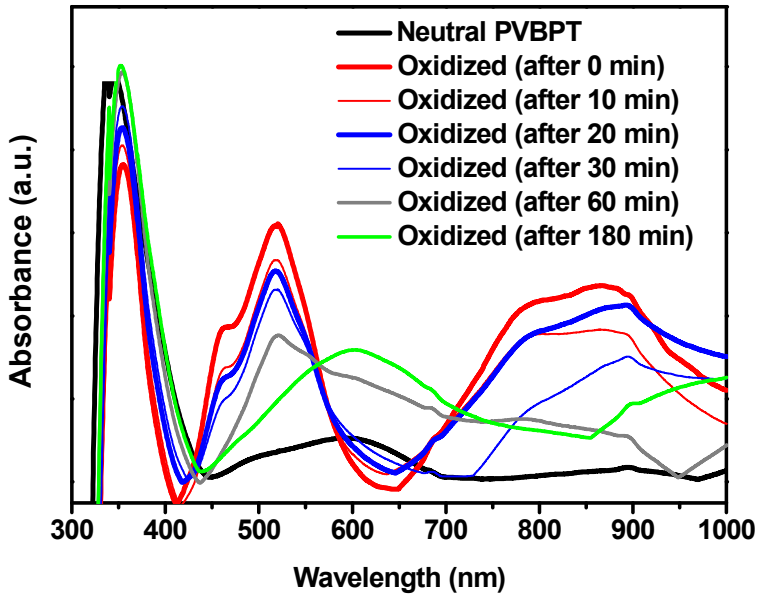

Figure 17. UV/Vis measurements on PVBPT spin-coated films for examining the radical cation decay over time. PVBPT spin-coated film on ITO, Ag/AgCl and Pt-wire were used as WE, RE and CE in 0.1 M TBAPC/ACN, respectively.

The neutral PVBPT has one large peak at 345 nm, followed by two smaller peaks at 594 and 892 nm. The absorbance measurements could be repeated after several hours without any significant changes in the peak position or intensity. For N-methylphenothiazine, the main peak was reported at 310 nm.[66] The small shift appears due to the bathochromic effect of the N-substitution by larger substituents.[66]After oxidation, the latter peak was slightly shifted to

350 nm and the in intensity decreased about 15% compared to the initial value. Simultaneously, a new peak is formed at 518 nm and at a broader peak is formed at 864 nm (Figure 17, oxidized (after 0 min). The two peaks are related to the radical cation and the dimer as already seen for PVPPP (Figure 13). The first peak at 350 nm stems from non-oxidized phenothiazine moieties in the polymer film. After turning off the bias potential, the signal intensity of the first peak related to the phenothiazine successively increased after 20 and 60 minutes almost back to its original intensity. At the same time, the peak intensities for both the radical cation and the dimer species decreased. The peak at 180 minutes revealed an absorbance curve which is quite similar to the absorbance curve of the neutral species. The UV/Vis studies demonstrated that the neutral polymer is quite stable in the electrolyte solution, whereas the oxidized species is probably converted back to the neutral state.

The radical decay process was also studied by UV/Vis for PVPPP on ITO film. The neutral PVPPP revealed a strong absorbance band below 350 nm with no further significant peaks. (Figure 18a). For PVPPP film oxidized at 1.2 V, the peak at 518 nm and a double peak at 778 and 859 nm were assigned to the radical cation species and the dimer as described for PVBPT. After turning off the potential, the UV/Vis intensity signal for the radical cation as well as the dimer decreased over time. However, the decay rate was much smaller than that for PVBPT. After 3h, the intensity of PVPBT decreased to 32% of the beginning peak intensity while for PVPPP the intensity decreased to 79% of the beginning intensity (Figure 18b). The decay rate indicates that PVPPP is more stable with respect to radical decay than PVBPT. Levy et al. studied the radical stability of various phenothiazine derivatives.[148] They reported that phenothiazine derivatives functionalized with non-branched n-alkyl chain at the N-position become more stable with increasing chain length. The increased stability stems from the larger surface area of the planarized radical cation which stabilizes the resonance structure. Thus, the longer spacer length between the polymer backbone in PVPPP compared to PVBPT has a stabilizing effect on the radical. The decay experiments give an insight to the decay kinetics of the radical cation. However, the reason for the radical decay has not been elucidated. To get a deeper understanding of the radical cation decay mechanism, following experiments were performed.

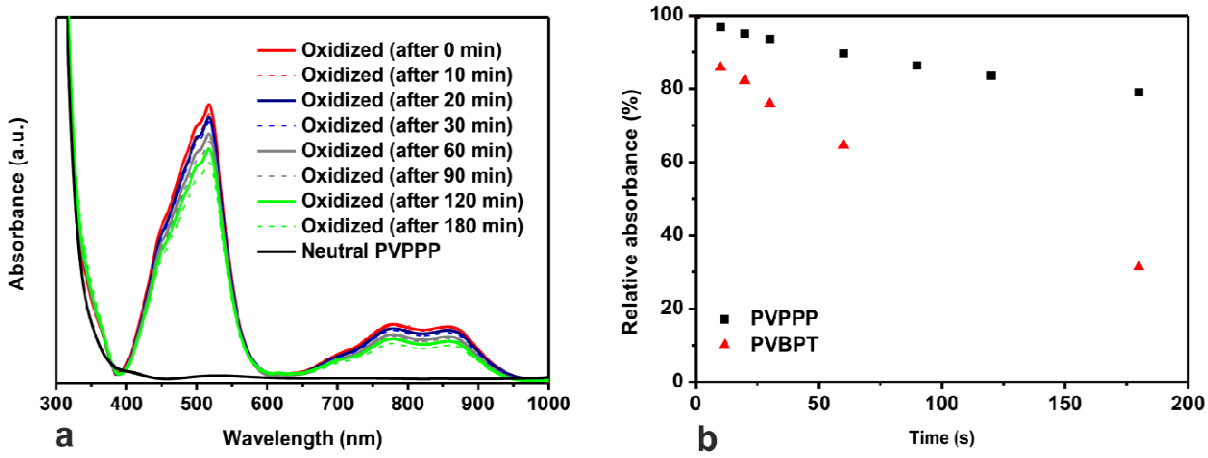

Figure 18. a) UV/Vis measurements on PVPPP spin-coated films for examining the radical cation decay over time, b) Comparison of radical decay kinetics for PVPPP and PVBPT. PVPPP spin-coated film on ITO, Ag/AgCl and Pt-wire were used as WE, RE and CE in 0.1 M TBAPC/ACN, respectively.

The decay process of an oxidized PVPPP film was recorded within the time scale of 10 hours via UV/Vis spectroscopy. Finally, the polymer film was re-oxidized at 1.2 V and the UV/Vis curve was recorded. If the radical decay process is an irreversible step, the signal intensity must decrease compared to the initial measurement. Otherwise, it can be suggested that the radical decay is a reversible step and takes place due to a self discharge mechanism. As a control experiment, the decay was examined with ESR spectroscopy. ESR allows the examination of unpaired electron species such as persistent radicals of phenothiazine. With the help of ESR spectroscopy, the kinetics studies from UV/Vis spectra were compared directly to the radical cation decay. The ESR experiments were conducted under the same conditions as for the UV/Vis experiments. To oxidize PVPPP in the ESR tube, a thin Pt-wire was coated with PVPPP which served as the working electrode.

The UV/Vis spectra revealed a decay of the radical cation signal intensity to 67% of the initial value after 10 hours at 517 nm (Figure 19a). By applying the bias potential of +1.2 V, the polymer film was re-oxidzed. The radical cation signal intensity increased after re-oxidation to 98% of the initial value. The peaks at 778 and 859 nm associated with the dimer also increase up to 80% of the original intensity. This means that radical decay is a reversible process. However, the formation of the dimer is not completely reversible since all the moieties need to reorient back to the original state. The ESR data confirmed the reversibility of the radical decay step as observed by UV/Vis experiments (Figure 19b). The neutral PVPPP exhibited no ESR signal. After the oxidation at 1.2 V, a signal at 334.99 mT appeared corresponding to a g-value of 2.0049 (2.0052 reported for benzylphenothiazine)[149] with no hyperfine splitting. The signal shape and its position suggest that the free electron is delocalized all over the aromatic ring systems, which appears as a carbon radical signal. The broadening of the signal is explained by the high local concentration of the radical species which influence their dipole moment mutually. After 10 hours, the integral of the signal was reduced to 61% with respect to the initial signal. The polymer was re-oxidized at 1.2 V and the ESR signal was recorded again. After applying the

oxidation potential, the signal intensity increased resulting in an increase of the integrated signal area up to 99% of the initial value. In conclusion, the ESR results confirmed the decay process of the radical cations of PVPPP observed by UV/Vis. The decay process occurs due to a reversible reaction of the radical cation which leads to a self discharge of the polymer.

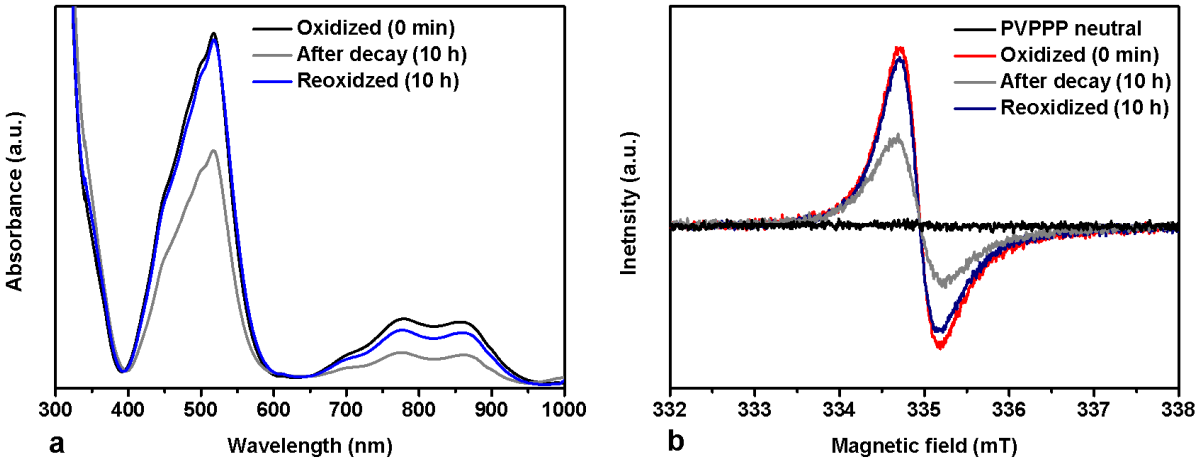

Figure 19. a) UV/Vis measurement of PVPPP radical cation directly after oxidation and after decaying over 10 hours. By applying an oxidation potential of 1.2 V, the PVPPP was re-oxidized, b) ESR measurements of PVPPP in the neutral and the oxidized state. The signal decay was observed after 10 hours and the after re-oxidation at +1.2 V. For the UV/Vis measurements, PVPPP spin-coated film on ITO, Ag/AgCl and Pt-wire were used as WE, RE and CE in 0.1 M TBAPC/ACN, respectively. For ESR measurements, a Pt-wire coated with PVPPP, Ag-wire and Pt-wire were used as WE, RE and CE in 0.1 M TBAPC/ACN, respectively.

One possible mechanism to explain the decay of the radical cation species is given by Sackett et al.[150] They propose that phenothiazine radical cation reacts with the nucleophiles in the electrolyte (in this case perchlorate ions) to form the neutral radical species.[69] In a successive disproportion reaction, the neutral radical reacts with the radical cation to form the neutral phenothiazine species as well as the phenothiazine cation. Both reaction steps are reversible, thus enabling the reformation of the radical cation (Scheme 32).

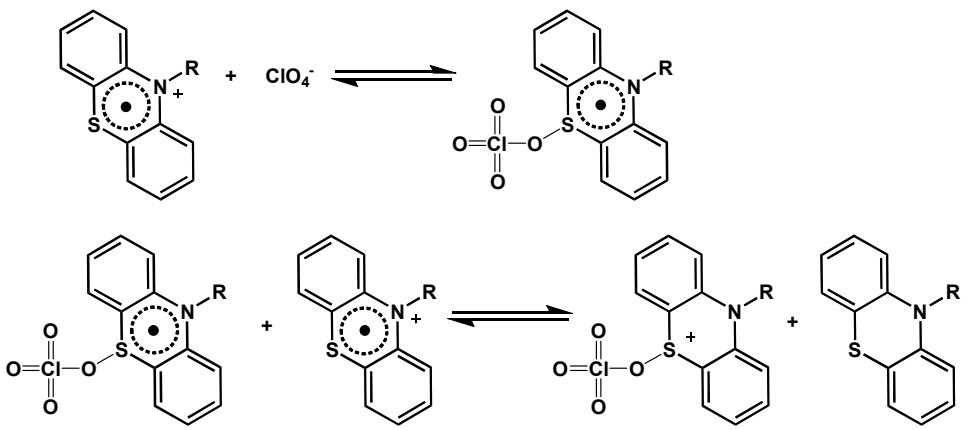

Scheme 32. Decay mechanism for phenothiazine radical cation in the electrolyte solution.

Although the nucleophiles in the electrolyte are responsible for the decay process of the radical cation, the type and concentration of the nucleophile also plays a role. Jelinek and coworkers found out that at increasing concentration of salts with the same anion as the counterion of radical cation species, the stability of the radical cation could be increased with respect to decay.[70] Surprisingly, the nucleophile has less effect on the radical cation decay at higher concentrations. For the radical cation of PVBPT, similar decay behavior was observed (Figure 20).

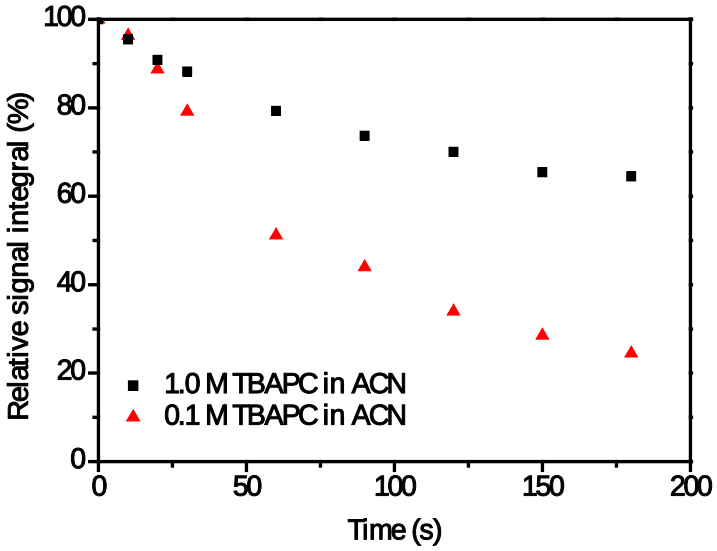

Figure 20. Decay rate comparison for PVBPT in 0.1 M and 1.0 M TBAPC/ACN observed with ESR.

In diluted electrolyte solution with 0.1 M concentration the ESR signal from the radical cation decreased in intensity and integral. The integral is reduced to 25% of the original value directly after the oxidation within 3 hours. In higher concentration of 1.0 M TBAPC the radical species revealed a slower decay process. The integral of the ESR signal is decreased to 65% of the initial intensity after 3 hours. Thus, higher concentration of the electrolyte solution support the stability of the radical cation, whereas in diluted electrolyte solution, nucleophilic attacks lead to reversible decay of the radical species. These results contradict with the decay mechanism described in Scheme 32. An alternative explanation for the higher stability of the radical cation in concentrated electrolyte solution is a shielding effect of the counterions. In concentrated solutions, counterions attached to the radical cation form a shielding shell around the radical cation. This shell prevents attacks from other nucleophiles and reduces the self discharge behavior. Furthermore, at high concentration nucleophilic attack is aggravated due to increased collision possibility of the nucleophiles.

Supposing the nucleophilic attack on phenothiazine leads to the decay process of the radical cation, the radical species should remain stable under exclusion of the electrolyte solution. It should therefore be possible to isolate and retain the persistent radical cation in dry state. To isolate phenothiazine radical cation polymer, a solution of PVBPT in THF was prepared.

$NOBF_4$was added as oxidation agent to precipitate the radical cation Polymer $PVBPT^{*+}BF_4^-$ which was then isolated and dried. While the neutral polymer is a white powder, the precipitated polymer has a dark red color indicating the phenothiazine radical moieties (Figure 21a, insets). The red colored polymer was inserted inside an ESR tube. During the measurement, the tube was heated to 80 °C to check whether the radical species is thermally stable (Figure 21a). The radical species resulted in a typical unpaired electron signal with no additional coupling at 334.81 mT (g = 2.0030). The range of the g-value was the same as for PVPPP whereas the small deviations come from interactions with the polymer backbone. The shorter the spacer length, the more the backbone can influence the radical moiety.[149] In addition, a spin density of 1.5 $*10^{21}$ radicals/g using galvinoxyl as a standard was estimated. This estimation leads to a spin density of about 0.7 radicals per repetition unit of the polymer. Thus, about 70% of the repetition units are oxidized chemically. With respect to thermal stability, further ESR spectra were recorded over several hours at 80 °C. No significant change in the signal intensity and shape was observed even after more than 70 hours. The integral below the ESR signal decreased to around 11% after 30 hours and the integral stayed constant at 89% of the initial value (Figure 21b). The temperature stability of the $PVBPT^{*+}$ BF_4^- is comparable to the stability of nitroxide based radicals such as 2,2,6,6, tetramethylpiperidine-1-oxyl (TEMPO)[151] which are stable up to 100 °C. This result can be explained by the stabilizing effect of the polymer matrix, which prevents the decomposition of the radical sites by disproportionation[70] or dimerization.[152] Zhou et al. observed a similar effect for phenothiazine anchored to mesoporous silica MCM-41.[72] In their case the phenothiazine radical cations were stabilized by pore cavities of the MCM-41. Taking the influence of the high temperature on the radical decay into account, dry $PVBPT^{*+}BF_4^-$ should remain stable under ambient conditions on spin-coated films for several months.[87]

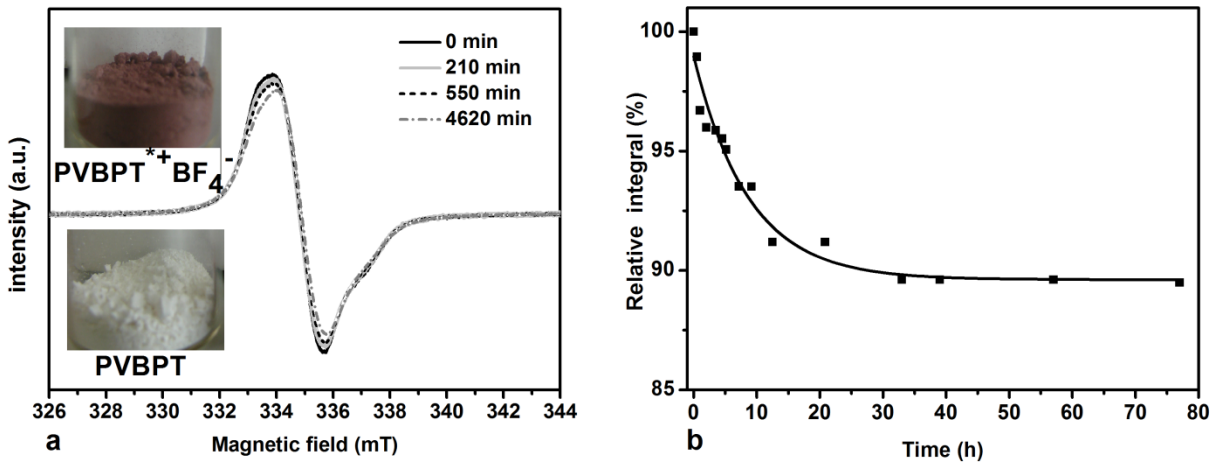

Figure 21. a) ESR signal measured over time for $PVBPT^{*+}BF_4^-$ powder at 80 °C. The inset shows the color change between the neutral PVBPT and the radical cation, b) decay rate of the radical cation signal for $PVBPT^{*+}BF_4^-$ powder over more than 70 hours.

In conclusion, PVPPP and PVBPT in the electrolyte solution revealed a radical decay process which takes place as a self discharge over several hours. The decay reaction was reversible according to UV/Vis and ESR data. Furthermore, the decay rate is larger for PVBPT than for

PVPPP due to the radical stabilizing effect of the propylene spacer chain. By increasing the concentration of the electrolyte, the decay rate was decreased. The increase of concentration results in better shielding of the radical cation species and slower self discharge. Thus, for maintaining the stability of the radical cation, increasing the concentration of the electrolyte solution is beneficial. In the dry state, PVBPT radical cation revealed the higher stability compared to the polymer in the electrolyte solution. Dry radical cation polymer $PVBPT^{*+}BF_4^-$ exhibited enormous stability with respect to decay even under heating at 80°C in the ESR experiments. The self discharge cannot take place because no electrolyte is present and the polymer matrix additionally stabilizes the radical cation. These findings are helpful with regard to designing new polymer for assembly of battery cells. By increasing the spacer length between the redox moiety and the polymer backbone, the redox state is stabilized and decelerates self discharge of the electrode active material. After examining the redox properties of the polymer and the stability of the radical cation state, the polymers were tested regarding their charge storage capacity. Therefore, in the next step the polymers PVBPT, PVPPP and PVMPT were used as cathode materials for assembly of battery cells.

4.4. Chrono potentiometry and battery assembly

To check the applicability of the phenothiazine based polymers as cathode active material for radical batteries, charging and discharging behavior of the polymers was examined in a battery half cell. The polymers PVPPP, PVBPT and PVMPT were spin-coated on ITO and CP measurements were performed on the spin-coated films. To obtain CP data, changes in potential were plotted against the capacity. The capacity is often used in CP measurements instead of the time to allow easier comparison of the data independent of the mass and the applied current. To obtain the capacity, the amount of the spin-coated polymer was estimated from the electrode surface area. Therefore, the film thickness and the polymer density of 1.04 g/cm^3 (for PS) were used. The measurements were performed at a C-rate of 10 C and the corresponding current i was calculated as follows:

$$i = \frac{n_m \cdot F \cdot (C-rate)}{3600} \tag{18}$$

n_m is the molar amount of the redox moieties which was obtained from the polymer mass m_p and the molar mass of the monomer M. From the resulting transition time τ at the applied current i, the capacity per mass C_m was calculated according to the equation:

$$C_m = \frac{i \cdot \tau}{m_p} \tag{19}$$

From the CP measurements, a capacity of $C_{m,c}$ = 79 Ah/kg was calculated with a plateau voltage of 0.89 V for PVPBT charging curve as shown in Figure 22a (forward scan). The theoretical capacity value of PVBPT is $C_{m,theo}$ = 85 Ah/kg. The theoretic value was calculated by dividing the Faraday constant F by the molar mass of the monomer M. According to the calculation, 93% of

all the PVBPT moieties have been oxidized. The discharging capacity however, was $C_{m,d}$ = 61 Ah/kg with a plateau voltage of 0.85 V (Figure 22a, backward scan). From the ratio between the discharge and charge capacity, a coulomb efficiency of 77% was obtained. Self discharging takes place during the charging process since the measured discharge capacity is smaller than the charge capacity ($C_{m,d}$ = 72% of $C_{m,theo}$ of PVBPT). This phenomenon is related to the decreased stability of the radical cation species in the electrolyte solution as observed in III.4.3. The plateau voltages are in good agreement with the CV peak position in Figure 11. For an ideal battery material, the voltage for both steps must be the same to ensure the charging and discharging takes place at the same potential.

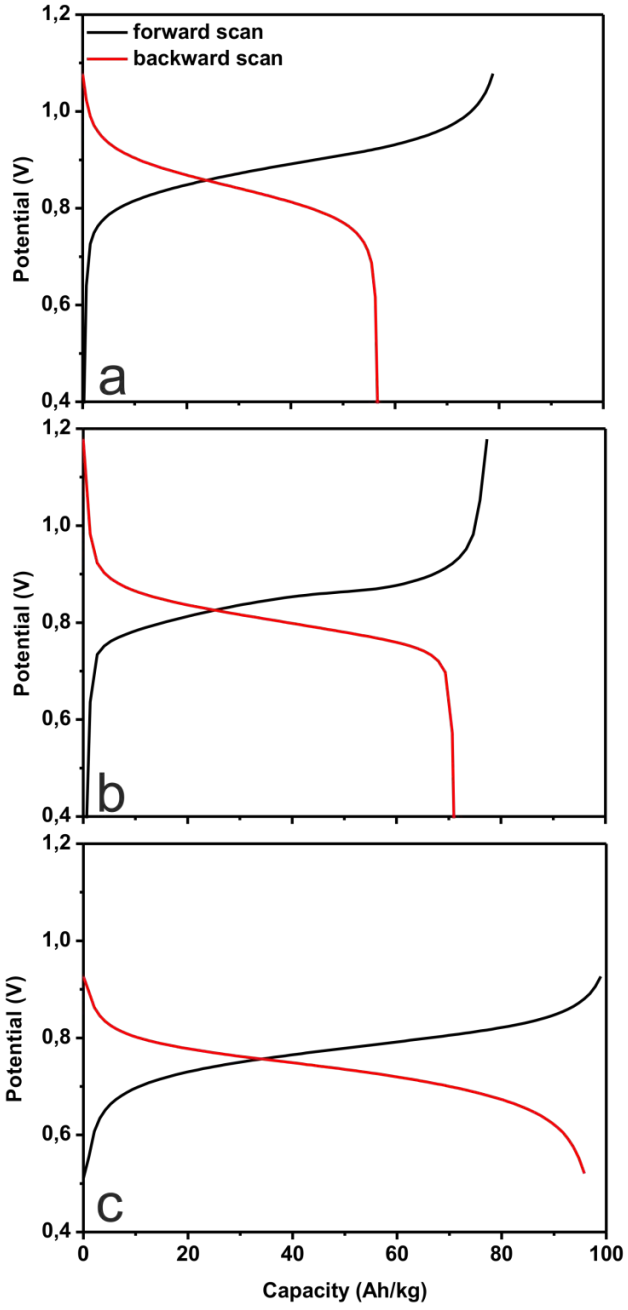

Figure 22. CP measurements of a) PVBPT b) PVPPP and c) PVMPT of the charging (forward) and discharging (backward) scan. Spin-coated film on ITO, Ag/AgCl and Pt-wire were used as WE, RE and CE in 0.1 M TBAPC/ACN, respectively.

For PVPPP, $C_{m,c}$ = 77 Ah/kg and $C_{m,d}$ = 72 Ah/kg were measured at the plateau voltage 0.84 and 0.81 V (Figure 22b). With $C_{m,theo}$ = 78 Ah/kg, the measured capacity corresponds to 99% and 92% of the theoretical value regarding the charge and discharge step. Compared to PVBPT, the stabilizing effect of the propylene spacer in PVPPP increases the life time of the charged state, resulting in a coulomb efficiency of 94%. In addition, the stabilizing spacer affects the capacity. More oxidized moieties can be formed due to quantitative reaction which in return increases the capacity. PVMPT revealed the highest capacities with $C_{m,c}$ = 98 Ah/kg and $C_{m,d}$ = 93 Ah/kg at the plateau voltage of 0.77 and 0.74 V. With $C_{m,theo}$ = 112 Ah/kg, the measured capacity corresponds to 87% and 83% of the theoretical value for the charge and discharge step. PVMPT has monomer units with lower molecular weight which increases the capacity (Figure 22c). Nevertheless, not all the moieties are accessible for oxidation, which explains the 13 to 17% lower capacity compared to theory. With respect to the coulomb efficiency, a value of 95% was obtained similar to PVPPP. It must be noted, that the charging and discharging takes place faster with respect to C-rate. Conventional lithium-ion rechargeable batteries are typically operated at C-rates below 10 C to avoid heating.[153] The capacity drops down dramatically as soon as the C-rate is increased above 10 C.

The determination of the capacity for the polymers in the spin-coated film allows checking the applicability of the polymer prior to their assembly in the battery cell. PVPBT already showed a strong self discharge during the CP measurements and was therefore not used for the battery assembly. PVPPP and PVMPT were chosen because of their decent capacity (C_m > 70 Ah/kg) and their good rechargeable behavior (coulomb efficiency > 90%). To assemble the battery, a composite with 10 weight% of polymer was prepared with PDVF and VGCF. PDVF serves as a binder whereas VGCF is an additive to improve the conductivity of the polymer. Before applying the polymer composite as cathode material, first their CP was measured on glassy carbon as working electrode to simulate the battery half cell. Both Polymers PVPPP and PVMPT were used to prepare the composite. CP experiments were then preformed at different C-rates to examine the charge and discharge rate of the composite. For PVPPP, the CP scan at 10 C, revealed a capacity of $C_{m,c}$ = 75 Ah/kg. $C_{m,c}$ decreased approximately 25% compared to the initial capacity while increasing to 50 C. The backward scan exhibits a capacity of $C_{m,d}$ = 72 Ah/kg at 10 C, indicating a reversible charging (Figure 23a). In the case of PVMPT, a capacity of $C_{m,c}$ = 86 Ah/kg was observed at 10 C. While increasing the C-rate to 50 C, the capacity decreased approximately 75% to $C_{m,c}$ = 21 Ah/kg. The backward scan exhibits a capacity of $C_{m,d}$ = 80 Ah/kg at 10 C, indicating a reversible charging for PVMPT as well (Figure 23b).

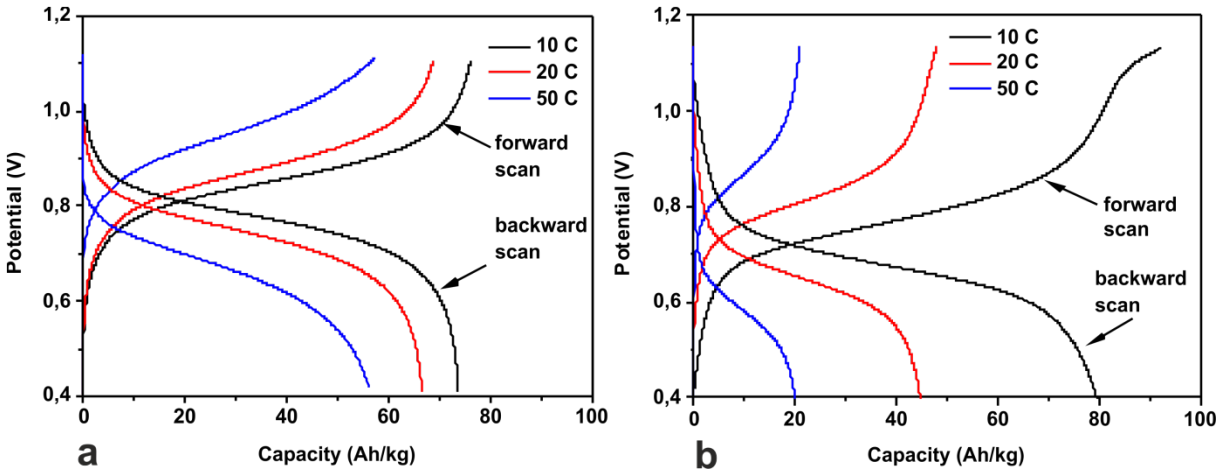

Figure 23. CP measurements of a) PVPPP and b) PVMPT polymer composite with VGCF and PVDF containing 10 weight% of the polymer at different C-rates. Blade coated film of the composite on GC, Ag/AgCl and Pt-wire were used as WE, RE and CE in 0.1 M TBAPC/ACN, respectively.

Further experimental capacity values, plateau voltage and coulomb efficiency are presented in Table 8. The experimental capacity $C_{m,c}$ of PVPPP at 10 C corresponds to 96% of the theoretical value. Unlike PVMPT, where 77% of the theoretical value was achieved, PVPPP can be oxidized quantitatively. By increasing the C-rate to 50 C, still 72% of the theoretical capacity was achieved for PVPPP. In contrast, the capacity dropped down to 19% of the theoretical value at 50 C for PVMPT. For both polymers the coulomb efficiency is over 90%, showing that the redox process is reversible in the composite. The electron transfer process takes place faster for PVPPP than for PVMPT in the composite. The difference of plateau voltage for the charge and discharge step increased from 90 mV to 260 mV for PVPPPP and from 90 mV to 260 mV for PVMPT when the C-rate was increased from 10 C to 50 C, respectively. This increase implies that the redox process is too fast for PVMPT and PVPPP at 50 C. The redox process is not complete and some moieties remain in their initial oxidation state.

Table 8. Measured plateau voltage, charging capacity and calculated percentage of the theoretical capacity and coulomb efficiency for PVPPP and PVMPT polymer composite at different C-rates.

Polymer	C-rate	Plateau voltage (charge/discharge in mV)	experimental capacity $C_{m,c}$ (Ah/kg)	% of theoretical capacity	Coulomb efficiency (%)
PVPPP	10	850/760	75	96	96
	20	880/740	67	86	97
	50	930/670	56	72	96
PVMPT	10	770/680	86	77	93
	20	810/660	47	42	96
	50	870/590	21	19	90

Further information about the diffusion process inside the composite film resulted from the CP experiments. With the Sand equation (9), the diffusion constant D_{app} for the electron exchange process was calculated at 10 C. The concentration of the oxidized species was determined for the composite containing 10 weight% of the redox active polymer and by assuming a density of 1.88 g/cm^3. The density was calculated from the densities of VGCF, PVDF and the polymer being 2, 1.76 and 1.05 g/cm^3 considering their weight percentage. For the charging step, D_{app} of $1.2*10^{-10}$ and $3.8*10^{-11}$ cm^2/s was obtained for PVPPP and PVMPT. These values are in good accordance with the diffusion constants obtained from CA experiments in Table 5.

Apart from the capacity C_m and the C-rate, cycle stability of the polymer during the charging and discharging steps is an important parameter for rechargeable battery applications. To measure the cycle stability, the CP experiment was repeated 10 times at 10 C for PVPPP polymer composite (Figure 24). After the 10th scan, $C_{m,c}$ = 75 Ah/kg was determined which is the same value as the initial capacity.

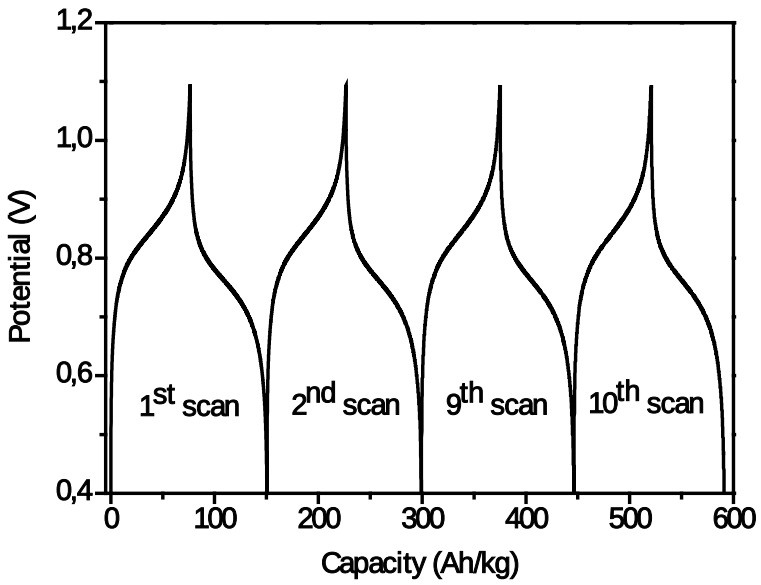

Figure 24. Long term stability measurements for PVPPP polymer composite on GC after 10 CP scans at 10 C. Blade coated film of the composite on GC, Ag/AgCl and Pt-wire were used as WE, RE and CE in 0.1 M TBAPC/ACN, respectively.

Thus, the charge and discharge of the PVPPP polymer composite can be repeated for at least 10 cycles without significant loss of the capacity. In addition, the shape of the curves remained the same, indicating long-term stability of the polymer with respect to charge and discharge behavior. As a general test, a rechargeable battery should be charged and discharged over at least 500 cycles without losing its capacity.[111] To examine the cycle stability under this working condition, the polymers were integrated in battery full cells. Therefore, battery coin cells were designed using a paste of PVPPP and PVMPT polymer composite on aluminum foil as cathode material (Scheme 33). Lithium metal was applied as anode material separated from the cathode

by a Teflon membrane. A commercially available electrolyte consisting of $LiPF_6$ in EC/DEC was used. To avoid air contact and prevent short circuits, the battery coin cell was sealed using a steel platelet and a formable lid.

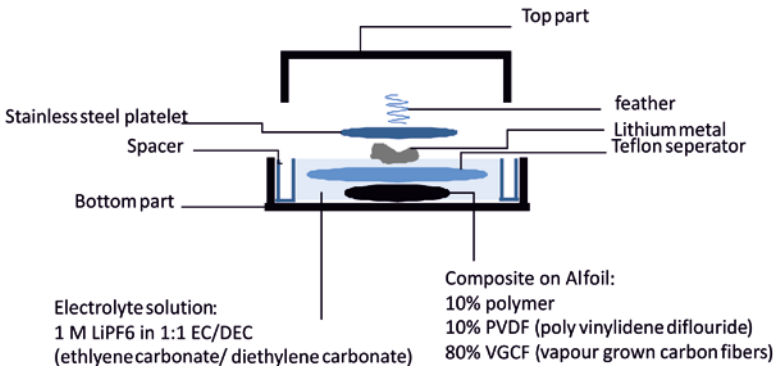

Scheme 33. Schematic structure of a coin cell battery using the polymer composite as cathode and Lithium metal as anode material.

The battery coin cell was tested with respect to its charging and discharging behavior in CP measurements. The capacity C_m was determined for the first and 500th cycle at the rate of 10 C to examine the long-term cycle stability (Table 9). Furthermore, the plateau voltage and coulomb efficiency were analyzed from the cycle stability tests. After the first cycle, the capacity of the battery coin cell with PVPPP as cathode material was $C_{m,c}$ = 55 Ah/kg, corresponding to 70% of the theoretical capacity. After 500 cycles, the capacity dropped down to $C_{m,c}$ = 48 Ah/kg, which is 12% less than the initial value. The coulomb efficiency also decreased from 92% to 83%. One possible explanation for the low experimental $C_{m,c}$ at the beginning is the loss of the cathode material during the cell assembly. For previous experiments performed in half cell, the oxidation step succeeded quantitatively. In the full cell battery, electrode active cathode material could break away from the aluminum foil as the cell was closed. Therefore, the composite mass is not available for redox reactions.

Table 9. Measured plateau voltage and charging capacity $C_{m,c}$ as well as calculated percentage of the theoretical capacity and coulomb efficiency for coin cell batteries with PVPPP and PVMPT polymer composite as cathode material at different C-rates. The values were measured after the first and the 500th cycle to observe long-term stability.

Polymer	Cycle number	Experimental capacity $C_{m,c}$ (Ah/kg)	% of theoretical capacity	Plateau voltage (charge/discharge in V)	Coulomb efficiency (%)
PVPPP	1	55	70%	3.69/3.55	92%
	500	48	61%	3.69/3.44	83%
	loss	12%			10%
PVMPT	1	72	64%	3.59/3.31	100%
	500	56	50%	3.64/3.34	84%
	loss	23%			15%

However, the experimental capacity decreased after 500 cycles which might be due to side reactions in the battery. Since during the charging and discharging lithium is oxidized and reduced, basic lithium salts are formed such as LiOH and LiF. The salt formation changes the pH value in the battery cell which leads to irreversible side reaction such as forming sulfoxide species on phenothiazine moieties.[150]

Nevertheless, PVPPP exhibited good performance as battery material with respect to reproducibility of the cycles (Table 9). The plateau voltage of around 3.7 V was around 200 mV higher compared to the lithium radical batteries based on PTMA.[111] The difference between the plateau voltages of 140 mV for the charging and discharging step was explained by geometrical change in the molecular structure of PVPPP. Since the phenothiazine units change from bent to planar structure, this might influence the electron transfer mechanism in the polymer composite. For PVMPT based polymer batteries, the $C_{m,c}$ = 72 Ah/kg was higher than PVPPP (64% of the theoretical value). For PTMA based lithium radical batteries, a capacity of $C_{m,c}$ = 77 Ah/kg was reported which corresponds to 70% of the theoretical value.[111] Compared to PVPPP, the polymer was less stable regarding the long-term cycle stability. After 500 cycles, the capacity decreased to around 23% to $C_{m,c}$ = 56 Ah/kg. Also the coulomb efficiency decreased around 15% to 84%. For PVMPT, a plateau voltage of around 3.6 V was determined similar to PVPPP. PVMPT shows better performance with respect to the capacity due to its low molecular mass. However, PVPPP revealed higher long-term cycle stability for the charge/discharge cycles. The higher stability is caused by the stabilizing effect of the propylene spacer on the radical cation species which is formed during the charging step. The high concentration of the electrolyte in the battery cell of 1 M stabilizes the radical cation. PVPPP has a slightly higher plateau voltage value than PVMPT, which is desirable for high voltage battery application in electronic devices. This type of battery is capable of charging within 6 minutes, which is enormous improvement compared to the charging time of convectional lithium ion batteries.

5. Summary and conclusion

The redox properties of the three phenothiazine bearing polymers PVBPT, PVPPP and PVMPT were investigated via CV. All three polymers exhibited quasi-reversible redox chemistry for the first oxidation step. The first oxidation wave appeared between 0.78 and 0.89 V. The shift of the oxidation potential depends on the substitution position of the phenothiazine moiety. PVBPT revealed the highest and PVMPT the lowest oxidation potential. The first oxidation was accompanied by the reversible appearance of a red colored species in the polymer film. The red colored species was identified as the radical cation by UV/Vis and ESR technique.

Apparent diffusion constants D_{app} of the overall electron transfer were measured by CA. The measured values were in the order of 10^{-9} to 10^{-11} cm^2/s for all three polymers. However, the diffusion constant for the PVBPT was slightly higher compared to PVMPT and PVPPP. The propylene spacer chain in PVPPP leads to separation of redox sites and reduces the interaction between these sites in the polymer. The heterogeneous electron transfer constant k^0 was

obtained by theoretical calculations from the CV and CA data. The values were in the order of 10^{-5} to 10^{-6} cm/s for all three polymers implying an electron transfer in the quasi-reversible regime. D_{app} also served to obtain the electron exchange rate between the immobilized redox moieties in the polymer chain. The determined electron self exchange rate k_{ex} decreased from approximately 10^6 $M^{-1}s^{-1}$ to 10^4 $M^{-1}s^{-1}$ in the sequence PVBPT, PVMPT and PVPPP. The values for k_{ex} imply a fast electron transfer in the same order as PTMA.[146,147] The N- substituted polymer PVBPT showed the fastest k_{ex}. The fast electron transfer was attributed to appropriate center to center distance between the neighboring redox moieties. The appropriate distance facilitates the rotation of the moieties in the proper juxtaposition for electron exchange. The polymer PVPPP showed the lowest electron exchange. The propylene spacer between the phenothiazine and the polymer backbone increases the rotational freedom of the redox moieties. Simultaneously, the distance between the moieties is increased which limits the interaction between them.

The stability of the radical cation species was examined with UV/Vis and ESR. One important finding was related to the effect of that spacer between the phenothiazine and the polymer backbone. The increase of the spacer chain stabilizes the radical cation formed by oxidation. Therefore, the decay of the radical cation concentration occurred more slowly for PVPPP compared to PVMPT. The decay of the radical cation was attributed to self discharge catalyzed by the electrolyte in the solution. The radical decay however is reversible and can be decelerated in highly concentrated electrolytes. Thus, the spacer chain decreases the electron self exchange rate but simultaneously increases the stability of the oxidized radical cation. In contrast to the solution stability, oxidized PVBPT radical cation showed outstanding thermal stability in solid state ESR experiments. After more than 10 hours of thermal treatment at 80 °C, the radical lost only about 10% of its original intensity. The stability of the radical cation species in solid state is a useful feature offering new perspectives for application as data storage media. This topic will be discussed in the following chapter IV.

In battery devices, the polymer exhibited good performance according to chrono potentiometric measurements. The highest capacities of around 86 and 72 Ah/kg were obtained for PVMPT in half cell and full cell devices due to the low molecular weight of the monomer unit. According to the decent coulomb ratio of over 90%, the use of composite material and the high concentration of the electrolyte have a stabilizing effect on the charging/discharging performance. In half cell device, coulomb efficiency up to 97% could be achieved for PVPPP which indicates quantitative access to the redox moieties. An important aspect is the C-rate limit of the cathode material. At C-rates over 10 C, the redox system could not follow the charging speed. This leads to 15% and 28% loss of the theoretical capacity in the case of PVPPP in half cell at 20 and 50 C. Thus, these systems are fast compared to conventional inorganic cathode materials but should be operated at C-rates below 10 C. In full cell battery device, the maximum capacity compared to theory is limited and was measured for PVPPP with 55 Ah/kg as 70% of theoretical value. This however can be optimized by the cell and electrolyte design to achieve

the maximum capacity. In addition, the cell potential of the full battery cell increased up to 3.7 V for PVPPP as cathode material. This finding is important for the design of battery cells with higher voltage supply, since the existing PTMA system have lower cell potentials in the order of 3.5 V. Furthermore, the polymers PVPPP and PVMPT proved long-term cycle stability. After 500 cycles, the performance of the polymers is reduced to 23% referring to the initial capacity for PVMPT. The stabilizing effect of the spacer in PVPPP increases the cycle stability in comparison to PVMPT. The effect of the spacer length should be considered in the synthesis of further phenothiazine based polymers. Compared to the nitroxide based p-type radical polymer, phenothiazine baring polymer revealed decent performance regarding the necessary criteria for charging and cycle stability. Better results should be obtained with further improvement of the design namely synthetic optimization, electrolyte choice and the blend composition of the active material.

IV. Scanning Probe Microscopy based data storage

Parts of the chapter were published in:

A. A. Golriz, T. Kaule, J. Heller, M. B. Untch, P. Schattling, P. Theato, M. Toda, S. Yoshida, T. Ono, H.- J. Butt, J. S. Gutmann, R. Berger, *Nanoscale,* 3, **2011**, 5049.

1. Introduction and motivation

Polymers with high redox active functional groups such as phenothiazine are interesting for data storage purposes. If their redox state is related to a change in conductivity, local switching of the conductive state can be induced on nanometer scale. To achieve switching on a nanometer scale, nano-sized probes which have a tip diameter around 10-20 nm can be used. SFM has proved to be an adequate technique for nanoscale switching. [154,165,170]If an electrically conducting coating is chosen for the tip, the polymer underneath can change its conductivity by applying the adequate oxidation potential of the polymer via the tip. The local change in conductivity can be measured with the same tip by probing with a different bias potential.

Phenothiazine based polymers such as PVMPT[86,87] were reported to exhibit reversible oxidation with electrochromic memory effect. In spin-coated films, an increase of conductivity five to six orders of magnitude was observed upon partial oxidation of 3-4 mol% of the phenothiazine moieties.[85] According to the results obtained in chapter III, the phenothiazine based polymer PVBPT shows reversible redox behavior under application of bias potential. The reversible redox chemistry of PVBPT is a useful property for data storage application. Once oxidized, stable radical cations are formed in PVBPT films changing the local conductivity of the polymer. The high stability of the radical cation is the key for long- term storage of information. Once the moieties are oxidized, they should maintain their oxidation state. Therefore, by oxidizing the polymer film on a nanometer scale using SFM techniques would allow to store bits of information over a long period of time as an oxidation pattern. PVBPT is also an interesting polymer due to its high thermal decomposition and glass transition temperature. Mechanical wear on the nanoscale leads to abrasion of the storage medium and to loss of the stored information. Thermal processes destroy the chemical nature of the polymer, deleting the chemically stored information. PVBPT films are thermally stable and mechanically robust which are fundamental properties for SFM based data storage. A further advantage of PVBPT as phenothiazine bearing polymer is that the electrochemical process is only located on the side chains. By oxidizing PVBPT, the local conductivity should be changed via intermolecular interaction of the phenothiazine moieties. The polymer backbone serves as mechanical stabilization and isolates the oxidized moieties which define the conductive pathways. The stabilization of the stored charges and the sufficient mechanical stability motivate the investigation of PVBPT for nanoscale patterning experiments.

The focus of the following chapter is investigating the applicability of PVBPT for patterning experiments based on conductive SFM. Patterning experiments were performed on spin-coated

PVBPT, including writing, reading and erasing by applying an adequate oxidation and reduction potential. Furthermore, the long-term storage stability of the written pattern was examined as well as the mechanical stability in SFM nanowear tests. Besides, possible conduction mechanisms of PVBPT and its oxidized species were evaluated and discussed. For use as SPM based storage media, polymers have to meet several criteria. In the following, a basic outline into memory types and categories is given. Furthermore, an overview of the literature concerning data storage based on SFM is presented and the resulting nanowear is elucidated.

2. Theoretical background

2.1. Memory types and categories

Memory devices are divided into two main categories: volatile and non-volatile memory. The volatile memory type includes random access memory (RAM) devices which have to be supplied by electricity to maintain the memory. Non-volatile memory includes read only memory (ROM) and hybrid memory. Electrically programmable ROM (EPROM) processors and write once read many times (WORM) devices such as compact discs and DVDs belong to the ROM category. Among the hybrid memories, ferroelectric based RAM (FeRAM) and the transistor based FLASH memory have gained high importance. Especially FLASH memories have emerged to the electronic market as USB memory, compact flash and SD-cards for cameras and other electronic devices. This type of memory requires low power consumption and allows fast access to stored data. A transistor type memory like FLASH contains a floating gate with an oxide layer as a barrier to maintain charges after injection from the control gate. The presence of the charge prevents the current flow between the source and the drain. This way a state with current flow and no current flow can be defined as 1 and 0, respectively.

Generally, most of the memory devices are based on inorganic components like metalloid oxides. Organic based memory devices (OMD) are nowadays becoming progressively the focus of recent research. Particularly, the aspect of the production cost, energy consumption and fast and reliable storage density are points which can be improved by organic materials. Nowadays, OMD can be categorized into three different types (Scheme 34).[154] Transistor type OMD, also called “organic field effect transistor” (OFET), consist for example of a semi conductor and/or a dielectric polymer such as poly(3-hexylthiophene) (P3HT) and polyvinyldiflouridine (PVDF), respectively. The dielectric component prevents the charge propagation at the floating gate, similar to the oxide layer for inorganic FLASH memories. All other components, namely source, drain, gate and electrodes are quite similar to inorganic field effect transistors. For capacitor type OMD, mainly ferroelectric materials are used which can permanently maintain their electric polarization and thus are non-volatile. Polymers with ferroelectric properties like PVDF with head to tail configuration, reversible polar orientation and crystalline morphology exhibit a hysteresis loop of the polarization depending on the electric field. The orientation of the polarized state, i.e. upward or downward polarization defines the on and off state, respectively.

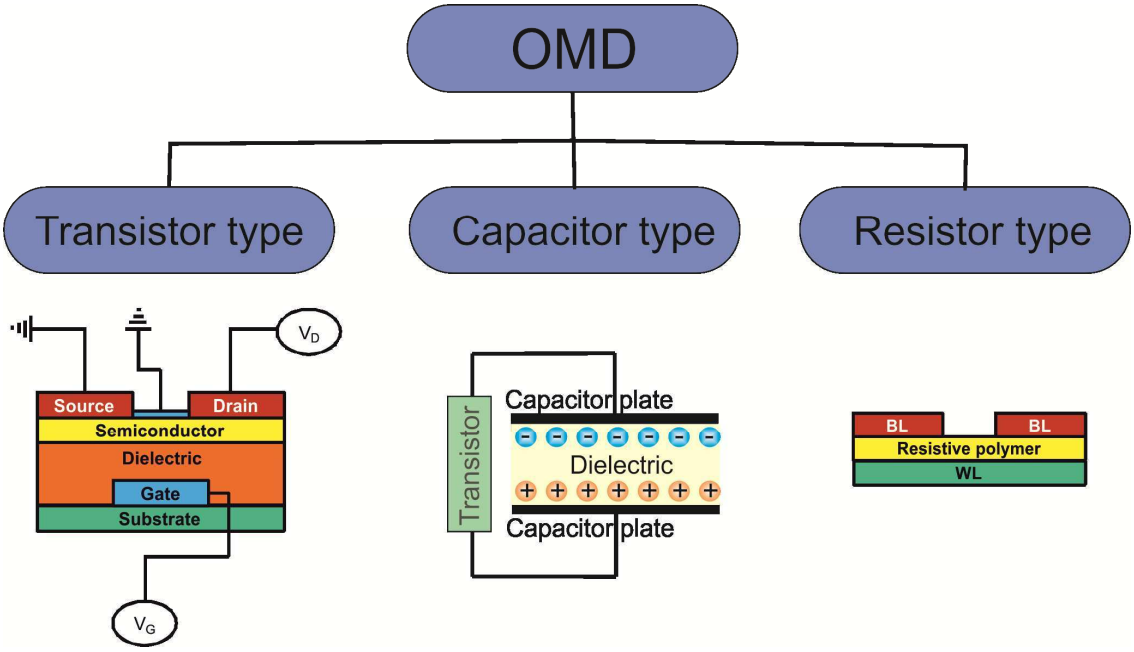

Scheme 34. Overview of OMD categories.

The resistor based memory also called "resistive RAM" (RRAM) has the simplest OMD architecture. Here, the storage principal is related to the electric bistability of an organic material in between two electrodes, namely "bit line" (BL) and "word line" (WL). Cross-bar structure of BL and WL on the bistable resistive materials are used to identify individual memory cells by the x and y coordinates. Bistable materials can switch their intrinsic properties between two stable states (on and off state) depending on the applied electric field. Switching might be due to charge transfer, phase change, conformation change or reduction/oxidation processes.[155] The resulting change in conductivity or current flow can finally be identified as switching between on and off state. Resistive OMD can be operated separately without the integration into the logical device.[156] Important parameters for resistive OMD are on/off ratio, storage density, power consumption, data retention, long-term stability and switching time. The on/off ratio defines the current ratio between the on or conducting state and the off or non-(less) conducting state. To minimize the error during the reading process in the cross-bar matrix, materials with high on/off ratio are desirable. Parasitic signal or background noise might disturb the signal processing during reading or writing step. Thus, high on/off ratio enables easy differentiation between the on and off state. In order to miniaturize the storage array and increase the storage density, SFM technique can be used to induce switching in the resistive film. Scanning probe techniques enable storage densities up 250 Tb/inch^2 which is in the atomic range.[157] This high storage density is the big advantage of SFM technique compared to the existing FLASH memory devices. However, the access time for reading and writing requires further enhancement of the SFM technique itself and of the used storage materials. Simple reading and writing modes with SFM techniques combined with bistable materials with good switching properties are necessary for this type of future data storage.

2.2. Conductive Scanning Force Microscopy based resistive devices

Scanning force techniques have been widely used to manipulate surfaces at atomic scale.[158-160] In 1992, Mamin et al. reported a SFM based storage technique which uses thermo-mechanical writing.[161] A polymer surface of PMMA is treated by a focused infrared laser on the SFM tip. Thus, the heated SFM tip can penetrate the PMMA film leading to formation of nano-sized indents. At a scan speed of 0.3 µs pits with a minimum diameter of several Å were formed. This type of memory storage enables storage density above the limit of 1 Tb/inch^2.[162,163] IBM developed this storage concept (Millipede project) using PS as storage media and multiple moving heatable tips.[164,165] However, the writing speed is limited by the slow kinetics of the melting process in the polymer film as well as by the mechanical resonance of the cantilever. To improve the data storage concept based on SFM, Kado et al. suggested the application of conductive mode of SFM.[166] Using a conductive SFM tip, they could locally switch the conductance of sputtered amorphous $GeSb_2Te_4$ film. They applied a bias potential of +3 V to write dot patterns inside the film and could read the written patterns by applying +0.5 V. The conductance change increases more than 100 times after the writing procedure. However, the authors speculate about two different mechanisms which give rise to the change in conductance. Either the chalcogenide undergoes a thermally induced phase change process due to joule heating or tunneling through a Shottkey barrier might be responsible for the increase of conductance. In a later publication Gotoh et al. associated the conductance change to a phase change mechanism.[167] Since then, many groups dedicated several works on RRAM based on conductive SFM.[168169] These works mainly deal with inorganic materials or in few cases with organic molecules like rotaxane[170] or charge transfer complexes[171] as storage medium.

In 2003 Ono et al. reported about electrical patterning of PANI/PMMA polymer blend films via conductive SFM.[172] The experiment was performed in contact mode applying a bias potential between the tip and the sample which was spin-coated on top of a conductive substrate. Current flow through the tip was then amplified and registered as an additional signal to topography (Scheme 35).

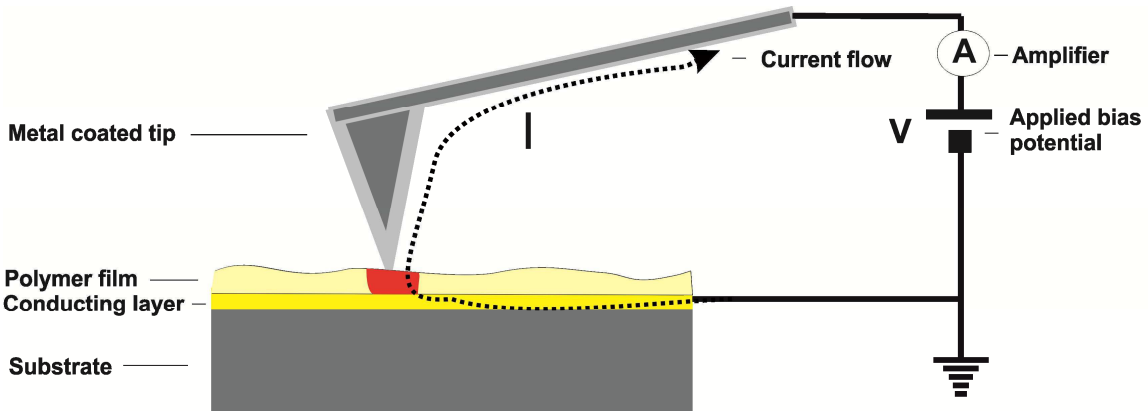

Scheme 35. Schematic setup of patterning of polymer films via conductive SFM.

The local conductivity of the PANI/PMMA polymer film was increased up to 1-2 orders of magnitude by application of bias potential. Referring to the storage density, the PANI/PMMA system revealed a bit size of around 150 nm. In a later publication Yoshida et al. showed that thin PANI brush films can be reversibly patterned by conductive SFM.[173] They observed that the conductivity of PANI decreases by application of +3 V bias potential and increases at -3 V, respectively. The switching mechanism was explained by reversible oxidation/reduction of the PANI film. The authors claim that the presence of water is necessary for the writing procedure due to protonation/doping of the PANI. In further works Yoshida et al. concentrated on enhancing the self ordering of the PANI and decreasing the storage size by using template structures such as electron beam lithography[174] or template forming polymers like PS/PMMA block copolymers.[175] However, conductive polymers like PANI tend to degrade thermally, electrochemically and under ambient conditions thus losing their conductive properties over time, as mentioned before. [176,177] From the mechanical point of view, PANI and other conjugated polymers are too rigid and cannot withstand mechanical force. Polymers like PVBPT are more stable with respect to chemical degradation and therefore an interesting alternative to conjugated polymers. Generally, during SFM experiments in contact mode the scanned surface suffers from nanowear processes and changes its morphology. In the following section an overview of the nanowear mechanisms especially regarding SFM is presented.

2.3. Nanowear and Scanning Probe Microscopy

Wear describes tribological interaction of the bonding surface with the environment which leads to removal or deformation of the material. Wear processes are of abrasive, corrosive, thermal, surface fatigue, adhesive, fretting and frictional nature.[178] Removal of the material can happen by plowing, delamination, cutting or cavitation. However, in many cases different friction mechanisms add up to give rise to higher surface damage. Characteristic properties of the surface like surface morphology, roughness and composition also contribute to the wear mechanism. Wear processes are critical issues for many industrial applications.[179] Mechanical components show traces of abrasive wear after being used in industrial machines. Especially in microelectromechanical systems where micro engines and actuators are under constant interactions, wear processes on a nanometer scale come into play. Wear processes on the nanometer scale has been studied by various groups.[180- 183] Bhushan et al. examined nanowear for SFM based data storage media.[184] They observed tip wear and sample wear in ferroelectric data storage based on lead zirconate titanate. By depositing surface lubricants like chemically bonded liquid lubricants of perfluoropolyethers, wear resistance of lead zirconate titanate surface was increased. Nanowear mechanisms for polymer surfaces are divided into two different categories depending on the applied force and the elastic modulus of the polymer. In thermoplasts such as PS, formation of regular bundles (also called “ripples”) occurs after several scans. The distance between the bundles depends on the molecular weight of the polymer and the applied force.[187] The bundles in the polymer film are formed due to the stick-slip mechanism of the SFM tip with the sample as described by Leung et al.[185] This means, the accumulated

material stuck to the tip forms hills and the tip slides over them and the process restarts. This nanowear mechanism is known as “rippling wear”. The rippling wear transforms to “pile up wear” (or tear mode) at increasing applied force or above glass transition temperature T_g. In the pile up wear, worn material accumulates at the rims of the scanned area.

The described wear mechanisms destroy the topographic properties of the surface and increase its roughness. Consequently, the lack of the mechanical stability during the writing and reading processes makes it impossible to store data reliably using SFM. One possibility for reducing nanowear is the use of a protection layer. Kaule et al. used plasma-polymerized norbonene to increase the nanowear resistance of PS layers measured with SFM.[186] They observed that the thin and elastic poly norbonene layer has a shielding effect towards lateral forces applied by the SFM tip during the scanning process. Berger et al. showed that nanowear based on SFM experiments is reduced by using crosslinked or grafted polymers.[187] To increase the surface resistance of the material, the polymer architecture plays an important role. PS and PMMA have already found application in thermo mechanical data storage devices based on SFM and therefore possess sufficient mechanical stability for this purpose. Using phenothiazine polymers like PVBPT with PS or PMMA backbone is an alternative method to store data using the electrical mode of the SFM like conductive SFM instead of thermal heating. The conductive SFM has two advantages. On the one hand, the polymer film does not have to be penetrated to store the information like in the case of thermo mechanical data storage. In contact mode, the polymer film is oxidized and therefore is less exposed to mechanical wear. On the other hand, the process is less time consuming, since the heat transfer takes place in μs regime whereas redox processes take place within nanoseconds. The fast redox process allows data transfer rates above 100 Mbit/s.[165] Finally, using small tip radius, the storage density can as well be increased, since the oxidation step takes place on molecular level.

3. Experimental

3.1. Materials and synthesis

The monomer VBPT was synthesized as described in II.4.3.2. The synthesis of the polymer PVBPT via ATRP is described in V.3.3.3. The synthesis of the radical cation polymer was performed according to III.3.2.

3.2. Methods

X-ray diffraction (XRD) patterns from polymer powders were obtained on a Bruker D8 diffractometer with Cu K_α radiation (40 kV, 40 mA, λ = 1.5418 Å).

For the patterning experiments with conductive SFM gold/PVBPT, substrates on glass were prepared by the following procedure: glass slides were cut in 1 cm x 1 cm x 0.1 cm slices, sonicated for 10 minutes subsequently with DCM, acetone, Alconox® and washed with Milli-Q water. Finally, the slices were dried with compressed air and dried at 100 °C in vacuum. The

substrates were coated by thermal evaporation of 3 nm Cr (0.3 Å/s) and 100 nm Au (1.0 Å/s). Afterwards the polymer layer was spin-coated on the gold surface at 1000 rpm for 60 s using a 5 g/L and 10 g/L PVBPT (M_w = 13400 g/mol) solution in dry DCM. The spin-coated substrates were then annealed in a DCM vapor at 50 °C following by annealing in vacuum at 100 °C. The film thickness of PVBPT was determined on bare glass slices using step profiler and X-ray reflectivity.

To perform the conductive SFM measurements on the PVBPT/gold substrates a MultiMode TUNA-TR scanning force microscope (Veeco Instruments, Santa Barbara, CA, USA) with a conductive cantilever (CSC17/Ti-Pt, MikroMasch, Talinn, Estonia, nominal spring constant 0.15 N/m) was used. The writing and reading experiments were carried out under ambient conditions in contact mode. A DC voltage was applied to the sample, while the tip was grounded. The current flow from the sample to the grounded tip was registered. For the writing process, generally a bias of U_W = +10 V on 3 µm with a speed of 0.3 µm/s was applied. To read the written pattern the bias was reversed to U_R = -6 V. Then we zoomed out and imaged with a speed of 5 µm/s while applying the reading bias potential. The base line of the current amplifier at +10 pA was corrected to 0 fA. The wear experiments were carried out on a NanoWizard scanning force probe microscope (JPK, Berlin, Germany) using contact mode cantilevers (NanoWorld, CONT-W, nominal spring constant 0.2 N/m). The exact spring constant for each cantilever was determined by thermal tuning. A surface of 3 µm was scanned 100 times with a load of 10 nN at the speed of 50 µm/s in contact mode. Then the scanned area was mapped in tapping mode to observe changes in the topography. In the second experiment, the latter procedure was repeated applying the minimal force needed to keep the tip in contact with the scanned surface (approximately 5 nN). The offset of the current images (+10 pA) was subtracted prior to processing. Temperature dependent measurements were carried out in a glove bag streamed with nitrogen and a heatable stage.

Kelvin Probe Force Microscopy measurements (KPFM) were performed following the frequency modulation method described by Zerweck et al.[188] The frequency was modulated at 3 kHz with driving amplitude of 3 V. KPFM measurements were done before and after writing on a scan area of 2 µm x 2 µm with a scan speed of 2 µm/s. In order to prevent drift effects, the writing in tapping mode was done at +3 V sample bias on a scan area of 1 µm x 1 µm. The tapping set point was set to 0.1 V in order to have a quasi contact. PPP-EFM cantilevers were used (Nanosensors, Neuchatel, Switzerland, nominal resonance frequency 75 kHz, conductive Pt/Ir coating).

4. Results and Discussion

4.1. Writing

The nanoscale patterning of the PVBPT spin-coated film was achieved by locally oxidizing the phenothiazine moieties using conductive SFM at an adequate writing bias potential (U_W) (Scheme 36a). Thus, the first challenge was to find the necessary V_W. In a subsequent step, the oxidation of the phenothiazine moieties was probed by scanning the oxidized area. The oxidation could then be visualized as changes in local conductivity in the oxidized area. To detect these areas, a reading bias potential (U_R) was applied to the sample while scanning the surface (Scheme 36b). The resulting current map contained information about changes in the local conductivity of the PVBPT surface.

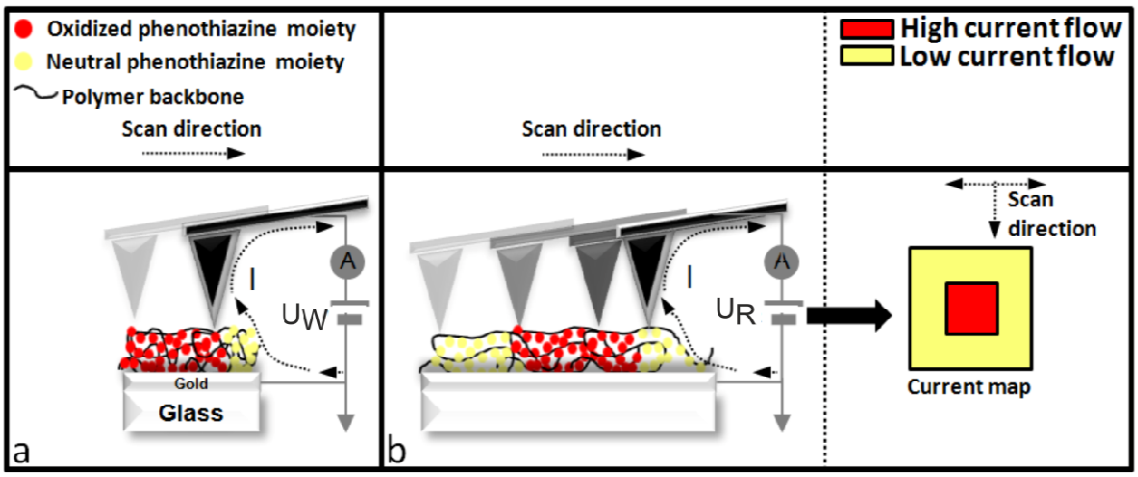

Scheme 36. Schematic overview of the conductive SFM operation in contact mode for gold films coated PVBPT: a) Writing step with the potential U_W, b) Reading step with the potential U_R and the corresponding current map.

In order to locally oxidize PVBPT, spin-coated PVBPT film on gold (acting as an electrode) was scanned in contact mode at a normal force of 5 nN. U_W was increased between the gold electrode and the tip in +2 V steps up to +10 V in areas of 3.0 µm x 0.3 µm starting from 0 V. Each increase in bias potential was separated by approximately 0.2 µm spacing. The spacing was achieved by reducing the bias potential to 0 V while scanning. During this writing procedure, the current was recorded (Figure 25). While applying U_W of +2 V to +4 V, the measured current slightly increased locally. Areas of 30 and 50 nm in diameter, with higher conductivity (above 1 pA) appeared in the current map (see arrows in Figure 25a). The number of these high current areas increased from 3 to 11 spots for an increasing U_W from +2 V to +4 V. Upon increasing U_W to +10 V, an increase of the current flow and the number of the conductive spots was observed (from 11 spots to over 50 spots when V_W was increased from +4 V to +6 V). To get more quantitative data of the local conductivity change, the average profile along the scanning direction of the entire current map was analyzed (Figure 25b). At +2 V and +4 V, the average current increase in the entire written field was too low to be determined. By increasing U_W to +6 V and +8 V, the average current difference increased to 100 ± 50 fA and 420 ± 130 fA. The

average current in the patterned area increased to 710 fA ± 380 fA at +10 V. The current maximum at U_W = +10 V is approximately 1000 fA. The current profile showed a strong lateral variation. The variation was attributed to changes in the contact area of the SFM tip with the sample surface while scanning. The increasing current value and the number of conductive spots obtained from the current map profile suggest that oxidation of the PVBPT film and the desired writing experiment were successful. At increasing U_w, the oxidation degree of the phenothiazine moieties constantly increases. To find out the origin of the conductive spots and the reason for the current increase, the PVBPT surface was scanned again. This time changes in the topography as well as current map were analyzed under applying different bias potentials V_R to read the written patterns.

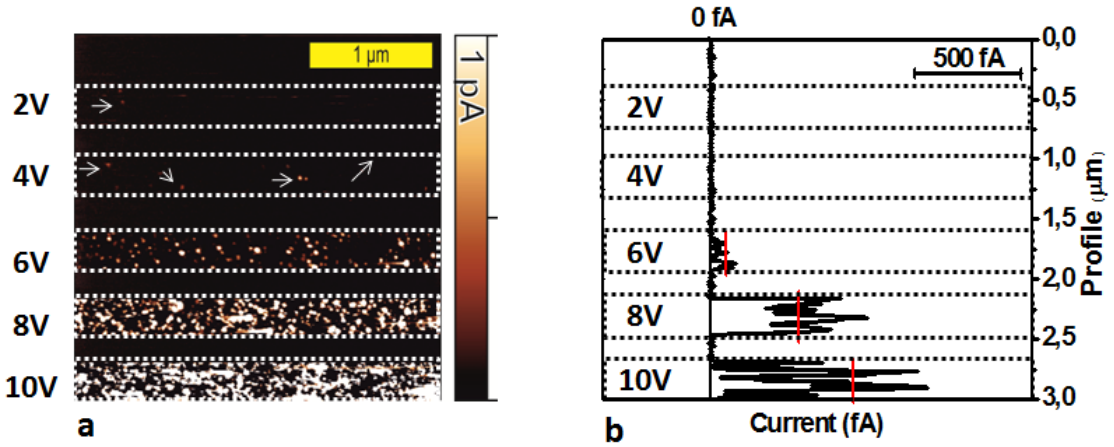

Figure 25. a) Current map of spin-coated PVBPT (45 ± 7 nm thick) on gold at different U_w with spacing between the patterns, b) Corresponding average profile of the current map along the scanning direction. The red line indicates the average current in the region with increased conductivity.

4.2. Reading

4.2.1. Determining the reading bias potential U_R

Local oxidation of the PVBPT should cohere with permanent local conductivity changes. Therefore, the areas previously patterned according to Figure 25 should be imaged at a larger scan size. Before starting the imaging of the patterned areas, the right value for U_R has to be identified. Therefore, a bias potential was applied on 100 spots in one selected patterned area starting from U_R = +4 V up to -6 V. The corresponding current was then detected at different U_R. The area patterned at U_W = +10 V was selected, since according to the writing experiments the most significant changes are expected in this area. For the analysis, the current difference between the patterned and non-patterned area was estimated from the current profiles (appendix, Table T 9). At U_R = +4 V, no significant further oxidation of the polymer should take place as concluded from the measured current flow during the writing procedure. No current difference could be detected for U_R = +4 V to -2 V for the written pattern. At U_R = -3 V, the patterned area became visible in the current map showing a current difference of 20 ± 95 fA

between written and non-written areas. The large error range in the current value is due to parasitic noise of the amplifier, since its current detection limit is approximately 50 fA. The current difference increased from 280 ± 82 fA to 602 ± 23 fA as U_R was increased from -5 V to -6 V. Thus, U_R = -6 V is an appropriate value for reading of the patterned area because at this bias potential the resulting current difference is high enough to be detected. In the next step, the current values obtained from the writing and reading current map were used to elucidate the conduction mechanism in the PVBPT film. Current-voltage analysis is often used in bistable films of RRAM to examine the mechanism of switching.[189- 192] For the current-voltage analysis, the absolute measured current values from the writing image in Figure 25b and from the reading image (appendix, Table T 9) were plotted against the absolute value of the applied bias potential. A linear dependency is obtained in the corresponding logarithmic plot for both writing and reading step (Figure 26).

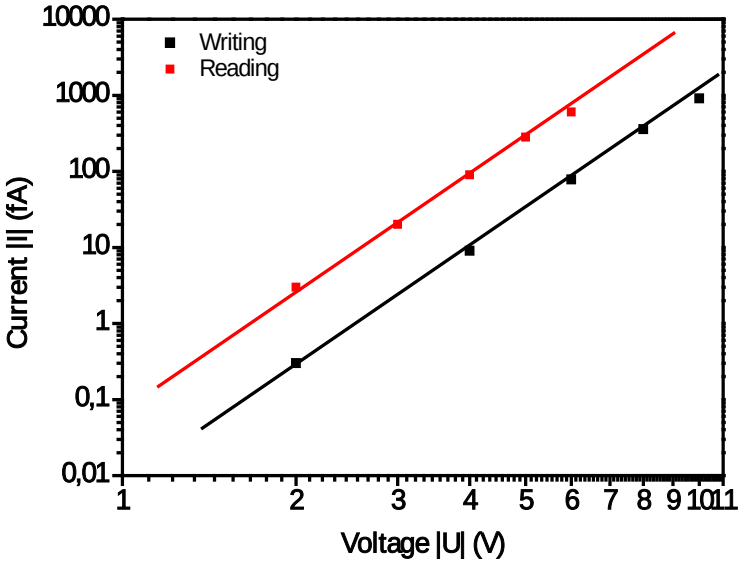

Figure 26. Log-log plot of the average current difference between patterned and non-patterned region against the applied bias potential for the writing and reading step.

The linear behavior of log $|I|$ - log $|U|$ plot indicates that the mechanism of the charge transfer in the polymer film can be described by the space charge limited current theory.[193] Injected charges are accumulated below the SFM tip on the polymer film forming a space charge. Therefore, the total charge injection and the resulting current are limited since the charges repel each other. From the slope of the lines, a characteristic exponent α can be deduced which is related to the energy distribution of the trapped sites. A' represents the static conductance:

$$\log|I| = \alpha \cdot \log|U| + A' \qquad (20)$$

The writing and reading steps have almost the same slope (α = 1.21 ± 0.03 for the writing step and α = 1.20 ± 0.02 for the reading step). Therefore, the energy distribution of the trapped sites must remain constant.[193] However, the increase of A' indicates an increase of the overall

conductance before and after patterning one order of magnitude. Thus, the conductance must have increased due to the oxidation of the polymer film. The increase of the conductance value is related to an increase of the local conductivity. After determining the appropriate reading bias potential U_R and the conduction mechanism, the current and topography map of the patterned areas were visualized in the next step.

4.2.2. Reading the surface current and topography

To examine the local conductivity, the current map of the patterned areas in Figure 25 was scanned while applying a bias potential of U_R = -6 V. At this value the highest current difference was observed according to IV.4.2.1. Therefore, the reading step was performed at U_R = -6 V. At U_R = -6 V, all patterns written at +2 V to +10 V were detected although patterns written at +2 V and +4 V are hardly identified (Figure 27a).

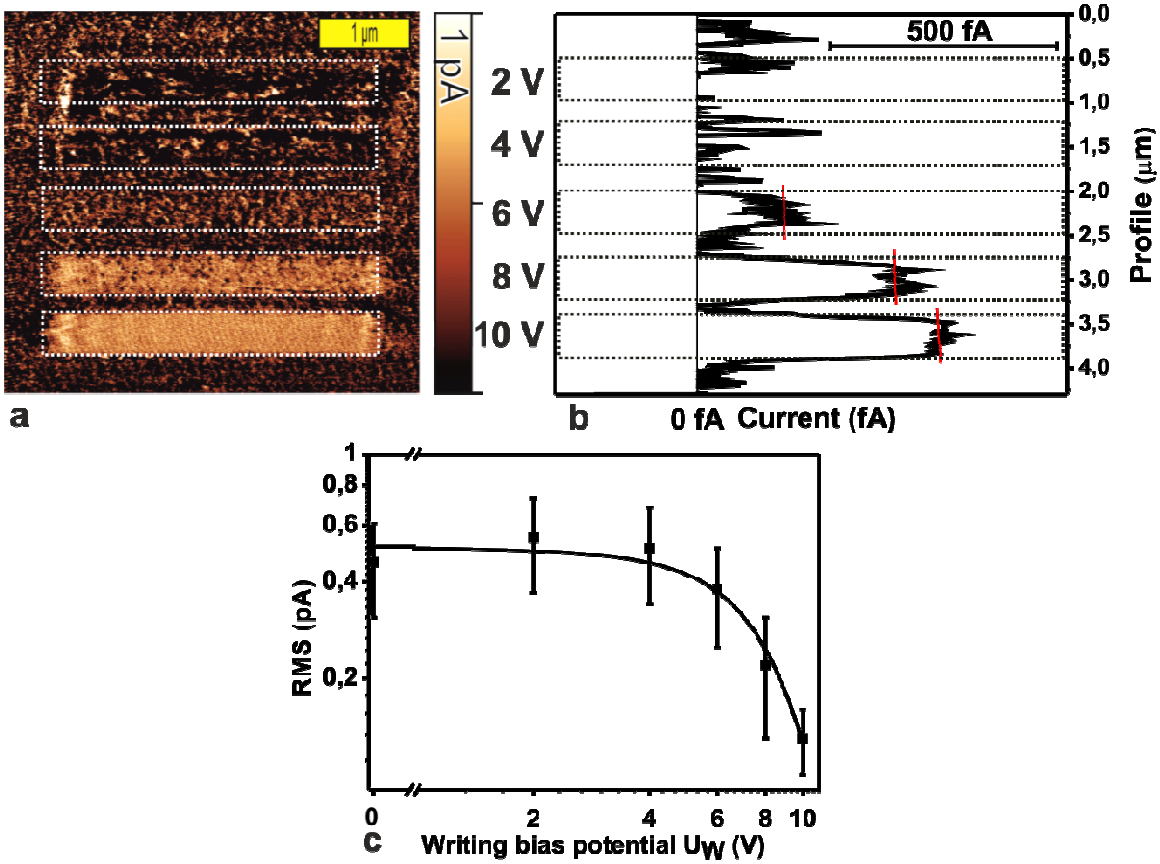

Figure 27. a) Current map of the patterned areas during the reading process at U_R=-6, b) Average profile of the current map along the scanning direction from the white dotted area in figure a. The red line indicates the average current in the region with increased conductivity, c) Logarithmic plot of the RMS value for the current map in the patterned region against the applied writing bias potential U_W.

The areas oxidized at U_W = +6 V, +8 V and +10 V exhibited a higher current flow compared to the non-patterned area. At U_W = +6 V, the current difference between high and low conducting regions along the scan direction was 152 ± 53 fA estimated from the average current profile (Figure 27b). The current difference increased to 432 ± 35 fA when the area was patterned with U_W = +8 V. The current profile showed an increase of around 530 ± 23 fA for the area patterned with U_W = +10 V. From the reading experiments it was concluded that writing bias potentials of

U_W above +4 V are necessary to oxidize PVBPT. There is a threshold value for oxidation potential between U_W = +4 V and +6 V. Above this value the moieties are mostly oxidized which results in an increase of the current. Furthermore, the variation of the current value in the patterned area decreases. This variation of current is visible around the average current profile in Figure 27b and decreases with increasing U_W. To quantify the current variation, the root mean square (RMS) of the patterned and no-patterned areas in the current map of Figure 27a was determined. From the plot of U_W against the RMS of the measured current in the patterned areas, the threshold value for the writing process was estimated. The plot showed a decrease of the RMS current value from 0.46 ± 0.15 pA to 0.13 ± 0.03 pA for the non-patterned and with U_W = +10 V patterned region, respectively (Figure 27c). The decrease of the RMS current value above U_W = +4 V below 0.4 pA indicates that the current signal became laterally more homogeneous when the applied U_W was increased. It was concluded from the decrease in the RMS current that more conductive pathways are formed when U_W is increased. This result corresponds with the results reported for PVMPT.[85] After oxidizing a few phenothiazine moieties, the conductivity of the PVMPT is increased when the threshold value for the oxidation process is reached.

Apart from the conductivity, one important aspect for SFM based data storage application is the surface topography. In addition to the current map, the corresponding topographic information to Figure 27a was obtained during the reading step. It is noteworthy that the corresponding topography image after writing only revealed a slight increase in height and surface roughness (Figure 28a and b). To quantify the increase in surface roughness, RMS of the topography was calculated in the patterned and non-patterned areas (Figure 28c). The RMS of the topography almost remained constant in the scanned area. In the area patterned with U_W = +2 V and +8 V, the RMS roughness was 0.79 and 0.8 nm. For the area patterned with U_W = +10 V, the RMS of the topography map increased from 0.79 nm to 1.01 nm (Figure 28c). The increase in height is at the limit of the SFM resolution and is in the order of 170 ± 130 pm for the area patterned with +10 V (corresponding to less than 1% increase) (Figure 28b). An increase of several nanometers in height for the topography of thin polymer films in conductive SFM experiments has already been reported by several groups.[194-197] For polymers such as PTMA [198] and poly[2-(N-carbazolyl)ethyl methacrylate-co-methacrylic acid] (PCEMMA)[197] an increase of the topography up to 7 nm (corresponding to approximately 12% increase) and 15 nm (corresponding to approximately 38% increase) was reported. The height increase in thin films PMMA, PCEMMA and PTMA deposited on gold has so far been explained by water based ionic drift mechanisms.[195] Joule heating leads to an increase of the segmental motion in the polymer chain and the drift of the dissociated ions in the water meniscus leads to the formation of conical shaped structures.[195]

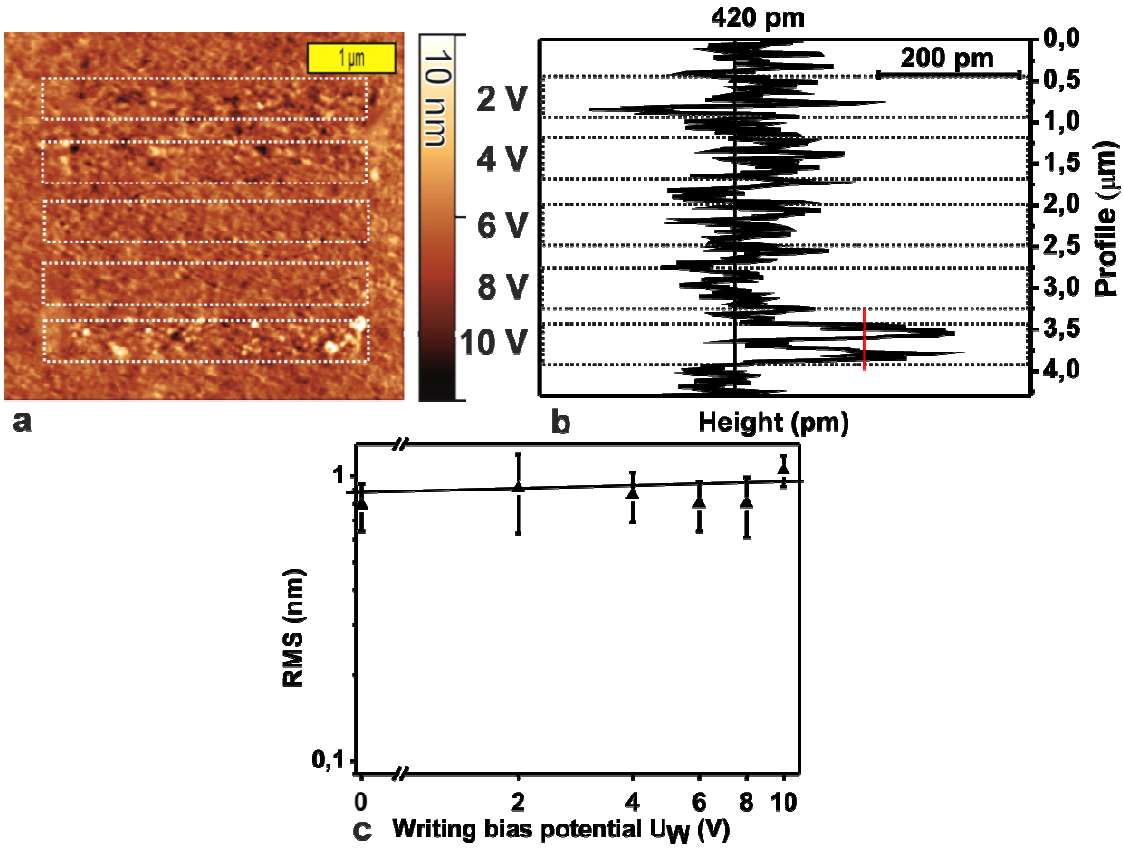

Figure 28 a) Topography image of the patterned area during the reading process at U_R=-6 V. b) Average profile of the topography along the scanning direction from the white dotted area in figure a, c) Logarithmic plot of the RMS roughness value for the topography map in the patterned region against the applied writing bias potential U_W.

These processes seem to play only a minor role for the PVBPT studied here and indicate a mechanically more stable film. However, the water meniscus between the tip and the sample plays an important role for the oxidation process. So far, the patterning of the PVBPT film was successfully demonstrated. Above the oxidation potential of U_W = +4 V, patterns are formed on the surface of the PVBPT film. At U_W = +10 V, clearly distinguishable patterns were written and detected at reading bias potential of U_R = -6 V. Therefore, the upcoming experiments were conducted with the latter writing and reading bias potentials. In further experiments, the goal was to find out the efficiency of the patterning process. The efficiency of the patterning depends on how fast the oxidation takes place on the PVBPT film. If the oxidation process is efficient enough, PVBPT film is oxidized quantitatively allowing clear distinction of the patterned and non-patterned regions with high resolution. In the following experiment, the oxidation speed was measured with SFM by variation of the scan speed during the writing experiments.

4.2.3. Effect of writing speed and humidity

The effect of the writing speed on the patterning efficiency of a PVBPT was examined on a spin-coated film with a thickness of 30 ± 5 nm (Figure 29). The highest current difference between the patterned and non-patterned area was obtained at the slowest scan speed of 0.3 µm/s, while the current difference at 15.0 µm/s was hardly visible (Figure 29a). Areas

patterned at scan speeds between 0.6 µm/s and 6 µm/s can be well distinguished. However, the pattern became less pronounced as the scan speed was increased. Figure 29b shows a logarithmic plot of the average current difference for the patterned and non-patterned areas at different scan speeds. This plot clarifies the optimal scan speeds to obtain best patterning results. The average current difference in the sigmoid shaped plot increases and reaches its saturation point with decreasing scanning speed. At this point, the current difference does not change significantly when the writing speed is reduced from 0.6 to 0.3 µm/s (from 2.45 ± 0.28 pA to 2.42 ± 0.19 pA). Even between 1.5 and 3.0 µm/s a current difference of around 1.50 ± 0.33 to 1.9 ± 0.32 pA was detected. Above 6.0 µm/s the current difference decreases below 0.91 ± 0.17 pA. Between 6.0 and 15 µm/s the decrease in current difference did not change significantly (ΔI = 0.16 ± 0.11 pA). On the one hand, it was concluded that the slower the scan speed, the more PVBPT moieties are oxidized. On the other hand, a writing speed below 1 µm/s did not significantly increase the patterning efficiency. The best patterning result is obtained at scan speeds between 1.5 and 0.6 µm/s. At this scan speed, electron transfer occurs more efficiently which then increases the conductivity of PVBPT. When all redox sites are oxidized the maximum of the conductivity is reached and no further increase can take place.

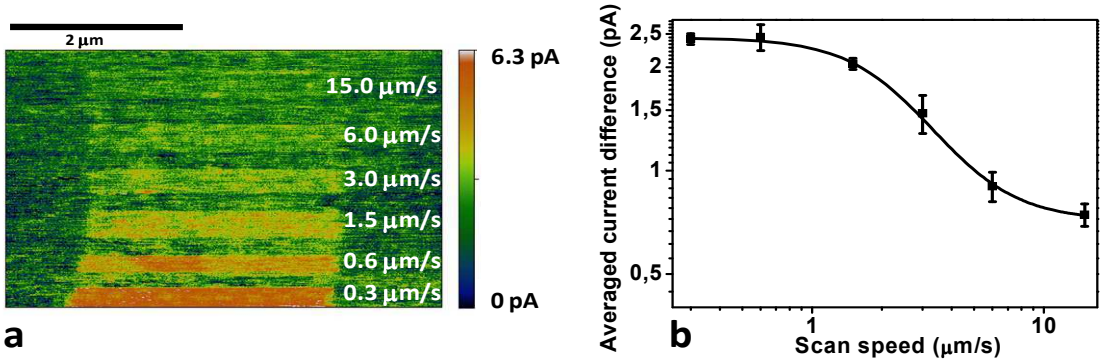

Figure 29. a) Current map of spin-coated PVBPT (Thickness: 30 ± 5 nm) on gold patterned with +10 V at different scanning speed on 3 µm x 0.3 µm. The patterns have an additional spacing of 160 nm. The reading was done by applying -6 V after zoom out at the speed of 5 µm/s, b) Logarithmic plot showing the dependency of current difference for the patterned and non-patterned areas by variation of the scanning speed.

Except for the scan speed, other parameters such as tip radius and geometry, humidity, surface roughness and film thickness contribute as well to the efficiency of the patterning experiments. At decreasing film thicknesses, the current difference in the patterned area increases due to the lower film resistance. Decreasing the film thickness from 45 ± 7 nm to 30 ± 5 nm led to an increase of the average current difference from 530 ± 23 fA to 2420 ± 190 fA at a writing speed of 0.3 µm/s and U_W = +10 V. Using a polymer film thickness of 110 ± 9 nm, no oxidation patterns were formed at all due to the high resistance of the film. Therefore, thin polymer films of PVBPT with thicknesses below 30 nm are adequate for patterning experiments.

An important parameter for the efficiency of the patterning experiment is humidity. The water of the surrounding humidity forms a meniscus between the tip and the sample which

contains small amount of dissolved ions. The water meniscus is the electrolyte which is necessary to perform the redox chemistry on PVBPT films. To examine the role of the water meniscus, patterning experiments at different temperatures were carried out. Three patterns were written and read at 25 °C and 90 °C and after cooling to 25 °C using a heatable stage in a glove bag streamed with nitrogen to control the humidity. At ambient temperature, a pattern was observed in the current map with an average increase of the current of 510 ± 65 fA (Figure 30b). In contrast, the pattern written was not visible after heating the sample to at 90 °C showing a current increase of below 50 ± 81 fA (Figure 30d). After cooling down the sample, the patterning was repeated successfully under controlled ambient conditions again revealing a current increase of 520 ± 77 fA (Figure 30f). No significant change in topography was observed during the patterning experiments (Figure 30a, c and d). Thus, when the amount of water on the polymer surface was reduced by heating to 90 °C, no oxidation pattern at the surface was observed.

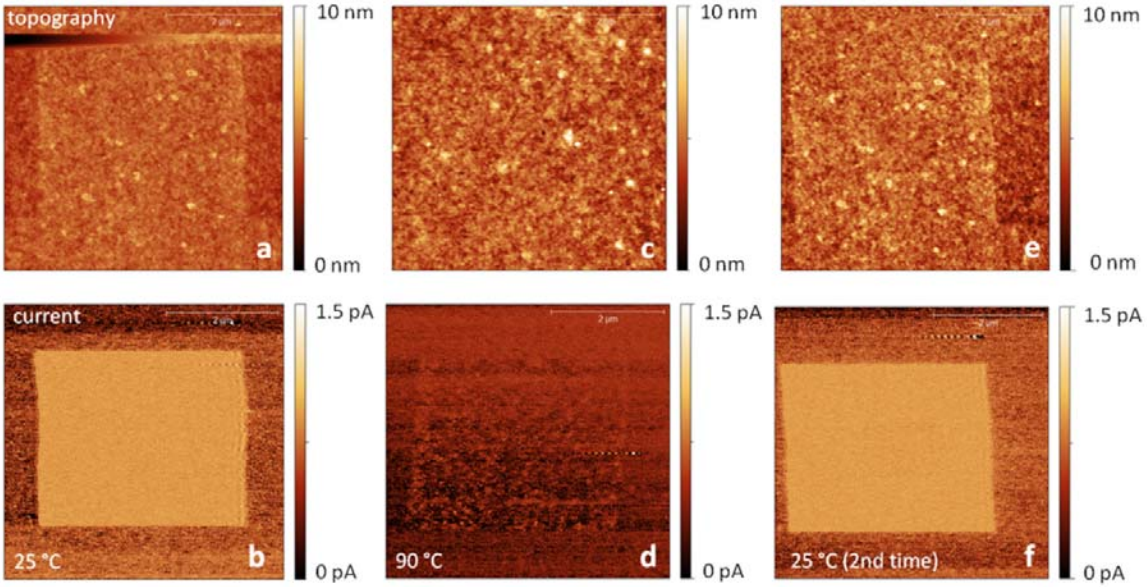

Figure 30. a) Topography map of patterned area at T=25 °C, c) after heating at T=90°C and e) after recooling to T=25 °C, b) Corresponding current map at T=25 °C, d) after heating at T=90°C and f) after recooling to T=25 °C.

Thus, the experiment proved that the water meniscus serves as an electrolyte and is necessary for charge compensation and oxidation process in the PVBPT films. Furthermore, the experiment confirmed that patterning of PVBPT is an electrochemical process. The changes in current observed in the SFM experiments result from the oxidation of the phenothiazine moieties and their reorganization. A further proof for the oxidation process was obtained from KPFM studies. If the oxidation takes place, a net positive charge should be formed on the surface of the PVBPT film because of the formation of the cation species. In these studies, the oxidized areas revealed a net positive surface potential of around +50 mV (appendix, Figure A 11). After the writing in contact mode, a square shaped pattern with potential increase of +54 mV was observed in the KPFM image (appendix, Figure A 11b). This indicates that a positive net charge at the surface of PVBPT must have formed. The positive net charge can only result from the

formation of the radical cation species of PVBPT. Thus, the KPFM experiment gives a further proof for the oxidation of PVBPT during the patterning process.

Nevertheless, the oxidation potential values for the SFM patterning experiments are much higher in comparison to the electrochemical results obtained by CV experiments. The CV data revealed an oxidation potential of 860 mV for PVBPT. For spin-coated films a writing potential of minimum U_W =+4 V was required in the SFM patterning experiments. Increased bias potentials for the SFM patterning experiments were reported for different systems.[172,198] For TEMPO based polymers similar writing and reading magnitudes for conductive SFM experiments were reported.[198] Even for a simple electrochemical oxidation of p-type semiconducting NiO films deposited on platinum, U_W of +7 V was necessary to incorporate oxygen inside the surface. One possible explanation for the high writing potentials is the high electrical resistance at the interface of the tip and the sample. The tip-sample resistance is much higher compared to the intrinsic sample resistance and additional resistances, which are situated in series. Assuming this, a significant drop in potential is expected at the tip-sample interface. Then, the potential drop within the polymer layer is significantly smaller being a factor of ≈ 5-10 for PVBPT. This factor corresponds to an on/off ratio of approximately 5 to 10, which is low compared to existing materials in the data storage field.[154] In conclusion, PVBPT spin-coated films were successfully patterned at U_W < +4 V and the written patterns were identified at U_R = -6 V without influencing the surface topography. The conduction mechanism of the writing and reading step was described by the space-charge limited current theory. The ideal writing speed was determined between 0.5 and 1.5 µm/s and the formation of the oxidized species was proved by KPFM and under humidity controlled SFM patterning experiments. In the next section, the reduction process of oxidized PVBPT was studied. By applying an adequate erasing bias potential , the written patterns should be erased for reversible data storage applications.

4.3. Erasing

PVBPT spin-coated films can be oxidized and reduced reversibly according to the CV data obtained in III.2.4.1, Figure 12. The same electrochemical reversible behavior is expected for PVBPT oxidized via conductive SFM. The oxidation of the PVBPT film with conductive SFM at a defined positive bias potential U_W led to the formation of patterns with an increase in conductivity according to the current map. The same procedure with a negative bias potential should erase the written pattern, when the reduction potential is reached. As a consequence, the local change in conductivity is restored to its original value and detected by a successive scan in the current map. The best method to investigate the erasing of PVBPT is to write a large pattern on the surface as described in IV.4.1. Then, in the center of the patterned area a reversed erase bias potential (U_E) is applied to the SFM tip in order to reduce PVBPT and erase the written pattern partially (Scheme 37a). The deleted part is detected as an overview image and read with U_R as shown in IV.4.2.2. (Scheme 37b).

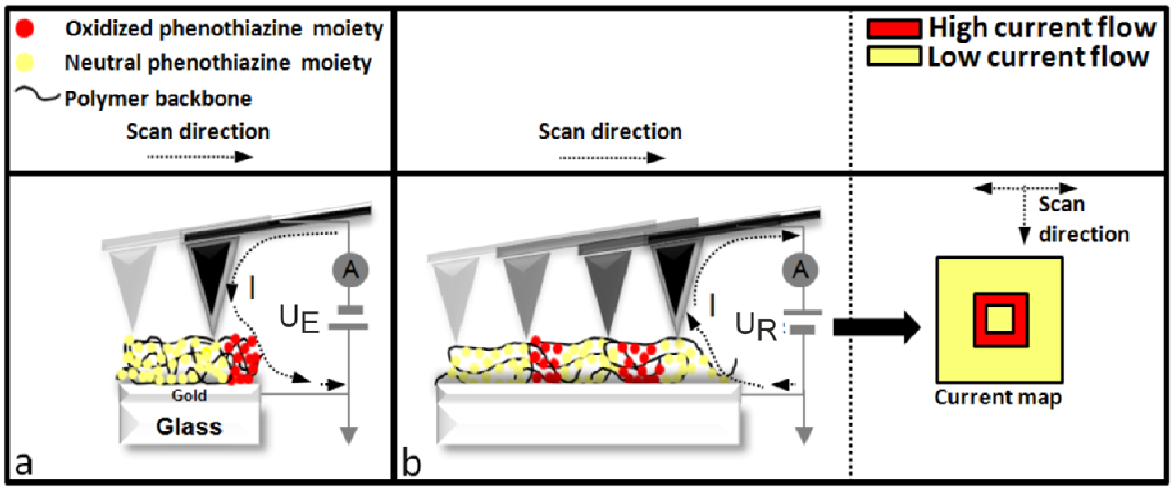

Scheme 37. Schematic overview of the conductive SFM in contact mode for gold films coated with PVBPT. a) Erasing step with the reversed bias potential U_E and b) reading step again with the bias potential U_R to detect erased and written areas after zoom out.

In the experiment, a single pattern was written at U_W = +10 V. Then, the written pattern was read at U_R = -6 V to prove the successful patterning (Figure 31a). The patterning resulted in an area with a size of 4.0 µm x 2.2 µm. The average current of the patterned area was 1081 ± 83 fA higher than the non-patterned area according to the average current profile. Quantitative data of the current maps were received from the histograms. In the current histograms, the pixels in the corresponding SFM image with defined current are analyzed. Pixels with a specific current are plotted as counts by their statistical occurrence at the current value. This way, shifts in current can be better quantified for example as statistical Gaussian distribution.

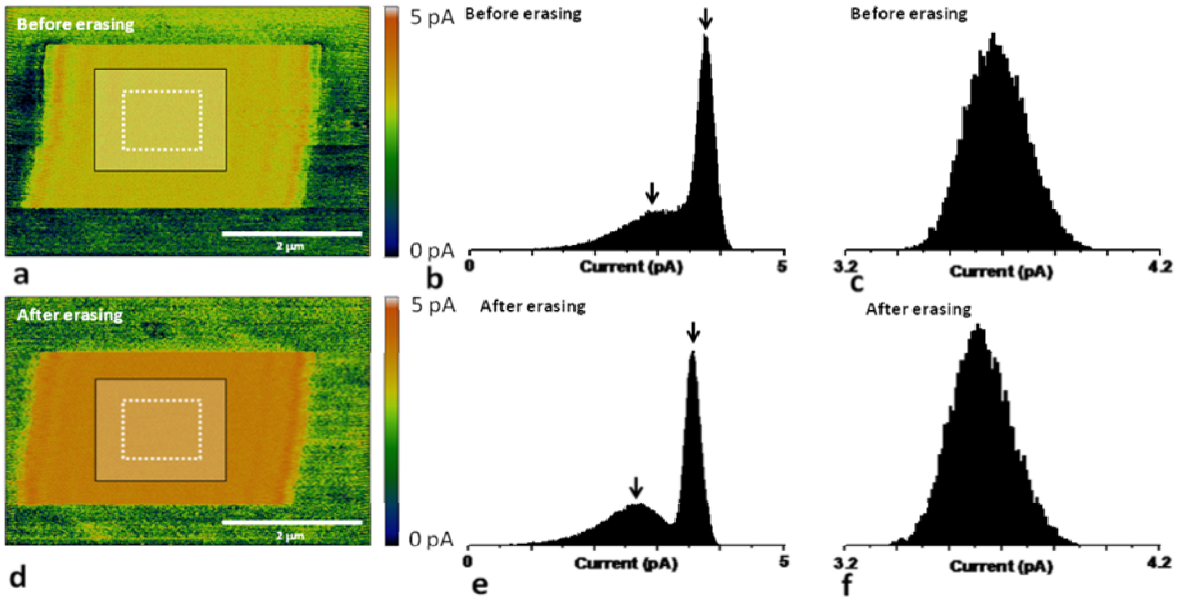

Figure 31. a) Current map of spin-coated PVBPT on gold patterned with U_W = +10 V on 4.0 µm x 2.2 µm at the speed of 0.3 µm/s before and d) after erasing. To erase the pattern partially, U_E = -12 V was applied on a region of 1.0 µm x 0.9 µm at the speed of 0.1 µm/s (whitely dashed line), b) Current histograms of the entire current map as shown in figure a and figure d before and e) after erasing. Left arrow shows the position of the current maximum in the non-patterned region whereas the right arrow identifies the current maximum of the patterned region, c) Current histograms of the area in the region marked with a black line around the erased area before and f) after erasing.

The first analysis was a histogram of the patterned image as shown in Figure 31a over the entire current map. Current histograms clearly showed the formation of the oxidized region (Figure 31b) in a bimodal distribution. The left arrow indicates the position of the current maximum in the non-patterned region whereas the right arrow identifies the current maximum of the patterned region with a current difference of 875 ± 121 fA. The value is in good accordance with the average current profile obtained from Figure 31a (1081 ± 83 fA). After successful patterning, partial erasing of the written pattern was investigated. Therefore, U_E = -12 V was applied on a small area of 1 µm x 0.9 µm in the center of the patterned area (Figure 31d, whitely marked area). To ensure the deleting process, the selected U_E was set to the maximum possible bias potential of the SFM setup. With the U_E smaller than U_R and U_W, no reading and writing process should occur. This procedure was repeated 3 times. The entire area was read at applying U_R = -6 V afterwards. However, no sign of deleting was observed in the current map (Figure 31d). The expected decrease of the current in the deleted area did not occur. A bimodal distribution of the current histogram revealed the existence of the patterned and non-patterned region in the entire image (Figure 31e). The absolute current value was shifted 186 ± 47 fA to negative direction. The relative shift of the peaks corresponding to the patterned and non-patterned area remained almost unchanged with 877 ± 102 fA. The statistics of the peak distribution was improved which leads to clear separation in the bimodal distribution. Current histogram with the size of 2.0 µm x 1.6 µm covering the area scanned at U_E = -12 V were prepared to study the effect before and after deleting (Figure 31c and f). In the case of a successful deleting process, a bimodal distribution is expected after scanning with U_E = -12 V due to reduction of the polymer and the subsequent decrease of the current signal. Expect for an absolute current shift of 168 ± 37 fA to negative currents after the deleting step (Figure 31f), no change in the shape and distribution of the current histogram was visible. The absolute current shift could be related to changes in electrostatic charge up of the SFM setup which decreases during the measurement. The decrease of the charge up also results in better signal to noise ratio and better resolution due to enhanced statistics.

Nevertheless, erasing the written pattern could not be achieved with an erasing bias potential of U_E = -12 V. Hyakutake et al.[199] investigated the patterning of PTMA films on gold via electrochemical oxidation with conductive SFM and reported a similar observation. They did not observe the reversible oxidation of the PTMA although the redox step should be reversible according to the CV measurements.[111] In case of PVMPT, it was observed that thin films of the oxidized polymer retain their high conductivity, even after they have been reduced.[87] In case of PVBPT film, a similar explanation for the remaining conductivity after partial reduction is assumed. The insensitivity of the conductance upon reduction could be explained by the molecular orientation of the phenothiazine units. After oxidation the phenothiazine rings become planar, which facilitates intermolecular interactions in a π-stacked rearrangement.[200] To prove the formation of π-stacked rings in PVBPT films due to redox chemistry, PVBPT in neutral and oxidized form were studied by XRD (Figure 32). When π-stacked structures are available,

XRD diffraction peaks are observed due to the presence of crystalline domains. From the diffraction angle Θ of the crystalline domain and the wavelength λ in the XRD experiment, the distance d_π between the π-stacked structures was estimated from by the following equation:

$$d_\pi = \frac{\lambda}{2 \cdot \sin(2\theta)} \tag{21}$$

In the XRD experiment, the neutral PVBPT showed two broad peaks at the diffraction angle 2 Θ= 12.53° (7.06 Å) and 19.89° (4.46 Å), which were related to the formation of the side stacking (bridging of the benzene rings)[133] and π-π-stacking of the bent phenothiazine rings[201] respectively (Figure 32a, black curve and Figure 32b, structure 1 and 2).

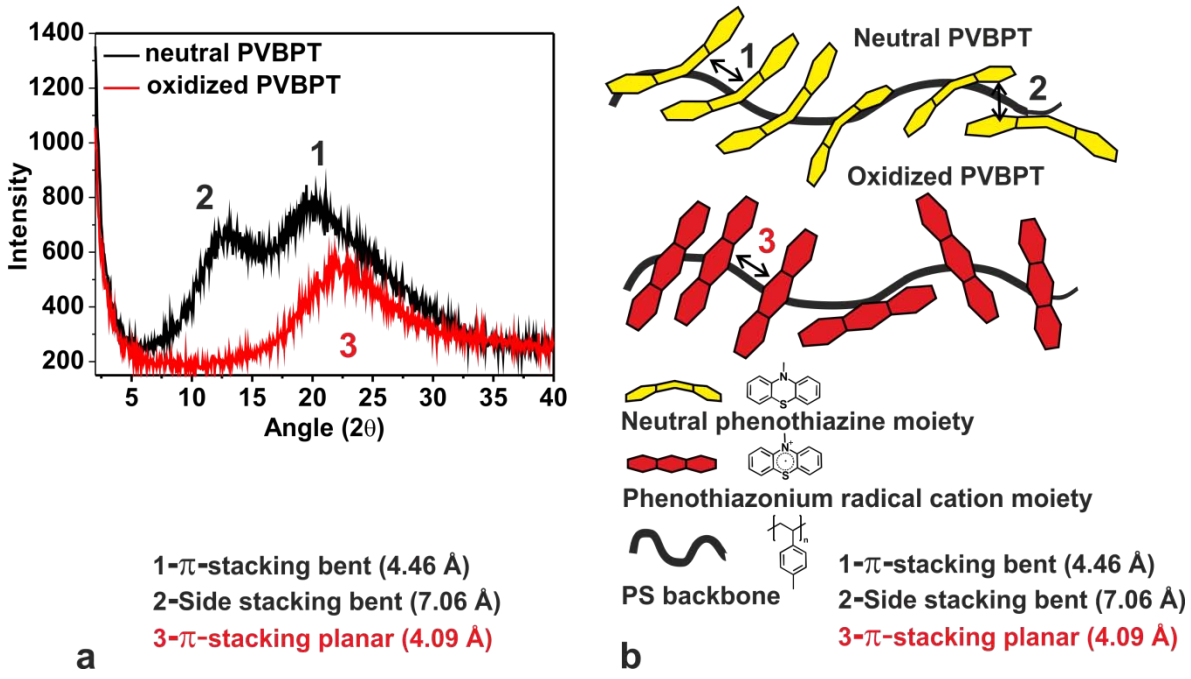

Figure 32. a) XRD data of neutral PVBPT and the oxidized form PVBPT$^{\bullet+}$BF$_4$ as powder. The peak positions are assigned to the formation of π-stacking (1) and side stacking (2) of the bent phenothiazine moieties for the neutral state and to the formation of π-stacking of the planar phenothiazine moieties in the oxidized state (3), b) Schematic overview of the PVBPT in the neutral and oxidized state indicating the stacking possibilities according to the XRD data.

In the oxidized state (PVBPT$^{\bullet+}$ BF_4^-), the planar rings can form π-stacked structures which resulted in a single broad peak at 2Θ = 21.75 ° (4.09 Å). The phenothiazine units are only rearranged in the π-stacked order when the side chains are oxidized (Figure 32a, red curve and Figure 32b, structure 3). Once the planar rings are rearranged in the π-stacked structure, they can hardly be separated throughout the entire polymer matrix. Besides, the segmental motion of the bulky moieties in the amorphous polymer matrix is restricted. Therefore, the side chains can only be reduced partially and not throughout the entire polymer film. The remaining oxidized moieties can still maintain a conducting state. This explanation corresponds well with the estimation of the writing threshold (Figure 27c). When the threshold oxidation potential is

reached, rearrangements are induced and the local conductivity in the patterned area increases. It is assumed that especially for PVBPT, the bulky moieties are hindered to interact with each other, since they have to rotate within the polymer matrix in the proper juxtaposition. After the oxidation, the original state can therefore not be restored applying a tip sample bias potential of U_E = -12 V. Thus, the conductive state is maintained. In conclusion, after patterning the surface of a PVBPT spin-coated film at a positive bias potential U_W, the written pattern could not be erased by application of a negative reversed bias potential U_E. The irreversibility of the patterning process is most probably caused by the organization of the phenothiazine moieties which cannot be reversed throughout the entire film. This result suggests that PVBPT is probably an adequate material for a WORM device. Once the data is written, the information is stored reliably and can be accessed several times. The application as a WORM device requires long-term stability of the stored information. Therefore, in the next section the storage stability is tested with conductive SFM.

4.4. Long-term stability

In order to check long-term stability of the oxidized state, three structures with an area of 3.5 µm x 0.20 µm were patterned at U_W =+6 V, +8 V and +10 V. Then, the structures were scanned at U_R = -6 V in a larger scan area. The first reading scan was conducted directly after the writing process (Figure 33a, first scan).

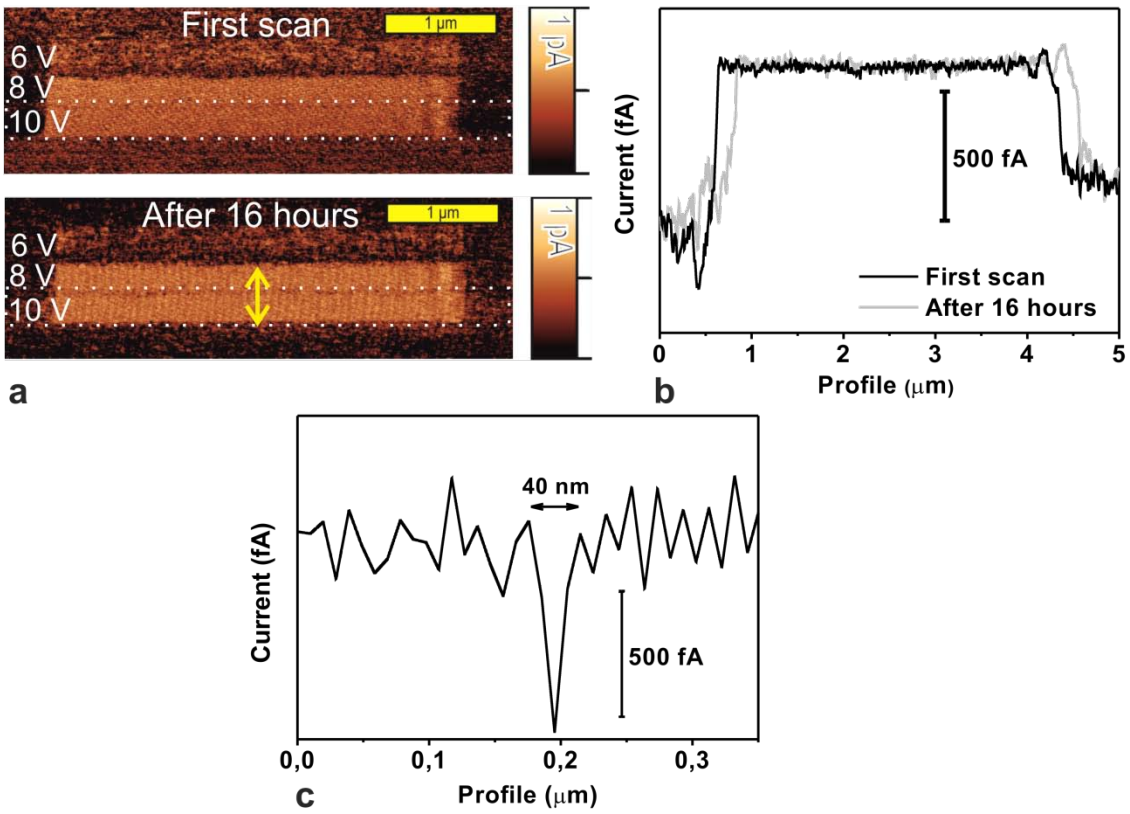

Figure 33. a) First reading image of the current map of spin-coated PVBPT on gold at different applied voltages. Second reading image of the current map after 16 hours, b) Average current profile of the white dotted area perpendicular to the scanning direction for the area patterned with U_W = +10 V, c) Average current profile across the yellow double sided arrow for the current image after 16 hours.

In agreement with the previous measurements, an increase in the current was detected. After the first reading scan on the patterned structures, the tip was retracted from the surface. Then, 16 hours later the tip was engaged again towards the surface and the current map was recorded at U_R = -6 V. After 16 hours all three written structures were still clearly visible (Figure 33a, after 16 hours). The current profile over the marked area patterned with U_W = +10 V showed a current difference of 583 ± 62 fA at the first scan and of 575 ± 84 fA after 16 hours, respectively (Figure 33b). This result confirms that the patterned areas remain stable for at least 16 hours. Furthermore, the average current profile was determined perpendicular to the scanning direction (Figure 33a, yellow double sided arrow in the current map after 16 hours). The resulting current profile (Figure 33c) was used to estimate the maximum achievable storage density using conductive SFM technique and PVBPT as storage media. A minimum spacing of 40 nm between the patterns could still be detected between the pattern written at U_W = +8 V and +10 V. Assuming a minimum bit dimension of 40 nm x 40 nm from the spacing distance and taking additional 40 nm spacing between the individual bits into account, every bit requires an area of 6400 nm^2. The maximum achievable storage density would be approximately 100 $Gbit/inch^2$. This value is only one order of magnitude smaller than storage densities achieved for IBM's Millipede storage device.[162,163] Under assumption of the optimal writing speed being approximately 1 μm/s according to IV.4.2.3, the maximum storage speed for PVBPT as storage device can also be estimated. If the writing speed in both directions is the same, an optimal writing speed of 1 $\mu m^2/s$ is obtained. From the bit size of 6400 nm^2 and by usage of up to 4000 writing SFM tips (as used for the Millipede)[202], a theoretical storage speed of 625 kbit/s is possible. In comparison, data transfer rates of 20 to 30 Mbit/s[203] can be expected for the Millipede system being approximately 50 times higher than the storage on PVBPT. In conclusion, patterns written with conductive SFM on PVBPT films remained stable over at least 16 hours. The good storage stability was related to the formation of the stable radical cation state. The radical cation is formed by oxidation of PVBPT film during the patterning which leads to an increase of the conductivity in the current map. The stability of the conducting state according to the conductive SFM long-term stability experiments well agrees with the data obtained from ESR measurements for $PVBPT^{\bullet+}BF_4^-$ in III.4.3. Thus, PVBPT is an appropriate polymer for long-term data storage via conductive SFM and regarding the storage density and speed. The final aspect for SFM based data storage is the study of mechanical stability. Polymer materials used for SFM based storage systems have to exhibit sufficient nanowear stability to maintain the stored information. In the next section, the mechanical stability of PVBPT films was examined by SFM nanowear experiments.

4.5. Mechanical stability

To perform the nanowear experiment on PVBPT films, a defined area was scanned 100 times in contact mode at a defined normal load. To analyze the resulting nanowear, the topography image of the polymer surface was compared before and after the nanowear experiment. Then, for quantitative analysis, the RMS surface roughness of the topography map was determined in

the scanned area. According to the nanowear experiment, scanning at the minimum normal load for the contact mode (≈5 nN) led to a negligible surface nanowear. An increase of the RMS roughness from 0.49 to 0.50 nm was observed which confirms the good mechanical stability of PVBPT films (Figure 34a). It is also noteworthy that spin-coated PVBPT films have a smooth surface topography with RMS values below 1 nm. The smooth surface topography is a further advantage for SFM data storage. Writing and reading on smooth surfaces reduces the operation errors and improves the storage quality. Increasing the normal load to 10 nN while repeating the scanning process for 100 times caused visible surface wear. The RMS roughness value increased from 0.46 to 0.85 nm (Figure 34b). This increase is lower compared to spin-coated PS films. For spin-coated PS films with a molecular weight of 111 kg/mol, an increase of the RMS surface roughness from 0.4 to 2.2 nm was reported.[187] The SFM image showed that aggregation occurs after repeated scans, leading to globular structures typical for surface wear of polymers.[204]

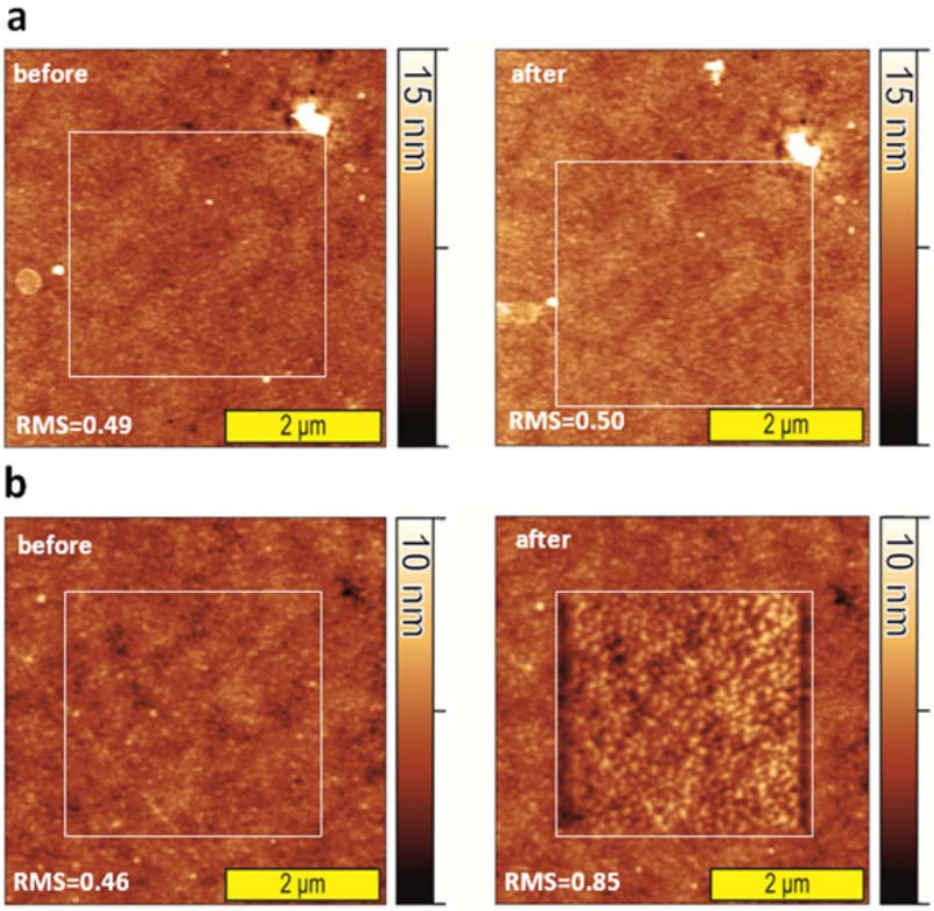

Figure 34. a) Surface wear test performed on a spin-coated PVBPT film. A scan of 5 nN load at a speed of 50 µm/s in contact mode was performed 100 times on 3x3 µm² (marked with a white rectangle), b) The same surface wear experiment as described in (a) was repeated with 10 nN load.

In conclusion, operating the SFM in contact mode at 5 nN load allows scanning the surface of the PVBPT film more than 100 times without the risk of damaging the polymer surface. Mechanical loads higher than 5 nN lead to changes of the surface topography. A load of approximately 5 nN is sufficient to keep the SFM tip attached to the surface during the writing and reading experiment. However, higher loads are desirable to guarantee a reliable writing and

reading process without risking the detachment of the tip. The detachment could lead to loss of information as well as writing and reading errors. Therefore, the mechanical stability of PVBPT films should be further improved for application as data storage medium.

5. Summary and conclusion

Spin-coated PVBPT films on a gold surface were successfully patterned with conductive SFM. Patterns with increased conductivity were written by electrochemical oxidation of the polymer at a positive writing bias potential over +4 V. These written patterns were identified in the SFM current image by using an adequate negative reading bias potential of -6 V. Space-charge limited current theory was deduced from the patterning experiments for the increase of conductivity during the writing and reading process. The patterning experiments could be repeated at different scan speeds and a scan speed of 1 µm/s in average was identified as the optimal scan speed for patterning PVBPT films. Furthermore, it was proven that the patterning is only possible due to the oxidation of PVBPT. In this context, the role of water as electrolyte was demonstrated. Deleting the written patterns was not successful. The irreversibility of the oxidation step was explained by the organization of the phenothiazine moieties in a π-π-stacking conformation as shown by XRD measurements. Especially in planarized rings of the oxidized radical cation, the π-π-stacking is energetically preferred and hinders the reduction process.

Remarkably, the written pattern remained stable over more than 16 hours without any significant loss in conductivity. This result confirmed the long-term thermal storage stability of the radical species according to the ESR measurements. Furthermore, the PVBPT films exhibited increased nanowear stability compared to spin-coated PS films. The topographic stability of PVBPT is an important factor for data storage application via SFM. Except for the good long-term storage and mechanical stability, PVBPT exhibited a good performance with respect to storage density and speed. The storage density of 100 Gbit/inch^2 and the storage speed of 625 kbit/s are in good agreement with the existing storage device systems. The on/off ratio of the polymer film was approximately 5 to 10, which is low compared to the existing polymeric materials such as polyimides.[205] The low on/off ratio is due to the minor molecular order within the polymer film. But even with the low on/off ratio, writing and reading of worked well and allowed clear distinction of the written pattern from the background noise. In conclusion, polymers with phenothiazine containing moieties like PVBPT are promising candidates for nanoscale data storage with SFM techniques. Especially as WORM devices, bits of information could be stored and used for archiving data reliably. Certain improvements are necessary to increase the performance of the storage medium PVBPT.

For enhancement of the device performance, an increase of the order in the polymer structure is necessary. Higher order can be achieved by synthesizing more defined polymer architecture such as grafted polymer brushes. Alternatively, the crystallinity of the polymer can be increased by molecular design of new phenothiazine monomers which facilitate π-π-interaction. By increasing the order in the polymer film, phenothiazine moieties can better

interact with each other via the proper juxtaposition of the moieties. Another aspect of improvement is the mechanical stability. To further increase the nanowear resistance of the polymer film, crosslinking and grafting are useful approaches. Especially with the help of grafting techniques it is possible to individually design the polymer architecture and increase the polymer order. Surface initiated ATRP as an example for a grafting technique allows the synthesis of grafted polymer brushes which possess increased mechanical stability compared to spin-coated films. By introducing cross-linkable monomers, the surface nanowear resistance can be further improved. ATRP approach offers methods to obtain nanowear resistant polymer surfaces for SFM based data storage. Therefore, in the next chapter, new synthetic approaches to grafted redox active polymer brushes are introduced and discussed.

V. Redox active polymer brushes

Parts of the chapter were published in:

A. A. Golriz, T. Kaule, M. B. Untch, K. P. Kolman, R. Berger, J. S. Gutmann, *Appl. Mater. Interfaces;* **2013**, DOI: 10.1021/am302869d.

1. Introduction and motivation

Redox active polymers in many cases face problems of incompatibility with inorganic substrates during processing due to their organic nature. In some cases, spin-cast processes lead to a dewetting behavior of the polymer film.[206] The dewetting often results in the formation of agglomerates and therefore in rough surfaces.[207] To prevent dewetting and increase the homogeneity of the polymer films, chemical surface functionalization can serve as an alternative method to the spin-cast process. Polymers can be attached to the substrate surface by means of chemical grafting techniques via grafting to or grafting from approach.[208] As an alternative to crosslinking of the polymer network, grafting is also used to prevent dissolution of polymer surfaces like in the case of organic electrode active materials.[209-212] Grafted polymers have a confined geometry by their covalent bonding and therefore cannot dewet from the surface when their grafting density (Γ_g) exceeds a certain limit.[213] Grafting density is defined as the number of polymer chains occupying a specific area. At a certain value of the grafting density, polymer chains are forced to stretch[214] to reduce their segmental interaction and they will form a so called "brush like structure".[215] In previous works, SFM based nanowear experiments revealed that grafted polymer brushes exhibit an increased mechanical stability especially on the nanometer scale.[216,217] This increased nanowear stability is a very important feature for polymers in the electronic industry.[218-220] Nanowear for example leads to loss of the stored information in the field of SFM based data storage as observed in the patterning experiments. Furthermore, nanowear can lead to loss of the electric properties of a conductive surface like electrodes.

In the previous chapter, PVBPT was used for SFM based patterning experiments. It was concluded that PVBPT can be regarded as an adequate candidate for data storage. However, the mechanical stability under increased applied force was not sufficient and led to surface deformation. Apart from reducing the dewetting and dissolution, grafted brush like polymer architecture could offer an alternative for improving mechanical properties of redox active polymers. Therefore, in this chapter my main focus lies on the synthesis of redox active polymer brushes with phenothiazine moieties via surface initiated ATRP (SI-ATRP).[221] This polymerization technique is chemically versatile, tolerant against impurities, water, aliphatic alcohols and other polar solvents as well as insensitive to traces of oxygen. With the latter SI-ATRP technique, polymer film thickness, architecture and composition can be controlled very precisely. A further advantage is that the initiators necessary for this grafting technique are either commercially available or can be accessed synthetically.[222] There are only a few groups

who have investigated redox active polymer brushes so far.[223-225] Most of them are based on large redox sites such as ferrocene which are difficult for direct polymerization. Small redox moieties such as TEMPO or phenothiazine could be interesting from the synthetic aspect due to their low steric hindrance.

In the following section, I will present two different synthetic approaches to obtain wear stable redox active surfaces with increased nanowear resistance (Scheme 38). For the first route, a conductive substrate ITO with a SI-ATRP initiator to form a self assembling monolayer (SAM) was functionalized. Then, VBPT as phenothiazine containing monomer was attached to the surface via grafting from polymerization (direct polymerization).

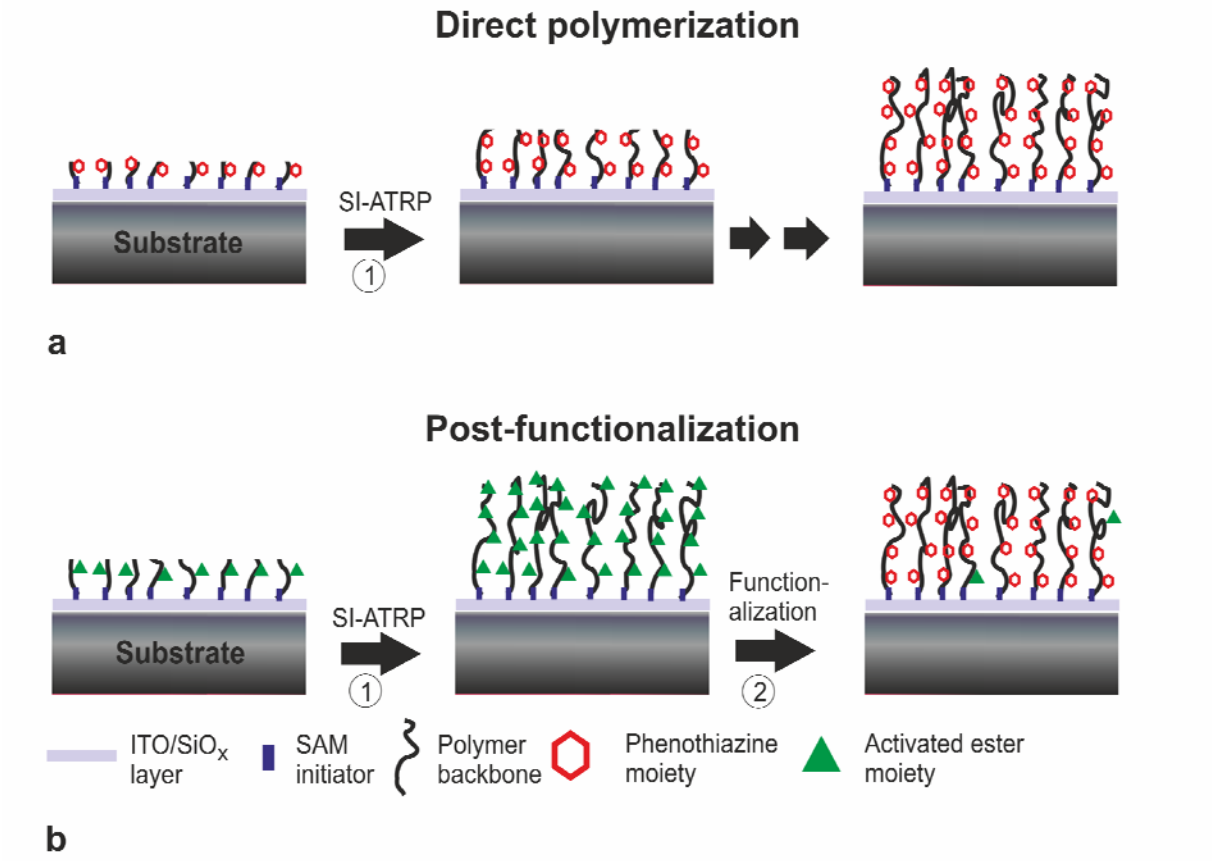

Scheme 38. Schematic overview of the phenothiazine based redox polymer synthesis. a) For the first synthetic route, the phenothiazine containing polymer PVBPT was grafted from Si/ITO substrate via SI-ATRP, b) For the second synthetic route, polymers with activated ester moieties were grafted from via SI-ATRP. Finally, these brushes were post-functionalized with phenothiazine redox moieties.

For the second route, SI-ATRP was used to polymerize a monomer with functional activated ester groups[93,107] (post-functionalization). Polymer brushes with activated ester groups on each repetition unit have been reported for reactive surface coating.[226,227] Through formation of stable amide bonds, organic moieties with primary or secondary amine groups can chemically be attached to the activated ester side groups in the polymer chain. The attachment takes place quantitatively under mild reaction conditions without using catalysts. After attachment of the activated ester polymer brushes via SI-ATRP, the functional polymer was then post-

activated ester polymer brushes via SI-ATRP, the functional polymer was then post-functionalized with different redox moieties based on phenothiazine. Two different redox moieties with one and two amine functionalities were chosen for the post-functionalization. The moiety with two amine groups can form crosslinked structures, whereas the moiety with a single amine group cannot build crosslinked bounds. Both methods were examined with respect to their chemical versatility, their resulting surface morphology and their wear resistance. To better understand the synthetic approach, a short overview of ATRP as polymerization technique and of polymer brushes is given. Furthermore, the X-ray techniques to characterize polymer brushes, namely X-ray reflectivity (XRR) and X-ray photo electron spectroscopy (XPS) are briefly elucidated.

2. Theoretical background

2.1. Atomic transfer Radical polymerization

ATRP belongs to the group of controlled living radical polymerizations. The terminology living polymerization implies that the polymerization reaction is not terminated by irreversible recombination or transfer of the radical polymer species P_n^*. Therefore, this type of polymerization results in narrow molecular weight distribution and enables sequential addition of further monomers to obtain block copolymers with individual polymer architecture.[228] Living polymerization have following characteristics:

- The concentration of the active radical species is kept at a constant and low value.
- The reaction rate of the activation step is equal to or higher than the reaction rate of the polymerization step.
- For the overall reaction kinetics, a first order reaction is assumed with respect to the monomer concentration. Therefore, a linear dependency of the conversion at logarithmic scale over time is obtained. An increasing curvature indicates slow initiation, whereas decreasing curvature is a hint at decreasing radical species due to termination.
- The polydispersity index (PDI) is reduced with increasing conversion. An increase implies the presence of termination reactions.

In the case of ATRP, the concentration of the active species is kept low by using activatable alkyl halide (R-X) species (Scheme 39).

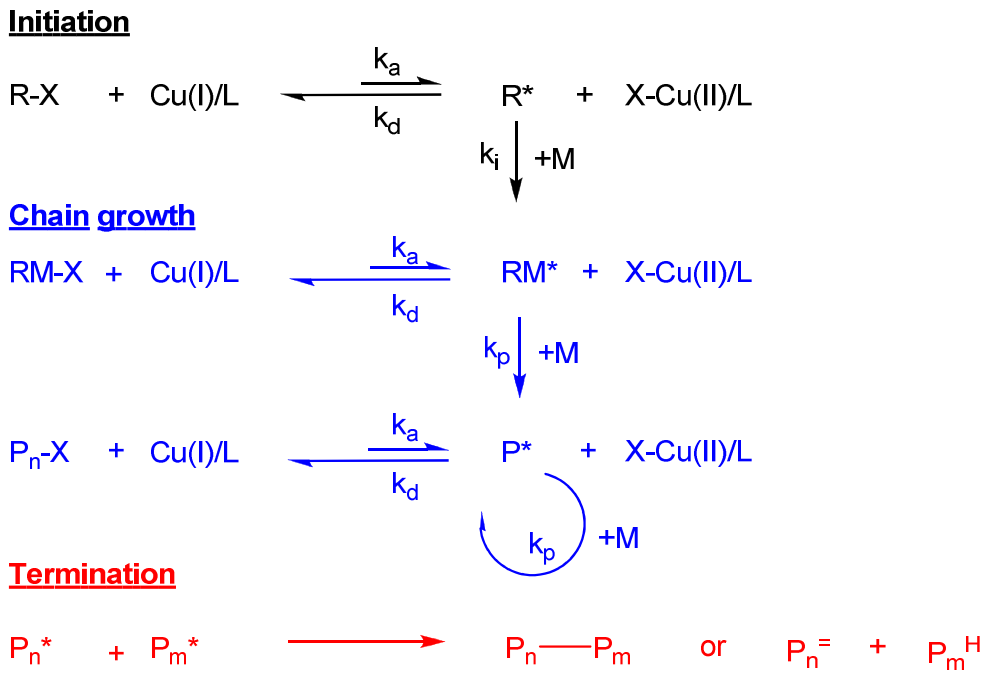

Scheme 39. Schematic mechanism for ATRP reaction.

In the initiation step, the radical initiator species is generated from the alkyl halide under cleavage of R-X bonds. The cleavage step is catalyzed by an organic-transition metal complex such as Cu(I)/L with an organic ligand L and Cu(I) ion as central atom. By addition of the alkyl halide and the formation of the radical R*, the complex is oxidized to X-Cu(II)/L. The radical R* reacts with a vinyl containing monomer M and thus initiates the polymerization. The formation of the radical species from the alkyl halide is a reversible process where the equilibrium is located on the alkyl halide side. To describe the reaction rate of the radical formation, k_a and k_d are introduced here as the activation and deactivation rate constant. The ratio k_a/k_d is described with the activation-deactivation equilibrium constant K_{eq}. The rate constant of the initiation reaction is defined as k_i and is typically smaller than K_{eq}. Once the monomer is added and the reaction initiated, the radical species can be deactivated by reacting with the X-Cu(II)/L complex to form again the halide species. Then, the chain growth starts by reaction of the oligomer RM-X with Cu(I)/L and successive addition of the monomer. For the chain growth step, k_p is defined as the rate constant of the monomer addition. The chain growth takes place stepwise through a series of successive activation-deactivation-addition steps leading to a halide terminated polymer chain P_n-X. In principle, the halide terminated can always be reactivated, enabling further monomer addition according to living polymerization. The reactivation therefore allows the synthesis of block copolymers with alternating blocks. Since nearly all alkyl halide molecules are activated already at the initial state simultaneously and due to the low termination rate, the ATRP enables a low molecular weight distribution. In addition, the concentration of X-Cu(II)/L increases due to termination reaction which in return drags the equilibrium towards the alkyl halide species. Since the number of radical chain ends is reduced, further termination is prevented. This phenomenon is called “persistent radical effect” (PRE). The PRE is the reason why ATRP is conducted as a living polymerization because it reduces the

radical concentration and subsequently the termination probability. Therefore, termination reactions via recombination and disproportionation as described in Scheme 39 do not take place frequently. The overall reaction rate for ATRP r_p is defined to be first order with respect to the concentration of monomer [M], Initiator [I_0] and the Cu(I)/L and X-Cu(II)/L complex ([Cu(I)/L] and [X-Cu(II)/L]):

$$r_p = k_p \cdot K_{eq} \cdot [M] \cdot [I_0] \cdot \frac{[Cu(I)/L]}{[X-Cu(II)/L]} \quad (22)$$

From the equation, it can be deduced that the overall reaction kinetics can be accelerated by adding Cu(I)/L complex as well as initiator and monomer. The Cu(I)/L complex concentration can also be increased by the addition of elemental copper (Cu(0)), which forms more Cu(I)/L by synproportionation with X-Cu(II)/L. The addition of deactivator (Cu(II) salts) decelerates the reaction rate by shifting the equilibrium towards the alkyl halide reaction and reducing the concentration of the radical species. Simultaneously, the high concentration of X-Cu(II)/L improves the polydispersity of the polymer by better reaction control and lower active chain end concentration.

Other parameters to control the reaction rate and polydispersity are given by the choice of the initiator, the ligand and the solvent. Initiators which have radical stabilizing effect with electron withdrawing groups such as CN or tertiary carbon atoms reveal improved reactivity. Alkyl halides with Br and Cl can be used for easy homolytic scission of the R-X bond. R-I bond tends to cleave in a heterolytic manner and the iodine metal complexes are light sensitive, which is why they are not used often for ATRP. Generally, initiators with similar molecular structure like the monomers such as benzyl halogenides for styrene or halogene esters for acrylates are preferred (Scheme 40, a). For the complexation, generally amine based ligands with double or multiple denticity are chosen with copper as central atom. The choice of ligand has an influence on the catalytic activity of the complex. For N,N,N',N'',N''pentamethyldiethylenetriamine (PMDETA; Scheme 40, c), K_{eq} was determined in the order of $2.79*10^{-7}$ l/(mol*s) in acetonitrile with ethyl 2-bromoisobutyrate (EBIB; Scheme 40, b).[229] A similar value was obtained for the ligand tris[2-(dimethylamino)ethyl]amine (Me_6tren; Scheme 40, d) with four coordination sites. The high K_{eq} allows fast equilibrium condition and increases the overall reaction rate. Therefore, the combination of PMDETA and EBIB was chosen to accelerate the polymer reaction for the upcoming experiments. The solvent affects the solubility of the complex which in turn leads to activation or deactivation of the reaction. Low soluble X-Cu(II)/L complex might precipitate which then will increase the reaction rate and the polydispersity. Using alkylated ligands or polar solvents, the solubility can be improved to obtain polydispersities with very narrow distribution below 1.1.[230] The good control of the polydispersity, the availability of the components and its applicability on a variety of monomers made ATRP an attractive polymerization technique also for industrial applications in the past few years.[231-234] ATRP is also used for producing functional polymer surface with variable architecture.

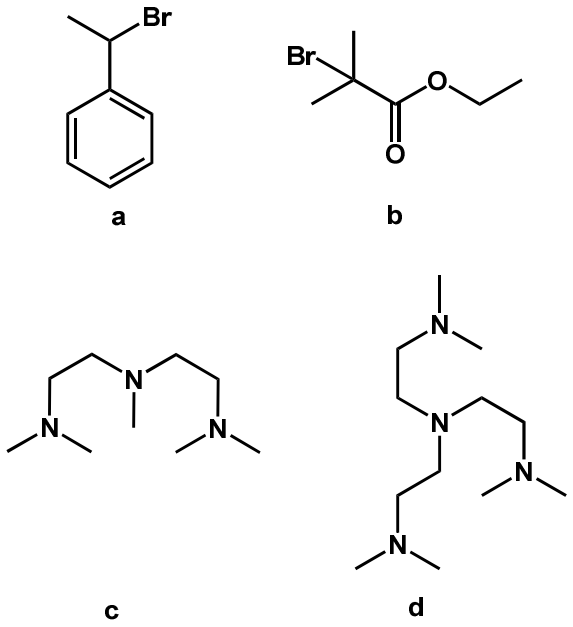

Scheme 40. Initiator and ligands used for ATRP reaction: a) Initiator (1-bromoethyl)benzene (BEB), b) initiator ethyl 2-bromoisobutyrate (EBIB), c) ligand N,N,N',N'',N''pentamethyldiethylenetriamine (PMDETA) and d) ligand tris[2-(dimethylamino)ethyl]amine (Me_6tren).

Among the synthetic possibilities, grafted polymers with controlled surface morphology were obtained by SI-ATRP. By controlling the grafting density of the polymer chains, brush-like architectures are accessible as well.[222,235,236]

2.2. Polymer brushes via SI-ATRP

Single polymer chains attached to a surface form a self assembling monolayer (SAM). Polymer chains can rather be anchored to the surface by ionic or covalent bonding. For covalent attachment, two possibilities are available. A polymer chain with a terminal functional group can react with another functionality which is anchored to the surface. This might be for example a reaction between an amine functionalized surface and a polymer with activated ester terminal group.[237] Other functional groups such as carboxylic acids and hydroxyl groups have also been used so far.[238] This type of surface attachment is also known as grafting to approach. This approach is limited to the achievable grafting density of the individual chains as well as the polymer film thickness. The limiting factors have kinetic as well as thermodynamic reasons. From the point of kinetics, the chemisorption of polymer chains on the surface slows down further diffusion of free polymer chains to the substrate. Furthermore, the reactive sites are blocked which prevents the surface reaction with increasing surface coverage. The thermodynamic aspect depends on the entropic loss of the polymer chain. Typically, the polymer chains are organized as random coils. These random coils start to interact and overlap with each other with increasing grafting density. Consequently, to reduce the unfavorable segmental interaction, polymer chains have to organize in a stretched formation losing their chain entropy. Since the loss of entropy cannot be compensated with enthalpic energy of bond formation, grafting to approaches result in film thicknesses of around 2-5 nm with low grafting densities.

The grafted coils are organized in the so called "mushroom conformation" in a distance which is larger than the gyration radius of the polymer coil (Scheme 41a).[239]

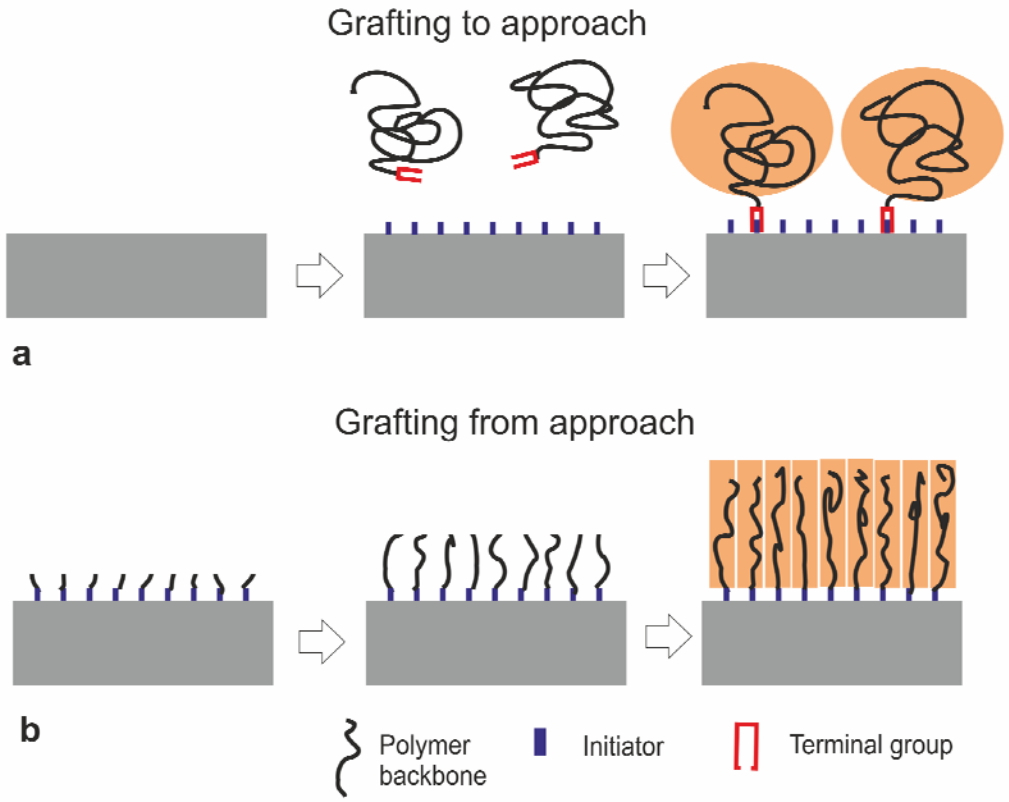

Scheme 41. Schematic presentation of a) grafting to and b) grafting from approach with subsequent effect on grafting density.

A grafting from approach allows higher grafting densities to obtain polymer brush structures. The close proximity of the neighboring chains forces them to stretch in order to avoid segmental interaction. Consequently, the free energy of the polymer brush is a sum of the interaction energy E_{int} and the entropic energy of the stretched chains E_{ent}:

$$E = E_{int} + E_{ent} \quad (23)$$

In the grafting from approach, the polymerization process is initiated at the surface (Scheme 41b). Therefore, radical initiators have to be anchored on the surface. Prucker et al. used an azo initiator attached to inorganic substrates or particles to grow PS chains at those surfaces.[239,240] The drawback of this technique is the poor control of the polymerization rate and polydispersity. Polymer chains grow inhomogeneously and form aggregated structures which hinder the diffusion of further monomers. Some of the initiation sites cannot be accessed and therefore the initiation efficiency and subsequently the grafting density is decreased. To increase the initiation efficiency and enable simultaneous growth of the polymer chains in grafting from approach, Ejaz et al.[241] and Ramakrishnan et al. [222] introduced SI-ATRP. They demonstrated successfully a living polymerization of methacrylate monomer from a silane based SI-ATRP radical starter. Homogeneous polymer brush films were obtained with grafting densities of around 0.8 chains/nm^2. Ell et al. succeeded in synthesizing grafted polymer brush films of PS with grafting

densities up to 0.44 chains/nm^2.[242] The advantage of SI-ATRP lies in the variety of monomers and good control of polymer film thickness and homogeneity. The monomer addition takes place stepwise and simultaneously from all the activated initiation sites on the surface and is controlled by subsequent deactivation and reactivation. Under these conditions polymer chains can grow homogenously and closely packed to form a stretched brush.

To achieve better control of the surface propagation rate, the amount of persistent radicals must be increased. The deactivation can be acquired classically by adding Cu(II) species to decelerate the reaction and deactivate the radical chain ends.[243] Alternatively, addition of free ATRP starter referred to as sacrificial initiator controls the reaction rate by forming terminated radicals inside the solution.[241] This way, the equilibrium is shifted towards the deactivated species. The molecular weight and distribution of the free polymer correlates well with the grafted polymer as shown by Von werne and Pyun.[244,245] Thus, the addition of sacrificial initiator allows the determination of monomer conversion as well as molecular weight and distribution from the bulk product in solution.

The concentration of active sites attached to the surface is generally low. On an area of 4 cm^2, approximately 2*10^6 initiator molecules are available assuming a cross-sectional area of ~0.2 nm^2 for the initiator. However, with a grafting density of 0.8 chains/nm^2, the number of the grafted polymer chains is around 3.2*10^5. In other words, only 16% of all initiator molecules are able to grow a polymer chain. This low initiator efficiency was explained by steric hindrance of the growing chains as observed by Yamamoto and coworkers. The authors could increase the initiator efficiency up to 100% by photo cleaving the initiator.[246] Jones et al. stated a proportional behavior between the film thickness d_f of the grafted polymer brush and the grafting density Γ_g[247]:

$$\Gamma_g = \frac{d_f \cdot \rho \cdot N_A}{M_n} \tag{24}$$

From the equation above, Γ_g can be calculated by knowledge of the polymer film thickness, the density of the bulk polymer ρ and the molecular weight M_n (N_A is the Avogadro constant). A linear increase of film thickness with increasing molecular weight (and time) is an indication for controlled living polymerization. For phenothiazine grafted brushes, the change in redox state is accompanied with charge formation of radical cation species. In the oxidized state, the polymer brush will behave as a poly electrolyte. Therefore, the salt concentration and the solvent might have influence on diffusion process which is caused by Coulomb interaction. The swelling of the poly electrolyte also attributes to the diffusion and is responsible for changes in film thickness.[248] Precise characterization of thin polymer brush films is an important topic of investigation. Optical light scattering and spectroscopic techniques such as XRR and XPS are often used in this case.[222,249] While XRR gives information about the film thickness and surface morphology, XPS helps to study the chemical composition of the surface.

2.3. X-ray reflectivity

For characterization of thin films in the nanometer scale like in the case of grafted polymer brushes, XRR is an adequate technique. The basic principle of XRR is based on partial reflection of a X-ray beam on a substrate.

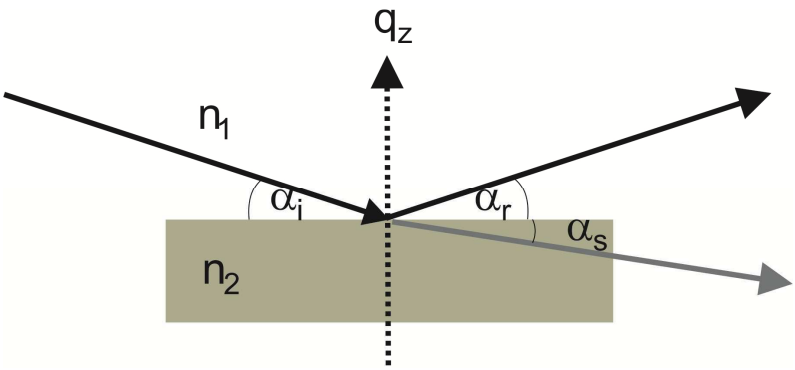

Scheme 42 Principle of Snell's law for light refraction and reflection.

Incident angle α_i and reflection angle α_r are equal at low incident angles below the critical value α_c for specular measurements. Under these circumstances, the wave vector transfer q of the incident beam with the wavelength λ is equal to wave vector transfer q_z perpendicular to the substrate:

$$q_z = \frac{4 \cdot \pi}{\lambda} \cdot \sin(\alpha_i) \tag{25}$$

Above α_c, partial refraction of the incident beam takes place according to Snell's law at the angle α_s:

$$n_1 \cdot \cos(\alpha_i) = n_2 \cdot \cos(\alpha_s) \tag{26}$$

In the equation, n is the refractive index of the media at its interface the beam is refracted. A typical XRR experiment is conducted at incident angles between 0.1 and 6° where the beam is refracted between air and the substrate. The refractive index is composed of the dispersion or scattering term δ_S as well as the absorption term β at the interface:

$$n = 1 - \delta_s + i \cdot \beta \tag{27}$$

Both values are material dependent and primarily correlate with the incident wavelength, mass density, atomic mass and form factors. Their value is in the order of 10^{-5} to 10^{-8} for organic materials which leads to refractive indices close to 1. The dispersion term δ_s furthermore includes the electron density σ_{el} and the number of electrons. σ_{el} correlates with the mass density and can e.g. be used to estimate the density of polymers. The absorption term β contains a mass absorption coefficient which is an element specific value. For air, the refractive index is n_1=1. At incident angles below α_c, no absorption takes place. Therefore, β and α_s are both equal

to zero. Combining equation (26) with equation (27), following equation is obtained for α_c under approximation of cos (α_c) ≈ (1- α_c^2)/2 for small angles:

$$\alpha_c \approx \sqrt{2 \cdot \delta_s} \tag{28}$$

The normalized reflectivity curve has an intensity of 1 below α_c. Above this material dependent angle, the reflectivity is reduced with a power of 4 with respect to α_i because absorption is occurred.[250] With further increase of α_i, the X-ray beam starts to penetrate the medium and the intensity falls off exponentially. The absorption decay is described by Fresnel coefficients r_f in terms of square root of the amplitude:

$$\overline{R_F} = \frac{I_r}{I_i} = |r_f|^2 = \left|\frac{\alpha_i - \alpha_s}{\alpha_i + \alpha_s}\right|^2 \tag{29}$$

$\overline{R_F}$ is the Fresnel reflectivity and contains the ratio of the reflected intensity compared to the incident intensity.

When a thin film is placed between the two media on top of the substrate, additional interference is observed in the reflectivity curve. Multiple reflection and refraction (and consequently constructive and destructive interference) occur at the interface between substrate and film as well as film and air resulting in so called “Kiessig oscillation” (Scheme 43a). Unlike the Si substrate, 40 nm thick PS film on Si exhibits regular fringe patterns in the decaying reflectivity curve (Scheme 43b).

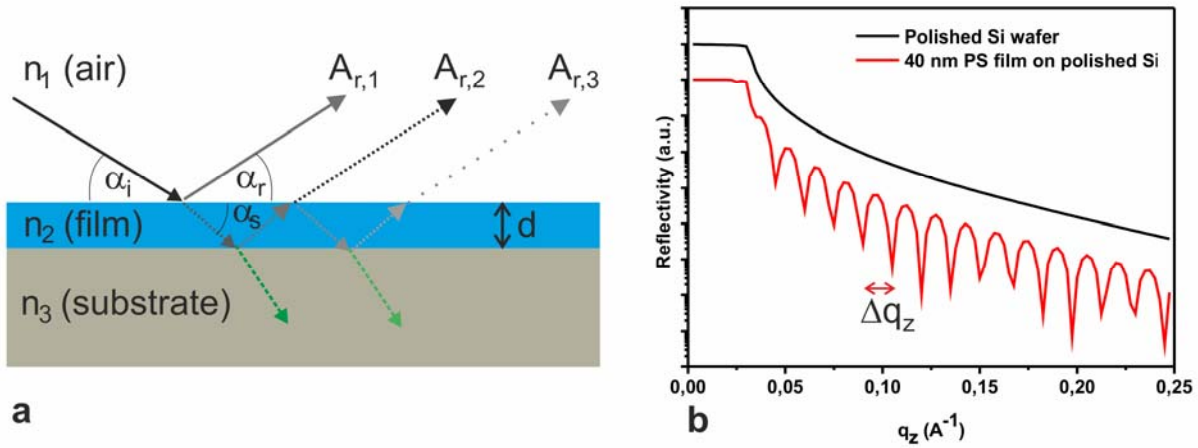

Scheme 43. a) Schematic presentation of X-ray reflectivity on thin films and b) resulting curves with Kiessig fringes compared to bare substrate.

From the difference between the minima or maxima of the fringes (shown as Δq_z), the thickness of the film on top of the substrate can be estimated:

$$d = \frac{2 \cdot \pi}{\Delta q_z} \tag{30}$$

The distance between the fringes increases when the film thickness decreases. The modulation amplitude of the fringes depends on the electron density difference between film and substrate. The electron density of carbon based PS is smaller compared to silicon based SiO_2 (Figure 35a). Furthermore, the roughness of the film surface and the substrate interface affects the shape of the reflectivity curve. Rough and irregular surface on nanometer scale causes diffuse scattering, damping and intensity decrease of the reflectivity. Microstructure waviness leads to deformation and broadening of the reflectivity curve (Figure 35b).

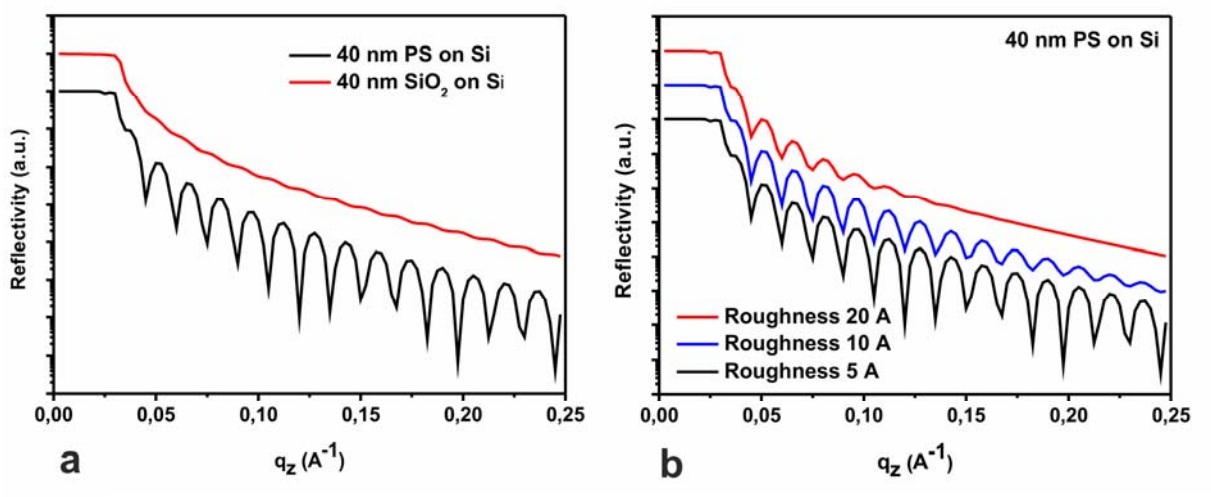

Figure 35. XRR curves for a) different layers on silicon and b) at different surface roughnesses.

According to Névot and Croce[251], the vertical thickness variation has a Gaussian distribution around the average thickness and is described by the standard deviation or RMS roughness σ. In the case of PS on Si, strong damping of the Kiessig oscillation occurs when the RMS roughness of the PS film is increased. The evaluation of reflectivity curves for monolayers on smooth substrates is feasible when the film/substrate roughness is in the range of 1-2 nm. However, especially for multilayer systems like in the case of polymer brushes, calculation of the reflectivity data has to be performed by simulations. In the current work, parratt formalism is used as integrated software to evaluate the data. Parratt is based on a recursion formula which calculates every layer's reflectivity as the ratio of the reflected and transmitted beam from the previous layer. This way, the obtained reflectivity curve can be fitted to obtain the necessary data about the thickness, roughness and density of polymer films.

2.4. X-ray photoelectron spectroscopy

Among the surface characterization techniques XPS or Electron Spectroscopy for Chemical Analysis (ESCA) is one of the most versatile methods. Chemical surface composition, uniformity and purity of elemental composition and electronic state of elements can be resolved with XPS. The technique, developed by Siegbahn et al.[252] in the mid 1960s is based on the photoelectric effect.[253,254] The sample surface is irradiated with an X-ray beam (e.g. Al K_α line with 1487 eV) which produces photo electrons from the atomic core under ultra high vacuum. The ultra high vacuum reduces the contamination probability for obtaining better signal to noise ratio. Core

electrons close to the nucleus have specific binding energy E_{bind} which differs within the elements. Electrons below the Fermi level with specific kinetic energies E_{kin} are ejected from 1-10 nm deep inside the sample. E_{bind} is calculated from E_{kin}, the incident energy of the beam E_{beam} and the spectrometer work function Φ_{spec}(Scheme 44) as shown below:

$$E_{bind} = E_{beam} - E_{kin} - \phi_{spec} = h \cdot \upsilon - E_{kin} - \phi_{spec} \quad (31)$$

Ejected electrons are collected by a cylindrical mirror analyzer when they have the right kinetic energy to reach the detector and be counted. The resulting electron signal count includes the contribution from two types of electrons. Beside the photoelectron from the core such as 1s electron for carbon atoms, auger electrons produce additional broad signals. They result from electrons falling from L level to K level and subsequent electron emission of an electron from L level to conserve the energy. The energy of the KLL auger electrons depends on the incident beam energy and can be shifted not to overlap with the photoelectron signals.

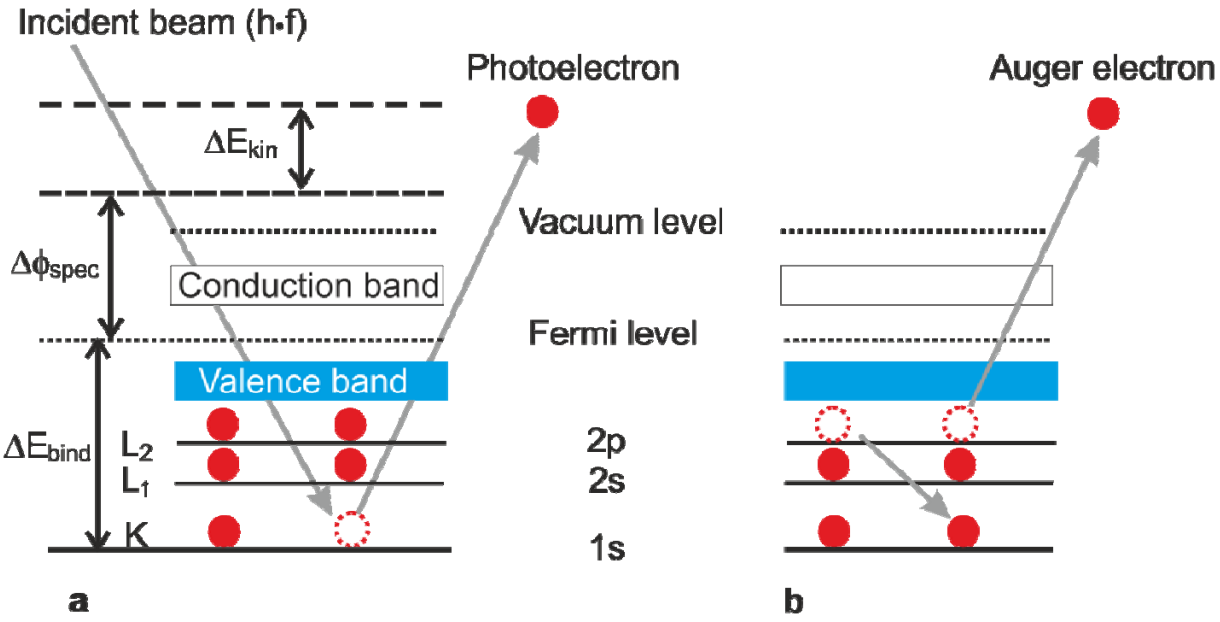

Scheme 44. Principle of a) Photoelectron effect and b) Auger electron in XPS.

In the XPS spectrum, core electrons of all elements starting from lithium are identified by their precisely defined binding energy line according to their orbitals. To generate atomic percentage values and to estimate the chemical composition, each raw XPS signal intensity is divided by a relative sensitivity factor and normalized over all detected elements for correction. The sensitivity factor enhances with increasing atomic mass and transition state. Transition metals such as copper and zinc are much easier to detect compared to lighter elements like nitrogen and carbon due to their high sensitivity factors. The binding energy signal is chemically shifted due to repulsive interaction of surrounding electrons as well as attracting effects of the nucleus. Its value is scaled up with the atomic mass and transition state. Neighboring atoms with electron withdrawing or electron pushing properties lead to an increase or decrease of the binding energy, respectively. Organic ester and acid groups are shifted up to 4 eV in their binding energy compared to hydrocarbon for carbon atoms in 1s state (Table 10).

Table 10. Binding energies for different elements and functional groups at specific transition states. The binding energy values in the parentheses demonstrate the range of the binding energy for the element depending on the substituents.[255]

Element or functional group	Transition	Binding Energy (eV)	Sensitivity factor (54 °)
C	**1s**	**284.4 (280-301)**	**1.00**
methylendilithium (Li2(CH3))		280.7	
hydrocarbon (C-H, C-C)		285.0	
amine (C-N)		286.0	
F bound to C (C-F)		287.8	
carbonyl (C=O)		288.0	
amide (N-C=O)		288.2	
ester/acid (O-C=O)		289.0	
perflourated carbon (CF_4)		296.7	
N	**1s**	**- (395-417)**	**1.82**
amine (C-N)		399.4	
amide (N-C=O)		400.2	
nitroxide (NO_2)		406.0	
O	**1s**	**- (526-540)**	**3.06**
	2s	**- (17-31)**	**0.13**
Si	**2s**	**150.7 (149-155.3)**	**0.83**
	2p	**99.6 (98-107)**	**0.84**
S	**2s**	**229.2 (218-238)**	**1.23**
	2p	**164 (160-238)**	**1.7**
Cl	**2p**	**- (192-209)**	**2.33**
Cu	**2p**	**932.8 (931-954)**	**31.77**
Zn	**2p**	**1021.6 (1020-1044)**	**39.16**

3. Experimental

3.1. Methods

The CV measurements were performed with the potentiostat Autolab PGSTAT 100 from Metrohm in a modified cell equipped with a stirrer and a nitrogen supply valve. A 0.1 M solution of TBAPC in dry DCM or ACN served as an electrolyte solution. ITO with grafted polymers was used as the working electrode and a platinum wire as the counter electrode, respectively. As reference, a Ag/AgCl electrode was chosen. The formal potential of the ferrocene/ferrocenium redox couple was determined to 0.44 V versus this reference electrode.

UV/Vis spectra were recorded on a Perkin Elmer Lambda-9 with ITO substrate as the background standard.

For the CV measurements and the XRR measurements, ITO substrates on glass as well as silicon wafers were prepared by the following procedure: glass slides (2.5 cm x 2.5 cm x 0.5 cm) and silicon wafer (Si-Mat, one side polished, 2.5 cm x 2.5 cm x 0.54 cm) were cut using a glass cutter and sonicated for 10 minutes subsequently with DCM, acetone, Alconox® and washed with Milli-Q water. Finally, the glass slides and the silicon wafers were dried with compressed air and dried at 100 °C in vacuum. On the glass slides, 100 nm of ITO were sputtered under argon flow. The ITO sputtered glass slides and the silicon wafers were cleaned in DCM, dried under air and cut in 1.1 cm x 1.1 cm slices.

XRR measurements on wafers were performed on a XRD 3003 TT, Seifert Ltd. GB diffraction system. Monochromatic and collimated X-rays were obtained from a Cu anode with a wavelength of λ = 0.154 nm. The thickness was determined according to parratt formalism.[256] Contact angle measurements were conducted on a Krüss, DSA10-MK2.

XPS measurements were performed on a SPECS Surface Nano Analysis machine using Al K_α radiation. The incidence angle of X-rays was 45° with respect to surface normal. All the measurements by XPS were performed at pressures lower than 3×10^{-9} mbar.

The nanowear experiments were carried out on a NanoWizard scanning force probe microscope (JPK, Berlin, Germany) using contact mode cantilevers (NanoWorld, CONT-W, nominal spring constant 0.2 N/m). The exact spring constant for each cantilever was determined by thermal tune. A surface of 3 x 3 μm^2 was scanned 100 times in contact mode with a load of 10 nN at a speed of 50 µm/s. Then, the scanned area was mapped in tapping mode to observe changes in the topography.

DSC and TGA measurements were done following the methods described in II.4.2. The simulation on PVBPT brushes was done as described in appendix, *Description of simulation.

3.2. Materials

New methylene blue N zinc chloride double salt (NMB; Acros, 97%), tetrabutylammonium perchlorate (TBAPC; Sigma Aldrich, 99%), acetic anhydride (Sigma Aldrich, ≥ 99%), copper (II) bromide ($CuBr_2$; Sigma Aldrich, 99%), ethyl 2-bromoisobutyrate (EBIB; Aldrich, 98%), dry toluene (Acros, 99.8%), acetone (Sigma Aldrich, 99.5%), dichloromethane (DCM; Acros, 98%), methanol (Fisher Scientific, HPLC grade), acetonitrile (ACN, Sigma Aldrich, HPLC grade), Dowex® Marathon MSC (H) ion exchange resin (Dowex; Sigma Aldrich), hydrogen peroxide (H_2O_2; Sigma Aldrich, 35%), ammonia (VWR, 28%), and aluminum oxide (Fluka, for chromatography) were used as received. The starter 3-(2-bromoisobutyryl)propyl)dimethyl chlorosilane (BIPDS) was synthesized following the procedure described by Ramakrishnan et al.[222] and purified by distillation. 10-(4-vinylbenzyl)-10H-phenothiazine (VBPT) was synthesized according to II.4.3.2. 2,5-di oxopyrrolidin- 1-yl 4-vinylbenzoate (DPVB) was synthesized according to II.4.3.19. (10-methyl-10H-phenothiazin-3-yl)methanamine (MPMA) was synthesized according to II.4.3.18. Anisole (Aldrich, 99%) and dimethylformamide (DMF; Acros, 99.9% extra dry) were used after deaerating by bubbling argon for 1.5 hours. Copper (I) bromide (CuBr; Sigma Aldrich, 98%) was purified by boiling 15 minutes in a 50 vol% Milli-Q water/acetic acid mixture before subsequent filtration. N,N,N',N'',N''pentamethyldiethylene-triamine (PMDETA; Sigma Aldrich, 99%) was purified by distillation under reduced pressure. Triethylamine (TEA; Sigma Aldrich, ≥ 99.5%) was distilled prior to use and kept under dry argon atmosphere.

3.3. Synthesis

3.3.1. Synthesis of PVBPT via ATRP

14.35 mg (0.10 mmol) CuBr, 1.50 g (4.76 mmol) VBPT, 20.9 µL (0.10 mmol) PMDETA were dissolved stepwise in a 50 ml Schlenk tube filled with 4 ml anisole under argon. 8.6 µL (0.067 mmol) EBIB were added to the solution under argon and the reaction mixture was degassed with three freeze-thaw cycles. The tube was then sealed and the mixture heated and stirred at 100 °C for 72 hours. Afterwards the tube was left at room temperature and vented with air. The viscous green solution was diluted with dry THF and Dowex was added while stirring until the solution was decolorized. To be sure to remove the copper residues, the solution was filtered through aluminum oxide and finally precipitated from methanol. After repeating the precipitation, the obtained polymer was dried at 60 °C in vacuum. (727 mg, yield= 73%). GPC: (M_n=9370 g/mol, PDI=1.43).

3.3.2. Functionalization of Si/ITO wafers with the initiator BIPDS

2 ITO and 2 silicon wafer (1 cm x 1 cm) were cleaned using the RCA method[257]: 25 ml Milli-Q water, 2 ml ammonia solution (28%) and 2 ml H_2O_2 solution (35%) were added to the pre-cleaned wafers as described before in the methods section V.3.1. The wafers were heated for 30 minutes at 85-90 °C in this solution. Subsequently, the wafers were washed twice with Milli-Q

water and once with methanol and dried with air. The dried wafers were functionalized in a special glass vessel at room temperature using a solution of 25 ml dry toluene, 0.4 ml TEA and 0.2 ml BIPDS under stirring in argon atmosphere for 20 hours. Finally, the functionalized wafers were cleaned over night in a soxhlet apparatus using DCM as extraction solvent.

3.3.3. Synthesis of PVBPT via ATRP

In a 50 ml Schlenk tube 14.35 mg (0.10 mmol) CuBr, 1.50 g (4.76 mmol) VBPT, 20.9 ml (0.10 mmol) PMDETA were dissolved stepwise in 2 ml anisole under argon. 8.6 ml (0.067 mmol) EBIB were added to the solution under argon and the reaction mixture was degassed with three freeze–thaw cycles. The tube was then sealed and the mixture heated and stirred at 100 °C for 72 hours. Afterwards the tube was left to cool down and vented with air. The viscous green solution was diluted with dry THF and Dowex was added while stirring until the solution was decolorized. To be sure to remove the copper residues, the solution was filtered through aluminum oxide and finally precipitated from methanol. The precipitation was repeated once again and the obtained polymer was dried at 60 °C under vacuum (1095 mg, yield = 73%). GPC: (M_n= 9400 g/mol, PDI= 1.43).

3.3.4. SI-ATRP on Si/ITO wafers using VBPT as monomer

2.5 g VBPT (7.93 mmol) were dissolved by heating under argon in 2.5 ml anisole (degassed by bubbling) in a Schlenk tube containing two initiator functionalized ITO and Si wafers in a special holder, respectively. The solution was degassed three times by evacuating the tube shortly. Then, 35.9 mg CuBr (0.25 mmol) and 52 µL PMDETA (0.25 mmol) were added under argon atmosphere to the reaction and stirred under heat. Finally, 37 µL EBIB (0.25 mmol) were added under argon and the reaction vessel was closed. The reaction mixture was degassed with three freeze-thaw cycles and the reaction continued for 24 hours at 100 °C. The wafers were removed out of the solution and cleaned over night in a soxhlet apparatus using DCM as extraction solvent. Finally they were dried under air at room temperature. The solution was diluted with DCM and Dowex was added while stirring until the solution was decolorized. After filtration, free polymer was then precipitated twice from methanol and dried over night at 60 °C in vacuum (2.05 g, 82%). GPC: (M_n=8600 g/mol, PDI=1.41).

3.3.5. SI-ATRP on Si/ITO wafers using DPVB as monomer

2.5 g DPVB (10.2 mmol) were dissolved by heating under argon in 3.0 ml DMF (degassed by bubbling) in a Schlenk tube containing two initiator functionalized ITO and Si wafers in a special holder, respectively. The solution was degassed three times by evacuating the tube shortly. Then, 17.9 mg CuBr (0.13 mmol) and 26 µL PMDETA (0.13 mmol) were added under argon atmosphere to the reaction and stirred under heat. Finally, 18 µL EBIB (0.13 mmol) were added under argon and the reaction vessel was closed. The reaction mixture was degassed with three freeze-thaw cycles and the reaction continued for 48 hours at 90 °C. The wafers were removed of the solution and cleaned over night in a soxhlet apparatus using DCM as extraction solvent. Finally, they were dried under air at room temperature. The solution was diluted with DCM and

Dowex was added while stirring until the solution was decolorized. After filtration, free polymer was then precipitated twice from methanol and dried over night at 60 °C in vacuum (1.84 g, 74%). GPC: M_n=14700 g/mol, (PDI=1.32).

3.3.6. Post-functionalization of grafted PDPVB using NMB and MPMA

PDPVB functionalized brushes on ITO and Si wafer (one of each) were inserted in a special Schlenk tube with a glass holder with 4 ml dried DMF. Subsequently, 50 mg of NMB or MPMA were dissolved in DMF and 50 µL dried TEA was added to the solution under argon. The synthesis of MPMA is described in II.4.3.18. The reaction was continued at 60 °C under argon atmosphere for 20 hours. The wafers were removed and cleaned for 48 hours in a soxhlet apparatus using methanol as extraction solvent. Finally, they were dried under air at room temperature.

4. Results and discussions

4.1. Direct polymerization

4.1.1. Polymer brush growth

As seen in chapter III and IV, PVBPT is a polymer with reversible redox behavior which could find application in the field of data storage. However, spin-coated polymer film of PVBPT could be further reduced. PVBPT polymer brushes were attached to ITO and silicon substrates by a grafting from polymerization of VBPT. For this purpose, SAM of ATRP silane starter BIPDS was formed on silicon and ITO surfaces. Then, VBPT was used for surface polymerization via SI-ATRP from the attached initiator. For better control of the polymerization reaction sacrificial initiator EBIB was added to the reaction mixture (Scheme 45). The synthesis of grafted PVBPT via SI-ATRP was performed successfully in good yields over 80%. The free polymer revealed molecular weights up to 13400 g/mol with PDI around 1.43. Thus, it was possible to polymerize VBPT not only via standard radical polymerization but also under controlled condition like in ATRP. The DSC measurement resulted in a T_g of 153 °C. TGA measurement showed a value of T_{onset}= 283 °C and T_{peak}= 426 °C for the onset and peak decomposition temperature. These results again confirmed the thermal stability of PVBPT. The static contact angle of water for the freshly prepared ITO substrate after RCA cleaning was 19 ± 6°. In comparison, the ITO layer functionalized with the initiator showed a static contact angle of 70 ± 4°. The average contact angle of the surface grafted PVBPT was measured to be 86 ± 3° regardless of the molecular weight. The increase in contact angle by 17 ± 4° indicates that polymerization has taken place successfully on the surface. XRR measurements were performed to obtain thickness and RMS roughness of the polymer brush films. Simultaneously, by adding sacrificial initiator, the molecular weight of the free polymer and its distribution was determined by GPC.

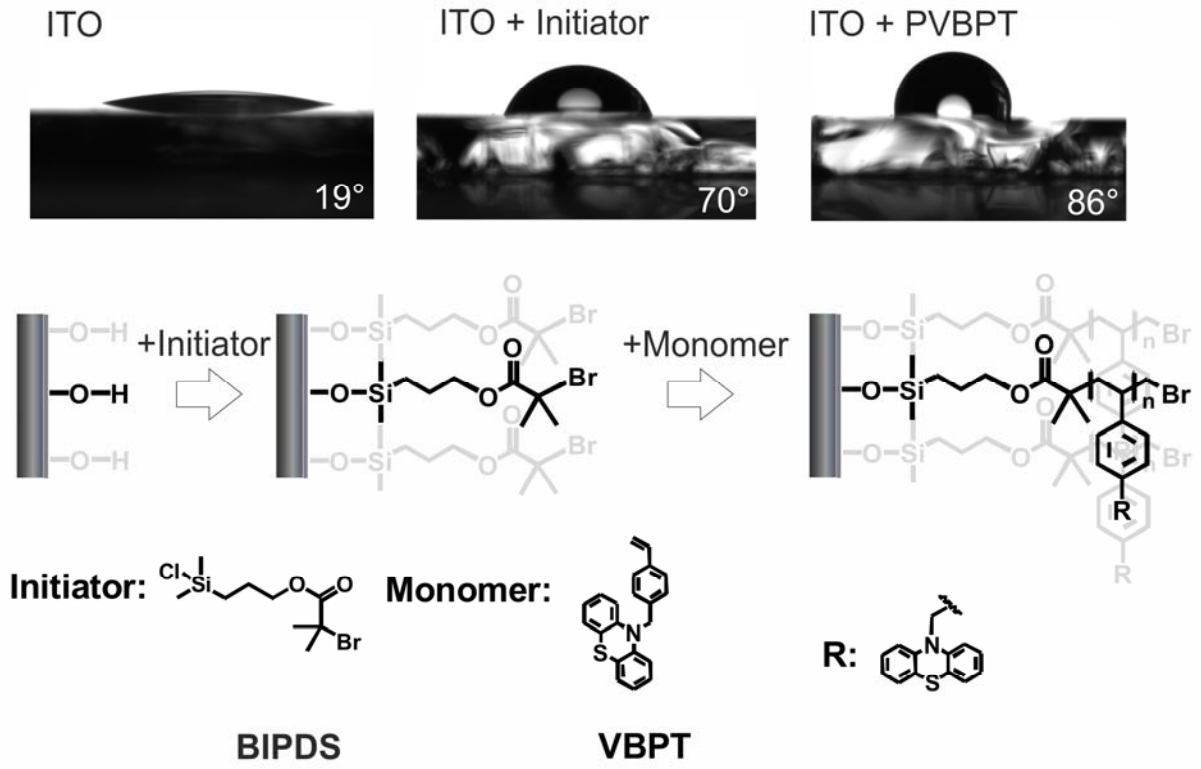

Scheme 45. SI-ATRP using silane starter BIPDS on Si/ITO surface. Contact angle measurements on ITO substrate after RCA cleaning, after attachment of the initiator and after the grafting from of the PVBPT brushes.

The molecular weight M_n obtained from the GPC can be related with the polymer brush film thickness. With increasing molecular weight of the free polymer, the distance Δq_z between the Kiessig fringes decreased indicating an increase of the polymer brush film thickness (Figure 36a). An increase of molecular weight M_n of the free polymer from 5700 to 22400 g/mol resulted in a linear increase of the thickness d from (4.86 ± 0.51) nm to (11.30 ± 1.33) nm (Figure 36b).

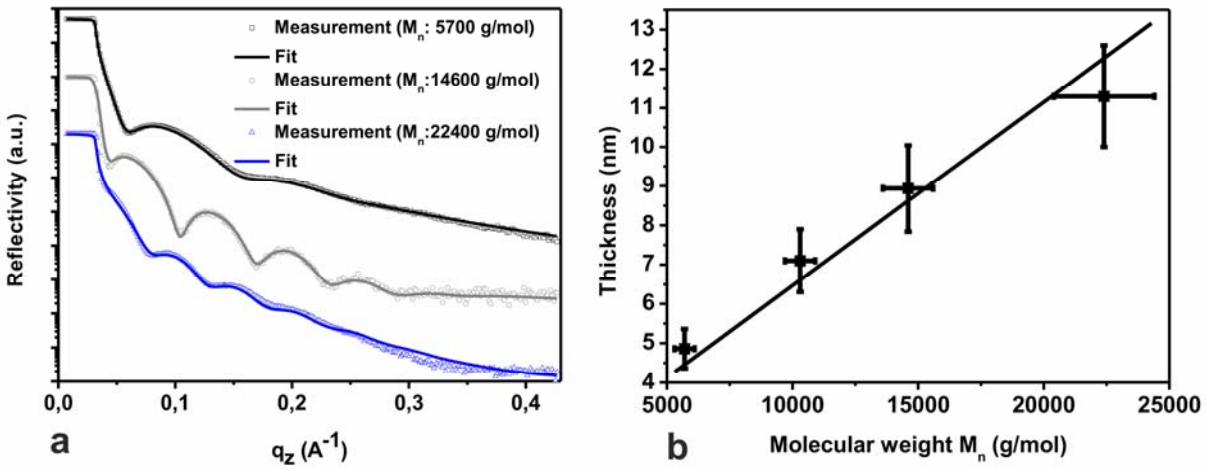

Figure 36. a) XRR curves of PVBPT grafted to silicon substrate with different molecular weights fitted according to parratt formalism, b) Thickness dependence of PVBPT grafted brushes to silicon substrate with increasing molecular weight of the bulk PVBPT.

The intercept of the line is at 1.8 ± 1.2 nm, which is close to zero as expected for SI-ATRP.[222] Polymer film is formed on top of the substrate as grafted brush with surface roughness below 1.5 nm (Table 11). Thus, it is assumed that the reaction takes place as a living polymerization and under controlled conditions. In addition, a grafting density of $\Gamma_{g,exp}$ = 0.31 ± 0.11 chains/nm^2 was calculated from the fitted XRR data (with a polymer density of ρ = 1.04 g/cm^3, M_n = 22400 g/mol) using equation (24). This value is in good accordance with the value provided from literature for grafted PMMA[222] and PS[242]. Especially for PS grafted brushes, which have the same backbone structure like PVBPT, a value of Γ_g = 0.44 chains/nm^2 was reported. Privalko et al. derived following empirical equation to estimate interchain distance *a* of different polymer chains.[258]

$$a = \sqrt{\frac{1.41 \cdot M}{100 \cdot n_m}} \tag{32}$$

In the above equation, M is the molar mass of the monomer unit and n_m the number of main-chain bonds. Using the equation above, a theoretical maximum interchain distance of a= 1.49 nm was estimated for PVBPT brushes. For the calculation, a helical conformation with a HC_1 geometry of the polymer chains was assumed. The estimation of a helical structure is justified for bulky polymers such as polyvinylcarbazole which have an interchain distance of around 1.2 nm.[259] PVBPT has similar steric hindrance like polyvinylcarbazole due to the bulkiness of the side chain. Molecular dynamic simulation of the PVBPT brush grafted to Si-wafer revealed short range and long range helical domains (Scheme 46) with a grafting density of $\Gamma_{g,theo}$ = 0.27 chains/nm^2.

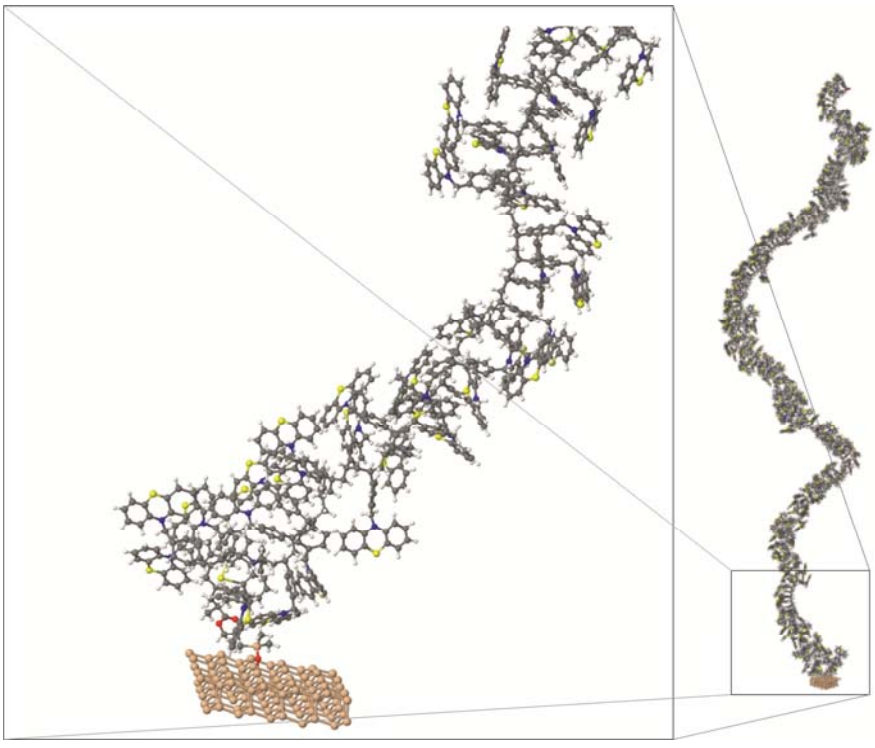

Scheme 46. Molecular Dynamic (MD) simulation of grafted PVBPT brush with 200 monomer units on silicon substrate (111 layer). The simulation was done as described in the appendix, *description of simulation.

Furthermore, the molecular weight of the repeating unit M = 315.42 g/mol and number of main-chain bonds in the chain repeating unit n_m = 2 were used. From these values, a theoretical grafting density of $\Gamma_{g,theo}$ = 1/ a^2 = 0.45 chains/nm^2 was calculated which represents the maximum theoretical grafting density for PVBPT grafted brushes. The synthesis of PVBPT grafted brushes was performed successfully via SI-ATRP. In the next step, the redox functionality of the grafted brushes was tested.

4.1.2. Redox functionality of PVBPT brushes

In order to prove the redox activity of the PVBPT brushes, CV measurements of the polymers grafted from ITO substrates were performed. For the grafted PVBPT brushes (M_n = 22400 g/mol, d = 11.3 nm), the CV diagrams revealed an anodic oxidation peak of $E^{0/+1}$ = 0.68 V and a cathodic reduction peak of $E^{+1/0}$ = 0.54 V at a scanning speed of 10 mV/s (Figure 37). Compared to spin-coated PVBPT films with oxidation potential of $E^{0/+1}$ = 0.89 V, the PVBPT polymer brush film revealed a shift of 210 mV towards lower potentials (Chapter III, Figure 12). The electrolyte solvent DCM compared to ACN contributes to facilitated oxidation process by stretching the polymer chains as a good solvent. In ACN, the oxidation potential of the polymer brush film was determined to $E^{+1/0}$ = 0.71 V indicating the effect of the solvent by collapse of the polymer brush chains. Further contribution comes from the lower thickness of the brush film. It is easier for the counter ions to diffuse inside the thin polymer film. Thus, the effect of diffusive overpotential is reduced.

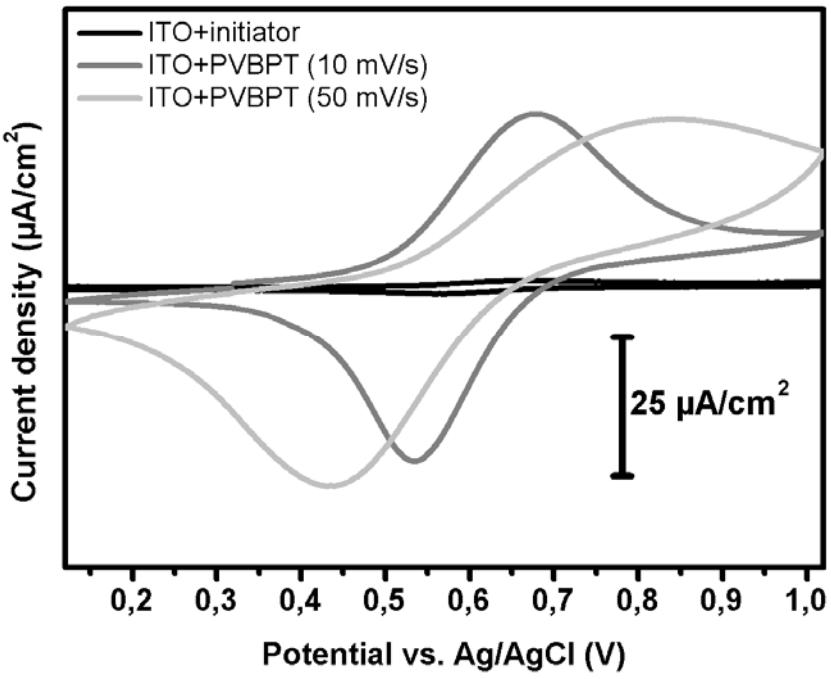

Figure 37. Cyclic voltammetry of grafted PVBPT (M_n = 22400 g/mol, d = 11.3 nm) on ITO substrates at different scan speed in 0.1 M TBAPC/DCM solution. The potential is measured with ITO, Ag/AgCl and Pt as the working, the reference and the counter electrode respectively.

The CV data for grafted PVBPT demonstrated separation when the scan speed was increased. With an increase of the scan speed from 10 mV/s to 50 mV/s, the anodic oxidation peak changed

from $E^{0/+1}$ = 0.68 V to approximately $E^{0/+1}$ = 0.83 V, respectively. Simultaneously, the cathodic reduction peak decrease from $E^{+1/0}$ = 0.54 V to $E^{+1/0}$ = 0.43 V, respectively. Consequently, the peak separation between the anodic and cathodic peak increased from ΔE_p = 140 mV to ΔE_p = 400 mV at 5 times higher scan speeds. The peak separation of the voltammograms at increased scan speed can be explained by diffusion behavior which leads to rather broader peaks and diffusion tails. This broadening is a further hint that overpotential plays an important role in the case of grafted PVBPT. Morishima et al. observed for PVMPT films a similar enhancement of overpotential with increasing scan rate.[87] For spin-coated PVMPT films on platinum (with a surface coverage of Γ= 0.29 μmol/cm^2), they measured an increase of the anodic oxidation peak from approximately $E^{0/+1} \approx$ 0.65 V to $E^{0/+1} \approx$ 0.80 V when the scan speed was increased from 20 to 200 mV/s. Simultaneously, the cathodic reduction peak decreased from $E^{+1/0} \approx$ 0.54 V to $E^{+1/0} \approx$ 0.42 V. This means that the peak separation increased from approximately ΔE_p = 120 mV to ΔE_p = 380 mV at increasing scan speed. This shift occurred due to the aggravated diffusion through the polymer film which also was observed for PVBPT grafted brushes. Further information obtained from the CV measurements was related to the diffusion coefficients for the redox process. The calculation resulted in diffusion constants of 8.49*10^{-14} and 8.55*10^{-14} cm^2/s for the oxidation and the reduction step, respectively. For the calculation, Randles-Sevcik equation (33) was used with concentration of the oxidized/reduced species of 3.3 mmol/cm^3. This equation results from the second law of Fick with regard to the concentration profile along the distance *x* from the electrode and the Nernst equation at T= 298 K:

$$j_P = 2.69 \times 10^5 \cdot n_e^{3/2} \cdot C_{0x}^* \cdot \sqrt{D_{0x}} \cdot \sqrt{\nu} \qquad (33)$$

In the equation above, n_e is the number of electrons, C_{ox}^*, the concentration of the oxidized (or reduced) species, D_{ox}, the diffusion constant of the oxidized (or reduced) species and ν the scan speed. The concentration resulted from a density of 1.04 g/cm^3 and a molecular weight for the repeating unit of 315 g/mol. Compared to the spin-coated PVBPT with apparent diffusion constants of around 1.5*10^{-9} cm^2/s as measured previously, the diffusion process is slowed down almost four to five orders in magnitude. However, equation (33) is valid for solution and therefore serves as a rough estimation. The high grafting density is probably one reason for the impeded diffusion. Besides, the polymer chains of the PVBPT brush have to reorient after the oxidation which is an energetically unfavorable process. The formation of the charged radical cation species changes the hydrophobic nature of the polymer. In return, further diffusion through the film is aggravated. After examining the redox properties of the grafted PVBPT brushes, the surface morphology was studied in the next step. The experiments served to observe the effects of the synthetic route on the surface roughness, the chemical composition and mechanical nanowear stability.

4.1.3. Surface analysis of PVBPT brushes

From the XRR data, information about the film thickness as well as surface RMS roughness was obtained. According to XRR, the roughness varies between 0.8 and 1.1 nm and is independent of the molecular weight (Table 11). However, according to the GPC results, the polydispersity of the free polymer increases from 1.4 to 2.3 when the molecular weight M_n increases from 5700 to 22400 g/mol.

Table 11. Molecular weight of PVBPT bulk polymer and surface properties of grafted PVBPT on silicon substrate at different molecular weights. (*For 1 µm²)

Experimental molecular weight M_n (g/mol)	Calculated molecular weight M_n (g/mol)	Experimental PDI	Thickness measured with XRR (nm)	Roughness measured with XRR (nm)	Roughness measured with SFM (nm)*
5700	10000	1.4	4.8	1.0	18.3
14600	25000	1.6	8.9	0.8	8.8
22400	50000	2.3	11.3	1.1	22.4

This indicates that the ATRP polymerization reaction becomes less controlled at higher molecular weights. The lack of control in the polymerization reaction has influence on the surface morphology. The surface of the polymer brush film was imaged via SFM. According to SFM data, the RMS roughness was much higher compared to XRR and varies between 8.8 and 22.4 nm independent of the polymer film thickness. A closer look on the topography revealed the existence of agglomerates on the top of the polymer brush film with diameters varying between 20 and 300 nm (Figure 38a). These agglomerates could not be removed by extraction or treatment in ultrasonic bath. In the phase image, the regions with higher topography correspond to a slight increase of the phase image in the order of 1-2° (Figure 38b). This contrast is quite low and indicates that the agglomerates most probably consist of the same material as the polymer. According to SFM images, the agglomerates must lie on top of a close polymer brush film as pointed out in Figure 38c. This statement is plausible since the Kiessig fringes in the XRR data indicate the existence of a polymer layer with smooth surface morphology.

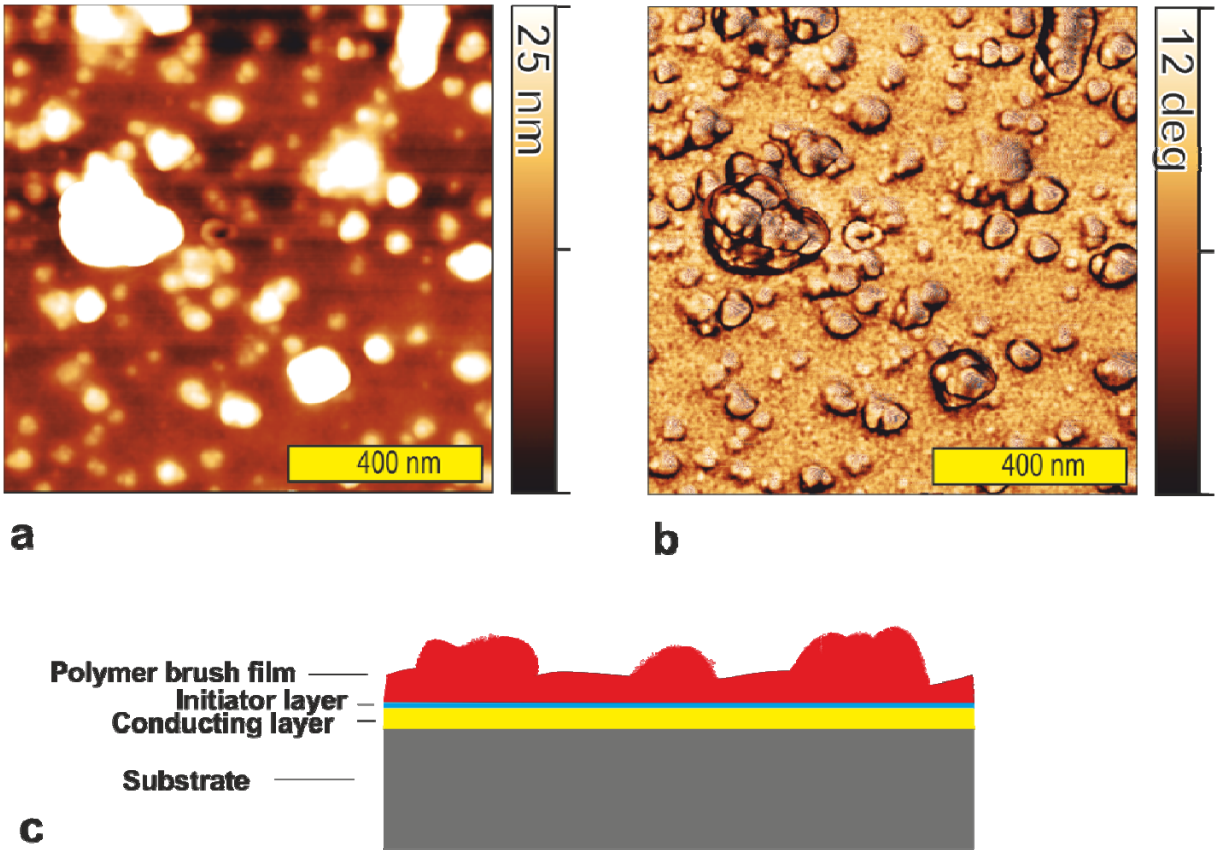

Figure 38. a) SFM topography image and b) SFM phase image for PVBPT grafted brushes on ITO substrate (M_n: 22400, d = 11.3), c) Scheme of agglomerate formation on top of PVBPT grafted brushes.

The origin and the chemical composition of the formed agglomerates, was examined with XPS (Figure 39). The measurements revealed ratios of 92.4%, 3.4% and 4.2% between carbon, nitrogen and sulfur atoms corresponding to the molecular formula of the grafted PVBPT brush, respectively. Theoretical calculation resulted in 91.3%, 4.3% and 4.3% for C, N and S with slight deviation from the experiment. Furthermore, it was disproved that the agglomerates come from the copper complex used for the ATRP, since no copper peak was present in the XPS spectrum. Thus, the agglomerates must come from the polymer itself during the grafting process. With respect to the high reaction temperature, it is probable that the polymerization reaction is partially thermally initiated. The polymer chains growing uncontrollably could agglomerate because of their low solubility and attach to the surface.

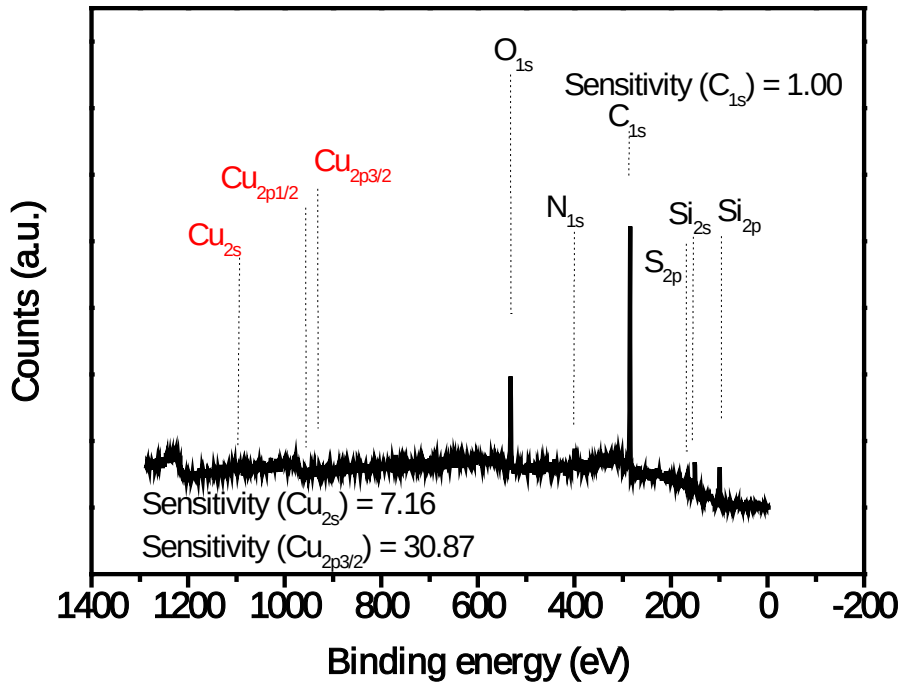

Figure 39. XPS spectrum of grafted PVBPT on silicon substrate.

The mechanical stability of the PVBPT grafted brushes on ITO was examined using SFM based nanowear experiments. Since the experiments can be conducted under defined force application, it's possible to draw conclusions about nanowear stability of the material. For SFM based nanowear experiments, the surface was scanned in contact mode with a defined load of 10 nN on the tip. After 100 repeated scans, the surface topography was then mapped to view morphological changes of the surface (Figure 40). Agglomerates with a diameter between 100 nm up to 1 µm were imaged on the surface before the nanowear experiment. After the nanowear experiment, the surface morphology did not change significantly. Only a few agglomerates were displaced by the tip movement upon the surface. Apparently, many of the agglomerates were pressed or flattened into the surface making the surface smoother. The RMS roughness decreased from 24 nm to 21 nm which confirmed the mechanical stability of the grafted brushes. In comparison to spin-coated PVBPT films, the polymer brush film exhibited higher mechanical wear stability under the same conditions (RMS increase from 0.46 nm to 0.85 nm as shown in chapter IV, Figure 34b). According to the works of Pihan et al.[260], particles imbedded in a polymer matrix are worn out and removed from the surface unless they can crosslink with the matrix. In the wear experiments, no particles were worn out, indicating that the agglomerates are not loose particles but embedded covalently on top or into the polymer film. The surface underneath the agglomerates did not reveal any topographical changes. In particular, formation of ripples and pile up at the scan edges did not occur. Thus, the agglomerates are probably covalently bound and must result from the polymerization step due to poor reaction control.

In conclusion, by using SI-ATRP to graft the PVBPT brushes from the substrate, nanowear resistant redox surfaces were obtained successfully. The presence of sacrificial initiator was obviously not enough to form sufficient amount of persistent radicals. Agglomerates were formed on the surface resulting from the poor control of the polymerization reaction. For better reaction control, Cu (II) salts can be added as deactivating agent to decrease the polydispersity. However, then the reaction rate will be further decreased. In the case of PVBPT brushes, the agglomerate formation already occurred at M_n below 10000 g/mol. For electronic functional media, homogeneous surfaces morphology is preferred. Agglomerates on the surface might be disturbing on the nanometer scale. Therefore, an alternative synthetic approach via post-functionalization was studied to improve the surface morphology of grafted polymer brushes.

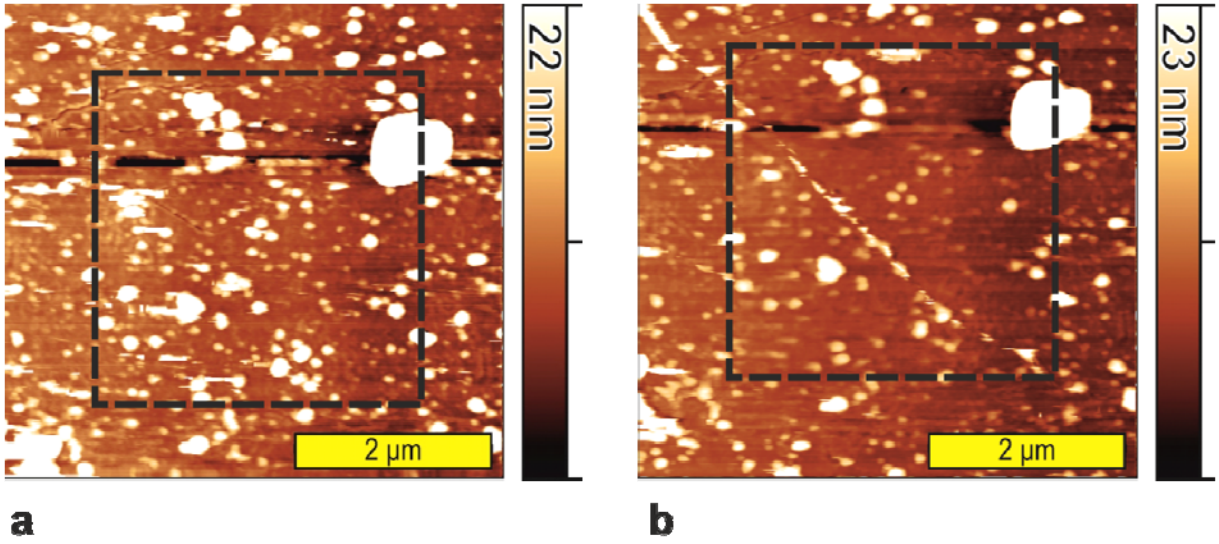

Figure 40. Nanowear experiment of PVBPT brushes on ITO substrate (M_n = 22400 g/mol, d = 11.3 nm) at 10 nN with the speed of 50 µm/s on 3x3 µm² (black dashed square): a) Topography image before the nanowear experiment, b) Topography image after the nanowear experiment.

4.2. Post-functionalization approach

4.2.1. Polymer brush growth

As an alternative route to the direct polymerization, the use of AE brushes to obtain redox active brush polymers was investigated. DPVB was polymerized via standard radical polymerization in Chapter II and successfully used to attach phenothiazine redox moieties such as AEPCA and MPMA to a PS backbone. DPVB is a less bulky monomer compared to VBPT and can also be polymerized easily via controlled radical polymerization. Vinyl benzoates monomers like DPVB are known to be easily polymerized via ATRP with high reaction rates.[261,262,226] However, the synthetic route to obtain grafted AE brushes via SI-ATRP was described by Orski et al.[226] without the use of sacrificial initiator. Therefore, determining the molecular weight M_n and correlating M_n with the film thickness was not possible. Furthermore, the synthetic approach in DMSO as solvent described by Orski et al. was not successful. The synthetic approach was therefore modified with addition of sacrificial initiator in DMF without using Cu(II) salts. This way, it was also possible to determine the molecular weight M_n of the free polymer. First, the

monomer was polymerized from the substrate via SI-ATRP (Scheme 45). Then, in a second step, the activated ester groups were replaced by phenothiazine based moieties. To functionalize the brushes, two different moieties were chosen (Scheme 47). Except for MPMA, the commercially available NMB was selected as phenothiazine moiety. NMB is mainly used as staining and contrast agent for cell biology.[263] MPMA only contains one primary amine group and should not lead to crosslinking by the reaction with the activated ester groups. NMB however has two secondary amine groups and can therefore bind with the activated ester brush by crosslinking. The additional crosslinking could further mechanically stabilize the polymer film coating.

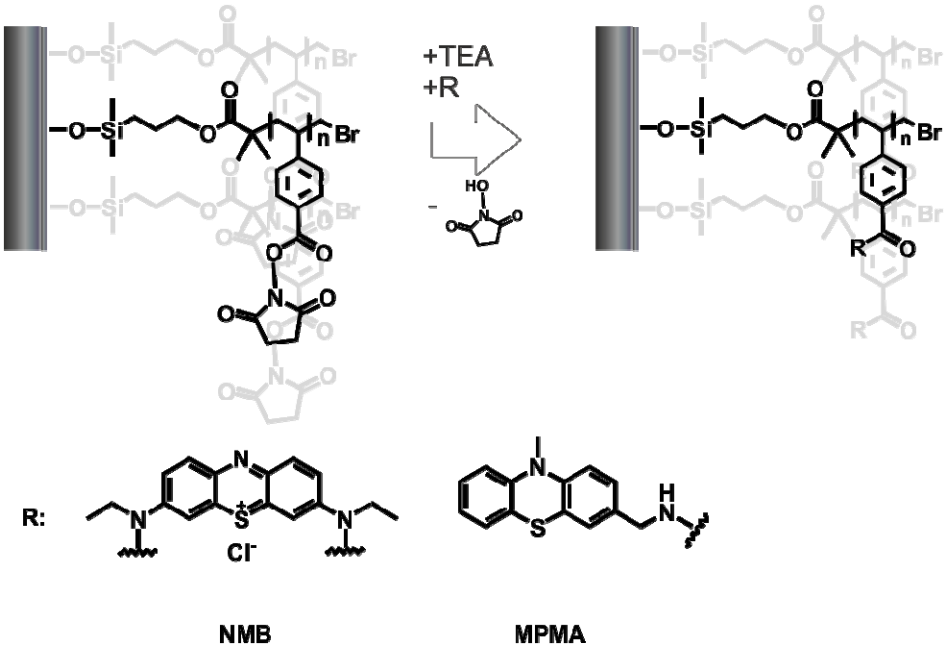

Scheme 47. Post-functionalization of poly-DPVB activated ester brushes with NMB and MPMA.

In the following, the PDPVB brush is referred to as AE polymer brush and the free PDPVB polymer referred to as AE polymer. After successfully attaching AE polymer brushes via SI-ATRP, film thickness and RMS roughness were measured with XRR. In addition, the molecular weight of the free AE polymer in the reaction solution was determined by GPC. The polymer film thickness increased with the molecular weight of the free polymer as can be seen from the decreasing Kiessig fringe distance (Figure 41a). A linear dependence of the grafted polymer film thickness with increasing M_n was observed. The linear fit has an intercept point at approximately 0.3 ± 0.7 nm (Figure 41b). The reaction took place under controlled conditions as expected for a living radical polymerization. Thus, the SI-ATRP successfully resulted in grafted AE polymer brush film.

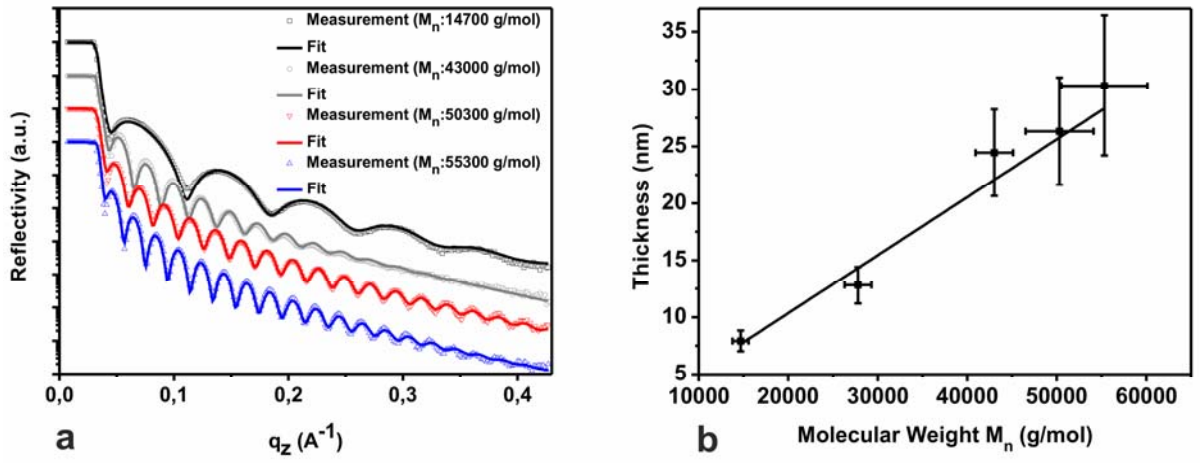

Figure 41. a) XRR curves of AE grafted brushes on silicon substrate with different molecular weights fitted according to parratt formalism, b) Thickness dependence of AE grafted brushes on silicon substrate with increasing molecular weight of the bulk AE.

The polydispersity of the bulk polymer slightly increased from 1.3 to 1.6 at increasing molecular weight from M_n = 14700 g/mol to 55300 g/mol. In comparison to the polydispersity of the bulk PVBPT (PDI =2.3), even at molecular weights above 50000 g/mol, the polymerization took place under more controlled conditions. The RMS roughness of the surface measured with XRR was below 1 nm (between 0.6 nm and 0.9 nm). The low RMS roughness indicates that the polymer film surface is more homogeneous compared to PVBPT grafted brush polymer films. Furthermore, the XRR data indicate that larger film thicknesses of around 30 nm can be obtained using DPVB as monomer (Table 12). The monomers are less bulky than the VBPT and simultaneously the succinimide groups increase their reactivity.

Table 12. Molecular weight of AE bulk polymer and surface properties of grafted AE polymer brush on silicon substrate at different molecular weights.

Experimental molecular weight M_n (g/mol)	Calculated molecular weight M_n (g/mol)	Experimental polydispersity	Thickness measured with XRR (nm)	RMS Roughness measured with XRR (nm)
14700	20000	1.3	7.9	0.6
43000	40000	1.5	24.5	0.9
50300	50000	1.6	26.3	0.6
55300	60000	1.6	30.3	0.8

For the AE brushes, a grafting density of $\Gamma_{g,exp}$ = 0.36 ± 0.02 chains/nm^2 was obtained from the simulation of the XRR curves with respect to the electron density (= polymer density) and from equation (24). For the calculation, a density of ρ = 1.08 g/cm^3 for AE polymer and a molecular weight of M_n = 55300 g/mol were used. A theoretical maximum interchain distance of a=

1.31 nm resulted for AE polymer brushes, using the equation (32). The calculation included an estimated helical conformation of the polymer chains with M = 245.23 g/mol and n_m = 2. This resulted in a theoretical maximum grafting density of $\Gamma_{g,theo}$ = 0.58 chains/nm² which is in good agreement with the experimental results. The successful grafting of AE polymer brushes allows the attachment of redox active moieties by substitution of the activated ester functional groups on each repetition unit. For successful attachment of the moieties to AE polymer brushes, primary or secondary amine groups are necessary. Two different redox moieties based on phenothiazine with one and two amine groups were attached to AE polymer brushes in the following section. With these experiments, it was possible to observe the effect of the functionalization on the surface morphology and with respect to mechanical stability. Especially, the effect of crosslinking on the mechanical stability by the use of a diamine moiety was studied.

4.2.2. Functionalization of AE polymer brushes

After grafting AE polymer brushes to ITO as a substrate, the active ester groups were functionalized in a second step with the moieties MPMA and NMB according to Scheme 47. The wafers were extracted thoroughly with a good solvent to remove non-reacted moieties. In order to show the successful attachment of the moieties to the AE polymer brushes, UV/Vis measurements were performed on grafted brushes before and after the functionalization with MPMA and NMB (for brush film thickness of 26.3 nm). For MPMA post-functionalized AE polymer brushes (ITO + AE + MPMA), two peaks were assigned at 319 and 400 nm. The latter peak can be assigned to the AE polymer brush (Figure 42).

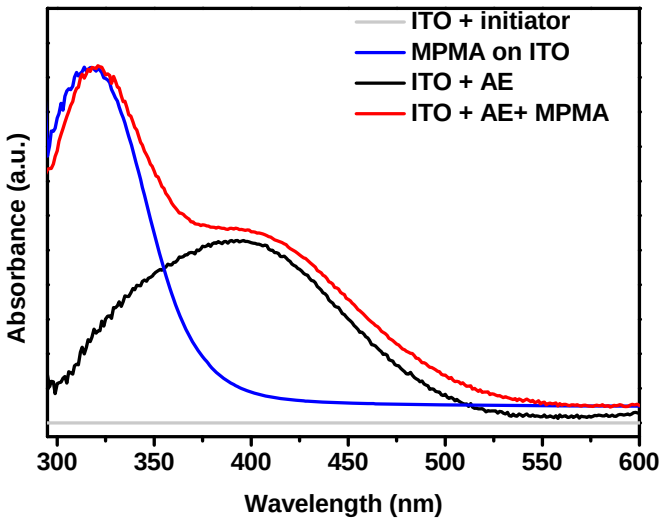

Figure 42. UV/Vis spectra of grafted AE polymer brush on ITO substrate before and after the reaction with MPMA. Spectra of MPMA spin-coated on ITO, ITO functionalized with the initiator, ITO with grafted AE and AE on ITO post-functionalized with MPMA.

The UV/Vis spectrum showed a broad distribution which is a hint for the conversion degree of the active ester moieties. Since the peak at 400 nm is present after the reaction with MPMA, presumably the reaction was not quantitative. In comparison, the free MPMA on ITO has only

one significant peak at 317 nm. In the literature for N-methylphenothiazine (with a similar structure as MPMA) a peak of 310 nm was reported.[66] The slight shift of MPMA resulted from the bathochromic effect of the methamine group. The bathochromic effect implies that the methamine functionality shifts the absorption spectrum towards larger wavelengths.

The conversion of NMB with the AE polymer brushed was observed with UV/Vis on a glass substrate over time to study the reaction kinetics of NMB with the activated ester moieties of the polymer brush. The lower absorbance of the pure quartz glass allows better signal to noise ratio compared to ITO. Functionalized glass wafer were removed out of the reaction solution and washed thoroughly with DMF to remove superfluous NMB. UV/Vis signal was then recorded after time intervals of 1, 2, 4, 8 and 23 hours (Figure 43a).

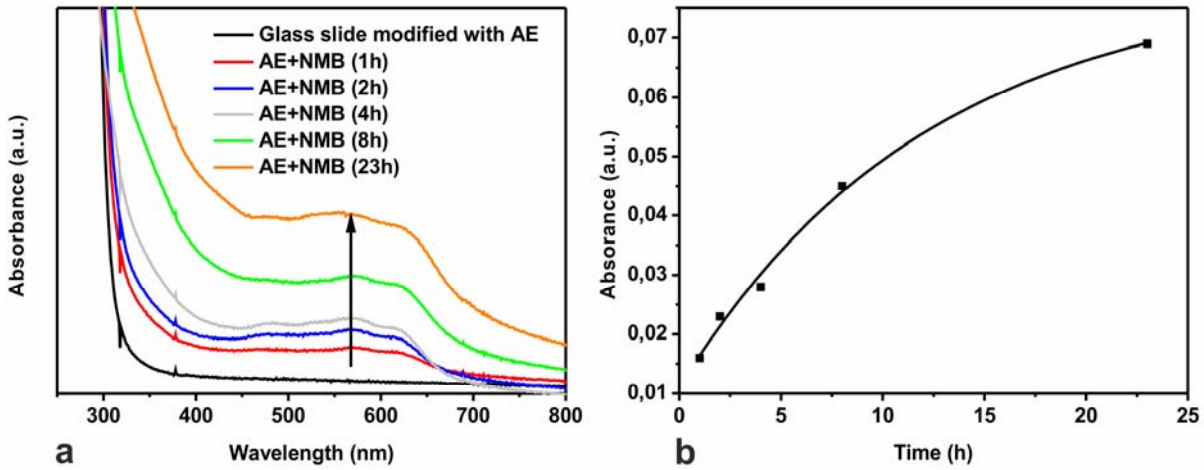

Figure 43. a) UV/Vis Vis spectra of grafted AE polymer brush on glass substrate before and after reaction with NMB after different time intervals, b) Plot of peak absorbance at 575 nm against time for kinetic studies of NMB with the activated ester moieties of the polymer brush.

The glass slide modified with AE polymer brush was transparent exhibiting no peak and strong absorption below 300 nm. After adding NMB, a broad peak at 575 nm appeared which increased approximately four times in absorbance with further reaction time from 1 hour to 23 hours. From literature, two peaks at 286 and 586 nm were assigned for NMB.[264,265] The first peak was not visible and was covered by an absorbance shoulder above 350 nm. The second peak at 575 nm corresponded to the literature value and was slightly shifted towards smaller wavelength. By plotting the absorbance against the time, the kinetic curve of the NMB reaction rate with the activated ester moieties of the polymer brush was obtained. The curve indicates a saturation behavior of the absorbance with time. Whit increasing reaction of the AE sites, further reaction of the moieties becomes more difficult. The sites are blocked and hinder further attachment of NMB to the remaining sites due to crosslinking. For both cases, a successful attachment of the moieties to the AE polymer brush was observed. However, it is assumed that the reaction did not take place quantitatively. To find out more about the conversion degree of the activated ester sites and about the redox functionality of the converted AE polymer brushes, CV measurements were performed.

4.2.3. Redox functionality of post-functionalized AE polymer brushes

To check the functionality, i.e. the redox activity of post-functionalized AE polymer brushes, CV measurements were performed in solution (Figure 44). The CV data showed no oxidation peak for the AE polymer brushes before functionalization (Figure 44a, AE on ITO). At the beginning, ITO substrates with AE polymer brushes post-functionalized with NMB were measured against Ag/AgCl. After modification with NMB, an anodic oxidation peak at $E^{0/+1}$ = 0.48 V and a cathodic reduction peak at $E^{+1/0}$ = 0.35 V at a scanning speed of 10 mV/s was observed (Figure 44a, AE + NMB). By increasing the scan velocity up to 50 mV/s the oxidation peak slightly shifts to $E^{0/+1}$ = 0.56 V. Simultaneously, the reduction peak shifts to $E^{+1/0}$ = 0.28 V. The free NMB revealed an oxidation peak at $E^{0/+1}$ = 0.34V and a reduction peak at $E_0{}^{+1/0}$ = 0.19 V with a scan velocity of 10 mV/s (Figure 44b). The sweep cycle could be repeated for more than 10 times without any significant change in the position and intensity of the peaks.

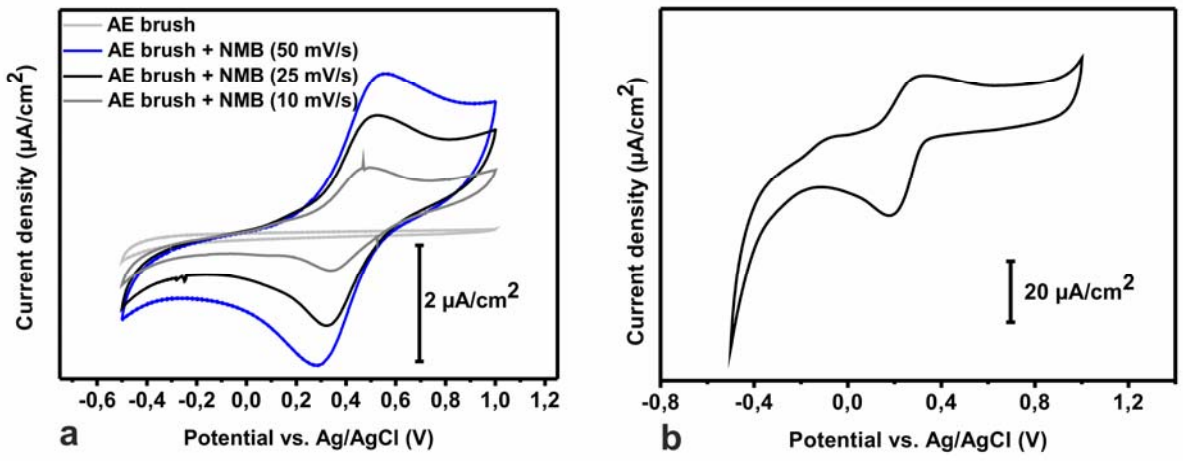

Figure 44. a) CV of grafted AE brush on ITO substrate at different scan speeds in 0.1 M TBAPC/ACN solution before and after reaction with NMB, b) CV of NMB-solution in $LiClO_4$ in ACN solution (0.1 mM/0.1 M) measured at the scan speed of 10 mV/s. The potential is measured with Ag/AgCl and Pt as the reference and the counter electrode, respectively.

The increased cycle stability and the stability at high scan speeds indicate that the moieties have been incorporated inside the polymer brush matrix. The peak separation between free NMB and NMB grafted to AE polymer brushes was ΔE_p = 0.15 V and 0.13 V, respectively. The shifts in the peak position for free NMB and NMB grafted to AE polymer brushes (around 140 mV) result from the overpotential at the ITO working electrode. The increased diffusion barrier at the polymer film/ITO interface led to an increase of the oxidation potentials. From the integral below the CV curves, the conversion degree of the AE polymer brushes with NMB was estimated. For a known concentration of 0.1 mM NMB in ACN, an integral of $1.68*10^{-5}$ µAV/cm² in the range of -0.14 V and 0.66 V was obtained. For the NMB grafted to the AE brushes, an integral of $5.87*10^{-7}$ µAV/cm² (range 0 to 0.8 V, shifted around the oxidation peak) was observed which corresponded to $7.49*10^{-9}$ mol NMB. Taking the molecular weight of M_n= 55300 g/mol and the grafting density of $\Gamma_{g,exp}$ = 0.36 chains/nm² of AE polymer brushes into account, $1.43*10^{-8}$ mol of activated ester groups were available on the grafted ITO surface of 1.21 cm² size. This means

that almost 52% of the active sites have been replaced by NMB. Thus, the reaction with NMB did not proceed quantitatively. However, it has to be considered that NMB has two amine functionalities which might react with the active ester groups. Therefore, the conversion degree can only be considered as a rough estimation. This observation can be explained by the hindered diffusion of the moiety through the polymer film. In the reaction solvent DMF, the AE polymer brushes are slightly swollen.[266] However, due to the bulkiness of NMB and its hydrophilic nature, NMB cannot completely penetrate the polymer film. In the case of thinner AE polymer brush films more active ester moieties can be converted with NMB. For AE polymer brush films with 7.9 nm thickness after the reaction with NMB, a conversion degree of 82% was determined via CV-measurements (Figure 45).

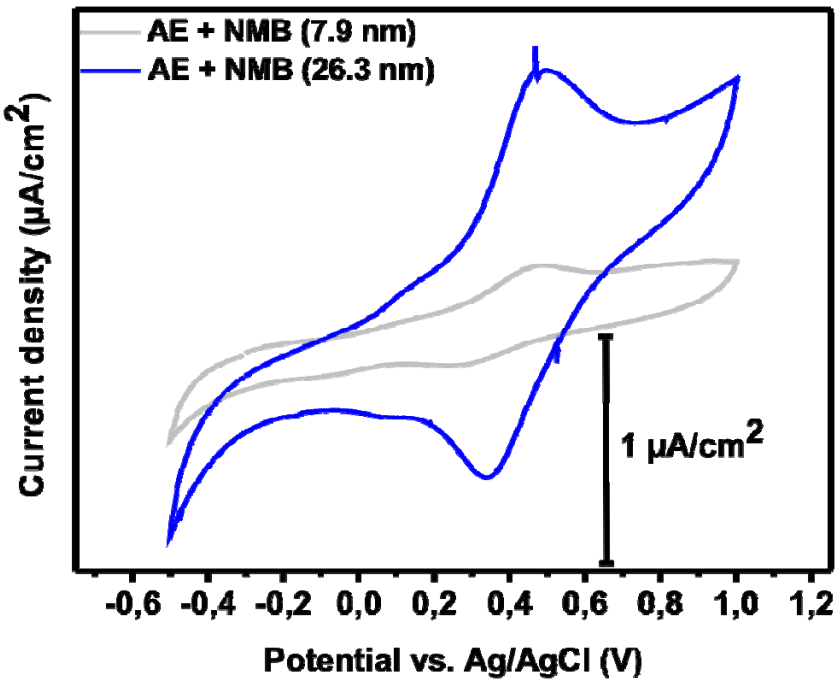

Figure 45. CV of AE polymer brushes with different thickness on ITO substrate (7.9 nm, 26.3 nm) post-functionalized with NMB in 0.1 M TBAPC in ACN solution at the scan speed of 10 mV/s. The potential was measured with Ag/AgCl and Pt as the reference and the counter electrode, respectively.

From the CV experiments, the diffusion constant of the oxidized and reduced species was calculated according to Randles-Sevcik equation (33). Using the concentration of 1.95 mmol/cm^3 (estimated from the density of 1.13 g/cm^3 and molecular weight of the repeating unit M of 579 g/mol), diffusion constants of $3.98*10^{-15}$ and $4.07*10^{-15}$ cm^2/s were obtained for the oxidation and reduction step respectively. The diffusion constant is much slower compared to the spin-coated PVBPT film (5 orders of magnitude) and even slightly slower (one order of magnitude) than PVBPT polymer brush film. The comparison with MPMA post-functionalized AE polymer brushes resulted in diffusion constants of $4.80*10^{-14}$ and $7.52*10^{-14}$ cm^2/s (estimated from the density of 1.05 g/cm^3 and molecular weight of the repeating unit M of 372 g/mol) from the CV experiments (appendix, Figure A 12). The CV experiments confirm that additional

crosslinking by NMB moieties leads to a decrease of the diffusion rate as previously observed by Kojima et al.[212] For a known concentration of 0.03 mM MPMA in ACN, the integration in the range of -0.04 and 0.76 V resulted in an area corresponding to $3.97*10^{-5}$ µAV/cm². For the MPMA grafted to the AE brushes, an integral of $5.53*10^{6}$ µAV/cm² (range 0 to 0.8 V, shifted around the oxidation peak) was observed which corresponds to $9.57*10^{-9}$ mol MPMA. Taking the molecular weight of M_n= 50300 g/mol and the grafting density of $\Gamma_{g,exp}$ = 0.36 chains/nm² of AE brushes into account, $1.43*10^{-8}$ mol of active ester groups are available on the grafted ITO of 1.21 cm² size. Thus, a conversion degree of approximately 67% was obtained for AE polymer brushes modified with MPMA. In conclusion, the CV data confirmed the successful post-functionalization of both moieties NMB and MPMA with the AE polymer brushes. To find out the effect of the post-functionalization on the surface morphology and on the nanowear stability, the surface was analyzed by SFM and X-ray methods. This way, it is possible to compare advantages and disadvantages of the post-functionalization technique with direct polymerization.

4.2.4. Surface analysis of AE brushes

Surface topography and film thickness

To examine the surface morphology, the surface topography of the AE polymer brushes was imaged with SFM before and after the reaction with the redox moieties NMB and MPMA. As already expected from the low RMS roughness according to the XRR data and the moderate polydispersity (Table 12), the surface of the AE polymer brush film must be quite smooth. The SFM topography images proved the formation of a very homogeneous AE polymer brush film independent of the molecular weight (Figure 46). For both film thickness of 7.9 and 30.3 nm for example, the RMS roughness was below 1 nm with 0.4 and 0.6 nm.

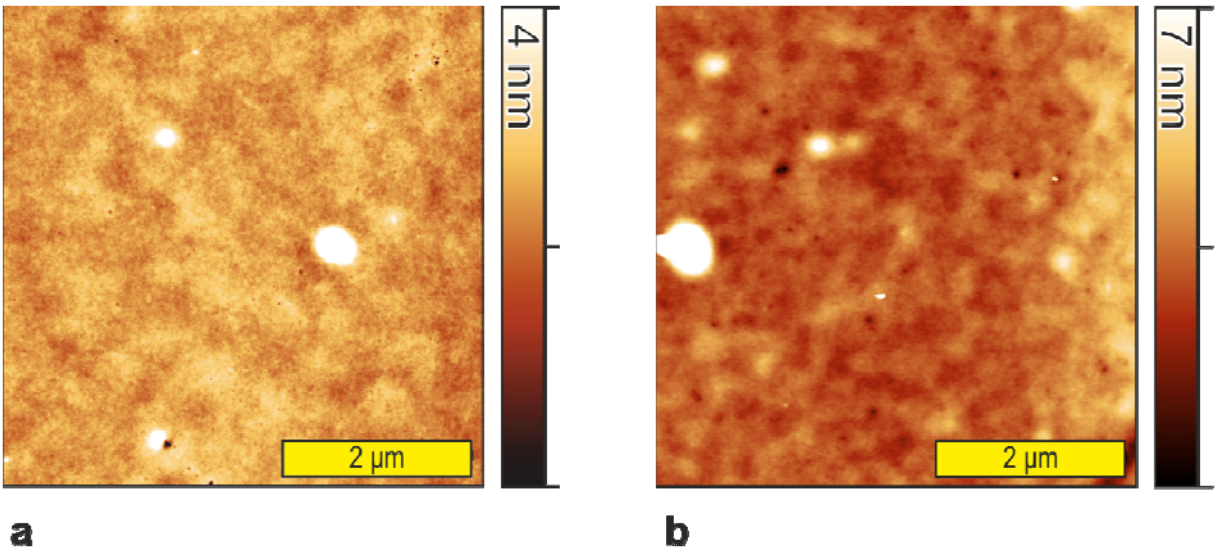

Figure 46 SFM Topography image of grafted AE films on ITO substrate for a) Thickness d = 7.9 nm and b) 30.3 nm.

Compared to PVBPT grafted brushes the AE polymer brushes resulted in more homogeneous films with respect to the topography and revealed almost no agglomerations of polymers. Thus,

a low polydispersity of the free polymer according to GPC data corresponded to increased homogeneity of the polymer brush film. The surface properties of the NMB and MPMA post-functionalized AE polymer brushes were examined with SFM (Figure 47). Before the reaction, the surface topography of the AE polymer brushes exhibited a RMS roughness of 0.3 nm (Figure 47a). However, the RMS roughness increased up to 4.3 nm and 2.4 nm after the reaction with NMB (Figure 47b) and MPMA (Figure 47c), respectively. The increase of the RMS roughness is related to the reaction of the moieties with AE brush which changes the chemical properties of the polymer brush. Those moieties which have reacted with NMB change the chemical nature of the polymer brush. Phase separation from non-reacted moieties can occur when there is no good solvent for both non-converted and converted regions. The effect of the phase separation leads to formation of nano-domains with dimple structures as shown by Ochsmann et al. for PS/PMMA mixed brushes.[237] By treatment of the mixed brushes with a selective solvent for PS brushes, a dimple like structure is formed reversibly due to phase separation of the PS brush domains. which also lead to an increase of the surface roughness.

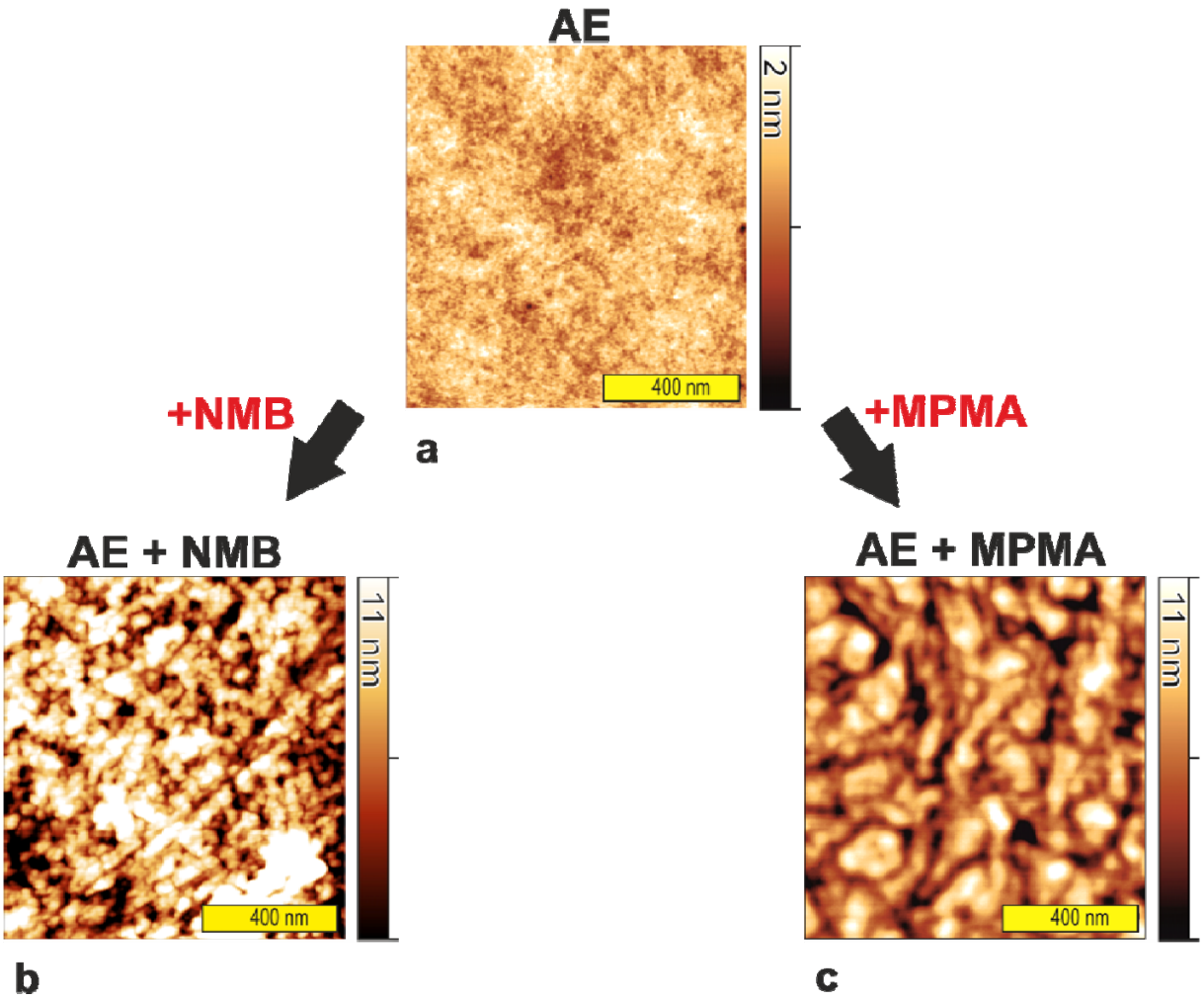

Figure 47. a) Topography image of grafted AE brush (brush thickness 26.3 nm) on silicon, b) Topography image of grafted AE brush on silicon after the post-functionalization with NMB c) and with MPMA.

As already seen from the CV data, the conversion degree with the redox moiety NMB was 30% higher for the AE polymer brush film with the thickness of 7.9 nm compared to 26.3 nm. Thus, it

is assumed that thinner polymer brush films react with higher conversion degree and the high conversion degree leads to less phase separation. Unlike the thin films, in thicker AE polymer brush films NMB can only react partially with the activated ester moieties. The penetration of the moieties through the film is aggravated which causes phase separation. The strong phase separation must consequently lead to an increase of the surface roughness (Scheme 48).

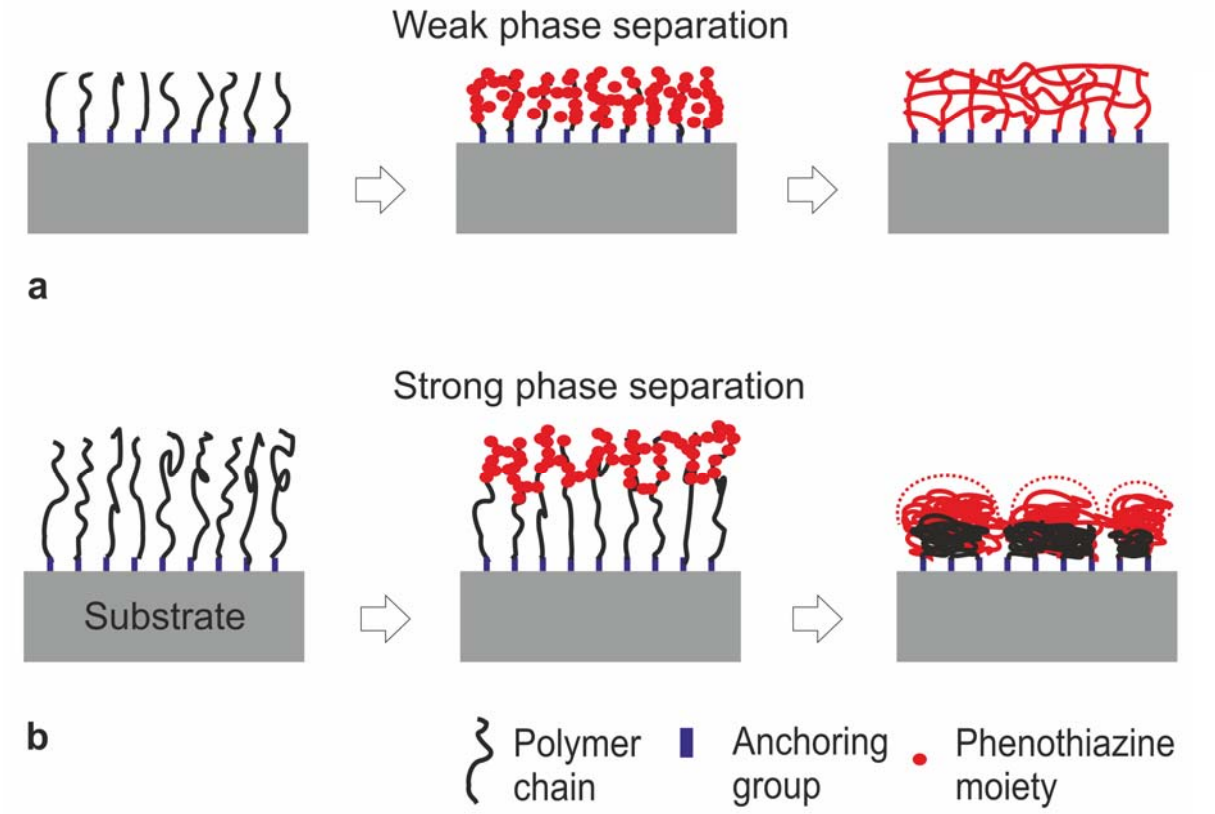

Scheme 48. Phase separation of AE polymer brushes due to non-quantitative reaction of NMB or MPMA with the activated ester moieties depending on the film thickness. a) Weak phase separation, b) Strong phase separation.

For NMB post-functionalized brushes, the RMS roughness calculated from XRR data increased with the thickness of the initial AE brush from 0.9 nm to 5.7 nm by increasing the thickness from 7.9 nm to 30.3 nm, respectively (Table 13). The RMS value before the reaction was determined between 0.6 and 0.9 nm.

Table 13. Change of thickness and roughness measured from XRR curves and from SFM data before and after reaction of AE brushes (different thickness) with NMB. (* for 1 µm²)

Run	Thickness measured with XRR before /after (nm)	RMS roughness measured with XRR before / after (nm)	RMS roughness measured with SFM before / after (nm)*
1	7.9 / 8.1	0.6 / 0.9	0.4 / 2.0
2	24.5 / 26.2	0.9 / 1.8	0.3 / 3.4
3	30.3 / 29.7	0.8 / 5.7	0.6 / 4.3

The thickness did not change significantly, except for a slight increase in the first and second run (0.2 and 0.7 nm) and a slight decrease (0.6 nm) in the third run. The RMS roughness measured by SFM, showed an increase of the RMS roughness from 2.0 nm to 4.3 nm, respectively. According to the XRR data, the roughness change was less prominent in the first run since the first, second and third Kiessig fringes were still visible after the reaction with NMB (appendix, Figure A 13). With increasing film thickness, the damping of Kiessig oscillation became stronger until at 30.3 nm, the oscillation completely vanished. The vanishing of the fringes is due to the increase of surface roughness which results in intensified scattering. Thus, the thicker the AE brush film, the more significant were the changes in the polymer film RMS roughness and surface topography after the modification. This increase in the RMS roughness was explained by phase separation taking place at higher molecular weights.[267] Since the reaction proceeds more slowly and less conversion of the activated ester moieties occurs, the grafting density (here in terms of post-functionalizing the activated ester moieties) is decreased. Post-functionalized regions form larger domains which tend to phase separate. Chemical reaction of the redox moieties NMB and MPMA obviously leads to changes of the surface topography. It would be of interest to examine the topographical changes with respect to chemical composition. Therefore, XPS measurements were performed to analyze the surface composition before and after the attachment of the redox moieties NMB and MPMA. In contrast to MPMA, NMB has the possibility to crosslink the AE polymer brushes because of its diamine functionality. With SFM nanowear experiments, the effect of the crosslinking on the nanowear stability of the AE polymer brushes after the reaction with both redox moieties was elucidated in the upcoming section.

XPS analysis and surface wear

To get a better understanding of the chemical processes on the surface, XPS measurements of AE brushes before and after the reaction with NMB and MPMA were performed (appendix, Figure A 14). In particular, the carbon peak before and after the reaction with NMB and MPMA was analyzed (Figure 48).

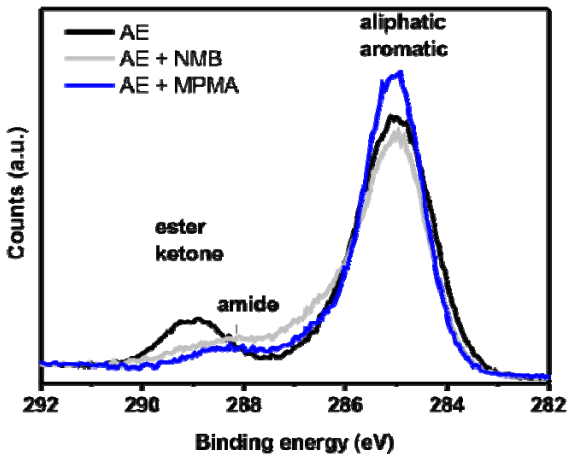

Figure 48. XPS spectra of the carbon (C_{1s}) peak from grafted AE brush on silicon substrate before and after functionalization with NMB and MPMA.

The aromatic and aliphatic signals appeared as a broad peak at around 285 eV. The ester bond of the activated ester brushes at around 289 eV widely disappeared and shifted to a new bond at around 288 eV, which is related to the amide bond after the reaction with NMB and MPMA. However, the broadening of the carbon peak at 288 eV indicated that some activated ester moieties did not react. The ratio between the elements confirmed the successful reaction of NMB with the AE polymer brushes (Table 14). After the reaction of the AE with NMB, the amount of carbon increased from 74% to 82% while the amount of oxygen decreased from 22% to 6% simultaneously. Additionally, the sulfur and chlorine content increased, indicating the attachment of NMB. Furthermore, no corresponding zinc peak for NMB was observed. The $ZnCl_2$ of the initially used NMB double salt must have been washed away after the reaction and subsequent extraction. The absence of $ZnCl_2$ is a further proof that NMB has reacted successfully with the brush moieties.

Table 14. Ratio between the elements C, N, O, S, and Cl for AE polymer brush grafted from silicon substrate measured with XPS before and after the reaction with NMB.

Element	AE polymer brush (Theory)	AE polymer brush (Experiment)	AE polymer brush +NMB (Theory)	AE polymer brush +NMB (Experiment)
C	72.2%	73.7%	83.3%	82.4%
N	5.6%	4.8%	7.1%	6.2%
O	22.2%	21.5%	4.8%	6.3%
S	-	-	2.4%	2.8%
Cl	-	-	2.4%	3.2%

For the attachment of MPMA to the AE polymer brushes, a good accordance of the theoretical and experimental XPS results were obtained (appendix, Table T 10). The amount of carbon increased from 74% to 86% while the amount of oxygen decreased from 22% to 6% simultaneously. Deviation from the theoretical value result from the non-quantitative reaction of MPMA with the AE polymer brushes. It is difficult to estimate the conversion degree from the XPS experiments since the peaks for amide and ester groups are so close to each other. Under consideration of the increase of the carbon amount from experiment and theory, the conversion can be estimated from the experiment to ratio of difference between the carbon amount before and after the reaction. For NMB and MPMA modified AE polymer brushes, a conversion degree of 78% and 98% was calculated. The calculated values are higher than the conversion degrees determined by CV experiments (52% and 67% for NMB and MPMA) but show the same tendency with respect to the reactivity with the AE polymer brushes. Nevertheless, the results from the CV experiments are in better agreement with the experimental observation from the UV/Vis.

In the following step, the mechanical stability was investigated with SFM. The nanowear test for the NMB post-functionalized AE brush exhibits high mechanical stability of the grafted polymer brush (Figure 49a).

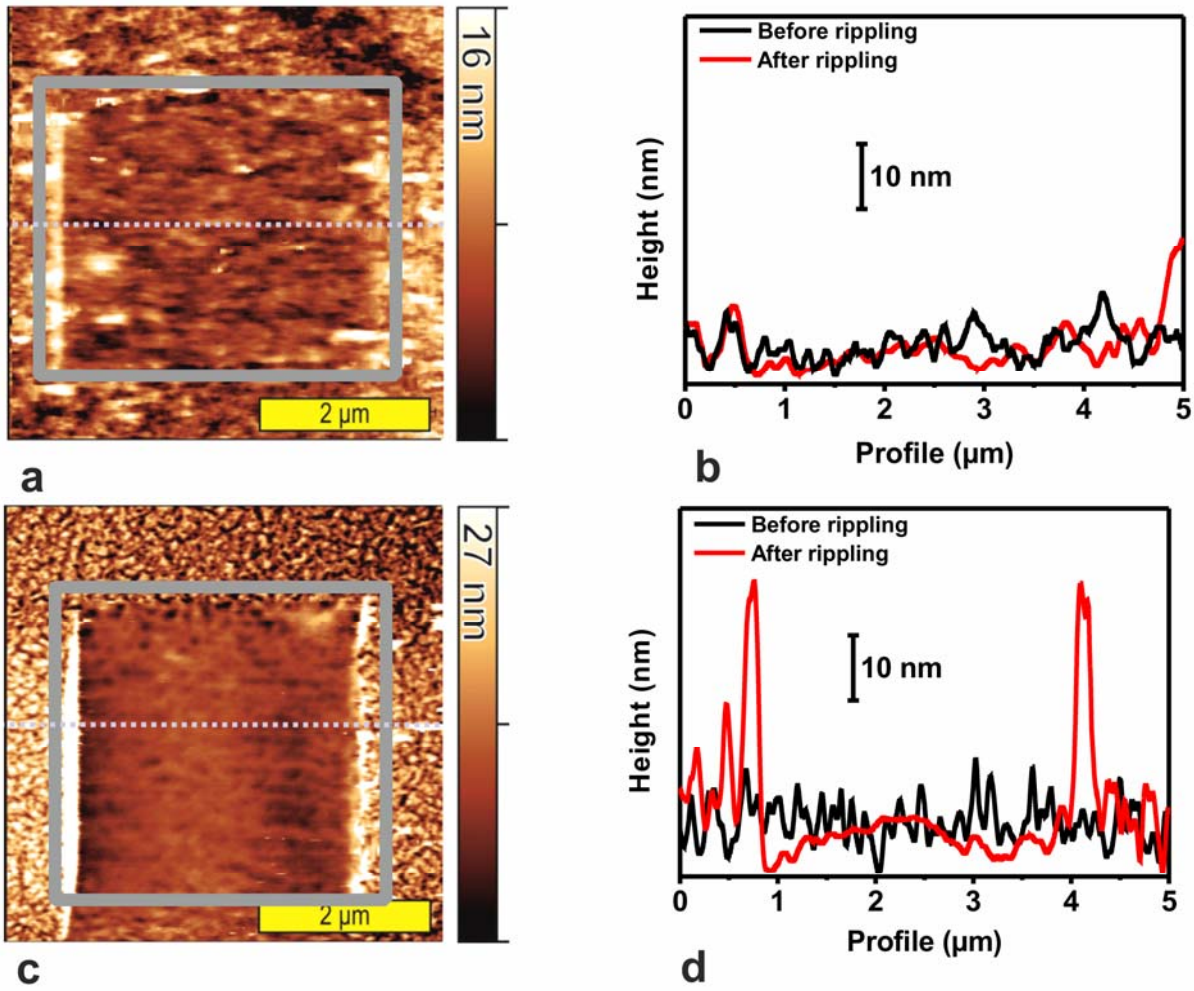

Figure 49. a) Topography image for NMB post-functionalized AE brushes after the nanowear (rippling) experiment, b) Corresponding average height profile along the red line before and after reaction with NMB, c) Topography image for MPMA post-functionalized AE brushes, d) Corresponding average height profile along the red line before and after reaction with MPMA.

The RMS roughness of the topography images decreased slightly from 2.8 nm to 2.5 nm after 100 scans in contact mode with an applied load of 10 nN. The scanned area showed a smoother surface after the nanowear experiment. A small amount of piled up material (~1-2 nm increase) was visible in the left edge of the line profile (Figure 49b). This pile up could arise from loose impurities on the surface. The nanowear experiment for the MPMA post-functionalized AE polymer brush revealed lower mechanical nanowear stability compared to NMB post-functionalized brushes (Figure 49c). At the edge of the scanned area, a strong pile up of the surface to around 40 nm was visible (Figure 49d). The difference between the nanowear stability of the NMB and MPMA functionalized brushes can be explained by the crosslinking ability of the redox moieties. MPMA has only one amine functional group. Therefore, it is not possible to form crosslinking between the brush chains. NMB however has two secondary amine groups and can function as crosslinking agent between the grafted polymer chains. This

additional crosslinking leads to the formation of a polymer network, which is then mechanically more stable.

5. Summary and Conclusion

Two different approaches for synthesizing redox active polymer brushes with phenothiazine moieties were presented in this chapter. Both approaches were successfully implemented and have their advantages as well as disadvantages. Polymer brushes with phenothiazine moieties on each repetition unit were successfully attached to a conducting ITO surface using direct polymerization via SI-ATRP. Above all, the so formed brushes revealed redox behavior on the surface. In addition, the obtained polymer brush surfaces showed an increased mechanical stability during the nanowear experiments. The synthesis of PVBPT and the direct polymerization technique were both performed as a single step reaction what is desirable with respect to the synthetic expense. The direct polymerization of monomers with phenothiazine redox moieties was interesting for obtaining redox active surfaces. However, the surface morphology revealed inhomogeneities due to agglomerate formation. Homogeneous surfaces with high grafting densities are desirable for SFM based data storage. On homogeneous surfaces, the topography has less impact on the scanning process during writing and reading in contact mode. By improving the reaction conditions, formation of the agglomerates might be suppressed. Other phenothiazine containing monomers with higher reactive backbone such as acrylates can be used instead. Furthermore, better reaction control can be achieved by addition of deactivating agent or by using activator controlled reaction condition such as activator generated by electron transfer (AGET)[268], activator regenerated by electron transfer (ARGET)[269] or initiators for continuous activator regeneration (ICAR).[270]

The activated ester approach resulted in homogeneous polymer brush films. Therefore, the approach with activated ester appeared a promising technique for synthesizing redox active surfaces for SFM based data storage. Grafted activated ester brushes with succinimide moieties using SI-ATRP were synthesized. Compared to PVBPT grafted brushes, the grafting density could be slightly increased by using activated ester brushes. A higher grafting density means more redox moieties in the patterned area which can help to increases the storage density. These brushes were then functionalized in the second step using the moieties NMB and MPMA. Both moieties reacted with the activated ester brush, which was proved using various techniques such as UV/VIS, CV and XPS. These data confirmed that the reaction did not take place quantitatively. Since the conversion of the moieties with the activated brush polymer units was not quantitative, phase separation took place. Consequently, the RMS roughness of the polymer film increased with film thickness. Thinner films proved to show less increase of the RMS roughness. Due to facile diffusion of the redox moieties through the polymer brush film, thinner films exhibited higher conversion ability. With respect to nanowear stability, activated ester brushes showed differences depending on the degree of crosslinking with the redox moiety. NMB functionalized brushes exhibited a higher nanowear resistance than MPMA functionalized

brushes. As expected, the additional crosslinking using NMB as the redox moiety resulted in more stable surfaces. With the post-functionalization technique, nanowear stable redox active polymer brushes could easily be synthesized. To improve the conversion reaction, more reactive amine moieties should be used. Especially primary amine groups are more reactive species compared to secondary amine. Also the film thickness is an important factor. Low film thickness facilitates the diffusion of the redox moieties and enables the reaction with the activated ester groups. With variation of the activated ester monomer and functional moieties nanowear stable redox surfaces can be obtained on almost every type of substrate for potential application in textile and electronic industry.

VI. Summary and Outlook

The focus of the current work was the synthesis of polymers with phenothiazine redox moieties and their applicability as energy and data storage media.

A series of new monomers with pendant phenothiazine moieties were successfully obtained by synthetic approach at the nitrogen atom (N-position) and the aromatic ring of phenothiazine and its derivatives. Polymers were then synthesized from vinyl and amine based monomers with direct polymerization and post-functionalization methods. The nucleophilic substitution of phenothiazine at the N-position is very simple and versatile, thus can be chemically accessed even by inexperienced chemists.

In the direct polymerization method, vinyl based monomers were easily polymerized by standard radical polymerization method. The key issue for the successful direct polymerization is the formation of stable radicals and subsequent inhibition of the polymerization reaction. The reactivity of the vinyl group should be higher than the inhibition reaction induced by the radical species. To obtain further new vinyl monomers with phenothiazine functionality, also coupling reactions have to be considered. Except for the Ullmann coupling, other synthetic approaches such as Suzuki coupling are useful alternatives to new vinyl monomers with expanded π-conjugation of the aromatic ring system. The expansion of the π-conjugation affects the redox behavior of the monomer and its resulting reactivity.[271] The obtained polymers could be used as new p-type hole transporting materials.[272,273]

In the post-functionalization method, activated ester polymers were functionalized with primary amine containing phenothiazine moieties. The use of activated ester polymers for obtaining phenothiazine bearing polymers is an advantageous alternative to direct polymerization. The synthetic approach is straight forward and quite versatile due to free choice of the molecular design. By choosing sterically unimpeded moieties with primary or secondary amine groups a combination of functional units can be introduced inside a polymer backbone. The possibility of using controlled radical polymerization to polymerize activated esters offers new methods to synthesize different polymer architectures. Phenothiazine moieties can be integrated in a combination with other functional monomers to obtain block copolymers[227], cross-linkable polymers[93] and grafted polymer brushes[226] for various applications in the electronic field. The use of activated esters should be considered as an alternative in two cases: if the density of redox moieties in the polymer chains is not important or if the polymerization of the moiety does succeed due to sterical or reactivity reasons.

To examine the applicability of polymers with phenothiazine redox moieties for the application as energy storage media, polymers were characterized electrochemically and by integrating them as cathode materials in battery coin cells. The coin cells featured decent charging capacities and could be charged and discharged for over 500 cycles only within several

minutes. With respect to the good cycle stability and fast charging time, these polymers could find application as cathode materials for ultra fast rechargeable battery devices. The stabilizing effect of the propylene spacer between phenothiazine and the polymer backbone should be considered to improve the chemical cycle stability of potential cathode materials[274] with similar molecular structure. Simultaneously, by choosing longer alkyl spacer than propylene, a decrease of the electron transfer rate would have a negative effect could on the overall redox performance.[31,111,120] By integration of phenothiazine polymers in battery cells, higher oxidation potentials compared to other organic redox groups like quinine[275] or TEMPO[111] are achievable. This potential increase is useful for designing battery devices with higher overall cell potentials. With respect to the synthetic efforts, phenothiazine based polymers are possible alternatives to TEMPO based polymers since they are accessible directly via radical polymerization.[111] Another advantage of the phenothiazine polymers is their electrochromic properties which could find possible application as indicator for showing the charging level in transparent and flexible all organic batteries.[112] Combination of the phenothiazine bearing monomers with other monomers having n-type functionality or polyelectrolyte functionality might be interesting for obtaining donor-acceptor type copolymers with electrochromic effect.

The application of phenothiazine bearing polymer for data storage purposes was successfully demonstrated. Spin-coated polymers films of the styrene based phenothiazine polymer PVBPT were used to store information by inducing nanoscale patterns with conductive SFM. The electrochemically written patterns were mechanically and long-term stable. Using phenothiazine bearing polymers as data storage medium in combination with conductive SFM is a very attractive method, especially with respect to the storage density and storage stability of the polymer film. The polymer films can be used in non-volatile high density WORM storage devices reaching storage densities up to 100 Gbit/inch^2.[162,165] For better performance of the system improvements of the patterning procedure are necessary. More stable experimental conditions are required to guarantee efficient and accurate patterning process.

One way to enhance the patterning process is by using precisely driven microelectro-mechanical systems.[257,276] Another method to improve the patterning conditions is to use a more defined electrolyte meniscus between the tip and the sample. This could be helpful to improve the electrochemical redox process in the polymer film. Possibly under more defined electrochemical conditions, the written patterns can also be erased since the electrochemical oxidation in the electrolyte solution is reversible. Nevertheless, the irreversibility of the writing process in the polymer has to be further investigated. Another possibility to improve the patterning process is to form a blend using a solid polyelectrolyte via copolymer lithographic methods.[175] This way, not only a more defined and homogeneous surface is obtained. In addition, the surface wear resistance and the conductivity can be enhanced by the use of a stabilizing lithographic template. Also the molecular polymer architecture can be further improved. This can be achieved by using polymer structures which allow easier rearrangement

of the phenothiazine redox moieties due to intramoleuclar rotation of the moieties. The facilitated rearrangement enhances the interaction between the moieties and should improve the bistable switching of the polymer film. The effect of grafting and crosslinking on the performance and mechanical nanowear stability of the phenothiazine polymer could be of further interest for their application as data storage medium.

Finally, grafted brushes of phenothiazine bearing polymers were synthesized via SI-ATRP. For the synthesis of the grafted brushes, two different synthetic routes were verified. In the direct polymerization route, phenothiazine containing monomers were directly grafted from the surface. In the post-functionalization route, activated ester brushes were first grafted from the surface and functionalized with the phenothiazine moieties in the second step. Both routes proved to be useful and elegant methods for the synthesis of redox active brushes, especially due to their chemical versatility. Thin and nanowear stable polymer brush surfaces can easily be produced by SI-ATRP with high grafting densities resulting in well defined films with redox active properties.

The direct polymerization is an easy one step reaction but limited to the choice of the monomer. For easy polymerization, monomers with low sterical hindrance and high reactivity are desirable. Besides, for every monomer individual parameters are necessary to control the polymerization reaction. For better control of the SI-ATRP polymerization reaction, small phenothiazine monomers with vinyl functionality could be used. Phenothiazine monomers with expanded aromatic rings would be interesting candidates since the aromatic rings should interact stronger with each other by π-π arrangement. Another method to control the polymerization reaction is using activator controlled reactions such as AGET[268], ARGET[269] and ICAR-ATRP.[270] These ATRP modified technique improves the reaction control especially for bulky monomers by generating activator species to increase the initiation rate of the polymerization.

The post-functionalization route via the activated ester polymer is a good alternative to the direct polymerization. The SI-ATRP polymerization of the activated ester monomers is quite straight forward. Furthermore, the system is not strongly limited by the choice of the amine moieties. In addition to redox active moieties, other small molecules with various functionalities[93,102] can be integrated inside the polymer brush film. By choosing molecules with diamine functionalities, the surface nanowear is additionally increased due to the crosslinking of the brushes. One limitation of the post-functionalization technique is the diffusion of the redox moiety to the activated ester groups in the polymer brush film. For quantitative conversion of the activated ester groups with the redox moieties, thinner polymer brush films should be used to facilitate penetration of the moieties. Proper choice of solution would also enhance the diffusion by stretching of the polymer chains and activation of the amine moiety. The versatility of the activated ester would allow the functionalization of different types of substrates. As an example, flexible substrates like conductive polyamide[277,278] surface could be used to graft

activated ester brushes. Redox functional groups like phenothiazine can be introduced in textiles for application as electronic devices such as solar panels and battery cells. Another possible field of application is switchable filters.[279] These filters have selective permeability towards size and charge of molecules depending on the redox impulse. Furthermore, patterning experiments with conductive SFM as done for spin-coated PVBPT should be performed on redox active polymer brushes to compare the effect of the grafting on the conductivity and the switching behavior. In summary, redox responsive bistable polymers and polymer brushes based on phenothiazine are candidate materials in the energy and data storage fields. In combination with activated ester polymer, they will find a broader field of application in the near future.

VII. Acknowledgements

Available in the printed version

VIII. Appendix

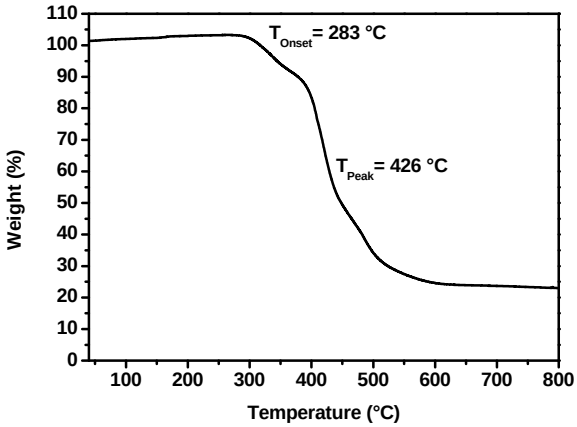

Figure A 1. TGA in nitrogen atmosphere (30 ml/min) at a heating rate of 10 °C/min from 40 to 800 °C for PVBPT with M_W ≈ 27300 g/mol and PDI ≈ 2.32.

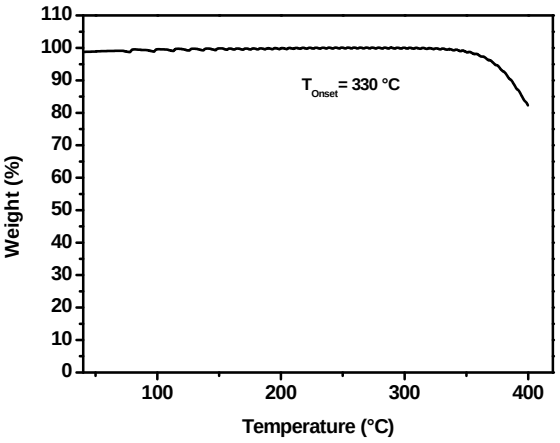

Figure A 2. TGA in nitrogen atmosphere (30 ml/min) at a heating rate of 10 °C/min from 40 to 400 °C for PVPPP with M_W ≈ 25800 g/mol and PDI ≈ 1.96.

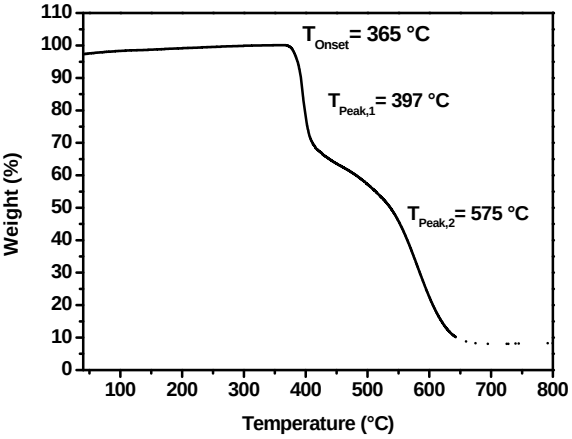

Figure A 3. TGA in nitrogen atmosphere (30 ml/min) at a heating rate of 10 °C/min from 40 to 800 °C for PVMPT with MW ≈ 26300 g/mol and PDI ≈ 2.53.

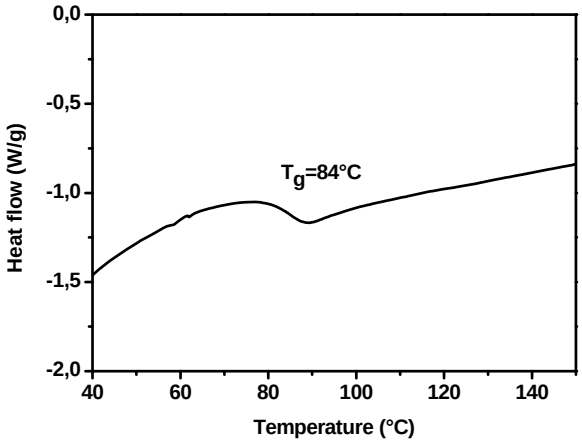

Figure A 4. DSC Measurement at nitrogen atmosphere (30 ml/min) at a heating rate of 10 °C/min from 40 to 220 °C for PVPPP with MW ≈ 25800 g/mol and PDI ≈ 1.96.

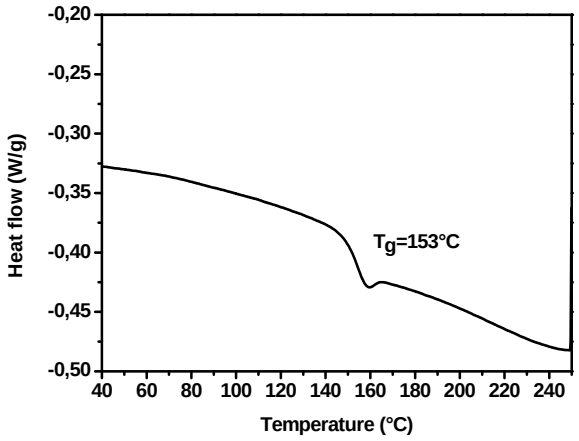

Figure A 5. DSC Measurement at nitrogen atmosphere (30 ml/min) at a heating rate of 10 °C/min from 40 to 250 °C for PVBPT with MW ≈ 27300 g/mol and PDI ≈ 2.32.

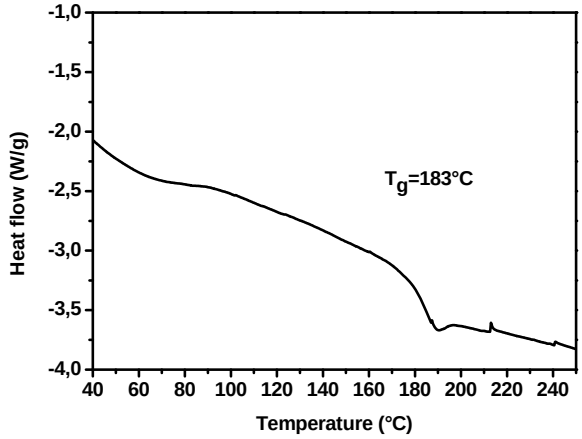

Figure A 6. DSC Measurement at nitrogen atmosphere (30 ml/min) at a heating rate of 10 °C/min from 40 to 250 °C for PVMPT with MW ≈ 26300 g/mol and PDI ≈ 2.53.

Table T 1. FTIR data evaluation for PPFMA before and after the reaction with AEPCA and AHPCA.

Wave number (cm^{-1})	Characteristic bond
2940, 3396	amide (N-H str. vib.)
1777	ester (C=O, str. vib.)
1674	amide (C=O str. vib.)
1514	aromatic (C=C str. vib.)
1463	amide (C-H deform. vib.)
1253	amide (C-N str. vib.)
1051	amide (C-O str. vib.)
994	ester (C-F, str. vib.)
808	aromatic (C-H out of plane def.)
756	amide (N-H out of plane def.)

Table T 2. FTIR data evaluation for PDPVB before and after the reaction with AEPCA and AHPCA.

Wave number (cm^{-1})	Characteristic bond
2940, 3310	amide (N-H str. vib.)
1772,1731	ester (C=O, str. vib.)
1667,1649	amide (C=O str. vib.)
1602	aromatic (p-subst. Str. vib.)
1514	aromatic (C=C str. vib.)
1425, 1364	amide (C-H deform. vib.)
1234	ester (C-O, asym. str. vib.)
1205	amide (C-N str. vib.)
1072	ester(C-O sym. str. vib.)
996-640	aromatic (C-H out of plane deform. vib.)
752	aromatic (C-S str. vib.)

Table T 3. FTIR data evaluation for PDPVB before and after the reaction with MPMA.

Wave number (cm^{-1})	Characteristic bond
2952, 3311	amide (N-H str. vib.)
1767, 1729	ester (C=O, str. vib.)
1661, 1641	amide (C=O str. vib.)
1603	aromatic (p-subst. Str. vib.)
1526	aromatic (C=C str. vib.)
1497, 1427	amide (C-H deform. vib.)
1462	amide (N-CH3 def. vib.)
1337, 1253, 1205, 1138	amide (C-N str. vib.)
1234	ester (C-O, asym. str. vib.)
1067	ester(C-O sym. str. vib.)
990-640	aromatic (C-H out of plane deform. vib.)
753	aromatic (C-S str. vib.)

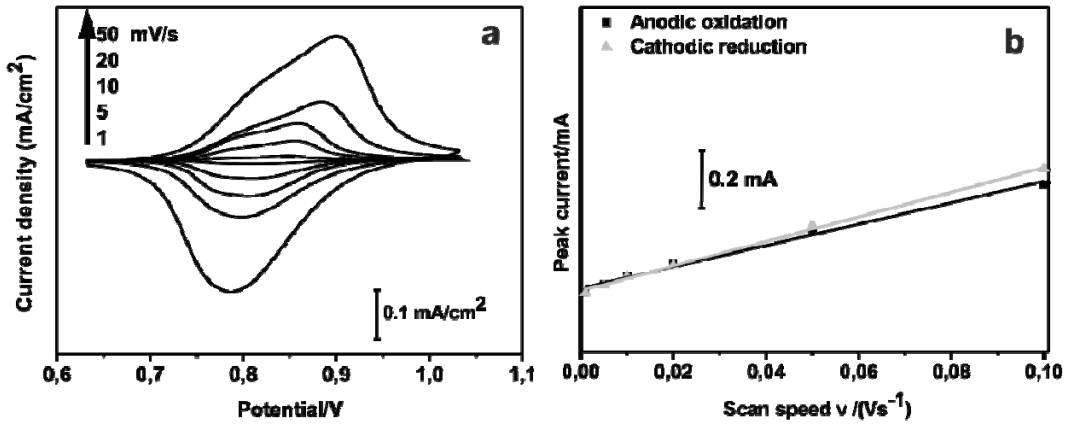

Figure A 7. a) CV of PPVPP in ACN with 0.1 M TBAPC on ITO using Ag/AgCl and Pt-wire as RE and CE in 0.1 M TBAPC/ACN, respectively, b) Corresponding peak current vs. scan speed plot of the CV data.

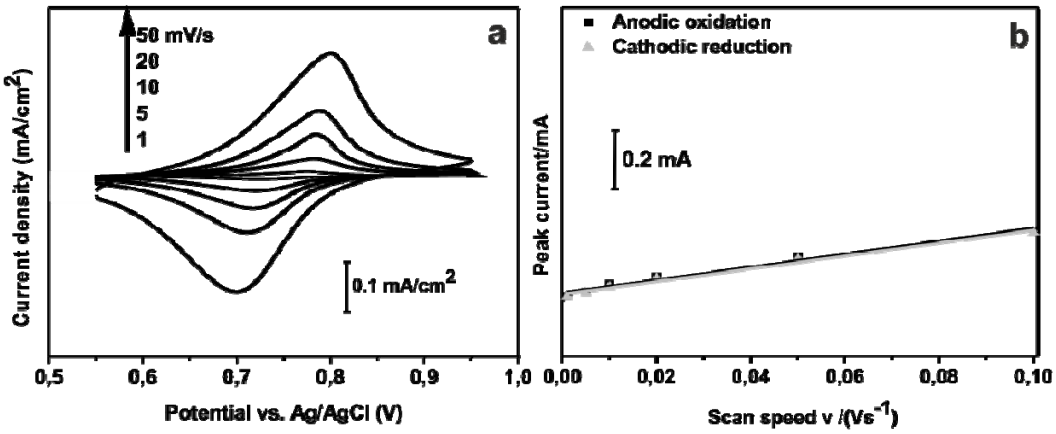

Figure A 8. a) CV of PVMPT in ACN with 0.1 M TBAPC on ITO using Ag/AgCl and Pt-wire as RE and CE in 0.1 M TBAPC/ACN, respectively, b) Corresponding peak current vs. scan speed of the CV data at different scanning speed.

Table T 4. Calculation of the slope from CV by plotting current peak against scan speed.

Polymer	Slopes calculated from CV (10^{-3} A*s/V)		
	Anodic step	Cathodic step	Δ
PVBPT	8.4 ± 0.5	8.0 ± 0.2	0.42 ± 0.24
PVPPP	3.7 ± 0.2	4.3± 0.1	-0.57 ± 0.09
PVMPT	2.2 ± 0.2	2.2 ± 0.1	0.02 ± 0.04

Table T 5. Calculation of surface coverage and concentration of the redox species from CV by plotting current peak against scan speed.

Polymer	Surface coverage calculated from CV (10^{-9} mol/cm^2)		Concentration C* calculated from CV (10^{-4} mol/cm^2)	
	Anodic step	Cathodic step	Anodic step	Cathodic step
PVBPT	3.4 ± 0.2	3.2 ± 0.1	5.5 ± 0.3	5.3 ± 0.2
PVPPP	1.5 ± 0.1	1.7± 0.1	2.6 ± 0.5	3.0± 0.4
PVMPT	0.9 ± 0.1	0.9 ± 0.1	1.8 ± 0.1	1.8 ± 0.3

Table T 6. Calculation of surface coverage and concentration of the redox species by integration of the CA curve.

Polymer	Surface coverage calculated from CA (10^{-9} mol/cm^2)		Concentration C* calculated from CA (10^{-4} mol/cm^2)	
	Anodic step	Cathodic step	Anodic step	Cathodic step
PVBPT	2.2 ± 0.1	2.7 ± 0.1	8.2 ± 0.8	8.4± 0.5
PVPPP	5.8 ± 0.1	6.2± 0.1	6.5 ± 0.8	6.6 ± 0.4
PVMPT	4.6 ± 0.2	5.6± 0.1	8.1 ± 0.6	8.1 ± 0.9

Table T 7. Calculation of the slope from the Cottrell plot.

Polymer	Slopes calculated from CV (10^{-3} mA*s$^{1/2}$)		
	Anodic step	Cathodic step	Δ
PVBPT	4.2 ± 0.1	4.6 ± 0.2	-0.4 ± 0.1
PVPPP	0.9 ± 0.2	2.5 ± 0.4	-1.6 ± 0.2
PVMPT	3.0 ± 0.2	2.4 ± 0.1	0.6 ± 0.1

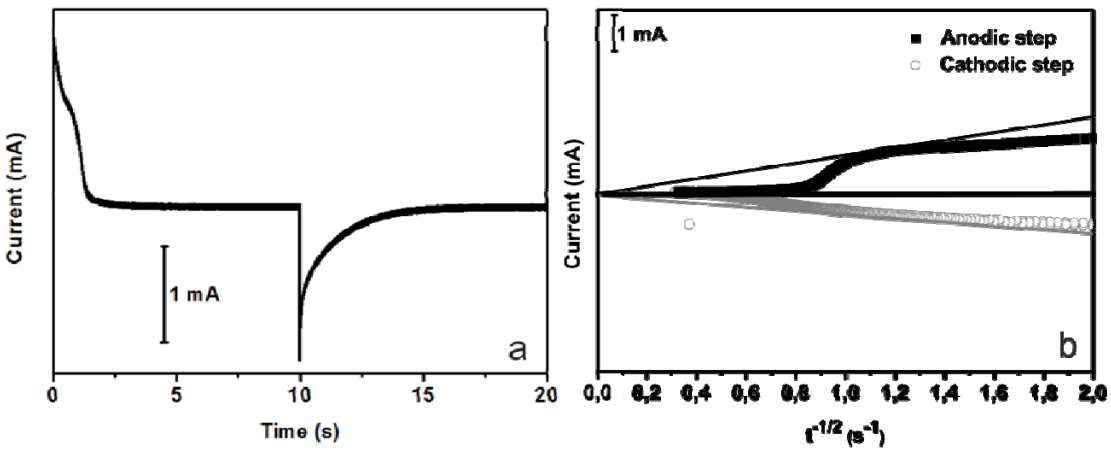

Figure A 9 a) Chrono amperogram of PVPPP on ITO. B) Cottrell Plot of PVPPP. Ag/AgCl and Pt-wire were used as RE and CE in 0.1 M TBAPC/ACN. respectively.

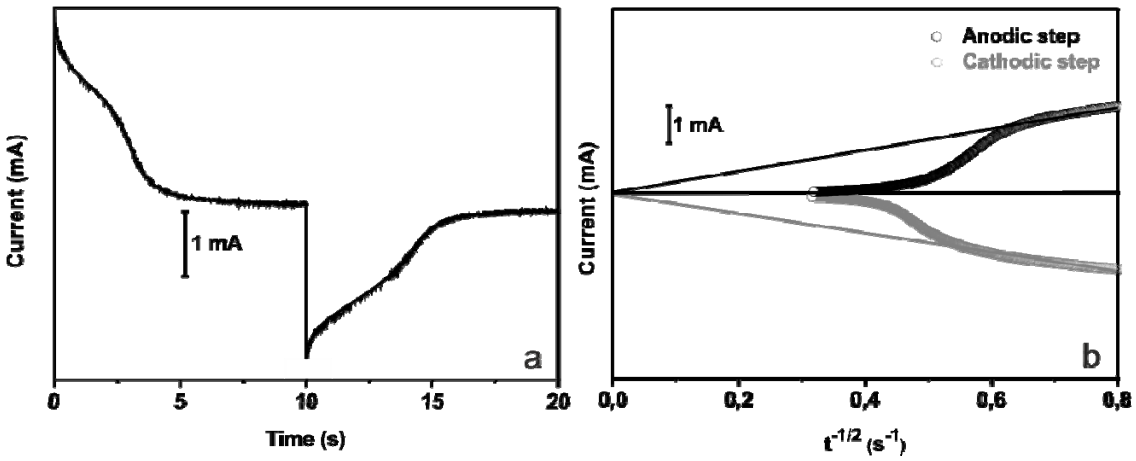

Figure A 10. a) Chrono amperogram of PVMPT on ITO. B) Cottrell Plot of PVMPT. Ag/AgCl and Pt-wire were used as RE and CE in 0.1 M TBAPC/ACN. respectively.

Table T 8. Critical ν_c calculated from CV according to Gileadi and Eisner

Polymer	Calculated critical scan speed ν_c from CV (10^{-3} mA*$s^{1/2}$)	
	Anodic step	Cathodic step
PVBPT	6.7 ± 2.3	16.2 ± 6.4
PVPPP	8.5 ± 3.1	14.8 ± 5.2
PVMPT	15.8 ± 2.8	9.3 ± 2.5

Table T 9. Current difference between patterned and non-patterned region at different reading bias potentials patterned at V_w =+10 V.

Reading bias (V)	Current difference (fA)
4	0 ± 95
2	0 ± 95
-2	3 ± 95
-3	20 ± 95
-4	90 ± 90
-5	280 ± 82
-6	602 ± 23

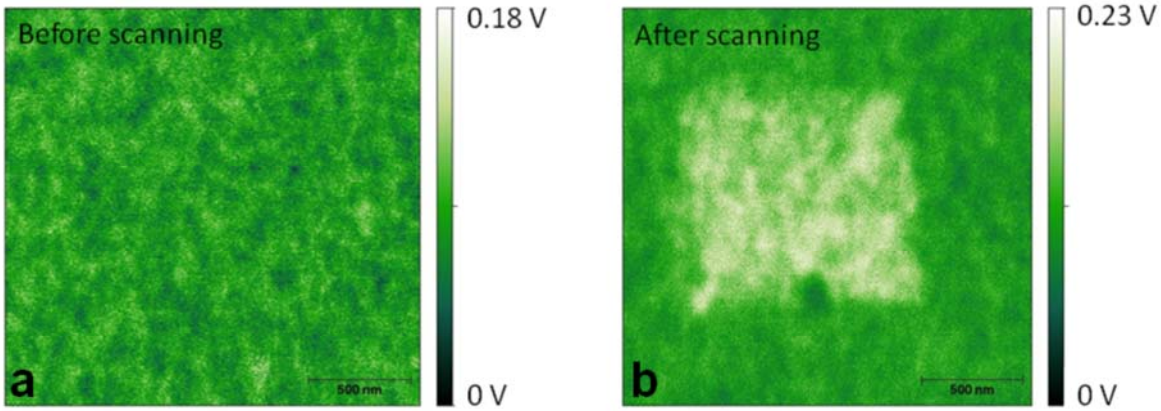

Figure A 11. KPFM before (a) and after (b) writing on a scan area of 2 µm x 2 µm with a scan speed of 2 µm/s showing the change in Kelvin potential.

***Description of the simulation**

PVBT polymer chain was initially subjected to molecular structure energy minimization by Discover Minimizer (10^5 iterations. Smart Minimizer – Steepest Descent and Conjugate Gradient methods). followed by bonding the polymer chain to silicon layer surface and further molecular structure energy minimization (5 x 10^4 iterations. Smart Minimizer – Steepest Descent and Conjugate Gradient methods). The simulation box was periodic and consisted of 5x5x1 unit cells of silicon and PVBT polymer chain. equivalent to the dimensions 1.92 nm x 1.92 nm x Z ($\gamma=120^0$. polymer chains bonding density was 0.31 chains/nm^2). The periodicity in the *Z* direction was eliminated by choosing the box length of 50 nm (approximately 10 nm beyond the length of the polymer chain). The force field is the polymer-consistent force field (PCFF). MD simulation was carried out in the NVT (number N. volume V and temperature T) ensemble. a time step of 1 fs and velocity scaling for temperature control. Simulated systems were subjected to 20 ps of MD for visual analysis of polymer chain geometry (5 snapshots at an interval of 1 ps). Visual model building. MD simulation and analysis were carried out using Materials Studio and Discover program from Accelrys. Inc.

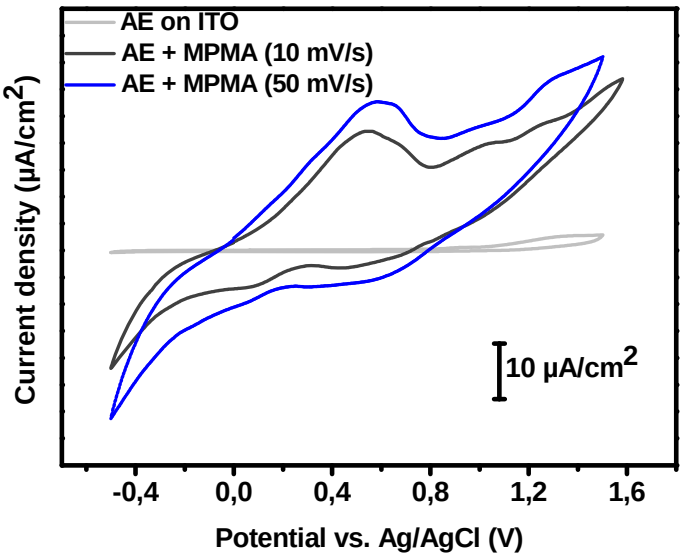

Figure A 12. CV of grafted AE polymer brush on ITO substrate at different scan speeds in 0.1 M TBAPC/ACN solution before and after reaction with MPMA. b) The potential is measured with Ag/AgCl and Pt as the reference and the counter electrode. respectively.

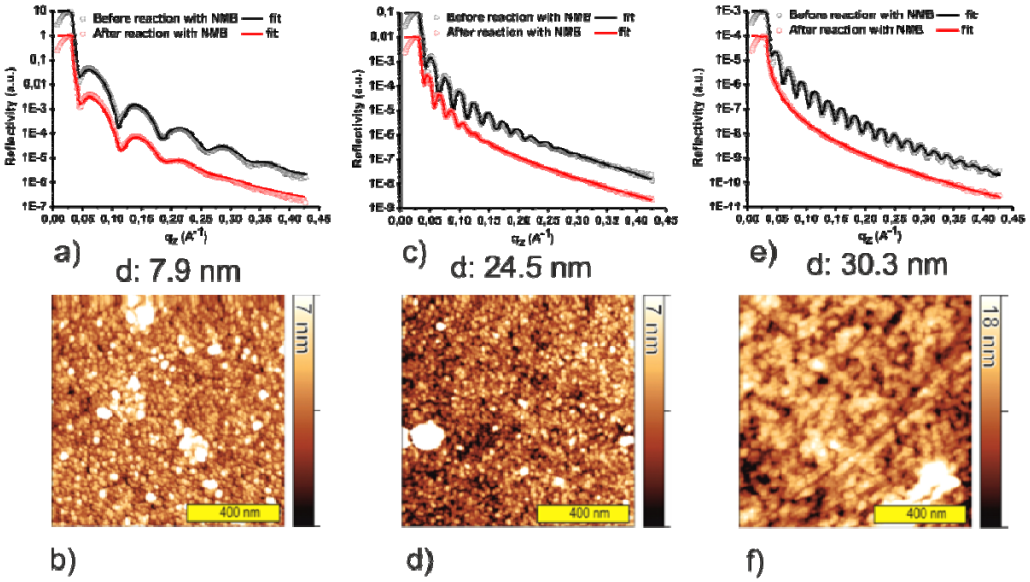

Figure A 13 XRR curves of AE polymer brushes on silicon substrate with different thicknesses before and after reaction with NMB for film thickness of a) 7.9 nm. c) 24.5 nm and e) 30.3 nm. Below the corresponding SFM topography images (b). d) and f)) of the surface after the reaction.

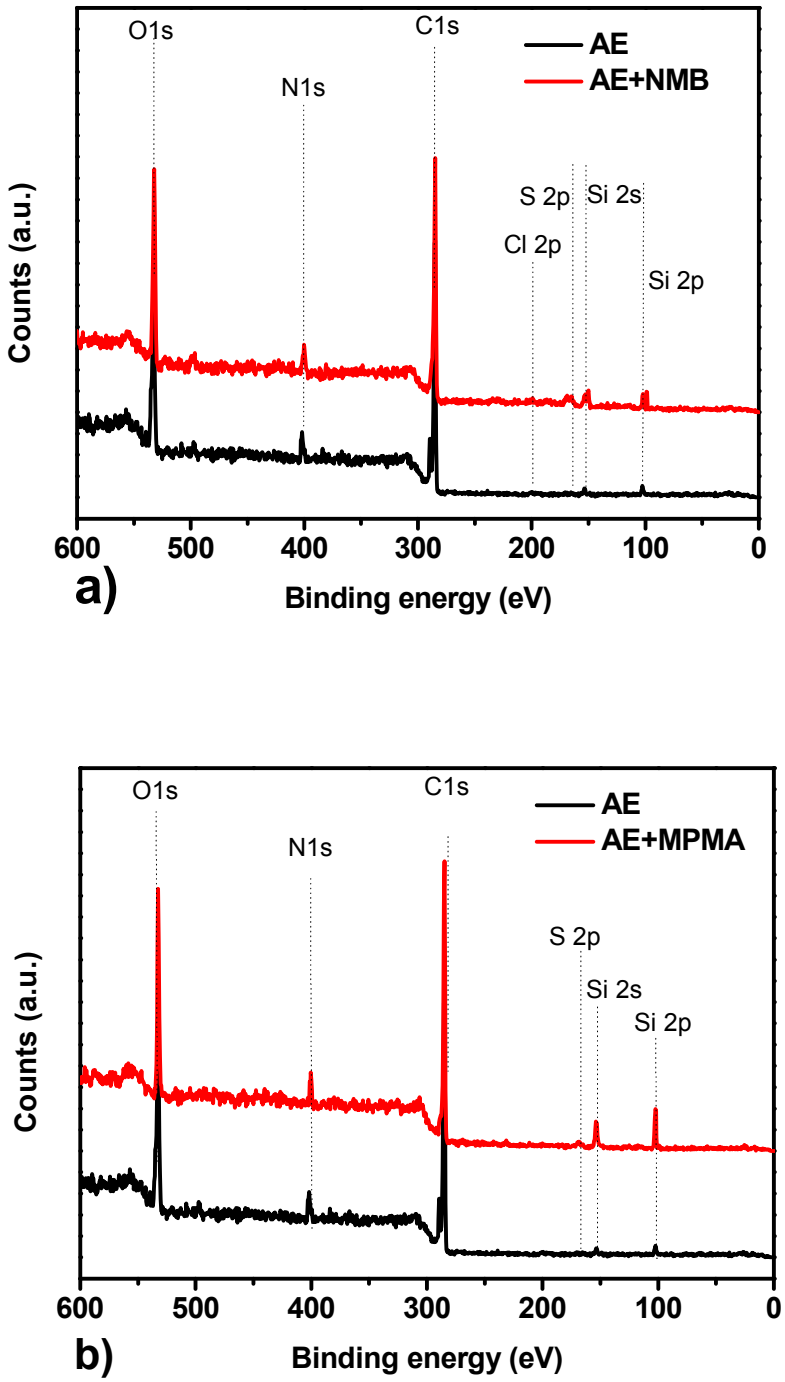

Figure A 14. XPS of grafted AE brushes on silicon substrate before and after reaction with a) NMB and b) MPMA.

Table T 10. Ratio between the elements C.N. O and S for AE grafted fromsilicon substrate measured with XPS after the reaction with MPMA.

Element	Theory	Experiment
C	85.2%	86.5%
N	7.4%	5.1%
O	3.7%	6.1%
S	3.7%	2.3%

IX. References

[1] H. Shirakawa, E. J. Louis, A. G. MacDiarmid, C. K. Chiang, A. J. Heeger, *J. Chem. Soc. Chem. Commun.* , 16, **1977**, 578.

[2] G. Inzelt, M. Pineri, J. Schultze, M. Vorotyntsev, *Electrochem. Acta,* 45, **2000**, 2403.

[3] M. Rehahn, *Chem. Unsere Zeit ,* 1, **2003**, 18.

[4] R. Tipnis, D. Laird, M. Mathai, *Mater. Matters*, 3, **2008**, 3, 92.

[5] Z. Bao, J. A. Rogers, H. E. Katz, *J. Mater. Chem*., 9, **1999**, S. 1895.

[6] H.-J. Butt, K. Graf, M. Kappl: "Physics and Chemistry of Interfaces", *Wiley-VCH*, **2003**, 138.

[7] H. E. Katz, Z. Bao, S. Gilat *Acc. Chem. Res.*, 34, **2001**, S. 359.

[8] C. J. Brabec, N. S. Sariciftci, J. C. Hummelen, *Adv. Funct. Mater*., 11, **2001**, 15.

[9] H. E. A. Huitema et al., *Adv. Mater.*, 14, **2002**, 1201.

[10] B. K. Crone et al., *J. Appl. Phys*., 9, **2002**, 10140.

[11] C. D. Dimitrakopoulos, P. R. L. Malenfant, *Adv. Mater.*, 14, **2002**, 99.

[12] A. Dodabalapur, *Solid State Comm.*, 102, **1997**, 259.

[13] L. Erdmann, L. Hilty, H. J. Althaus, S. Behrendt, R. Hischier, C. Kamburow, B. Oertel, D. P. Wäger, T. Welz, "Einfluss von RFID-Tags auf die Abfallentsorgung", *Umweltbundesamt,* **2009**.

[14] Y. H. Wang, M. K. Hung, C. H. Lin, H. C. Lin, J. T. Lee, *Chem. Comm.,* 47, **2011,** 1249.

[15] NEC News Room: "http://www.nec.co.jp/press/en/1203/0504.html", **2012**.

[16] Nanomarkets report: "http://www.nanomarkets.net/index.php/news /article/products_using_ organic_transistors_ and_memory _to_reach_21.6_billion_by_2015., **2007**.

[17] A. A. Zakhidov, J. K. Lee, H. H. Fong, J. A. Defranco, M. Chatzichristidi, P. G. Taylor, C. K. Ober, G. Malliaras, *Adv. Mater.,* 20, **2008**, 3481.

[18] J. Z. Wang, Z. H. Zheng, H. W. Li, W. S. Huck, H. Sirringhaus, *Nature Mater.,* 3, **2004**, 171.

[19] T. Sekitani, H. Nakajima, H. Maeda, T. Fukushima, T. Aida, K. Hata, T. Someya, *Nature Mater.,* 8, **2009**, 494.

[20] G. Horányi, G. Inzelt, *J. Electroanal. Chem.*, 264, **1989**, 259.

[21] J. Janata, M. Josowicz, *Nature Mater.,* 2, **2003**, 19.

[22] H. S. Nalwa: "Handbook of Organic Conductive Molecules and Polymers" ,*Wiley, New York*, 3rd ed., **1997**.

[23] A. Facchetti, *Chem. Mater.,* 23, **2011,** 733.

[24] T. Yamamoto, H. Kokubo, M. Kobashi, Y. J. Sakai, *Mater. Chem.* , 16, **2004** , 4616.

[25] Q. D. Ling, D. J. Liaw, E. H. Teo, C. Zhu, D. H. Chan, E. T. Kang, K. G. Neoh, *Polymer,* 48, **2007**, 5182.

[26] D. E. Herbert, J. B. Gilroy, W. Y. Chan, L. Chabanne, A. Staubitz, A. J. Lough, I. Manners, *J. Am. Chem. Soc. ,* 131, **2009**, 14958.

[27] B. J. Holliday, T. M. Swager, *Chem. Comm.,* 1, **2005**, 23.

[28] J. Grazulevicius, P. Strohriegl, J. Pielichowski, K. Pielichowski, *Prog. Polym. Sci.,* 28, **2003**, 1297.

[29] K. Oyaizu, H. Nishide, *Adv. Mater.,* 21, **2009**, 2339.

[30] Y. H. Wang, M. K. Hung, C. H. Lin, H. C. Lin, J. T. Lee, *Chem. Comm.,* 47, **2011**, 1249.

[31] H. Nishide, T. Suga, *Elechtrochem. Soci. Interf.,* 14, **2005**, 32.

[32] A.R. Katritzky and A.J. Boulton: "Advances in Heterocyclic Chemistry", *Academic Press, New York*, 9, **1968**, 322.

[33] R. G. Hicks: "Stable radicals : fundamentals and applied aspects of odd-electron compounds", *Wiley*, **2010**.

[34] D. Griller and K. U. Ingold, *Acc. Chem. Res.*, 9, **1976**, 13.
[35] a)M. Gomberg, *Ber. Dtsch. Chem. Ges*., 33, **1900**, 3150. b), M. Gomberg, *J. Am. Chem. Soc*., 22, **1900**, 757.
[36] H. Wieland, E. Popper, and H. Seefried, *Ber. Dtsch. Chem. Ges*., **55**, 1816–1834 (1922)
[37] a)M. Gomberg, *Ber. Dtsch. Chem. Ges*., 30, **1897**, 2043. b) M. Gomberg, *J. Am. Chem. Soc*., 20, **1898**, 773.
[38] M. J. Sabacky, C. S. Johnson, Jr., R. G. Smith, *et al* ., *J. Am. Chem. Soc*., 89, **1967**, 2054.
[39] K. Schreiner and A. Berndt, *Angew. Chem. Int. Ed*., 13, **1974**, 144.
[40] C. F. Koelsch, *J. Am. Chem. Soc*., 79, **1957**, 4439.
[41] H. Tukada, *J. Am. Chem. Soc*., 113, **1991**, 8991.
[42] H. Wieland and K. Roth, *Ber. Dtsch. Chem. Ges*., 53, **1920**, 210.
[43] A. Studer, K. Harms, C. Knoops et al., *Macromolecules*, 37, **2004**, 27.
[44] K. H. Meyer and W. Reppe, *Ber. Dtsch. Chem. Ges.* , 54, **1921**, 327.
[45] Y. Miyazaki, A. Inaba, M. Sorai et al., *J. Phys. Chem. B*, 112, **2008**, 8144.
[46] E. Ressouche, J. X. Boucherle, B. Gillon et al ., *J. Am. Chem. Soc*., 115, **1993**, 3610.
[47] M. Tamura, Y. Nakazawa, D. Shiomi et al., *Chem. Phys. Lett* ., 186, **1991**, 401.
[48] L. J. Ignarro, G. M. Buga, K. S. Wood et al., *Proc. Natl. Acad. Sci. USA*, 84, **1987**, 9265.
[49] S. Goldschmidt and K. Renn, *Ber. Deutsch. Chem. Gesel.* B55, **1922**, 628.
[50] S. Goldschmidt, *Ber. Deutsch. Chem. Gesel.* B53, **1920**, 44.
[51] A. R. Forrester, J. M. Hay and R. H. Thomson: "Organic Chemistry of Stable Free Radicals", *Academic Press, New York*, **1968**, 137.
[52] Ronald E. Hester and Kenneth P. J. Williams, *J. Chem. Soc.*, Perkin Trans. 2, **1981**, 852.
[53] U. Shmidt, *Angew. Chem. internat. Edit.*, 3, **1964**, 602.
[54] Y. Sato, M. Kinoshita, M. Sano, and H. Akamatu, *Bull. Chem. Soc. Jap.*, 40, **1967**, 2539.
[55] P. D. Sullivan and J. R. Bolton, *J. Magn. Ressonance*, 3, **1969**, 356.
[56] R. Foster and P. Hanson, *Biochim. Biophys. Acta.*, 112, **1966**, 482.
[57] A. Bernthsen, *Ber. Deut. Chem. Ges.*, 13, **1883**, 2896.
[58] S. P. Massie, *Chem. Rev.* , 54, **1954**, 797.
[59] D. Pan, D. L. Phillips, *J. Phys. Chem. A*, 103, **1999**, 4737.
[60] D. Clarke, B. C. Gilbert, P. Hanson,M. C. Kirk, *J. Chem. Soc. Perkin Trans. II* , 2, **1978**, 1103.
[61] G. P. Brown, S. Aftergut, Nature, 193, 1962, 361.
[62] J. P. Billon, *Bull. Soc. Chim. France*, **1960**, 1784.
[63] B. König, M. Pelka, H. Zieg, T. Ritter, H. B. Laurent, R. Bonneau, J. P. Desvergne, *J. Am. Chem Soc.*, 121, **1999**, 1681.
[64] D. T. Miles, R. W. Murray, *Anal. Chem.*, 73, **2001**, 921.
[65] W. Huang, M. Helvenston, J. L. Casson, R. Wang, J.-F. Bardeau, Y. Lee, M. S. Johal, B. I. Swanson, J. M. Robinson, D. Li, *Langmuir*, 15, **1999**, 6510.
[66] C. S. Krämer, T. J. J. Müller, *Eur. J. Org. Chem.*, **2003**, 3534.
[67] C. S. Barkschat, S. Stoycheva, M. Himmelhaus, T. J. J. Müller, *Chem. Mater.* , 22, **2010**, 52.
[68] A. W. Franz, S. Stoycheva, M. Himmelhaus, T.J. J. Müller, *Beilstein J. Org. Chem.*, 6, **2010**, 1.
[69] P. H. Sackett, R. L. Mccreery, *J. Medic. Chem.,* 22, **1979**, 1447.
[70] I. Jelinek, I. Nemcova, P. Rychlovsky, *Talanta,* 38, **1991**, 1309.
[71] Y. Huiwang, M. Z. Zhu, T. Liu, Q. Xiangguo, *Res. Chem. Intermed.,* 29, **2003**, 191.
[72] Z. Zhou, A. W. Franz, M. Hartmann, A. Seifert, T. J. Müller, W. R. Thiel, *Chem. Mater.,* 20, **2008**, 4986.
[73] M. D. Pace, O.-K. Kim, *Synth. Met.*, 25, **1988**, 333.
[74] S. Z. Ozkan, G. N. Bondarenko, A. V. Orlov, G. P. Karpacheva, *Polymer Science B,* 51, **2009**, 149.
[75] M. Grigoras, A. Farcas, I. Cianga, C. I. Simionescu, *Polym. Bull.*, 26, **1991**, 139.
[76] S. K. Kim, J. H. Lee, D. H. Hwang, *Synt. Met.*, 152, **2005**, 201.

[77] D.-H. Hwang, S.-K. Kim, M.-J. Park, J.-H. Lee, B.-W. Koo, I.-N. Kang, S.-H. Kim, T. Zyung, *Chem. Mater.*, 16, **2004**, 1298.
[78] J. -S. Kang, J. -W. Park, J. -H. Lee, S. -Y. Oh, *Mol. Cr. Liq. Cr.*, 462, **2007**, 267.
[79] X. Kong, A. P. Kulkarni, A. A. Jenekhe, *Macromolecules* 36, **2003**, 8992.
[80] M. W. Thesen, B. Höfer, M. Debeaux, S. Janietz, A. Wedel, A. Köhler, H. H. Johannes, H. Krueger, *J. Polym. Sci., A* (48), **2010**, 3417.
[81] W. Klöpffer, W. Willicks, *Die Makromolekulare Chemie,* 115, **1968**, 156.
[82] E. Gipstein, W. A. Hewett, O. U. Need, *J. Polym. Sci. A* ,8 , *1970*, 3285.
[83] A. Rybak, J. Jung, W. Ciesielski, J. Ulanski, *Mater. Sci. Poland,* 24, **2006**, 527.
[84] Z. Gomurashvili, J. V. Crivello, *Macromolecules,* 35, **2002**, 2962.
[85] Y. Morishima, I. Akihara, S. I. Nozakura, *J. Polym. Sci.,* 23, **1985**, 661.
[86] Y. Morishima, Y. Itoh and A. Koyagi, *J. Polym. Sci., Polym. Chem.Ed.*, 21, **1983**, 953.
[87] Y. Morishima, I. Akihara, H. S. Lim, S. i. Nozakura, *Macromolecules,* 20, **1987**, 978.
[88] B. A. Kowert, L. Marcoux, A. J. *J.* Bard, *Am. Chem. Soc.*, 94, **1972**, 5538.
[89] J. C. Yoder, J. P. Roth, E. M. Gussenhoven, A. S. Larsen, J. M. Mayer, *J. Am. Chem Soc.,* 125, **2003**, 2629.
[90] S. F. Nelsen, R. F. Ismagilov, K. E. Gentile, M. A. Nagy, H. Q. Tran, Q. Qu, D. T. Halfen, A. L. Odegard, J. R. Pladziewicz, *J. Am. Chem Soc.,* 120, **1998**, 8230.
[91] C. Bodea, I. Silberg, *Adv. Heterocycl. Chem.* , 9, **1968**, 321.
[92] N. B. Mckeown, S. Badriya, M. Helliwell, M. Shkunov, *J. Mater. Chem.,* 17, **2007**, 2088.
[93] P. Theato, *J. Polym. Sci. Part A* , 46, **2008**, 6677.
[94] M. Pittelkow, R. Lewinsky, J. Christensen, *Organic Syntheses*, **2007**, 84, 209.
[95] D. Li, J. Ren, J. Li, Z. Wang, G. Bo, *Dyes and Pigments,* 49, **2001**, 181.
[96] A. Burger, A. C. Schmalz, *J. Org. Chem.* , 19, **1954**, 1841.
[97] N. Marion, E. C. Ecarnot, O. Navarro, D. Amoroso, A. Bell, S. P. Nolan, *J. Org. Chem.*, 71, **2006**, 3816.
[98] B. P. Fors, P. Krattiger, E. Strieter, S. L. Buchwald, *Org. Lett.*, *10*, **2008**, 3505.
[99] R. E. Tundel, K. W. Anderson, S. L. Buchwald, *J. Org. Chem.*, *71*, **2006**, 430.
[100] H. Becker, H. Vogel, *Chem. Engin. Techn.,* 29 (8), **2006**, 931.
[101] A. Pollak, H. Blumenfeld, M. Wax, R.L. Baughn, G.M. Whitesides, *J. Am. Chem. Soc.*, 102, **1980**, 6324.
[102] P. Theato, J.U. Kim, J.C. Lee, *Macromolecules*, 37, **2004**, 5475.
[103] A.E. Ivanov, *J. Macromol. Sci. Pure. Appl. Chem*., 36, **1981**, 1999.
[104] F. G. Bordwell, G. E. Drucker, H. E. Fried, *J. Org. Chem.* , 46, **1981**, 632.
[105] K. Eller, E. Henkes, R. Rossbacher, H. Höke: "Amines, Aliphatic, Ullmann's Encyclopedia of Industrial Chemistry", Wiley-VCH Verlag, **2005**.
[106] M. Eberhardt, R. Mruk, R. Zentel, P. Theato, *Europ. Pol. Journal,* 41, **2005**, 1569.
[107] K. Nilles, P. Theato, *Europ. Pol. Journal,* 43, **2007**, 2901.
[108] J. M. Tarascon, M. Armand, *Nature,* 414, **2001**, 359.
[109] D. Macinnes, M. A. Druy, P. J. Nigrey, D. P. Nairns, A. G. Macdiarmid, A. J. Heeger, *Chem. Comm.,* 7, **1981**, 317.
[110] W. Baochen, L. Gi, L. Changzhi, W. Fosong, *J. Pow. Source,* 24, **1988**, 115.
[111] H. Nishide, S. Iwasa, Y. J. Pu, T. Suga, K. Nakahara, M. Satoh, *Electrochem. Acta,* 50, **2004**, 827.
[112] H. Nishide, K. Oyaizu, *Science,* 319, **2008**, 737.
[113] T. Suga, H. Ohshiro, S. Sugita, K. Oyaizu, H. Nishide, *Adv. Mater.,* 21, **2009**, 1627.
[114] G. Inzelt, "Conducting Polymers-A New Era in Electrochemistry", Springer-Verlag, **2008**.
[115] W. Waskitoaji, T. Suga, H. Nishide, *Int. Workshop on adv. Mater. For New and Renew. E,* CPl 169, **2009**, 13.

[116] F. B. Kaufman, A. M. Schroeder, E. M. Engler, S. R. Kramer, , J. Q. Chambers, *J. Am. Chem. Soc.* , 102, **1980**, 483.
[117] M. E. G. Lyons, *Electroactive Polymer Electrochemistry,* Plenum Press: New York, **1994**.
[118] P. G. Pickup, R. W. Murray, *J. Am. Chem Soc.,* 105, **1983**, 4510.
[119] R.A. Marcus, *J. Chem. Phys*, 24, **1956**, 966.
[120] T. Suga, Y.-J. Pu, K. Oyaizu, H. Nishide, *Bull.Chem.Soc.Jpn*, *77*, **2004**, 2203.
[121] V. J. Heinze, *Angew. Chem.,* 96, **1984**, 823.
[122] H. Lund, M. M. Baizer: "Organic Electrochemistry", 3. Auflage, Marcel Dekker, New. York , **1991**.
[123] R.S. Nicholson, Ana. Chem. 37, **1965**, 1351.
[124] R.J. Klinger and J.K. Kochi, *J. Phys. Chem.*, 85, **1981**, 1731.
[125] E. Gileadi and U. Eisner, *J. Electroanal. Chem.* , 28, **1981**, 81.
[126] A. J. Bard, L. R. Faulkner," Electrochemcal Methods", *John Wiley & Sons, New York*, 2nd ed., **2001**.
[127] E. Laviron, *J. Electroanal.Chem.,* 100, **1979**, 263.
[128] B. Speiser*, Chem. in unserer Zeit* , 62, **1981**, 62.
[129] J. C. Myland, K. B. Oldham, *Anal. Chem.,* 72, **2000**, 3972.
[130] F. H. Beyerlein , R. S. Nicholson, *Anal. Chem.*, 40, **1968**, 286.
[131] V. M. Schmidt: "Elektrochemische Verfahrenstechnik", John Wiley & Sons, **2003**, 162
[132] M. Drescher, *Chem. in unserer Zeit,* 46, **2012**, 150.
[133] Z. Zhou, "Phenothiazine, thiazolium and sulfonic acid functionalized hybrid materials and their applications in electronics, optics and catalysis", *dissertation, TU-Kaiserslautern,* **2009**.
[134] B. Paduszek, M. K. Kalinowski, *Electrochem. Acta,* 28, **1983**, 639.
[135] J.-P. Billon, G. Cauquis, J. Combrisson, and A. M . Li, *Bull. Soc. Chim. France*, 11-12, **1960**, 2062.
[136] K. Memminger, Cyclische und Oligomere Phenothiazin-Derivate: Modelle Für neuartige Lochtransport-materialien, *dissertation, Ruprecht-Karls-Universität*, **2007**.
[137] P. C. Dwivedi, K. G. Rao, S. N. Bhat, C. R. Rao, *Spectrochimica Acta*, 31, **1975**, 129.
[138] D. Sun, S. V. Rosokha, J. K. Kochi, *J. Am. Chem Soc.*, **126**, **2004**, 1388.
[139] T. Suga: "Redox-Active Radical Polymers: Synthesis and Application as an Organic-Derived Secondary Battery", *dissertation, Waseda-Univer*sity, **2007**.
[140] M. Ucar, A. O. Solak, M. L. Aksu, M. Toy, *Turk. J. Chem.,* 26, **2002**, 509.
[141] N. K. Bhatti, M. S. Subhani, A. K. Qureshi, A. Rahman, *Turk. J. Chem.,* 29, **2005,** 659.
[142] S. Bollo, S. Finger, J. Sturm, L. J. Nunez-Vergara, J. Squella, *Electrochem. Acta,* 52, **2007**, 4892.
[143] H. H. Yang, R. L. Mccreery, *Anal. Chem.,* 71, **1999**, 4081.
[144] H. J. Dahms, *Phys. Chem.* , 72, **1968**, 362.
[145] I. Ruff, V. J. *J.* Friedrich, *Phys. Chem.*, 75, **1971**, 3297.
[146] K. Nakahara, K. Oyaizu, H. Nishide, *J. Mater. Chem.,* 22, **2012**, 13669.
[147] K. Oyaizu, Y. Ando, H. Konishi, H. Nishide, *J. Am. Chem Soc.,* 130, **2008**, 14459.
[148] L. Levy, T. N. Tozer, L. D. Tuck, D. B. Loveland, *J. Medic. Chem.,* 15, **1972**, 898.
[149] D. Clarke, B. C. Gilbert, P. Hanson, C. M. Kirk, *J. Am. Chem Soc. Perk.,* 2, **1978**, 1103.
[150] P. H. Sackett, J. S. Mayausky, T. Smith, S. Kalus, R. L. Mccreery, *J. Medic. Chem.,* 24, **1981**, 1342.
[151] J. C. J. Bart, "Plastics additives: advanced industrial analysis", *IOS Press*, **2006**.
[152] M. Borzo, J. C. Heubeck, J. A. Potenza, B. E. Wagner, *J. Coll. Interf. Sci.*, 97, **1984**, 428.
[153] R. Mukherjee, A. V. Thomas, A. Krishnamurthy, N. Koratkar, *ACS Nano,* 6 (9), **2012,** 7867.
[154] Q. D. Ling, D. J. Liaw, C. Zhu, D. H. Chan, E. T. Kang, K. G. Neoh, *Prog. Polym. Sci.,* 33, **2008,** 917.

[155] A. Stikeman, *Technol. Rev.*, 105, **2002**, 31.
[156] D. Prime, S. Paul, *Phil. Trans. Roy Soc A.,* 367, **2009**, 4141.
[157] R. Bennewitz, J. N. Crain, A. Kirakosian, J. L. Lin, J. L. Mcchesney, D. Y. Petrovykh, F. J. Himpsel, *Nanotechnology,* 13, **2002**, 499.
[158] D. M. Eigler, E. K. Schweizer, *Nature*, 344, **1990**, 524.
[159] A. Sato, Y. Tsukamoto, *Nature*, 363, **1993**, 431.
[160] H. J. Mamin, P. H. Guethner, and D. Rugar, *Phys. Rev. Lett.*, 65, **1990**, 2418.
[161] H. J. Mamin and D. Rugar, *Appl. Phys. Lett.*, 61, **1992**, 1003.
[162] P. Vettiger et al., *IEEE Trans. on Nanotechnology*, 1, **2002**, 39.
[163] A. Jo, W. Joo, W. H. Jin, H. Nam, J. K. Kim, *Nature Nanotechnology,* 4, **2009,** 727.
[164] Storage concept for Millipede: "http://www.zurich.ibm.com/st/storage/concept.html", **2002**.
[165] P. Vettiger, J. Brugger, M. Despont, U. Drechsler, U. Dürig, W. Hgberle, M. Lutwyche, H. Rothuizen, R. Stutz, R. Widmer, G. Binnig, *Microelectron. Eng.,* 46, **1999,** 11.
[166] H. Kado, T. Tohda, *Appl. Phys. Lett.,* 66, **1995,** 2961.
[167] T. Gotoh, K. Sugawara, K. Tanaka, *J. Non-Cryst Sol.,* 299-302, **2002**, 968.
[168] M. H. Lee, C. S. Hwang, *Nanoscale,* 3, **2011,** 490.
[169] R. Waser, R. Dittmann, G. Staikov, K. Szot, *Adv. Mater.,* 21, **2009,** 2632.
[170] M. Cavallini, F. Biscarini, S. Léon, F. Zerbetto, G. Bottari, D. A. Leigh, *Science,* 299, **2003**, 531.
[171] X. Yu, H. Peng, C. Ran, L. Sun, R. Zhang, Z. Liu, *Appl. Phys. Lett.,* 86, **2005**, 1331051.
[172] T. Ono, S. Yoshida, M. Esashi, *Nanotechnology,* 14, **2003**, 1051.
[173] S. Yoshida, T. Ono, S. Oi, M. Esashi, *Nanotechnology,* 16, **2005,** 2516.
[174] S. Yoshida, T. Ono, M. Esashi, *Nanotechnology,* 18, **2007**, 505302.
[175] S. Yoshida, T. Ono, M. Esashi, *Nanotechnology,* 19, **2008**, 475302.
[176] J. Stejskal, R. G. Gilbert, *Pure Appl. Chem.,* 74 (5), **2002**, 857-867.
[177] R. Mazeikiene, A. Malinauskas, *Europ. Pol. Journal,* 38, **2002,** 1947.
[178] R. Chattopadhyay: "Surface Wear-Analysis, Treatment, and Prevention", *OH, USA: ASM-International*, **2001**.
[179] M. H. Jones, and D. Scott: "Industrial Tribology: the practical aspects of friction, lubrication, and wear" *New York, Elsevier Scientific Publishing Company*. , Ed. 8, **1983**.
[180] U. Kunze, B. Klehn, *Adv. Mater.,* 11, **1999**, 1473.
[181] R. H. Schmidt, G. Haugstad, W. L. Gladfelter, *Langmuir,* 19, **2003**, 10390.
[182] X. P. Wang, M. M. T. Loy, X. Xiao, *Nanotechnology,* 13, **2002**, 478.
[183] R. Kaneko, E. Hamada, *Wear,* 162-164, **1993,** 370.
[184] B. Bhushan, K. J. Kwak, M. Palacio, *J. Phys.: Condens. Matter,* 20, **2008**, 365207.
[185] O.M. Leung, M.C. Goh, *Science*, 255, **1992**, 64.
[186] T. Kaule, Y. Zhang, S. Emmerling, S. Pihan, R. Foerch, J. Gutmann, H. J. Butt, R. Berger, U. Duerig, A. W. Knoll, *ACS Nano,* 7, **2013**, 748.
[187] R. Berger, Y. Cheng, R. Förch, B. Gotsmann, J. S. Gutmann, T. Pakula, U. Rietzler, W. Schärtl, M. Schmidt, A. Strack, J. Windeln, H. J. Butt, *Langmuir,* 23, **2007**, 3150.
[188] U. Zerweck, C. Loppacher, T. Otto, S. Grafström, L. M. Eng, *Phys. Rev. B*, 71, **2005**, 125424.
[189] A. Bandyopadhyay, A. J. Pal, *Appl. Phys. Lett.,* 82, **2003**, 1215.
[190] A. Bandyopadhyay, A. J. Pal, *Appl. Phys. Lett.,* 84, **2004**, 999.
[191] K. L. Wang, T. Y. Tseng, H. L. Tsai, S. C. Wu, *J. Polym. Sci., A,* 46, **2008**, 6861.
[192] K. Kim, S. Park, S. G. Hahm, T. J. Lee, D. M. Kim, J. C. Kim, W. Kwon, Y. G. Ko, M. Ree, *J. Phys. Chem. B,* 113, **2009,** 9143.
[193] H. Wang, M. Bruna, P. Olivero, S. Borini, F. Picollo, O. Budnyk, F. Bosia, P. B. Pastuović, N. Skukan, M. Jaksić, E. Vittone, *IOP Conf. Ser.: Mater. Sci. Eng.,* 16 012004, **2010,** 1.

[194] A. Majumdar, P. I. Oden, J. P Carrejo, L. A. Nagahara, J. J. Graham, J. Alexander, *Appl. Phys. Lett.*, 61, **1992**, 2293.
[195] X. N. Xie, H. Chung, C. H. Sow, A. Bettiol, A. T. S.Wee, *Adv. Mater.,* 17, **2005**, 1386.
[196] X. N. Xie, H. Chung, C. H. Sow, K. Adamiak, A. T. S. Wee, J. Am. Chem. Soc., 127, **2005**, 15562.
[197] C. Huang, G. Jiang, R. Advincula, *Macromolecules,* 21, **2008**, 4661.
[198] K. Oyaizu, A. Hatemata, W. Choi, H. Nishide, *J. Mater. Chem.,* 20, **2010**, 5404.
[199] T. Hyakutake, J. Y. Park, Y. Yonekuta, K. Oyaizu, H. Nishide, R. Advincula, *J. Mater. Chem.,* 20, **2010**, 9616.
[200] T. Uchida, M. Ito, K. Kozawa, *Bull. Chem. Soc. Japan*, **1983**, 56, 577
[201] M. Sailer, "Elektronische Kommunikation auf molekularer Ebene: Aufbau und Untersuchung höherer Phenothiazin-Oligomere und -Polymere", *dissertation, Ruprecht-Karls-Universität*, **2006**.
[202] Millipede memory: "http://www.ieeeghn.org/wiki/index.php/IBMs_ Millipede_Memory_Chip", **2013**.
[203] Millipede memory: "http://de.wikipedia.org/wiki/Millipede", **2013**.
[204] S. L. Weber, N. Haberkorn, P. Theato, R. Berger, *Nano Letters,* 10, **2010**, 1194.
[205] S. G. Hahm, S. Choi, S. H. Hong, T. J. Lee, S. Park, D. M. Kim, J. C. Kim, W. Kwon, K. Kim, M. J. Kim, O. Kim, M. Ree, *J. Mater. Chem.,* 19, **2009**, 2207.
[206] G. Reiter, *Phys. Rev. Lett.,* 68, **1992**, 75.
[207] X. Yang, J. Loos, *Macromolecules,* 40, **2007**, 1353.
[208] R. Barbey, L. Lavanant, D. Paripovic, N. Schüwer, C. Sugnaux, S. Tugulu, H. A. Klok, *Chem. Rev.,* 109, **2009,** 5437.
[209] L. Bugnon, C. J. H. Morton, P. Novak, J. Vetter, P. Nesvadba, *Chem. Mater.*,19, **2007**, 2910.
[210] Y. H. Wang, M. K. Hung, C. H. Lin, H. C. Lin, J. T. Lee, *Chem. Comm.,* 47, **2011**, 1249.
[211] T. Ibe, R. B. Frings, A. Lachowicz, S. Kyo, H. Nishide, *Chem. Comm.,* 46, **2010**, 3475.
[212] K. Kojima, T. Nakahira, K. Honzawa, S. Iwabuchi, *Macromol. Rap. Com.,* 7, **1986**, 365 - 368
[213] S. Alexander, *Journal de Physique,* 38, **1977**, 977.
[214] P. G. de Gennes, *Macromolecules,* 13, **1980**, 1069.
[215] S. T. Milner, *Science,* 251, **1991**, 905.
[216] R. Berger, Y. Cheng, R. Förch, B. Gotsmann, J. S. Gutmann, T. Pakula, U. Rietzler, W. Schärtl, M. Schmidt, A. Strack, J. Windeln, H. J. Butt, *Langmuir,* 23, **2007**, 3150.
[217] B. Bhushan, K. J. Kwak, M. Palacio, *J. Phys.: Condens. Matter,* 20, **2008,** 365207.
[218] B. Gotsmann, A. W. Knoll, R. Pratt, J. Frommer, J. L. Hedrick, U. Duerig, *Adv. Func. Mat.,* 20, **2010**, 1276.
[219] B. Gotsmann, U. T. Duerig, S. Sills, J. Frommer, C. J. Hawker, *Nano Letters,* 6, **2006**, 296.
[220] M. H. Lee, C. S. Hwang, *Nanoscale,* 3, **2011**, 490.
[221] K. Matyjaszewski, J. Xia, *Chem. Rev.,* 101, **2001,** 2921.
[222] A. Ramakrishnan, R. Dhamodharan, J. Rühe, *Macromol. Rap. Com.,* 23, **2002**, 612.
[223] T. K. Tam, M. Ornatska, M. Pita, S. Minko, E. Katz, *J. Phys. Chem. C,* 112, **2008**, 8438.
[224] G. L. Whiting, H. J. Snaith, S. Khodabakhsh, J. W. Andreasen, D. W. Breiby, M. M. Nielsen, N. C. Greenham, R. H. Friend, W. S. Huck, *Nano Letters,* 6 (3), **2006,** 573-578
[225] B. Y. Kim, E. L. Ratcliff, N. R. Armstrong, T. Kowalewski, J. Pyun, *Langmuir,* 26, **2010**, 2083.
[226] S. V. Orski, K. H. Fries, G. R. Sheppard, J. Locklin, *Langmuir,* 26, **2010**, 2136.
[227] D. Kessler, N. Metz, P. Theato, *Macromol. Symp.,* 254, **2007,** 34.
[228] K. Matyjaszewski, T. P. Davis, "HANDBOOK OF RADICAL POLYMERIZATION", *Wiley Interscience,* **2002**.
[229] K. Matyjaszewski, H.-J. Paik, P. Zhou, S.J. Diamanti, *Macromolecules,* 34, **2001**, 5125.
[230] T.E. Patten, J. Xia, T. Abernathy, K. Matyjaszewski, *Science* , *272*, **1996**, 866.

[231] K. Davis, H.-J. Paik, K. Matyjaszewski, *Macromolecules*, 32, **1999**, 1767.
[232] T. Grimaud, K. Matyjaszewski, *Macromolecules*, *30*, **1997**, 2216.
[233] J.S. Wang, K. Matyjaszewski, *J. Am. Chem. Soc.* , 117, **1995**, 5614
[234] D.M. Haddleton, M.C. Crossman, K.H. Hunt, C. Topping, C. Waterson, K.G. Suddaby, *Macromolecules*, 30, **1997**, 3992.
[235] S. K. Nett, G. Kircher, J. S. Gutmann, *Macromol. Chem. Phys.,* 210, **2009**, 971.
[236] S. Ding, J. A. Floyd, K. B. Walters, *J. Polym. Sci. A,* 47, **2009,** 6552.
[237] J. W. Ochsmann, S. Lenz, P. Lellig, S. G.J. Emmerling, A. A. Golriz, P. Reichert, J. You, J. Perlich, S. V. Roth, R. Berger, J. S. Gutmann, *Macromolecules*, 45, **2012**, 3129.
[238] D. Julthongpiput, Y. H. Lin, J. Teng, E. R. Zubarev, V. V. Tsukruk, *Science,* 125, **2003**, 15912.
[239] O. Prucker, J. Rühe, *Macromolecules*, 31, **1998**, 592.
[240] O. Prucker, J. Rühe, *Macromolecules*, 31, **1998**, 602.
[241] M. Ejaz, S. Yamamoto, K. Ohno, Y. Tsujii ***and*** T. Fukuda, *Macromolecules*, 31, **1998**, 5934.
[242] J. R. Ell, D. E. Mulder, R. Faller, T. E. Patten, T. L. Kuhl, *Macromolecules*, 42, **2009**, 9523.
[243] K. Matyjaszewski, P. J. Miller, N. Shukla, B. Immaraporn, A. Gelman, B. B. Luokala, T.M. Siclovan, G. Kickelbick, T. Vallant, H. Hoffmann and T. Pakula, Macromolecules, 32, **1999**, 8716.
[244] T. Von Werne and T. E. Patten, J. Am. Chem. Soc., 121 (32), **1999**, 7409–7410
[245] J. Pyun, S. J. Jia, T. Kowalewski, G. D. Patterson, K. Matyjaszewski, *Macromolecules*, 36, **2003**, 5094.
[246] S. Yamamoto, M. Ejaz, Y. Tsujii, T. Fukuda, *Macromolecules*, 33, **2000,** 5608.
[247] R. L. Jones and R. W. Richards: "Polymers at Surfaces and Interfaces", *Cambridge University Press, Cambridge*, **1999**.
[248] N. A. Kumar and C. Seidel, *Macromolecules*, 38, **2005**, 9341.
[249] M. D. Rowe, B. A. Hammer, S. G. Boyes, *Macromolecules,* 41, **2008**, 4147.
[250] M. Tolan: "X-ray scattering from soft matter thin films", *Springer-Verlag,* **1999**.
[251] L. Névot and P. Croce, *Rev. Phys. Appl.* ,15, **1980**, 761.
[252] K. Siegbahn et al.,*Nova Acta Regiae Soc. Sci.*, 20, **1967.**
[253] H. Hertz, *Ann. Physik*, 31, **1887**, 983.
[254] A. Einstein, *Ann. Physik*, 17, **1905**, 132.
[255] NIST XPS Home page: "http://srdata.nist.gov/xps/Default.aspx", **2013**.
[256] L. G. Parratt, *Phys. Rev.* ,95, **1954**, 359.
[257] G. G. Bumbu, G. Kircher, M. Wolkenhauer, R. Berger, J. S. Gutmann, *Macromol. Chem. Phys.,* 205, **2004**, 1713.
[258] V. P. Privalko, *Macromolecules,* 13, **1980**, 370.
[259] A. Kimura, S. Yoshimoto, Y. Akano, H. Hirata, S. Kusabayashi, N. Kasai, *J. Polym. Sci. A*, 2, **1970**, 643.
[260] S. A. Pihan, S. G. Emmerling, H. J. Butt, J. S. Gutmann, R. Berger, *Wear,* 271, **2011**, 2852.
[261] K. A. Aamer, G. N. Tew, *J. Polym. Sci. A*, 45, **2007**, 5618.
[262] A. Godwin, M. Hartenstein, A. H. E. Müller, S. Brocchini, *Polym. Preprints* , 41, **2000**, 1002.
[263] W. G. Son, J. Kim, J. P. Seo, J. Yoon, M. Choi, L. Y. Lee, I. Lee, *Vet. Anaesth. Analg.,* 38, **2011**, 510.
[264] R. Ali, O. B. Siew, *Jurnal Teknologi,* 45, **2006**, 31.
[265] L. X. Sun, A. M. Reddy, N. Matsuda, A. Takatsu, K. Kato, T. Okada, *Anal. Chim. Acta,* 487, **2003**, 109.
[266] G. G. Bumbu, M. Wolkenhauer, G. Kircher, J. S. Gutmann, R. Berger, *Langmuir,* 23, **2007**, 2203.
[267] D. F. Siqueira, K. Kohler, M. Stamm, *Langmuir,* 11, **1995,** 3092.

[268] W. Jakubowski, K. Matyjaszewski, *Macromolecules*, 38, **2005**, 4139.
[269] K. Matyjaszewski, H. Dong ,W. Jakubowski ,J. P. and A. Kusumo*, Langmuir*, 23, **2007**,4528.
[270] H. Dong, , W. Tang, K. Matyjaszewski, *Macromolecules*, 40, **2007**, 2974.
[271] D. Sun, S. V. Rosokha, J. K. Kochi, *J. Am. Chem Soc.,* 126, **2004**, 1388.
[272] N. v. Malm, J. Steiger, R. Schmechel, H. v. Seggern, *J. Appl. Phys.,* 89, **2001**, 5559.
[273] Y. Shang, Y. Wen, S. Li, S. Du, X. He, L. Cai, Y. Li, L. Yang, H. Gao, Y. Song, *J. Am. Chem Soc.,* 129, **2007**, 11674.
[274] M. Winter, J. O. Besenhard, *Chemie in unserer Zeit*, 33, **1999**, 252.
[275] L. Michaelis , M. P. Schubert, *Chem. Rev.*, 22, **1938**, 437.
[276] S. Igarashi, A. N. Itakura, M. Toda, M. K. Chue, A. N. Chifen, R. Förch, R. Berger, *Sensors and Actuators B* , 117, **2006**, 43.
[277] O. Meincke, D. Kaempfer, H. Weickmann, C. Friedrich, M. Vathauer, H. Warth, *Polymer,* 45, **2004**, 739.
[278] Lanxess homepage, High heat resistance and good coating adhesion: Conductive polyamide 6 for powder coating: "http://lanxess.com/en/corporate/about-lanxess/company-news/?tx_editfiltersystem _pi1[cmd]= detail&tx_editfiltersystem_news_pi1[uid]=16997", **2010**.
[279] Y. Wu, L. Nolan, S. Coyle, K. Lau, G. G. Wallace, D. Diamond, *29th Annual International Conference of the IEEE: Engineering in Medicine and Biology Society, EMBS*, **2007**, 4090.

X. Abbreviations

a	interchain distance
A	electrode surface area
a.u.	arbitrary unit
A’	static conductance
abs.	absolute
ACN	acetonitrile
AE	activated ester
AEPCA	N-(2-aminoethyl)-10H-phenothiazine-10-carboxamide
AHPCA	N-(6-aminohexyl)-10H-phenothiazine-10-carboxamide
A_i	absorbance intensity
AIBN	azobisisobutyronitrile
aliphat	aliphatic
APT	10-allyl-10H-phenothiazine
aromat	aromatic
ATR	attenuated total reflection
ATRP	atomic transfer radical polymerization
BBA	4-bromobenzaldehyde
BCP	1-bromo-3-chloropropane
BL	bit line
BOC	*N*-tert-butoxycarbonyl
BPC	tert-butyl phenyl carbonate
BPVT	1-(3-bromopropyl)-4-vinylbenzene
br	broad
c	speed of light
C(0,t)	time dependent concentration of the redox species at the electrode interface
CA	chrono amperometry
CE	counter electrode
C_m	capacity per mass
$C_{m,c}$	capacity per mass in the charging step
$C_{m,d}$	capacity per mass in the discharging step
$C_{m,theo}$	theoretical capacity per mass
C_{Ox}	concentration of the oxidized species
C_{Ox}^*	concentration of the oxidized species at the electrode interface
CP	chrono potentiometry
C-rate	charging rate
C_{Red}	concentration of the reduced species
C_{Red}^*	concentration of the reduced species at the electrode interface
CV	cyclic voltammetry
CVB	1-(chloromethyl)-4-vinylbenzene
d	duplett
D_{app}	apparent diffusion constant
dB	decibel
DBN	di-tert-butyl nitroxide
DCC	N,N'-Dicyclohexylcarbodiimide
DCC	N,N'-Dicyclohexylcarbodiimide
DCM	dichloromethane
dd	double duplett
D_{ex}	self exchange diffusion constant
df	film thickness
DMAP	4-(dimethylamino)-pyridine

DME	dimethoxyethane
DMF	dimethylformamide
DMSO	dimethylsulfoxide
D_{phys}	physical diffusion
DPPH	1,3-nitroxide N,N -diphenyl-N-picrylhydrazyl
DPVB	2,5-di oxopyrrolidin- 1-yl 4-vinylbenzoate
Δq_z	difference of wave vector transfer in z-direction between Kiessig fringes
DSC	differential scanning calorimetry
d_π	distance between π-stacked rings
E	electrode potential
E_0	standard electrode potential
$E_{1/2}$	average between the anodic and cathodic peak potential
E_{beam}	indcident beam energy
E_{bind}	specific binding energy
EC	ethylene carbonate
EDA	ethylenediamine
E_E	final potential
E_{ent}	entropic energy of the stretched chains
E_{eq}	electrode potential at equilibrium
E_{int}	interaction energy between chain segments
E_{kin}	specific kinetic energy
E_{pa}	anodic peak potential
$E_{pa/2}$	half wave anodic potential
E_{pc}	cathodic peak potential
EPROM	Electrically Programmable Read Only Memory
E-rate	discharging rate
E_S	Startting potential
ESI-MS	electron spray ionization mass spectroscopy
ESR	electron spin resonance
ET	electron transfer
F	Faraday constant
f	frequency
FeRAM	ferroelectric based random access memory
FTIR	Fourier Transformed Infrared
g	Landé factor
G	Gauss
GC	glassy carbon
GHz	giga hertz
GPC	gel permeation chromatography
h	Planck constant
H	magnetic field
HC_1	helical C_1 symmetry
HDA	1,6-hexanediamine
HOMO	highest occupied molecular orbital
i_p	peak current
i_{pa}	anodic peak current
$i_{pa/2}$	half wave anodic current
i_{pc}	cathodic peak current
ITO	indium tin oxide
j	current denisty
j_{Far}	faradaic current density
k_0	standard heterogeneous rate constant
k_a	activation rate constant
k_d	deactivation rate constant

K_{eq}	activation-deactivation equilibrium constant
kHz	kilo Hertz
k_i	initiation rate constant
k_p	rate constant of the polymer growth setp
KPFM	Kelvin probe force microscopy
l	path length
L	ligand
LAH	lithium aluminum hydride
LUMO	lowest unoccupied molecular orbitals
m	multiplet
M	molar mass of monomer
M.p.	melting point
MAC	methacryloyl chloride
MB	methylene blue
mBOC	mono N-tert-butoxycarbonyl
MHz	mega Hertz
MMA	methyl methacrylate
M_n	number average *molecular weight*
MP	N-methylphenothiazine
MPCA	10-methyl-10H-phenothiazine-3-carbaldehyde
MPCN	10-methyl-10H-phenothiazine-3-carbonitrile
MPCO	10-methyl-10H-phenothiazine-3-carbaldehyde oxime
MPE	1-(10-methyl-10H-phenothiazin-3-yl)ethanone
MPEMA	1-(10-methyl-10H-phenothiazin-3-yl)ethyl methacrylate
MPET	1-(10-methyl-10H-phenothiazin-3-yl)ethanol
MPHDA	N-((10-methyl-10H-phenothiazin-3-yl)methyl)hexane-1,2-diamine
MPMA	(10-methyl-10H-phenothiazin-3-yl)methanamine
MTPPB	methyltriphenylphosphonium bromide
MVPT	10-methyl-3-vinyl-10H-phenothiazine
n	refractive index
N_A	Avogadro constant
n_e	number of electrons
NHS	N-hydroxysuccinimide
n_m	molar amount of the redox moieties
NMB	new methylene blue
NMF	N-methylfomanilid
NMP	1-methyl-2-pyrrolidone
NMR	nuclear magnetic resonance
NO	nitric oxide
n_{Ox}^*	number of oxidized species at the electrode interface
OFET	organic field effect transistor
OLED	organic Light Emitting Diodes
OMD	organic based memory devices
p	pentet
P3HT	poly(3-hexylthiophene)
PANI	polyaniline
PBA	4-(10H-phenothiazine-10-yl)benzaldehyde
PBS	4-bromostyrene
PC	propylene carbonate
PCC	phenothiazine-10-carbonyl chloride
PCEMMA	poly[2-(N-carbazolyl)ethyl methacrylate-co-methacrylic acid]
PDI	polydispersity index
PDPVB	poly 2,5-di oxopyrrolidin- 1-yl 4-vinylbenzoate
PE	printable electronics

PFF	pentafluorphenol
PFMA	perflourphenyl methacrylate
PLED	polymer Light Emitting Diodes
PMMA	poly methylmethacrylate
P_n	polymer chain segment
PNMA	poly(N-tert-butyl-N-nitroxymethacrylamide)
POC	phosphorus oxychloride
PPFMA	poly perflourphenyl methacrylate
PPFMA	poly perflourphenyl methacrylate
ppm	parts per million
PS	polystyrene
Pt	platinum
PTBO	potassium tert-butoxide
PTMA	poly(2,2,6,6-tetramethylpiperidinyloxyl-4-yl methacrylate)
PVBPT	poly10-(4-vinylbenzyl)-10H-phenothiazine
PVDF	polyvinyldiflouridine
PVMPT	poly-3-vinyl-N-methylphenothiazine
PVPPP	poly10-(3-(4-vinylphenyl)propyl)-10H-phenothiazine
q	quartet
quart	quarternary
q_z	wave verctor transfer in z direction
R	the universal gas constant
R	organic rest
RAFT	reversible-Addition Fragmentation Chain Transfer
RAM	random access memory
RE	refernce electrode
r_f	Fresnel coefficient
R_f	Fresnel reflectivity
RFID	radio frequency identification
RMS	route mean square
ROM	read only memory
RRAM	resistive Random Access Memory
s	singulett
SAM	self assembling monolayer
SCE	saturated calomel electrode
SFM	scanning force microscopy
SI-ATRP	surface initiated atomic transfer radical polymerization
SOMO	singly Occupied Molecular Orbital
t	triplet
T	Measurement temperature
t	measurement time
Tb	terabit
TBAEC	tert-butyl 2-aminoethylcarbamate
TBAPC	tetrabutylammonium perchlorate
TBPEC	tert-butyl 2-((10-methyl-10H-phenothiazin-3-yl)methylamino) ethylcarbamate
t_d	current decay time
TEA	triethylamine
TEMPO	2,2,6,6-tetramethylpiperidine-1-oxyl
TFA	trifluoroacetic acid
T_g	glass transition
TGA	thermogravimetry analysis
THF	tetrahydrofuran
TLC	thin layer chromatography
TNPIO	4,4,5,5-tetramethyl-2-(4-nitrophenyl)-4,5-dihydro-1H-imidazole-3-oxide-1-oxyl

T_{onset}	onset temperature
TPCEC	tert-butyl 2-(10H-phenothiazine-10-carboxamido)ethylcarbamate
TPCHC	tert-butyl 2-(10H-phenothiazine-10-carboxamido)hexylcarbamate
T_{peak}	peak temperature
U_E	erasing bias potential
U_R	reading bias potential
UV/Vis	ultra-violet /Visible
U_W	writing bias potential
VBA	4-vinylbenzoic acid
VBPT	10-(4-vinylbenzyl)-10H-phenothiazine
VPPP	10-(3-(4-vinylphenyl)propyl)-10H-phenothiazine
WE	working electrode
WL	word line
WORM	write once read many times
x	distance from the electrode surface
X	halogen group
XPS	X-ray photo electron spectroscopy
XRD	X-ray diffraction
XRR	X-ray reflectivity
α	energy distribution exponent of the trapped sites
α_c	critical incident angle
α_{ET}	charge transfer coefficient
α_i	incident angle
α_r	reflection angle
α_s	Snell's refraction angle
β	absorption term
ΔE_p	peak separation between anodic and cathodic peak
$\Delta E_{pa,1/2}$	width of the peak at half wave anodic current
ε	molar extinction coefficient
Γ	surface coverage of the electrode
Γ_g	grafting density
δ	chemical shift
δ_c	center to center distance between neigbouring moieties
δ_s	dispersion term
η	overpotential
λ	wavelength
μ_B	Bohr magneton
ν	scan speed
ν_c	critical scan speed
σ_{el}	electron density
τ	transition time
Φ_{spec}	spectrometer work function

XI. Curriculum vitae

Available in the printed version

Publications

- A. A. Golriz, T. Suga, R. Berger, H. Nishide, J.S. Gutmann*, J. Power Sources*, **2013**, in preparation.
- A. A. Golriz, T. Kaule, M. B. Untch, K. Kolman, R. Berger, J.S. Gutmann, *Appl. Mater. Interf.*, **2013**, DOI: 10.1021/am302869d.
- C. Tonhauser, A. A. Golriz, C. Moers, R. Klein, H.-J. Butt, H. Frey, *Adv. Mater.*, 24, **2012**, 5559.
- R. S. Kappes, F. Schönfeld, C. Li, A. A. Golriz, M. Nagel, T. Lippert, J. S. Gutmann, H.-J. Butt, *J. Appl, Phys.*, **2012**, submitted.
- J. W. Ochsmann, S. Lenz, P. Lellig, S. G. J. Emmerling, A. A. Golriz, P. Reichert, J. You, J. Perlich, S. V. Roth, R. Berger, J. S. Gutmann, *Macromolecules*, **2012**, 45, 3129-3136.
- L. García-Fernández, J. Cui, C. Serrano, Z. Shafiq, R. A. Gropeanu, V. San Miguel, J. I. Ramos, M. Wang, G. K. Auernhammer, S. Ritz, A. A. Golriz, R. Berger, M. Wagner, A. del Campo, Adv. Mater., **2012**, DOI: 10.1002/adma.201203362.

- A. A. Golriz, T. Kaule, J. Heller, M. B. Untch, M. Toda, S. Yoshida, T. Ono, H. J. Butt, J. S. Gutmann, R. Berger, *Nanoscale*, 3, **2011**, 5049.

- H.-J. Butt, M. B. Untch, A. A. Golriz, S. A. Pihan, R. Berger, *Phys. Rev.*, E (83), **2011**, 061604.

Presentations

- A. A. Golriz et al., oral presentation: "Redox active polymers based on phenothiazine moieties for energy and data storage application", *Invited guest at National Institute for Material Science, Tsukuba (Japan),* **2012**.

- A. A. Golriz et al., poster presentation: "Redox active polymers with phenothiazine moieties as p-type cathode material in rechargeable radical batteries", *SPM Workshop at MPIP, Mainz (Germany)*, **2011 (Poster price winner: 1st place)**.

- A. A. Golriz et al., oral presentation: "Patterning the Conductivity of Redox Active Polymers with Phenothiazine Moieties", *MRS Spring Meeting, San Francisco (USA)*, **2011**.

- A. A. Golriz et al., oral presentation: "Redox active polymers with phenothiazine moieties for nanoscale patterning via conductive scanning force microscopy", *Invited guest at Graduate School of Engineering of Tottori University, Tottori (Japan),* **2011**.

- A. A. Golriz et. al., poster presentation: "A 'Radical' Breakthrough in Polymer Memory Devices", *Zigmondy Colloqium, Münster (Germany*), **2010**.